# Advanced vibro-acoustic condensed models for multi-layer structures

Arasan Uthayasuriyan

N°d'ordre NNT : 2021LYSET009

**THÈSE de DOCTORAT DE L'UNIVERSITÉ DE LYON**
opérée au sein de
**École nationale des travaux publics de l'État**

**École Doctorale** N° ED162
**MEGA de Lyon**
**(Mécanique, Energétique, Génie civil, Acoustique)**

**Spécialité / discipline de doctorat** : Acoustique

Soutenue publiquement le 02/11/2021, par :
**Arasan UTHAYASURIYAN**

# Advanced vibro-acoustic condensed models for multi-layer structures

## Modèles condensés vibro-acoustiques avancés pour les structures multicouches

Devant le jury composé de :

| | | | |
|---|---|---|---|
| Ouisse, Morvan | Professeur des Universités | FEMTO-ST, ENSMM | Président |
| Dazel, Olivier | Professeur des Universités | LAUM, Université du Maine | Rapporteur |
| Ouisse, Morvan | Professeur des Universités | FEMTO-ST, ENSMM | Rapporteur |
| Rouleau, Lucie | Maître de Conférences | LMSSC, CNAM | Examinatrice |
| Ninic, Jelena | Assistant Professor | University of Nottingham | Examinatrice |
| Bécot, François-Xavier | Docteur | Matelys – Research Lab | Examinateur |
| Tanner, Gregor | Professor | University of Nottingham | Examinateur |
| Chronopoulos, Dimitrios | Associate Professor | K.U. Leuven | Co-directeur de thèse |
| Gourdon, Emmanuel | IDTPE HDR | LTDS, ENTPE | Co-directeur de thèse |
| Chevillotte, Fabien | Ingénieur de recherche | Matelys – Research Lab | Invité |

# Abstract

This thesis concerns the development of analytical condensed models to predict the vibro-acoustic responses of planar multi-layer structures. Typical structural components in, e.g., aerospace applications involve multi-layer composite panels and evaluation of vibro-acoustic indicators (for example, transmission loss) of these multi-layer structures through finite element analysis would result in expensive computational power and time. This is due to an increase in the total number of degrees of freedom which results from a complete description of each different layer in the multi-layer system. This challenge could be tackled by employing a condensed and equivalent single layer that simulates the vibro-acoustic behaviour of the multi-layer system which would require lesser computational storage that effectively reduces the computation time. In addition, condensed models enable us to understand the physical behaviour of the multi-layers at different frequency regimes. The existing equivalent plate models describe the propagation of bending and shear waves in multilayers, giving a useful prediction for vibroacoustic indicators across the range of audible frequencies if the multilayer structure does not contain soft material in terms of longitudinal compression. As the compressional (or dilatational) wave propagation is not employed in current models, they are applicable only to relatively thin multilayer systems.

In this context, this doctoral thesis addresses the four major research advancements made to these models. The first advancement focuses on the limits of applicability of plate theories, which are commonly employed in many vibroacoustic applications. As there are no clear-cut analytical expressions available in the literature for the frequency limits of plate theories, these expressions are obtained for an elastic solid layer of isotropic nature, through wavenumber and admittance analysis. Refined expressions for exact coincidence and critical frequencies are also provided by comparing the propagative wavenumbers in the single-layer plates. The Transmission Loss (TL) computations using plate theories are compared to the TL computed using the Transfer Matrix Method (TMM) for a variety of thin/thick and soft/stiff materials, to validate these frequency limits.

A simple condensed (or equivalent) plate model is developed as a second advancement, for three-layer sandwich structures made of isotropic materials. Even though the existing condensed plate models provide matched response with that of the principles of elasticity,

these models would consume considerable time for implementation processes. Therefore, to overcome this challenge, a simpler and easier version of the equivalent plate model is developed by observing the physical behaviours of a three-layer structure. The model requires only four key parameters that are sufficient to describe the natural behaviour of the three-layer structure at all frequencies. Validation of this simple model has been done by comparing its response with the existing equivalent plate model as well as the experimental data, which are observed to be well-matched.

In the third advancement, an advanced vibro-acoustic condensed model is developed for symmetric multi-layer structures including its dilatational effects. The novelty of this model lies in capturing both symmetric and anti-symmetric motions of the multi-layers while the existing condensed plate models could handle only the anti-symmetric motions. The condensed layer obtained through the presented model will have three dynamic mechanical properties by describing two decoupled admittances correspond to symmetric and anti-symmetric motions. The model is validated with the transmission loss responses obtained from the TMM for different multi-layer configurations.

As a final advancement of this thesis, a Finite Element (FE) scheme is proposed, to compute vibro-acoustic indicators from the novel condensed model that is developed as the third advancement of this thesis. The FE scheme consists of two decoupled condensed plates with corresponding dynamic intrinsic properties that are obtained from the new condensed model. Through multiple validation cases, the computational efficiency of the proposed condensed FE scheme has been shown, in comparison with the conventional three-dimensional FE approach.

**Keywords:** Condensed models, Equivalent plate models, Plate theories, Multi-layer structures, Flexural rigidities, Wavenumbers, Finite element analysis, Dilatational motion

# Résumé

Cette thèse concerne le développement de modèles analytiques condensés pour prédire les réponses vibro-acoustiques de structures multicouches planes. Le premier chapitre présente le contexte général suivi des objectifs de la thèse. Les composants structurels typiques des applications aérospatiales, par exemple, nécessitent l'utilisation de panneaux composites multicouches et l'évaluation des indicateurs vibro-acoustiques (par exemple, la perte par transmission) de ces structures multicouches par le biais d'une analyse par éléments finis entraînerait une puissance et un temps de calcul coûteux. Ceci est dû à une augmentation du nombre total de degrés de liberté résultant d'une description complète de chaque couche dans le système multicouche. Ce défi pourrait être relevé en utilisant une couche unique condensée équivalente qui simule le comportement vibro-acoustique du système multicouche, ce qui nécessiterait moins de stockage informatique et réduirait efficacement le temps de calcul. De plus, des modèles condensés nous permettent de comprendre le comportement physique des multicouches à différents régimes fréquentiels.

Le deuxième chapitre présente la revue de littérature détaillée des modèles vibro-acoustiques couramment utilisés pour analyser et caractériser les structures multicouches. Les publications clés concernent les modèles analytiques, y compris les modèles condensés (ou équivalents), et les méthodes expérimentales sont rassemblées pour fournir l'état de l'art du sujet d'étude.

Le troisième chapitre détaille l'arrière-plan théorique d'une méthode vibro-acoustique générique appelée "Méthode des Matrices de Transfert (TMM)", qui est traitée comme une méthode de référence pour comparer les modèles développés dans cette thèse. Une procédure de condensation préliminaire est présentée à partir de la matrice globale obetnue par la TMM.

Dans le quatrième chapitre, des expressions analytiques pour les limites fréquentielles de validité des théories des plaques couramment utilisées sont dérivées. Ces expressions sont obtenues pour une couche solide élastique de nature isotrope, par analyse du nombre d'onde et de l'admittance. Des expressions affinées pour les fréquences de coïncidence et critiques sont également fournies en comparant les nombres d'onde de propagation

dans les plaques monocouches. Les calculs de perte par transmission (TL) utilisant les théories des plaques sont comparés au TL calculé à l'aide de la TMM pour une variété de matériaux minces/épais et souples/rigides, afin de valider ces limites fréquentielles.

Le cinquième chapitre présente un modèle simple de plaque condensée (ou équivalente) pour des structures sandwich à trois couches constituées de matériaux isotropes. Même si les modèles de plaques condensées existants sont déjà très robustes, ces modèles peuvent prendre un temps considérable à implémenter. Par conséquent, pour surmonter ce défi, une version plus simple de modèle de plaque équivalente est développée en observant les différents comportements physiques d'une structure à trois couches.

Le sixième chapitre présente un modèle condensé vibro-acoustique avancé pour les structures multicouches symétriques épaisses, incluants les effets de dilatation. La nouveauté de ce modèle réside dans la capture des mouvements symétriques et antisymétriques des multicouches alors que les modèles de plaques condensées existants ne consideraient que les mouvements antisymétriques. La couche condensée obtenue grâce au modèle présenté aura trois propriétés élastiques dynamiques en décrivant deux admittances découplées correspondantes à des mouvements symétriques et antisymétriques.

Dans le septième chapitre, un schéma d'éléments finis (FE pour Finite Elements en Anglais) est proposé, pour calculer des indicateurs vibro-acoustiques à partir du nouveau modèle condensé donné par le sixième chapitre de cette thèse. Le schéma FE se compose de deux éléments de plaques condensées découplées avec des propriétés intrinsèques dynamiques correspondantes qui sont obtenues à partir du nouveau modèle condensé. Grâce à plusieurs cas de validation, l'efficacité de calcul du schéma FE condensé proposé est démontrée, en comparaison avec l'approche FE tridimensionnelle usuelle.

**Mots clés:** Modèles condensés, Modèles de plaques équivalentes, Théories des plaques, Structures multicouches, Rigidités en flexion, Nombres d'onde, Analyse par éléments finis, Mouvement de dilatation

## Acknowledgements

I would like to express my heartfelt thanks to my colleagues at Matelys-Research Lab, especially François-Xavier Bécot, Fabien Chevillotte and Luc Jaouen, who provided immense professional support and guidance throughout my research journey. Apart from the professionalism, their kind hearts helped me to lead a comfortable life in France, for which I am deeply thankful.

I am also grateful to my supervisors Dimitrios Chronopoulos, Emmanuel Gourdon and Gregor Tanner for the productive and constructive guidance on my research work. I would also like to acknowledge Olivier Dazel for the helpful inputs on the periodic boundary conditions.

I have to thank my colleagues, in particular, Abhilash Sreekumar, Vivek Thaminni Ramamoorthy and Fabien Marchetti for the pleasant discussions in and out of the research.

I sincerely acknowledge the European Commission which fully funded my research through the Marie Curie ITN project under the name 'No2Noise' (Grant No: 765472). Special thanks to the coordinators and managers of the 'No2Noise' project who facilitated me with the administrative procedures.

Finally, I would like to thank my family and friends for having faith in me and the constant support they gave throughout these years.

# Contents

# Nomenclature

| Symbol | Unit | Definition |
|---|---|---|
| $[K], [M], [C]$ | | Stiffness, mass and coupling matrices respectively |
| $[\breve{K}], [\breve{M}]$ | | Stiffness and mass matrices of anti-symmetric condensed plate respectively |
| $[\overline{K}], [\overline{M}]$ | | Stiffness and mass matrices of symmetric condensed plate respectively |
| $[H], [Q]$ | | Kinetic and compression energy matrices respectively |
| $\{W\}, \{P\}$ | | Nodal vectors of solid and fluid phases respectively |
| $\{\breve{W}\}, \{\overline{W}\}$ | | Nodal vectors of anti-symmetric and symmetric condensed plates respectively |
| $\{w_n\}$ | | Nodal displacement vector of air layer |
| $[B]$ | | Coupling matrix of anti-symmetric and symmetric condensed plates |
| $[B_b], [B_s]$ | | Strain-displacement matrices of bending and shear contributions respectively |
| $[D_b], [D_s]$ | | Constitutive stiffness matrices of bending and shear contributions respectively |
| $[N], [N^*]$ | | Shape function matrices of solid and fluid phases respectively |
| $[I_m]$ | | Inertial matrix |
| $\mathbf{V}$ | | State vector |
| $[T]$ | | Transfer matrix |
| $t$ | s | Time |
| $t_{\text{oblique}}$ | s | Transmission loss computation time for oblique wave excitation |
| $t_{\text{diffuse}}$ | s | Transmission loss computation time for diffuse field excitation |
| $u_x, u_y, u_z$ | m | Displacement along $x, y$ and $z$ directions respectively |
| $u_x^0, u_y^0, u_z^0$ | m | Mid-plane displacement along $x, y$ and $z$ directions respectively |
| $v_x, v_y, v_z$ | m s$^{-1}$ | Velocities along $x, y$ and $z$ directions respectively |
| $\sigma_{xz}, \sigma_{zz}$ | Pa | Shear and normal stresses respectively |
| $\phi_x, \phi_y$ | rad | Rotations about $x$ and $y$ directions respectively |
| $\phi$ | | Open porosity |
| $\rho_0$ | kg m$^{-3}$ | Air density |
| $\rho$ | kg m$^{-3}$ | Density |
| $\rho_{\text{eq}}$ | kg m$^{-3}$ | Equivalent density |
| $\widetilde{\rho}_{\text{eq}}$ | kg m$^{-3}$ | Equivalent dynamic density |
| $\widetilde{\rho}$ | kg m$^{-3}$ | Dynamic density |
| $\breve{\rho}_A$ | kg m$^{-3}$ | Dynamic anti-symmetric density |
| $\overline{\rho}_S$ | kg m$^{-3}$ | Dynamic symmetric density |
| $E$ | Pa | Young's modulus |
| $\widetilde{E}$ | Pa | Dynamic Young's modulus |
| $\widetilde{E}_{\text{eq}}$ | Pa | Equivalent dynamic Young's modulus |
| $E_{\text{ref}}$ | Pa | Young's modulus of the reference layer |

| Symbol | Unit | Definition |
|---|---|---|
| $p$ | Pa | Dynamic pressure |
| $P_0$ | Pa | Air equilibrium pressure |
| $c_0$ | m $s^{-1}$ | Speed of sound in air |
| $c$ | m $s^{-1}$ | Wave speed |
| $\widetilde{c}$ | m $s^{-1}$ | Dynamic wave speed |
| $h$ | m | Thickness of a layer |
| $h_t$ | m | Total thickness of the multi-layer |
| $b_{i,\text{eff}}$ | m | Transformed width of the $i-$th layer |
| $m_s$ | kg $m^{-2}$ | Total or equivalent mass per unit area |
| $\mathcal{M}$ | kg $m^{-2}$ | Mass per unit area of the skin |
| $\nu$ | | Poisson's ratio |
| $\nu_{\text{eq}}$ | | Equivalent Poisson's ratio |
| $\widetilde{\nu}$ | | Dynamic Poisson's ratio |
| $\nu_{\text{ref}}$ | | Poisson's ratio of the reference layer |
| $\eta$ | | Damping or loss factor |
| $\widetilde{\eta}$ | | Dynamic loss factor |
| $\widetilde{\eta}_{\text{eq}}$ | | Equivalent dynamic loss factor |
| $\eta_0$ | Pa s | Dynamic viscosity of air |
| $D$ | N m | Complex bending stiffness |
| $\widetilde{D}_{\text{eq}}$ | N m | Equivalent dynamic bending stiffness |
| $D_{\text{low}}$ | N m | Low-frequency asymptote of dynamic bending stiffness |
| $D_{\text{high}}$ | N m | High-frequency asymptote of dynamic bending stiffness |
| $D_T$ | N m | Bending stiffness at transition frequency |
| $G$ | Pa | Shear modulus |
| $\widetilde{G}_{\text{eq}}$ | Pa | Equivalent dynamic shear modulus |
| $G^*$ | Pa | Corrected shear modulus |
| $K$ | Pa | Bulk modulus |
| $\widetilde{K}$ | Pa | Dynamic bulk modulus |
| $\widetilde{K}_{\text{eq}}$ | Pa | Equivalent dynamic bulk modulus |
| $\lambda, \mu$ | Pa | Lamé coefficients |
| $\Pi_0$ | $m^2$ | Static viscous permeability |
| $\Pi_0'$ | $m^2$ | Static thermal permeability |
| $\kappa$ | | Shear correction factor |
| $\kappa_0$ | W $m^{-1}$ $K^{-1}$ | Air thermal conductivity |
| $k$ | rad $m^{-1}$ | Wavenumber |
| $k_0$ | rad $m^{-1}$ | Wavenumber of the incident air |
| $k_{\text{eq}}$ | rad $m^{-1}$ | Equivalent wavenumber |
| $k_t$ | rad $m^{-1}$ | Transverse wavenumber of the incident air |
| $k_p$ | rad $m^{-1}$ | Propagating wavenumber |
| $k_b$ | rad $m^{-1}$ | Bending wavenumber |
| $k_m$ | rad $m^{-1}$ | Membrane wavenumber |
| $k_s$ | rad $m^{-1}$ | Corrected shear wavenumber |
| $k_{RM}$ | rad $m^{-1}$ | Reissner-Mindlin plate wavenumber |
| $A_0$ | rad $m^{-1}$ | Lamb wavenumber of zeroth-order anti-symmetric mode |
| $S_0$ | rad $m^{-1}$ | Lamb wavenumber of zeroth-order symmetric mode |
| $\delta_l, \delta_s$ | rad $m^{-1}$ | Longitudinal and shear wavenumber respectively |

| Symbol | Unit | Definition |
|---|---|---|
| $\omega$ | rad $s^{-1}$ | Angular frequency |
| $f$ | Hz | Frequency |
| $f_{\text{comp}}$ | Hz | Compressional frequency |
| $f_{\text{cut-on}}$ | Hz | Cut-on frequency |
| $f_{\text{thin/thick}}$ | Hz | Frequncy limit of thin plate theory |
| $f_{\text{coinc}_{\text{thin}}}$ | Hz | Coincidence frequency of thin plate |
| $f_{\text{coinc}_{\text{thick}}}$ | Hz | Coincidence frequency of thick plate |
| $f_{\text{cri}_{\text{thin}}}$ | Hz | Critical frequency of thin plate |
| $f_{\text{cri}_{\text{thick}}}$ | Hz | Critical frequency of thick plate |
| $f_{\text{plate/solid}_{\text{oi}}}$ | Hz | Frequency limit of plate theories for oblique incidence |
| $f_{\text{plate/solid}_{\text{df}}}$ | Hz | Frequency limit of plate theories for diffuse field |
| $f_T$ | Hz | Transition frequency |
| $\theta$ | rad | Incident angle of the plane wave |
| $\theta'_x, \theta'_y$ | rad | Rotations of thin plate about $x$ and $y$ directions respectively |
| $Z_0$ | N s $m^{-3}$ | Characteristic impedance of air |
| $Z_s$ | N s $m^{-3}$ | Surface impedance |
| $Z_c$ | N s $m^{-3}$ | Characteristic impedance |
| $Z_A$ | N s $m^{-3}$ | Anti-symmetric impedance |
| $Z_S$ | N s $m^{-3}$ | Symmetric impedance |
| $Z_{\text{ep}}$ | N s $m^{-3}$ | Plate impedance |
| $Z_{\text{thin}}$ | N s $m^{-3}$ | Thin plate impedance |
| $Z_{\text{thick}}$ | N s $m^{-3}$ | Thick plate impedance |
| $Z_{\text{eq}}$ | N s $m^{-3}$ | Anti-symmetric impedance from equivalent plate model |
| $Z_{\text{S,eq}}$ | N s $m^{-3}$ | Equivalent symmetric impedance |
| $Z_{\text{A,eq}}$ | N s $m^{-3}$ | Equivalent anti-symmetric impedance |
| $Y_A$ | $m^3$ $N^{-1}$ $s^{-1}$ | Anti-symmetric admittance |
| $Y_S$ | $m^3$ $N^{-1}$ $s^{-1}$ | Symmetric admittance |
| $\widetilde{Y_S}$ | $m^3$ $N^{-1}$ $s^{-1}$ | Approximated symmetric admittance |
| $Y_{\text{eq}}$ | $m^3$ $N^{-1}$ $s^{-1}$ | Anti-symmetric admittance from equivalent plate model |
| $C_p$ | J $kg^{-1}$ $K^{-1}$ | Specific heat at constant pressure |
| $C_v$ | J $kg^{-1}$ $K^{-1}$ | Specific heat at constant volume |
| $C_k$ | | Ratio of bending and corrected shear wavenumbers |
| $C_y$ | | Minimum value of ratio between admittances |
| $\overline{C}$ | Pa | Compressional modulus |
| $\mathcal{C}$ | m $Pa^{-1}$ | Compliance of the core |
| $\Lambda$ | m | Viscous characteristic length |
| $\Lambda'$ | m | Thermal characteristic length |
| $\lambda_l$ | m | Longitudinal wavelength |
| $\lambda_{\text{min}}$ | m | Minimum wavelength |
| $\lambda_{\text{air}}$ | m | Air wavelength |
| $\alpha$ | | Sound absorption coefficient |
| $\alpha_0$ | | Static viscous tortuosity |
| $\alpha_\infty$ | | High frequency limit of the tortuosity |
| $\gamma_0$ | | Specific heat ratio |
| $\gamma'$ | | Coupling factor |
| $\epsilon$ | | Error percentage between wavenumbers of plate theories |
| $\epsilon'$ | | Fictitious value in flat shell stiffness matrix |

| Symbol | Unit | Definition |
|---|---|---|
| $\sigma$ | N s m$^{-4}$ | Airflow resistivity |
| $\tau$ | | Power transmission coefficient |
| $\vartheta$ | | Penalty factor on the shear modulus |
| $\psi$ | rad | Azimuthal angle of the plane wave |
| $\xi, \varrho$ | | Local coordinate directions of finite element |
| $q$ | N m$^{-2}$ | Load per unit area |
| $\bar{q}$ | | Number of finite elements per wavelength |
| $r$ | | Number of nodes |
| $w_n$ | m | Out-of-plane displacement |
| $\breve{w}_n, \overline{w}_n$ | m | Anti-symmetric and symmetric out-of-plane displacements respectively |
| $I_z$ | kg | Mass moment of inertia per unit area |
| $R$ | | Reflection coefficient |
| $\hat{R}$ | | Slope factor at transition frequency |
| $S$ | N m | Membrane stiffness |
| $T$ | | Pressure transmission coefficient |
| $X, Y$ | | Shear and structural geometric parameter respectively |

# Glossary

| | |
|---|---|
| 2D | Two-dimensional |
| 3D | Three-dimensional |
| dofs | Degrees of freedom |
| TMM | Transfer Matrix Method |
| FTMM | Finite Transfer Matrix Method |
| TL | Transmission Loss |
| FE | Finite Element |
| FEM | Finite Element Method |
| BEM | Boundary Element Method |
| SEA | Statistical Energy Analysis |
| DFT | Discrete Fourier Transform |
| CFT | Continuous Fourier Transform |
| IWC | Inhomogeneous Wave Correlation |
| FAT | Force Analysis Technique |
| CFAT | Corrected Force Analysis Technique |
| ESL | Equivalent Single Layer |
| CLT | Classical Lamination Theory |
| FSDT | First order Shear Deformation Theory |
| HSDT | Higher order Shear Deformation Theory |
| HOT | Higher Order Theory |
| LW | Layer-Wise |
| ZZ | Zig-Zag |
| RKU | Ross, Kerwin and Ungar |
| DB | Delany-Bazley |
| DBM | Delany-Bazley-Miki |
| JCA | Johnson-Champoux-Allard |
| JCAL | Johnson-Champoux-Allard Lafarge |
| JCAPL | Johnson-Champoux-Allard Pride Lafarge |
| BC | Boundary Condition |
| PML | Perfectly Matched Layer |

# List of Tables

# List of Figures

# Chapter 1

# Introduction

The global transport industries are leading worldwide in the advancement and production of structural products. In spite of that, the transport industries are facing three important challenges namely a) Oil dependency , b) Emission control and c) Competition [1]. Continuous technological developments is inevitable and crucial to overcome these challenges and to maintain a healthy success rate against its competitors. From the structural perspective, efficiency of the structure depends on the high strength to weight ratio of the materials used, especially in aeronautical and automotive industries. In the modern transport applications, multi-layer structures are of the relevance in this regard and this is achieved by reducing the structural mass without affecting the structural integrity which will greatly lead to low operation costs, fuel costs and consumption of energy.

Composites are materials made of at least two or more constituent materials with significantly different physical and chemical properties. As an example, a fibre reinforced composite will have two different materials called (a) fibre (typically glass or carbon) and (b) matrix (typically epoxy resin). When these two constituents are combined, they exhibit good or improved structural performance compared to their individual material characteristics. For example, in civil engineering applications, reinforced concretes and composite wood (plywood) are widely used. Although composites are good to improve the structural performance, they are not preferred candidates for the vibro-acoustic ap-

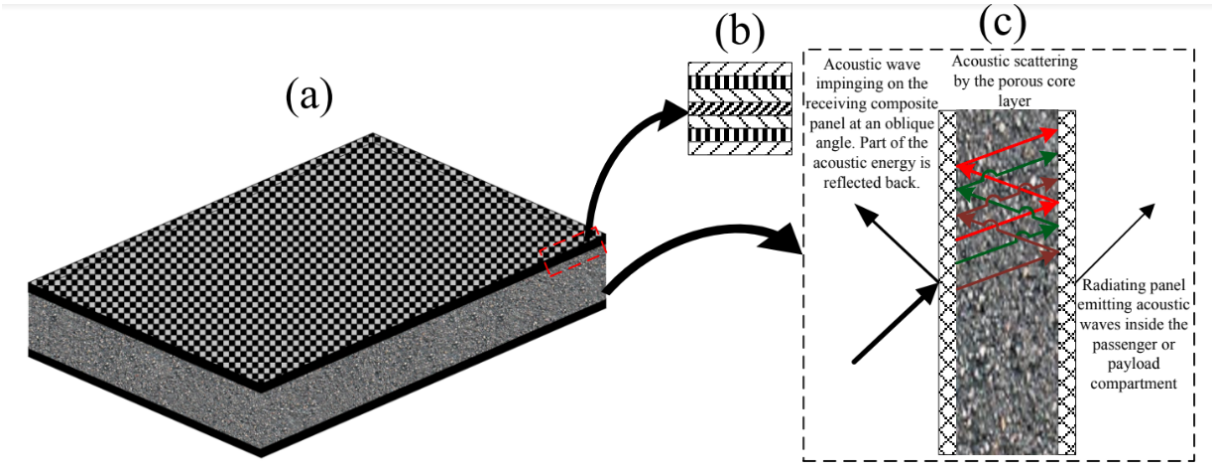


Figure 1.1: An illustrative example of a complex layered and composite panel, coupled with a metal foam layer (a), combining high structural rigidity, high acoustic attenuation, high structural damping and low mass. An illustration of the typically anti-symmetric layering for the composite face sheet (b), as well as of the acoustic transmission phenomenon through the modelled multi-layer structure (c) is also shown.

plications. As they are lightweight structures, they result in lower transmission loss at lower frequencies. Due to their higher stiffness along different directions, they often result in a valley of lower critical frequencies. Further, they lower the transmission loss after this critical valley as they are low dissipative in nature.

Comfort is the key factor which affects the quality and competitiveness of the structural products. Affecting the lives of humans worldwide, noise is the major form of the environmental pollution which has severe effects on the socio-economic relations. Though composite materials exhibit superior structural characteristics, they are found to be performing poor in vibration and acoustic isolation levels. Also, due to the increasing thickness, a very well known lightweight sandwich structure (made of composites Fig. 1.1) allows multiple number of vibration and acoustic waves propagating within them that affects their overall vibro-acoustic performance [2].

Increase in noise levels up to 7 dB (within certain frequency ranges) has been observed in the composites from replacing the conventional aerospace metallic structures. To improve the mechanical efficiency, passenger safety and comfort, vibro-acoustic isolation is unavoidable and important. Active noise control and visco-elatic damping mechanisms are usually employed, but this often leads to complex and heavy systems. While offering

Figure 1.2: Multi-layered structure with composite materials and poro-elastic foams.

improved vibro-acoustic behaviours, these "sound packages" compromise the lightweight benefits that comes from employing composite materials.

An exciting new alternative to these conventional sound packages is the employment of poro-elastic materials within these multi-layered composites. These porous materials can be coupled with existing multi-layer composite segments either as an additional poro-elastic layer, or as poro-elastic inclusions within a single layer. Poro-elastic materials are comprised of at least two phases: a solid phase constituted of the pore skeleton, and a fluid phase constituted of the interstitial pore fluid. This fluid is quite often assumed to be air, for acoustic studies. Multi-layers formed by combining layers of different nature (composites stacked with porous sound packages as shown in Fig. 1.2) offer many advantages over the conventional materials. In general, multi-layer structures have very high vibration damping capacity when compared to metallic structures, and they are far lighter than the active noise control mechanisms.

Multi-layers are also widely employed in the building industry, where sound insulation is a critical criterion. While using the traditional materials, such as concrete walls, increasing the thickness of a homogeneous layer increases the surfacic mass but also the bending stiffness. However, the usage of thick walls is not financially feasible. Another type of multi-layered material, known as a sandwich, was then used to attain performance comparable to or greater than traditional materials while having reduced wall thicknesses and costs. Sandwiches are also employed in transportation (for example, vehicle glazing) and personal protection (helmets, vests by ball).

Multi-layer materials are primarily appreciated for their versatile mechanical characteristics, which traditional homogeneous materials do not provide. Knowledge of their dynamic behaviour, on the other hand, is required to fully leverage their potentials. The characterization of the structure then appears as a fundamental aspect of the design process.

## Objectives and structure of the thesis

As different types of materials are used in the multi-layer system, modelling of this system often requires suitable mesh types for the material used and increases the total mesh count in the classical Finite Element modelling. Additionally, it would lead to high computation time due to these complexities. On the other hand, for particular frequency bands, it is still a significant challenge to design sandwich structures (multi-layered system) having optimized damping properties along with good sound insulation performances. Therefore, in many engineering cases, it is of high interest to condense the behaviour of a multi-layer system to a single layer material. This aims at reducing the mesh size of the Finite Element (FE) model, which will lead to less computation time.

Although the existing condensed (or equivalent) plate models are widely used, they make certain assumptions about the types of waves propagating in the structures. For example, if a multi-layer structure contains any soft layer which is sensitive to longitudinal compression, the breathing (or compressional) mode needs to be accounted in the theoretical formulation of the condensed models to correctly predict the vibro-acoustic behaviour of the system. Since the current condensed models assume constant normal displacement along the multi-layer thickness (thereby ignoring the thickness stretching motions of the structure), they restrict their applicability to only relatively thin multi-layer structures. Further, the existing models can be applied only if the layers are thin and made of either isotropic or orthotropic in nature. This means that, in cases of soft or thick layers and poro-elastic inclusions in the multi-layer system, these models cannot be applied. On the

similar line, since the commonly employed plate theories for vibro-acoustic applications do not include compressional motion of the structure, estimating an upper frequency limit of these theories is necessary for the safe application of them. Additionally, the existing condensed models often lead to considerable time for the implementation due to their complex approaches. This doctoral thesis will attempt to tackle the above-mentioned challenges by developing robust, accurate and efficient tools for predicting sound and vibration transmission through layered media comprising poro-elastic materials. An advanced condensed model would be developed which can be applied to thick multi-layer systems including poro-elastics by capturing possible types of propagating waves in the structure.

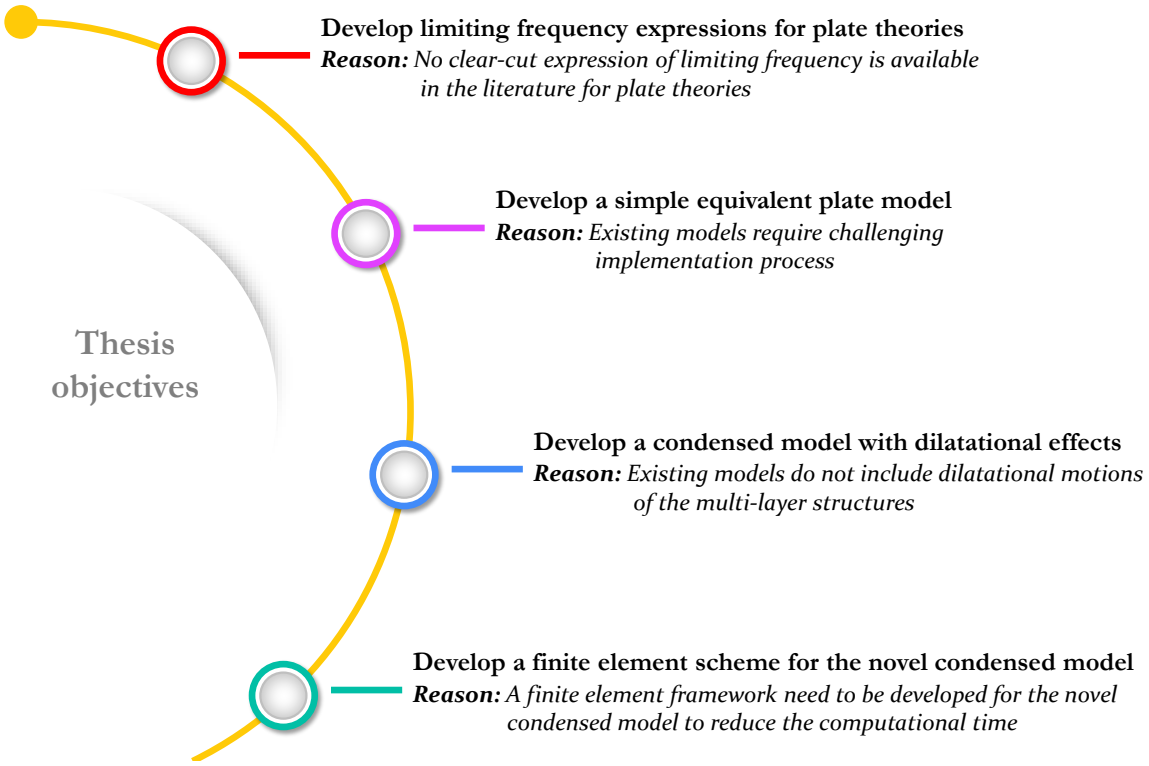


Figure 1.3: Objectives of the thesis.

In line with this context, as shown in Fig. 1.3, the scientific objectives of this thesis are:

1. Develop analytical expressions for the frequency limits of commonly employed plate theories in vibro-acoustic applications;

2. Develop a simple condensed (or equivalent) plate model for three-layer structures to facilitate the implementation processes;

3. Develop a condensed model for the multi-layer system which could simulate the compressional behaviour of the soft/thick and poro-elastic materials used in the layup;

4. Develop a finite element scheme to implement the novel condensed model to simulate all fundamental wave propagations including dilatational motion of multi-layer structures.

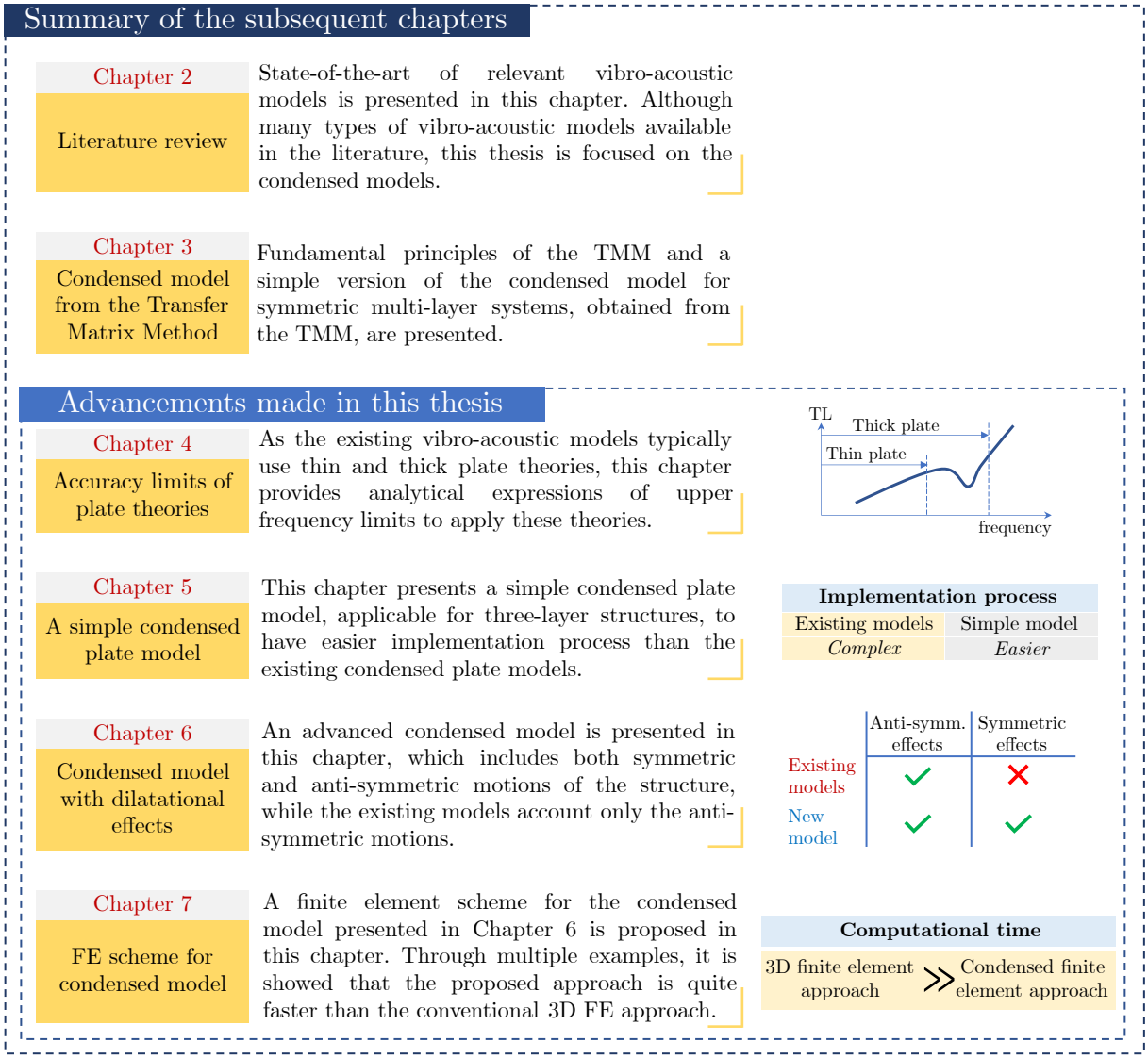


Figure 1.4: Organization and summary of the subsequent chapters of this thesis.

Regarding the structure of this thesis, along with the comprehensive review of the existing literature, each of the above-mentioned objectives is addressed in a dedicated chapter as shown in Fig. 1.4.

## Publications and conference presentations

The scientific articles and conference presentations produced from the outcomes of this thesis are listed below:

**Published articles**

- **Arasan, U.**, Marchetti, F., Chevillotte, F., Tanner, G., Chronopoulos, D., Gourdon, E. (2021). "On the accuracy limits of plate theories for vibro-acoustic predictions". *Journal of Sound and Vibration*, 493, 115848.

- **Arasan, U.**, Marchetti, F., Chevillotte, F., Jaouen, L., Chronopoulos, D., Gourdon, E. (2021). "A simple equivalent plate model for dynamic bending stiffness of three-layer sandwich panels with shearing core". *Journal of Sound and Vibration*, 500, 116025.

- Marchetti, F., **Arasan, U.**, Chevillotte, F., Ege, K. (2021). "On the condensation of thick symmetric multilayer panels including dilatational motion". *Journal of Sound and Vibration*, 502, 116078.

**Submitted for review**

- **Arasan, U.**, Sreekumar, A., Chevillotte, F., Triantafyllou, S. P., Chronopoulos, D., Gourdon, E. (2021). "Condensed finite element scheme for symmetric multi-layer structures including dilatational motion". *Journal of Sound and Vibration*.

**Conference presentations**

- **Arasan, U.**, Chevillotte, F., Jaouen, L., Chronopoulos, D., Gourdon, E. (2019). "Comparison of transmission loss prediction using condensed equivalent plate models". *23rd International Congress on Acoustics (ICA 2019).*

- **Arasan, U.**, Chevillotte, F., Chronopoulos, D., Gourdon, E., Marchetti, F., Ege, K., Bécot, F.-X. (2020). "Comparison of equivalent plate models using wavenumber approach". *e-Forum Acusticum (FA2020).*

# Chapter 2

# Literature review

## 2.1 Introduction

In recent years, multi-layered partitions have been used widely for better sound comfort and noise attenuation. Advanced composite structures are one type of multi-layered systems which are being used increasingly in various industries such as aerospace and aircraft industries. Sandwich composites which exhibit high stiffness with light weight are widely used in the transportation and construction industries. As the acoustic and vibration behaviours are related, the characterization of materials and some special models are essential to study the acoustic phenomena. Since the interactions between the different layered materials affect the acoustic performance of the multi-layered system, it is not always optimized by assembling only the best materials.

With various different damping configurations and testing methods [3–6], viscoelastic layers in the multi-layer system are employed to control the resonance response of the structures. In this direction, theoretical model of damped thin structures was introduced by Kerwin Jr [7]. Further, this had been extended [8–11] for general beam and plate boundary conditions. A more accurate theory [9] was developed, accounting for shear and rotational inertia in the skins and discrete displacement field for the layers. An analytical method considering flexural, longitudinal, rotational and shear deformations in all layers

of sandwich beams with multiple constrained layer damping patches is proposed by Kung and Singh [12]. For general multi-layer structures with unlimited number of layers, general laminate models were developed [13, 14] which demonstrated the requirement of high computational effort.

Since there are various types of vibro-acoustic methods available in the literature, this chapter is divided into four main sections to discuss the state-of-the-art on the analyses of the multi-layer structures: 1) Section 2.2 provides an overview of generic vibro-acoustic methods, that are commonly employed across various industrial applications, such as Transfer Matrix Method (TMM), Finite Element (FE) models and Statistical Energy Analysis (SEA), 2) Section 2.3 presents the experimental methods to assess the vibro-acoustic response of multi-layer structures, 3) Section 2.4 details various analytical multi-layer models that focus on specific configurations of multi-layers and 4) Section 2.5 presents the condensed (or equivalent) plate models which aim to reduce the computational effort compared to other methods.

## 2.2 General vibro-acoustic methods for multi-layer structures

### 2.2.1 The Transfer Matrix Method (TMM)

The Transfer Matrix Method (TMM), also known as the Thomson-Haskell method [15–17], is a highly thorough analytical approach because of its capacity to simulate acoustic fields in multi-layered media such as fluid, plates, elastic solid and poro-elastic layers. Each layer is assumed to have infinite lateral dimensions and its wave propagation is described through the transfer matrices. Due to the generality nature of the TMM, it covers the whole range of structures: single-walls of thin and thick types, double-walls, and sandwich structures. Because of its versatility, this approach is highly convenient: wave propagation through a layer is accomplished using matrix multiplication, and layers of different kinds (fluids, elastic solids, visco-elastic and poro-elastic materials, etc.) could

be coupled via interface matrices. When the multi-layer sound packages comprise poro-elastic materials, the TMM approach to handle the poro-elastic layer and its interface conditions with other types of layers are described by several researchers [18–21]. It may be worth to mention that the sound propagation inside the poro-elastic layer and its associated transfer matrix are defined by the Biot theory [22, 23].

Due to the assumption of infinite lateral directions, few extensions are proposed [24–28] to increase the ability of TMM to calculate the response of finite-sized structures. These theories aim to correct the low frequency response of the TMM, as the finite dimensions of the structure mostly affect the vibro-acoustic response in low frequencies. Even though the method is mathematically exact, divergences in its results are observed by several authors [29–33]. This is especially true for high frequency computations and/or thick layers. Therefore, Dazel et al. [34] have proposed a numerical method that is stable at high frequencies using Stroh formalism [35]. This strategy differs from the TMM by expressing the wave propagation inside a layer through non-redundant state variables, while the TMM describes the same with both redundant and non-redundant state variables. Despite this key difference between these two methods, the stable numerical method is shown to be equivalent to the TMM.

As the TMM uses the principles of elasticity to define the transfer matrices, it is considered to be complete and can be treated as reference for planar structures, for the purpose of comparison, to many other analytical models. Since the models presented in this thesis are also compared against the TMM for validation, the next chapter is dedicated to describe the principles of the TMM and ways to compute vibro-acoustic quantities.

### 2.2.2 FEM/BEM models

Analytical and statistical models show well behaviour in medium and high-frequency ranges. This may not be the case in the low-frequency region, when factors such as the panel's finite size and boundary conditions are significant. Numerical methods such as

finite and boundary element methods are usually employed to solve for the vibro-acoustic problems in such situations. For sound transmission loss problems in building acoustics and transportation, the Finite Element Method (FEM) and Boundary Element Method (BEM) have been widely employed. These approaches need volume discretization, which results in a large number of degrees of freedom and a high calculation time at higher frequencies. The benefit of these techniques is that all aspects of interest in the structure may be represented and incorporated in the model while taking into consideration the finite size effects of the real structure. As a result, the FEM and BEM were employed to tackle sound transmission loss problems of complicated structures incorporating poro-elastic materials [36, 37]. Since poro-elastic materials fall under absorbing media, the finite element techniques to handle the absorbing materials have been developed through various approaches. Among them, few simple approaches [38–40] and some sophisticated displacement approaches [37, 41–44] using Biot's theory are commonly used. These displacement approaches are generally called as $(u, U)$ formulation (where $u$ and $U$ denote the displacement vectors of the solid and fluid phases of the poro-elastic material, respectively) in the literature.

Although the $(u, U)$ formulation is shown to be accurate, it has disadvantages of huge computational storage and solution time due to heavily loaded frequency dependant matrices [37, 44]. Therefore, to overcome these issues, a mixed $(u, p)$ formulation (where $p$ denote the pressure vector of the fluid phase of the poro-elastic material) has been proposed [45–47] which is also shown to be accurate. As this particular method would be utilized in the later chapters, for the purpose of validating the novel analytical models developed in this thesis, few necessary details of this approach are presented next. It may be noted that this numerical approach leads to an additional advantage of converting the problem into the classical form of fluid-solid interaction, as shown below:

$$\begin{pmatrix} [K] - \omega^2[M] & -[C] \\ -[C]^T & \dfrac{[H]}{\omega^2} - [Q] \end{pmatrix} \begin{Bmatrix} \{W\} \\ \{P\} \end{Bmatrix} = \begin{Bmatrix} 0 \\ 0 \end{Bmatrix}, \tag{2.1}$$

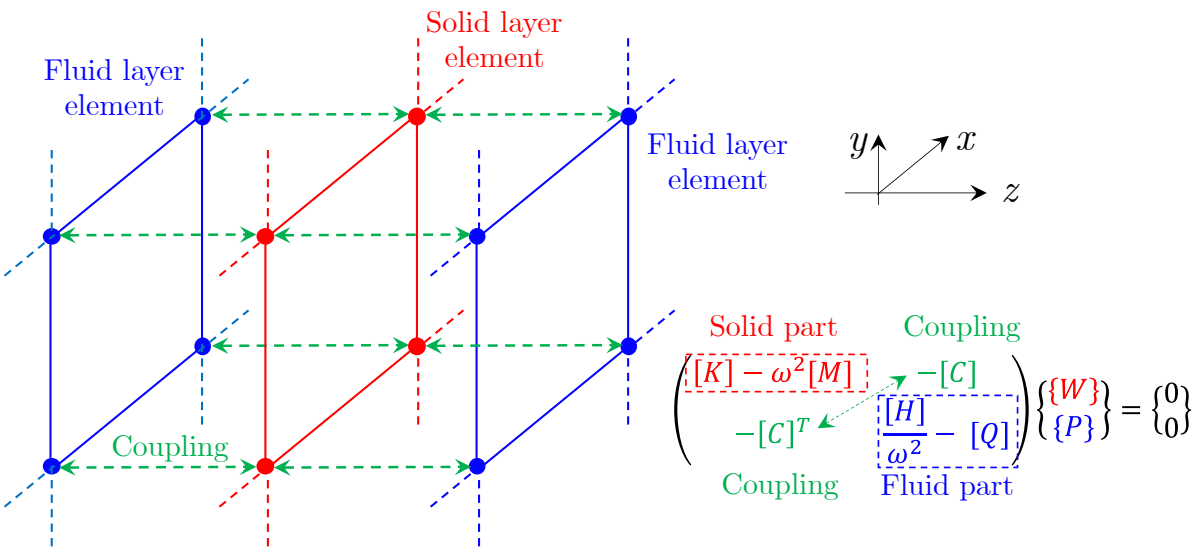


Figure 2.1: Schematic representation of a plate element embedded between the fluid elements.

where $\{W\}$ and $\{P\}$ denote the global nodal variables of solid and fluid phases respectively and $\omega$ is the angular frequency. $[K]$ and $[M]$ represent the stiffness and mass matrices of the solid phase respectively, while $[H]$ and $[Q]$ represent the kinetic and compression energy matrices of the fluid phase respectively. The matrix $[C]$ serves as a coupling between the solid phase displacement variables and fluid phase pressure variables. In other words, $[C]$ can be a fluid-solid coupling for poro-elastic media or between a fluid and a solid domain. As an example, the finite element setup of a solid layer surrounded by the air layers to compute transmission loss is shown in Fig. 2.1. The solid layer is meshed with elements containing nodal displacement variables ($\{W\}$) and the air layers are meshed with elements containing nodal pressure variables ($\{P\}$). Depending on the nature of these three layers, Eq. (2.1) would take the following forms:

- If all layers are solid, then the global matrix would be,

$$([K]-\omega^2[M])\{W\}=\{0\}, \tag{2.2}$$

which turns into a pure vibration problem.

- If all layers are fluid, then the global matrix would be,

$$\left(\frac{[H]}{\omega^2} - [Q]\right)\{P\} = \{0\}, \tag{2.3}$$

  which turns into a pure fluid dynamics problem governed by the Helmholtz equation.

- If there are solid and fluid layers, then the nodal displacement variables of the solid part and the nodal pressure variables of the fluid part are coupled through the coupling matrix, $[C]$ which results into the Eq. (2.1).

- In case of poro-elastic layer (which contains both solid and fluid phases), the global matrix still takes the form given in Eq. (2.1) while the element matrices are governed by the frequency dependent (or equivalent) properties [48, 49].

**A note on the fluid-solid coupling:** When the fluid phase and solid phase are met at an interface, the normal displacement of solid phase and fluid phase must be equal to ensure the continuity, and this continuity condition creates the coupling between the two different phases. Since the fluid phase has only pressure degrees of freedom, the coupling condition could be formulated by relating the fluid particle pressure ($p$) and normal displacement ($w_n$) through Euler's equation as shown below.

$$\frac{\mathrm{d}^2 w_n}{\mathrm{d}t^2} = -\frac{1}{\rho_0}\frac{\partial p}{\partial n} \Rightarrow w_n = \frac{1}{\rho_0 \omega^2}\frac{\partial p}{\partial n}, \tag{2.4}$$

where $t$ represents time and $\rho_0$ is the density of air. The weak form of the above relation can be written as,

$$\rho_0 \omega^2 \int_\Gamma w_n \delta p \,\mathrm{d}\Gamma + \int_\Gamma (\nabla p \cdot n)\delta p \,\mathrm{d}\Gamma = 0, \tag{2.5}$$

where $\delta p$ is the admissible variation of the pressure $p$ and $\Gamma$ is the surface of the fluid-solid interface. If the field variables are discretized with shape functions as,

$$w_n \approx \langle N_f \rangle \{W\}; \quad \delta p \approx \langle N_p \rangle \{P\} \tag{2.6}$$

then the following integral would be expressed in terms of a fluid-solid coupling matrix which couples the solid displacement and the fluid pressure as,

$$\int_{\Gamma} w_n \delta p \, \mathrm{d}\Gamma \approx \langle P \rangle \, [C] \{W\}. \tag{2.7}$$

In the case where a thin structure is surrounded by air cavities and a single mesh is used for both solid and fluid domains, Lagrange multipliers could be introduced in Eq. (2.1) to create the coupling between the fluid and solid phases [50].

In another class of finite element methods for computing the vibro-acoustic response of the multi-layer structures, Alimonti et al. [51] developed a hybrid-FE method which approximates the effect of sound packages as a Green function which behaves as a locally reacting system. This will be then applied as an impedance condition onto the main structure (which is modeled with finite elements). Although the goal of this approach is to reduce the computational burden that arises from modeling the sound package (poro-elastic material, for example) with 3D finite elements, it does not account for all types of structural and elastic responses (like bending and shear) of the sound package. Other researchers [52–54] have developed modal methods to simulate the acoustic response of automotive structures. For example, Acher et al. [54] computed the vibro-acoustic response of a trimmed truck cabin by condensing the impedance matrix of the acoustic treatments and projected it on the modal space of the complete system.

On the limitations side, in general, numerical methods suffer from huge computational time and storage requirements for high-frequency range computations. In few situations, it may lead to complex implementation processes as well, especially when full three-dimensional modelling is employed [55]. Few approaches such as multi-scale FEM [56], Schur's complement method [57], Craig-Bampton method [58] etc., are some reduction methods which help to reduce the computational costs of the finite element method.

### 2.2.3 SEA models

Usually, Statistical Energy Analysis (SEA) are employed to solve vibro-acoustic problems involving finite-length rooms and buildings. SEA divides the system under study into components or modal subsystems, and the response of each subsystem is characterized in terms of its mean energy. Energy balance equations are constructed as a function of modal densities, internal loss factors, and coupling loss factors to explain the energy transfer between two subsystems. The technique is valid only when the modal density of all systems (cavities, rooms, plates etc.) is sufficiently high, limiting its applicability to the medium and high-frequency ranges. The response of the subsystems is governed by resonant modes, which means that only resonant transmission can be modelled. This is considered as a key assumption of SEA. The readers may refer to [59] for comprehensive description of SEA method. Forced or non-resonant transmission, which results in the mass-law for single walls, could only be considered artificially. Similarly, the mass-spring mass resonance process in double-wall partitions must be explicitly considered.

Crocker and Price [60] were the first to utilize SEA to forecast the transmission loss of a single wall separating two rooms. The panel radiation resistance is used to describe the connection between room and plate modes. The model was later modified to include double walls by taking into account a room-plate-cavity-plate-room system [61]. The compressional frequency or mass-spring-mass resonance frequency of double walls could not be estimated since the cavity is represented as a resonant system. Brekke [62] investigated the transmission loss of triple partitions using SEA and incorporated the non-resonant coupling condition between the panels via the air stiffness in the cavity. Craik [63] provided an overview of the usage and potential of SEA in acoustical applications. Sound transmission via metal connections in masonry hollow walls [64] or studs in lightweight constructions [65] was included into SEA models of double walls. While the paths of structure-borne transmission could be accurately predicted, SEA models struggled to predict transmission into and out of cavities. In general, SEA would require inputs (such as energy carrying waves through the structure, transmission factor etc.)

from other methods like TMM, FEM and/or experimental measurements to calculate the sound transmission loss across the multi-layer structures of finite size [66–68].

## 2.3 Experimental methods

This section gives the summary of the experimental techniques used in the vibro-acoustic field to identify the mechanical properties of the structural system. With respect to other vibro-acoustic models which could be used to compare the experimental data, different approaches are available to model the multi-layer systems [14, 69–75].

### 2.3.1 Fourier transform methods

Among the methods for assessing fields at medium and high frequencies, the Discrete Fourier Transform (DFT) may be distinguishable, which assumes homogenous material characteristics in the structure. This technique, which is popular due to its speed, assumes that the field is known on a uniform grid and is 2D-periodic on the outside. In the case of anisotropic structures, spatial changes in mechanical characteristics may be detected through this method. DFT offers several advantages, including speed and bijectivity. The reader may remind that bijectivity is the property of a method that ensures not missing any field information if reverse transformation is performed between two different domains (for example, the transformation between spatial and wavenumber domains). DFT does not, however, identify the imaginary component of the wave number and is susceptible to aliasing and edge effects. As a result, the investigated wavenumber domain is exactly proportional to the dimension and resolution of the measuring grid.

Ferguson et al. [76] use the Continuous Fourier Transform (CFT) to overcome the limitation posed by DFT. It allows increasing the discretization of the wavenumber domain, and therefore it increases the precision of the results. According to Berthaut [77], this transformation is no longer bijective. Berthaut further notes how flexible this approach is, since it may be used on a non-uniform measuring grid. However, mastering the folding with such a grid is challenging. Furthermore, CFT is still limited to recognizing only the

real part of the wave number.

### 2.3.2 Inhomogeneous Wave Correlation (IWC) approach

In order to estimate the damping of the structure, Ferguson's method introduced the concept of correlation of the measurement field with a virtual field. This principle has already been observed in the work of Hillström et al. [78] where the virtual field is composed of two plane waves (forward and backward propagative) of different amplitude. McDaniel et al. [79] used the method of Hillström et al. [78] by adding the evanescent waves in the virtual field. The different amplitudes of each wave are identified by the least squares method, whose error between the reconstructed field and the real field is calculated for different complex wave numbers. An optimal correlation is obtained when this error is minimal. Berthaut et al. [80] propose a similar method called IWC for Inhomogeneous Wave Correlation, where the virtual field is only composed of a propagating plane wave defined by a complex wave number. A correlation index is calculated for each frequency and direction as a function of the wave number and the damping of the plane wave.

Berthaut et al. [80] applied their technique to isotropic plates as well as plates provided with stiffeners. Subsequently, Ichchou et al. [81] modeled honeycomb sandwiches from a thin Love-Kirchhoff plate, whose parameters were identified using the method IWC. Finally, Cherif et al. [82] used the IWC method to characterize a composite structure.

### 2.3.3 Wave correlation by Hankel's functions

An experimental method to estimate the equivalent material properties of a multi-layer plate (sandwich structure) by adopting a complex wavenumber fit using Hankel's functions and the image source method, was recently developed by Roozen et al. [83]. A multi-layer plate is initially excited with a point load and the measured field is correlated to the analytical or "virtual" field obtained from the Hankel's functions. The complex valued wave number is fitted with the experimental vibration field obtained, from which

the equivalent material properties are found by assuming the thin plate model.

### 2.3.4 Corrected Force Analysis Technique (CFAT) approach

In the recent years, an experimental technique called Force Analysis Technique (FAT) has attracted many researchers for the purpose of identifying the unknown material parameters of the structures. It was initially developed by Pezerat and Guyader [84] to identify the point sources (forces or moments) on the beams from vibration measurements and its equation of motion. Later, this approach was extended to plates [85] as well. Since this is an inverse experimental approach, this method is very sensitive to the uncertainties in the measurement. To overcome this problem and regularize the method, a corrective method called CFAT (Corrected FAT) was suggested by Leclere and Pézerat [86]. This section intends to provide the summary of the CFAT method that is used to find the equivalent properties of the multi-layer plate.

By considering $x$ and $y$ as in-plane directions and $z$ as the thickness direction, the complex bending stiffness of the thin homogeneous plate is related to normal displacement ($u_z$) by the equation of motion as:

$$D\nabla^4 u_z(x,y) - m_s\omega^2 u_z(x,y) = q(x,y). \tag{2.8}$$

In the above equation, $D$ is the complex bending stiffness of the plate, $m_s = \rho h$ is the mass per unit area, $u_z(x,y)$ is the normal displacement and $q(x,y)$ is the applied load. For the source identification in the homogeneous plate (where usually the structural parameters are known), the normal displacement $u_z(x,y)$ is measured on a regular sampling mesh. From the corrected finite difference scheme suggested by CFAT, the fourth order displacement derivative can be estimated. Knowing all the terms on the left side of the Eq. (2.8), the unknown quantity $q(x,y)$ (vibration source) can be estimated.

The same approach has been extended for the identification of unknown structural parameters [87, 88]. The method is applied in an area far from the source, where the

loads can be neglected ($q(x, y) \approx 0$). In this area, the Eq. (2.8) can be rewritten as follows:

$$D = m_s \frac{\omega^2 u_z(x, y)}{\nabla^4 u_z(x, y)}. \tag{2.9}$$

As mentioned earlier, the displacement field is measured and CFAT is used to estimate the fourth order derivative. $m_s$ is measured using weighing machine and caliper. Finally, the Young's modulus and loss factor can be obtained as follows:

$$E = \frac{12D(1-\nu^2)}{h^3}; \quad \eta = \frac{\Im(D)}{\Re(D)}. \tag{2.10}$$

Note that the Poisson's ratio must be known beforehand to get the Young's modulus. Usually, $\nu = 0.3$ is assumed, as it is valid for classical isotropic materials. For the multi-layer plate, the above methodology can be adopted to get the equivalent material properties $(D_{\text{eq}}, E_{\text{eq}}, \eta_{\text{eq}})$ by satisfying the assumption that the equivalent homogeneous plate with same $m_s$ and $h$ would yield the normal displacement field at a given frequency.

## 2.4 Analytical multi-layer models

A multi-layer structure is initially characterized as an equivalent plate. Then a multi-layer model has to be employed to identify the properties of a given layer. Two paths can be adopted to model these structures. The first is to use a complete model, allowing to describe the three-dimensional behavior of the structure using a very large number of degrees of freedom and parameters [89, 90]. These models are often developed for a specific type of structure, loading case or limiting conditions [91]. The second approach is to use a reduced or condensed model to reduce the number of degrees of freedom and parameters of the structure, which are to be identified. In addition to this, condensed models would serve as useful tools to understand the physical behaviours of the multi-layer structures in different frequency ranges.

This section deals with only the reduced models of continuous multi-layer plates made up of viscoelastic or isotropic layers. Discontinuous shapes of some materials, such as,

for example, honeycombs or porous materials (poro-elastic layers) will not be considered. The reduced models differ essentially by the choice made on the kinematics to describe the behavior of the multi-layer structure. Different types of kinematic fields are considered to describe the behaviour: 1) displacement formulation, 2) stress formulation and 3) mixed field formulation, i.e. both displacement and stress at the same time. This last formulation is particularly interested in the case of multi-layer because it allows to apply the continuity conditions on both displacements and stresses at the interfaces between the layers. Carrera [92] refers to these conditions by giving them the name $C_z^0$ requirements. These conditions also imply that the layers are well bonded to each other.

The large number of multi-layer models existing in the literature have led some authors such as Reddy and Robbins Jr [93] or Carrera [69, 94] to develop few classifications. Three main categories of multi-layer models emerge from these classifications: 1) Equivalent Sing Layer (ESL), 2) Layer-Wise (LW) and 3) Zig-Zag (ZZ). The following sections detail each one of these classifications with various examples.

### 2.4.1 Equivalent Single Layer (ESL) models

The Equivalent Single Layer (ESL) models group all the layers together and describe the displacement response of the multi-layer as a homogeneous plate at low-frequency. The dynamics of the multi-layer is then governed by the kinematic field of the ESL plate. This treatment of multi-layer plate is advantageous as the number of kinematic variables does not depend on the number of layers, and therefore it considerably reduces the number of degrees of freedom and the complexity of the model. Thus, the ESL models were easily adopted by the community for their ease of implementation and their speed of computation for any number of layers. The reader is advised not to get confused between ESL models using static equivalent properties and another class of models called 'condensed (or equivalent) plate models' where the natural response of the multi-layer structure is condensed into an equivalent layer defined with frequency-dependant material properties. This type of models is the subject of this thesis, and a particular focus is given in Section 2.5 to discuss its background.

However, since the description of the multi-layer is global, the individual behaviour of each layer cannot be modelled with this approach. As ESL models describe the displacement field with constant material parameters, they are limited to compute only low-frequency behaviour of the multi-layer structure. The order of expansion (for the displacement field) of the model is also an important criterion. A high order brings a more detailed description of the behaviour in thickness, giving access to the identification of higher order modes.

**Thin plate model**

The equivalent single layer models of order one refer to classical plate theories such as the Love-Kirchhoff [95, 96] or Classical Lamination Theory (CLT) for composite laminates. As this model assumes the plane sections remain straight and normal to the neutral axis of the plate, it ignores the effects of rotational inertia and transverse shear. These assumptions lead us to the definition of the following displacement field:

$$\begin{Bmatrix} u_x(x,y,z) \\ u_y(x,y,z) \\ u_z(x,y,z) \end{Bmatrix} = \begin{Bmatrix} u_x^0(x,y) \\ u_y^0(x,y) \\ u_z^0(x,y) \end{Bmatrix} - z \begin{Bmatrix} \frac{\partial u_z^0(x,y)}{\partial x} \\ \frac{\partial u_z^0(x,y)}{\partial y} \\ 0 \end{Bmatrix}, \tag{2.11}$$

where $u_x^0, u_y^0, u_z^0$ are the mid-plane displacements.

The above displacement field is more suitable for thin structures, as it is reasonable to assume the propagation of only bending waves in those structures. Therefore, the Love-Kirchhoff model is often called as the thin plate model as it is suitable for modelling thin plates (such as thin aluminium, steel, carbon fibre composites etc.) in a domain where the frequency-thickness product remains relatively low. Thick plate models were then suggested to model thicker structures such as sandwiches in high frequency domains.

**Thick plate model**

Reissner [97], Hencky [98] and Mindlin [99] developed as a First order Shear Deformation Theory (FSDT) for thick plates. Unlike Love-Kirchhoff's model, the rotation of

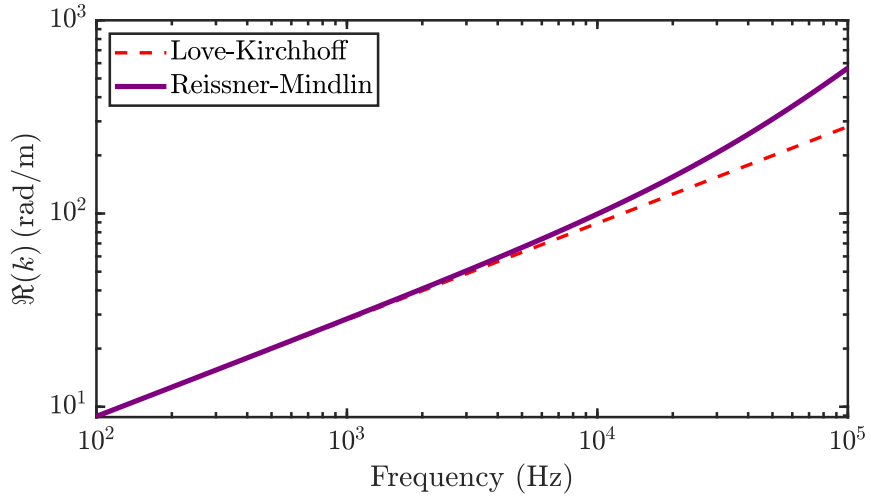


Figure 2.2: Dispersion curves obtained from two fundamental plate theories for a plasterboard layer (thickness: $h = 12.5$ mm, Young's modulus: $E = 3$ GPa, density: $\rho = 700$ kg m$^{-3}$, Poisson's ratio: $\nu = 0.3$).

the cross-section is taken into account and this results in generation of a transverse shear in the structure through the thickness. Fig. 2.2 shows the difference in the propagating wavenumbers obtained with thin and thick plate theories for a plasterboard layer of 12.5 mm. As the thick plate model accounts for both bending and transverse shear, it deviates from the thin plate theory after 5000 Hz.

Two new kinematic variables ($\phi_x$ and $\phi_y$) are used to describe this shear, in the displacement field of the structure:

$$\begin{Bmatrix} u_x(x,y,z) \\ u_y(x,y,z) \\ u_z(x,y,z) \end{Bmatrix} = \begin{Bmatrix} u_x^0(x,y) \\ u_y^0(x,y) \\ u_z^0(x,y) \end{Bmatrix} - z \begin{Bmatrix} \frac{\partial u_z^0(x,y)}{\partial x} + \phi_x(x,y) \\ \frac{\partial u_z^0(x,y)}{\partial y} + \phi_y(x,y) \\ 0 \end{Bmatrix}, \tag{2.12}$$

where $\phi_x$ and $\phi_y$ are the rotations about $x$ and $y$ directions which the normal to the mid-plane makes with the $z-$axis.

Although it accounts for transverse shear, the strain and stress fields associated with this transverse shear are constant across the thickness. This approximation does not allow the condition of zero stresses to be applied to the lower and upper surfaces of the plate ($\sigma_{zz}(z = \pm h/2) = 0$, where $h$ is the total thickness of the structure) which is an essential

condition in the modelling of the dynamic response of thick plate [100]. Consequently, the dispersion curves obtained from the FSDT theory are different from that of three-dimensional models such as Lamb [101] or higher orders such as Reddy's model et al. [102]. This subject is also treated by Margerit [103] using a comparison between the FSDT theory and the finite element model of Shorter [14].

**Note on the shear correction factor:** The shear correction factor ($\kappa$) is introduced in the thick plate theory to correct the approximation made on the transverse shear. As Margerit [103] underlines, this correction factor can be calculated in different ways. The first and best known consists in equalizing the cut-off frequency of the first shear mode given by the FSDT model with the three-dimensional models, leading to $\kappa = \pi^2/12$ in the isotropic case. We can also note that $\kappa = 5/6$ in the static case [104]. A second way to calculate this correction factor is by equalizing the asymptotic value of the phase velocity of the bending mode. This possibility is much more complex as it depends on the Poisson's ratio and remains quite close to the results of $\kappa = \pi^2/12$ for classical Poisson's ratio. In the case of anisotropic materials, the correction factor is applied independently to each of the stiffnesses of the Hooke's matrix connecting the transverse shear stresses to the deformation field [105]. In this manuscript, the value of $\kappa$ is taken as $5/6$ for further calculations.

### Higher order plate models

Mindlin's theory has inspired several authors [106–111] on the choice of displacement field order (greater than one) to best describe the shear behaviour in the thickness direction. These theories are commonly called as High order Shear Deformation Theory (HSDT). These models are developed with a high-order description of membrane displacements in order to describe the behaviour due to transverse shear. Despite this, the normal displacement is each time considered to be constant through the thickness and thus neglecting any deformation along the thickness axis. Note that the 'normal displacement' means normal to the surface and refers to the displacement along the thickness direction or wave propagation direction. When dealing with thin structures, it is some-

times called as out-of-plane displacement. There are, however, several theories called as High Order Theory (HOT) where the three components of the kinematic field are of high order. Such a description of the transverse component of displacement provides access to the identification of "breathing" modes (symmetrical Lamb modes). Among these models, we can notably refer to the work by Whitney and Sun [112] of order 1 on the transverse displacement. On the same line, we can also refer to the theory by Zenkour [113], developed for beams.

### 2.4.2 Layer-Wise (LW) models

Layer-Wise (LW) models are sometimes referred to as piece-wise models because, unlike ESL models, each layer is interpreted as a plate with its own kinematics and its own number of kinematic variables. Continuity equations of the displacements and the constraints at the interfaces between the layers are then added to the model. Therefore, the total number of kinematic variables depends on the number of layers of the multi-layer structure. Due to this reason, LW models fall into the category that is opposite to ESL models, with higher accuracy but longer computation time. The complexity and precision of the model depend on the order of expansion of each of the layers, which ultimately decides the computation time (see Figure 2.3).

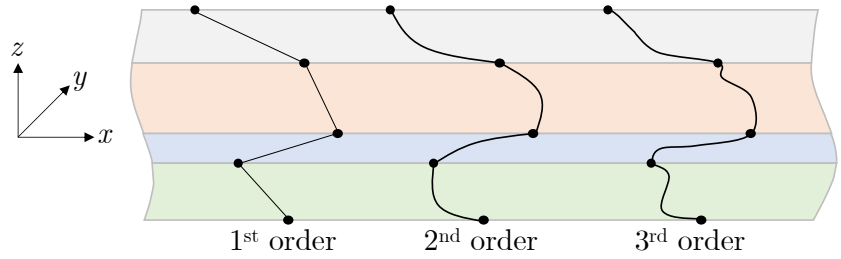


Figure 2.3: Examples of displacement fields of different orders postulated by the Layer-Wise models for a multi-layer composed of four layers.

We can, for example, refer to the model of Ghinet and Atalla [71] postulating a Mindlin kinematics for each layer of a three-layer structure. The number of kinematic variables specific to each layer is five, while the interlayer forces are three per interface. Therefore, this model has a total of $(5 \times 3) + 3(3-1) = 21$ independent variables. Ghinet and Atalla

also introduced the possibility of studying the dilation mode of a sandwich composed of a soft core and stiffer skins. The dilatation mode, usually governed by the sandwich core, cannot be represented by a Mindlin kinematics. Consequently, Ghinet and Atalla use a complementary displacement field for the core, where the transverse displacement is linear, and the shear distribution is defined by trigonometric functions. A kinematics similar to that of Ghinet has also been observed in Srinivas model [114]. Reddy [115] extended this formulation to a higher order by adding a linear description of the normal displacement for each layer. Subsequently, Nosier et al. [116] used Reddy's model to determine the first eigen frequencies of composite plates and compare them with the results of an accurate model as well as other theories like ESL models.

### 2.4.3 Zig-Zag (ZZ) models

We have seen so far that the ESL and LW models have opposite characteristics. The former is quick and easy to use, but the individual behavior of each layer is not taken into account. The second offers better precision but has significant computation times. The Zig-Zag (ZZ) theory brings a compromise between these two models. Like the LW formulation, the main idea of Zig-Zag models is to postulate a kinematic field for each layer. The continuity conditions are, however, formulated to relate the kinematic variables of one layer to the other layer. Therefore, ZZ models fall into the category of ESL models, since their number of kinematic variables also does not depend on the number of layers.

Zig-Zag models are introduced by Lekhnitskii [117] whose stress field formulation was developed for beams, and later it was extended to orthotropic and anisotropic structures by Ren [118]. The shear stresses are described by four independent kinematic variables whose associated expansion orders are parabolic. A similar formulation has been proposed by Ambartsumian [119] with two kinematic variables for the shear and therefore preserving the same number of variables as the FSDT theory. This model was extended to anisotropic structures by Whitney [120]. Subsequently, Murakami [121] applied the mixed formulation of Reissner [122] in the case of multi-layer plates. The displacement field proposed in this

model consists of a refinement of the FSDT theory by the addition of a Zig-Zag function, while the stress field remains independent and parabolic in each layer. A higher order extension was then proposed by Toledano and Murakami [123] and more recently by Demasi [124].

Guyader and Lesueur's model [125, 126], for orthotropic laminates, falls into the category of Zig-Zag models. This theory, based on the assumptions of Sun and Whitney [127], considers a kinematic similar to that of Mindlin for each layer. The continuity relations at the interfaces make it possible to reduce the total number of kinematic variables to the five degrees of freedom of the first layer. An energy method based on the Hamilton functional is then used to write the equations of motion as a function of these five kinematic variables. A particular solution of plane wave type is then suggested to identify the dispersion curves of the structure. Guyader and Lesueur's model was extended to the anisotropic case by Woodcock [128]. Subsequently, Loredo et al. [74] gave a general formulation of the displacement field whose Zig-Zag effect was defined by four functions called warping functions. Castel [129] used different definitions of these functions and few years later, Loredo [130] extended his model by taking into account the deformation along the thickness direction of the structure. The notion of warping functions has already been used in the work of Pai [104], where their expressions have been determined from the continuity conditions of displacements and constraints at the interfaces.

## 2.5 Condensed (or equivalent) plate models

All the previous models are generally used to compute the natural propagating wavenumbers of the multi-layer structure, or the Transmission Loss (TL). Other methodologies such as condensed (or equivalent) models aim to identify an equivalent single layer that describes the behaviour of the multi-layer by means of dynamic intrinsic properties. The readers are warned not to be confused with ESL models, described in Section 2.4.1. The ESL models are used to describe the behaviour of the multi-layer structure at low-frequency with constant material properties, whereas the condensed models are defined

dynamic material properties which could compute behaviours at all frequencies. This kind of models would serve as a handy tool to reduce the computational time significantly in the finite element modelling, as the multi-layer structures are modelled as single layer with dynamic properties. This section details about a few existing condensed (or equivalent) plate models in the literature. It may be noted that the main focus of this thesis is to improve these existing models to be able to apply them on wide applications.

### 2.5.1 Guyader model

By employing classical plate theory on the multi-layer viscoelastic plate, Guyader and Cacciolati [125, 131] developed an analytical model to determine the equivalent complex bending stiffness as a function of frequency. In this model, each layer is assumed to have Mindlin type displacements or in other words each layer is modelled by considering bending, membrane and shear effects as proposed by Sun and Whitney [127]. Displacement and shear stress continuity conditions are applied to obtain the equations of motion of the multi-layer plate, which are interestingly expressed as a function of displacement field of the first-layer only. Under the assumption that the transverse displacement is the same for both equivalent single layer and the multi-layer plate, this model determines the equivalent bending stiffness by using Love-Kirchhoff (thin plate) theory with the following characteristic equation.

$$A_4 D^{3/2} + A_3 D - A_1 A_4 D^{1/2} - A_1 A_3 + A_2 = 0, \tag{2.13}$$

where $A_1 = \lambda_1 - \dfrac{\lambda_5^2}{\lambda_3}$, $A_2 = \omega\sqrt{m_s}\left(\lambda_4 - \dfrac{\lambda_5\lambda_6}{\lambda_3}\right)^2$, $A_3 = \omega\sqrt{m_s}\left(\lambda_2 - \dfrac{\lambda_6^2}{\lambda_3}\right)^2$, $A_4 = \lambda_{37}$. $m_s = \sum \rho_i h_i$ is the total mass per unit area and the constants $\lambda_i$ are defined in the Appendix B.

After computing the equivalent bending stiffness ($\widetilde{D}_{\text{eq}}$) as a function of frequency, the other equivalent homogeneous material properties are obtained as given below.

$$\widetilde{E}_{\text{eq}} = \widetilde{D}_{\text{eq}} \frac{12(1-\nu_{\text{eq}}^2)}{h_t^3}, \tag{2.14a}$$

$$\nu_{\text{eq}} = \frac{\sum_{i=1}^{n} \nu_i h_i}{\sum_{i=1}^{n} h_i}, \tag{2.14b}$$

$$\rho_{\text{eq}} = \frac{\sum_{i=1}^{n} \rho_i h_i}{\sum_{i=1}^{n} h_i} = \frac{m_s}{h_t}, \tag{2.14c}$$

$$\widetilde{\eta}_{\text{eq}} = \frac{\Im(\widetilde{D}_{\text{eq}})}{\Re(\widetilde{D}_{\text{eq}})} = \frac{\Im(\widetilde{E}_{\text{eq}})}{\Re(\widetilde{E}_{\text{eq}})}, \tag{2.14d}$$

where $\widetilde{E}_{\text{eq}}, \nu_{\text{eq}}, \rho_{\text{eq}}, \widetilde{\eta}_{\text{eq}}$ are the equivalent Young's modulus, Poisson's ratio, mass density and loss factor of the multi-layer plate respectively. Also, $h_t = \sum_{i=1}^{n} h_i$ is the total thickness of the plate and the subscript '$i$' denotes the $i-$th layer of the $n-$layer structure. As the equivalent complex bending stiffness depends on frequency, the equivalent Young's modulus and loss factor are also functions of frequency. After obtaining $\widetilde{D}_{\text{eq}}$ from Eq. (2.13), the following expression is used to find the equivalent bending wavenumber of the multi-layer structure:

$$k_{\text{eq}_{\text{bending}}} = \sqrt{\omega \sqrt{\frac{m_s}{\widetilde{D}_{\text{eq}}}}}. \tag{2.15}$$

.

### 2.5.2 RKU model

Ross, Kerwin and Ungar (RKU) developed a simplified dynamic model for a three layer system to find the equivalent material properties. The model is initially developed for beams, which was later used for plates as well. The complete derivation can be found in the articles [7, 132–134] as well as in the book by Beranek and Ver [135]. Following is the short summary of the RKU model.

Let us consider a three layer system as shown in the Figure 2.4. The plate is unbounded in the $x$ and $y$ directions. If the second layer is considered to be visco-elastic in nature compared to the top and bottom stiff layers, the RKU model provides the following

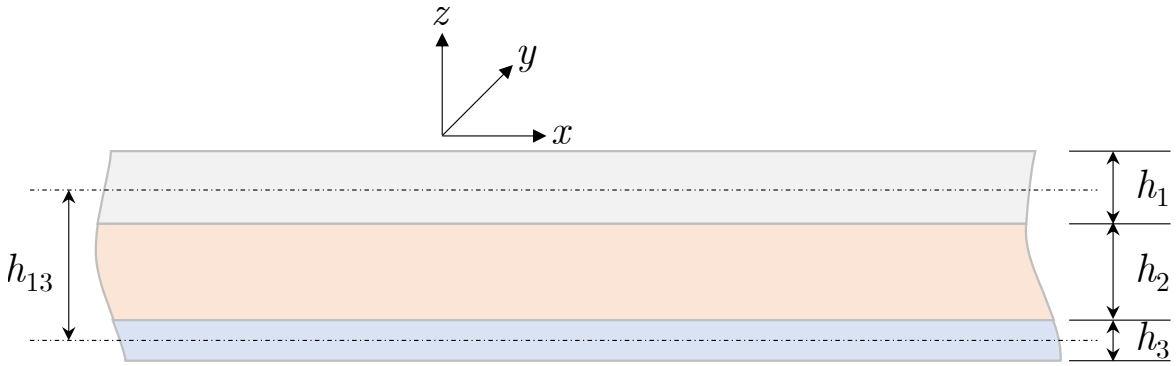


Figure 2.4: Cross-section of a three-layer structure.

expression for the equivalent bending stiffness of the plate:

$$\widetilde{D}_{\text{eq}} = (D_1 + D_3)(1 + XY/(1 + X)), \tag{2.16}$$

where

$$D_1 = \frac{E_1 h_1^3}{12(1-\nu_1^2)}; \quad D_3 = \frac{E_3 h_3^3}{12(1-\nu_3^2)}; \tag{2.17a}$$

$$X = \frac{G_2 S}{h_2}\frac{1}{k^2}; \quad Y = \frac{12 h_{13}^2}{S(E_1 h_1^3 + E_3 h_3^3)}; \quad S = \frac{1}{E_1 h_1} + \frac{1}{E_3 h_3}. \tag{2.17b}$$

The usual material property notations are followed here. In the above equations, $X$ and $Y$ are called as shear parameter and structural geometric parameter, respectively. As mentioned in the book by Beranek and Ver [135], the shear parameter $X$ is a measure of how well the viscoelastic layer (layer 2) couples the flexural motions of the two structural components (layer 1 and layer 3). Also, the maximum value of the equivalent loss factor is given by the following relation.

$$\eta_{\text{eq,max}} = \frac{\eta_2 Y}{2 + Y + 2/X_{\text{opt}}}; \quad X_{\text{opt}} = \frac{1}{\sqrt{(1+Y)(1+\eta_2^2)}}, \tag{2.18}$$

where $\eta_2$ is the loss factor of the layer 2. Since $\widetilde{D}_{\text{eq}}$ is the function of the propagating wave number, the bending wave number from the thin plate theory is replaced for $k$, that finally forms a non-linear equation in $\widetilde{D}_{\text{eq}}$ from Eq. (2.16). Due to this non-linearity, an iterative procedure shown below is followed to compute the equivalent bending stiffness

$\widetilde{D}_{\text{eq}}$. The equivalent material properties mentioned in the final block of Figure 2.5 are

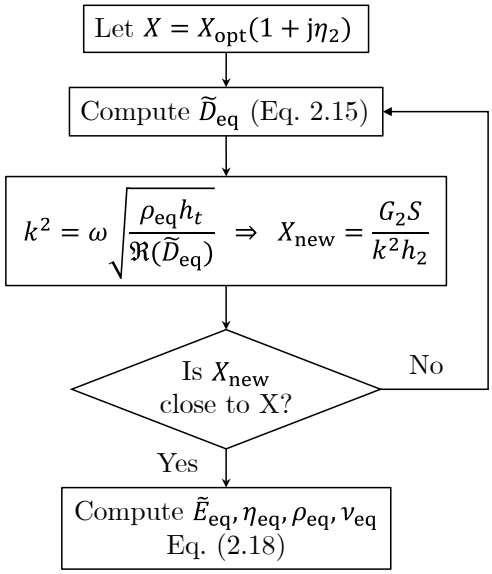


Figure 2.5: Iterative procedure of the RKU model to find equivalent material properties

expressed as:

$$\widetilde{E}_{\text{eq}} = \widetilde{D}_{\text{eq}} \frac{12(1-\nu_{\text{eq}}^2)}{h_t^3}; \quad \rho_{\text{eq}} = \frac{\sum_{i=1}^{3} \rho_i h_i}{\sum_{i=1}^{3} h_i}; \quad \nu_{\text{eq}} = \frac{\sum_{i=1}^{3} \nu_i h_i}{\sum_{i=1}^{3} h_i}; \tag{2.19a}$$

$$\eta_{\text{eq}} = \frac{\eta_2 XY}{1 + (2+Y)X + (1+Y)(1+\eta_2^2)X^2}. \tag{2.19b}$$

Throughout this manuscript, the complex number $\sqrt{-1}$ is denoted by the letter 'j'.

### 2.5.3 Added stiffness model

This model is based on computing the equivalent properties just by adding the respective individual layer properties. The material property of each layer (for example, the bending stiffness) is obtained with respect to the neutral axis of the multi-layer plate. It may be noted that the bending stiffness computed from this model is valid only at the low-frequency. The summary of the procedure to be followed is explained below.

Let us consider a multi-layer system as shown in Figure 2.6. The plate is considered to be infinitely extended in the $x$ and $y$ directions. First, the neutral axis of the multi-layer plate is computed based on the similar approach followed for composite beams [136].

For this purpose, two assumptions are made to facilitate the calculation. The width of the multi-layer plate is initially assumed to be of unit distance, and the first layer is assumed to act as a reference layer to calculate the transformed widths of the remaining layers.

Except the reference layer, transformed widths $b_{i,\text{eff}}$ of the all other remaining layers are computed based on the modified transformation factor for plates, as given by the Eq. (2.20).

$$b_{i,\text{eff}} = \frac{E_i}{E_{\text{ref}}} \frac{1-\nu_{\text{ref}}^2}{1-\nu_i^2}. \tag{2.20}$$

The neutral axis of the modified system with transformed widths is computed from:

$$\bar{z} = \frac{\sum z_i b_{i,\text{eff}} h_i}{\sum b_{i,\text{eff}} h_i}, \tag{2.21}$$

where $z_i$ is the $z-$distance from the origin to the mid-section of the $i-$th layer. The flexural rigidities of all the layers are added to get the equivalent bending stiffness of the multi-layer plate as,

$$D_{\text{eq}} = \sum_{i=1}^{n} \frac{E_i}{1-\nu_i^2} \frac{(z_{ui}-\bar{z})^3 - (z_{li}-\bar{z})^3}{3}, \tag{2.22}$$

where $z_{ui}$ and $z_{li}$ are measured from the origin as shown in the Figure 2.7. The remaining equivalent properties are calculated as it is done in the Guyader model (from Eq. (2.14a) to Eq. (2.14d)). It may be noted that the $D_{\text{eq}}$ from added stiffness model is the low frequency asymptote of Guyader or RKU models. As described by Boutin and Viverge [72], $D_{\text{eq}}$ computed from this model is used to explain the situation where all the layers in the multi-layer structure behave as a monolithic plate, which is governed by the "global bending".

### 2.5.4 Recently developed condensed models

Since the RKU model is mainly applied to three-layer sandwich structure with soft core, Zarraga et al. [137, 138] developed a model to find the equivalent properties of a

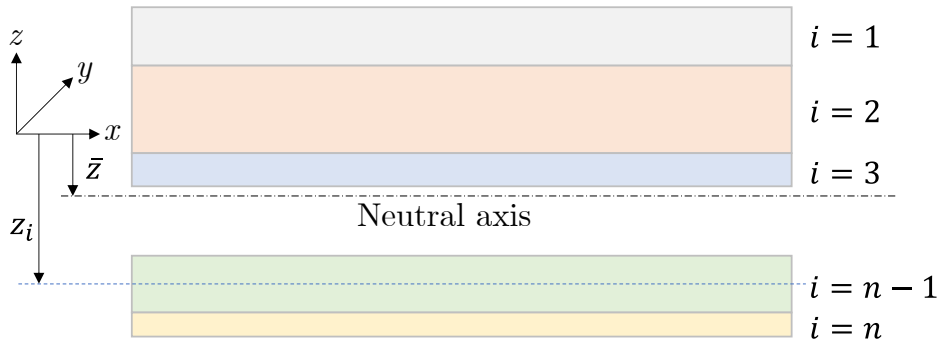


Figure 2.6: Multi-layer structure of $n$ layers

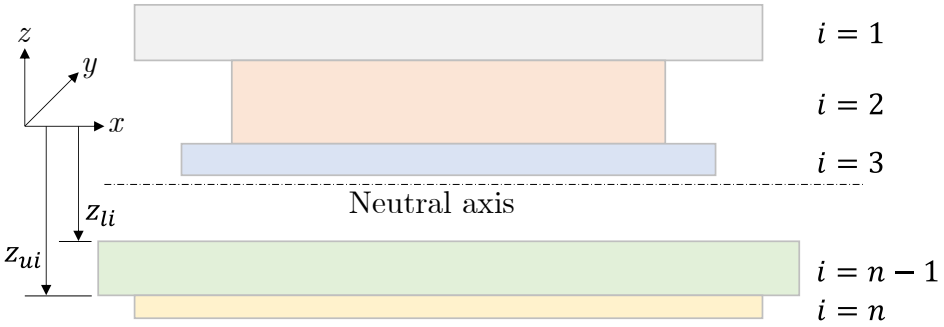


Figure 2.7: Multi-layer structure with transformed width on each layer

three-layer structure by considering both bending and shearing stiffness of all the three layers. Although the three-layer model [138] performs well at low and mid-frequencies, it does not correspond to the correct behaviour at higher frequencies, as the inner bending of skins is not considered in the model. With a similar approach described by Guyader and Cacciolati [131] for multi-layer plate consisting of only isotropic layers, Marchetti et al. [139] recently developed an equivalent plate model for multi-layer thin plates made of orthotropic layers with arbitrary ply orientations.

One may observe that all these condensed models allow only anti-symmetric modes to propagate in the multi-layer structure. This is because, the normal displacement or velocity is assumed to be constant throughout the thickness which results in only bending, shear and membrane modes to propagate. In the majority of the industrial applications, the multi-layer system would have softer or thicker layer that allows symmetric mode (or dilatational mode) to propagate even at low frequencies (50-500 Hz). For this kind of applications, the existing condensed models cannot be used as they do not capture the symmetric mode of the multi-layer structure.

## 2.6 Conclusion

In this chapter, literature review of the commonly used vibro-acoustic methods for multi-layer structures are discussed. Initially, the generic methods such as the Transfer Matrix Method (TMM), Finite Element Method (FEM), Statistical Energy Analysis (SEA) are summarized. Experimental methods to find the condensed plate properties of the multi-layer structures are also discussed, along with detailed summaries of relevant analytical approaches. Finally, existing condensed plate models, which is the topic of this thesis, are detailed to compute the condensed (or equivalent) plate properties of the multi-layer structure. It is observed from the literature review that the condensed plate models capture the effect of anti-symmetric motions such as bending, shear and membrane but lack in capturing symmetric motions of the multi-layer structures.

# Chapter 3

# Condensed model from the Transfer Matrix Method (TMM)

This chapter presents the principles of the Transfer Matrix Method (TMM) which is a general method for modelling acoustic fields in layered media which include fluid, elastic and poro-elastic layers. The method assumes planar multi-layer structure with infinite lateral dimensions of the layers and represents the plane wave propagation in different media in terms of transfer matrices. Interface matrices describe the continuity conditions between different layers, depending on the nature of the two layers. Since this method has its foundation from the theory of elasticity, it is complete and considered as a reference method to validate many vibro-acoustic models. As the new models developed in this thesis are applicable to various kind of materials (such as fluid, solid and poro-elastic), transfer matrices for these materials are presented in this chapter. Further, the method to compute vibro-acoustic indicators such as transmission coefficient, absorption etc., are also presented. Finally, a simple version of the condensed model for symmetric multi-layer systems is presented from the condensed transfer matrix obtained from TMM.

## 3.1 Principle of the TMM

A semi-infinite multi-layered system with homogeneous isotropic layers (Fig. 3.1) can be considered as a bi-dimentional system, taking $z-x$ the plane as the incident plane. On the schematic representation of the multi-layer system shown in Fig. 3.1 which has '$n$' layers, a fluid is enclosing (in this case air) on both sides, a plane acousic wave is excited at an incident angle $\theta$. Various wave types can propagate in the layers, according to their nature. The $x$-component of the wave number (or transverse component) for each wave propagating in the infinite medium is equal to,

$$k_t = k_0 \sin\theta, \tag{3.1}$$

where $k_0 = \omega/c_0$ is the wave number in free air, $\omega = 2\pi f$ is the angular frequency, $f$ is

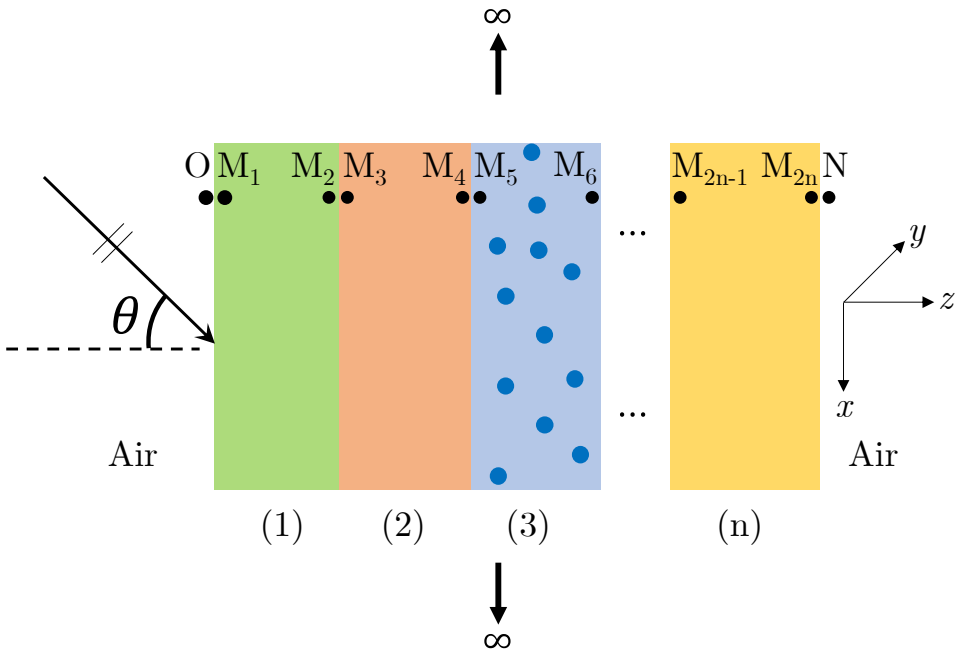


Figure 3.1: Oblique plane wave incidence on a multi-layer structure with infinite lateral dimensions.

the excitation frequency and $c_0$ is the speed of sound in air. Sound propagation in the $i-$th layer is represented by a transfer matrix, $[T]$ such that

$$\mathbf{V}(M_{2i-1}) = [T^i]\mathbf{V}(M_{2i}). \tag{3.2}$$

The components of the vector $\mathbf{V}(M)$ are the variables which describe the acoustic field at a point $M$ of the medium.

## 3.2 Transfer matrices of fluid and elastic solid layers

### 3.2.1 Fluid layer

Ideal fluids cannot resist changes in shape, but only changes in volume. As a result, only a longitudinal wave can propagate in a fluid layer, with a wave number $k = \omega/c$. $c$ is the speed of sound of the fluid. The acoustic field in a fluid layer is completely defined in each point $M$ by the vector,

$$\mathbf{V}^f(M) = \begin{bmatrix} p(M) & v_z^f(M) \end{bmatrix}^T, \tag{3.3}$$

where $p$ and $v_z^f$ are the acoustic pressure and the velocity component of the fluid in the $z$-direction, respectively. It may be noted that each propagative wave is defined by two state variables: pressure (or stress) and velocity. It enables to have its intensity (i.e., its level and its direction). Another way to describe the propagative wave is to use incident and reflected components. A $2 \times 2$ transfer matrix $[T^f]$ relates the pressure and velocity at the right-hand and left-hand side of the layer,

$$[T^f] = \begin{bmatrix} \cos(k_z h) & \mathrm{j}\dfrac{\omega\rho}{k_z}\sin(k_z h) \\ \mathrm{j}\dfrac{k_z}{\omega\rho}\sin(k_z h) & \cos(k_z h) \end{bmatrix}, \tag{3.4}$$

with $k_z = \sqrt{k^2 - k_t^2}$, the $z$-component of the wave number in the fluid, $\rho$ the density of the fluid and $h$ the thickness of the layer.

In case of a dissipative fluid layer (where the properties of the fluid are dependent on the frequency), the transfer matrix still takes the form given by Eq. (3.4), but density and speed of sound in the fluid takes the following form due to the dissipative nature of

the layer.

$$\rho \rightarrow \widetilde{\rho}, \quad c \rightarrow \widetilde{c} = \sqrt{\frac{\widetilde{K}}{\widetilde{\rho}}}, \tag{3.5}$$

where $\widetilde{K}$ is the frequency dependent bulk modulus of the dissipative fluid layer. The reader may recall that the symbol $\sim$ represents the dependency with frequency.

### 3.2.2 Isotropic elastic solid layer

In an elastic solid layer, two types of waves can propagate: a longitudinal wave and a transverse wave. The wave numbers of the longitudinal and shear waves in the elastic solid layer, $\delta_l$ and $\delta_s$ respectively, are given by:

$$\delta_l = \omega\sqrt{\frac{\rho}{\lambda + 2\mu}}; \quad \delta_s = \omega\sqrt{\frac{\rho}{\mu}}, \tag{3.6}$$

where $\rho$ is the density of the elastic solid and the Lamé coefficients ($\lambda$ and $\mu$) are calculated from the Young's modulus $E$ and the Poisson ratio $\nu$ as follows,

$$\lambda = \frac{E\nu}{(1+\nu)(1-2\nu)}; \quad \mu = G = \frac{E}{2(1+\nu)}. \tag{3.7}$$

Based on the type of backing at the rear end, the frequency of the first compressional mode of an elastic layer is given as

$$f_{\text{comp}} = \frac{1}{\gamma h}\sqrt{\frac{\lambda + 2\mu}{\rho}}, \tag{3.8}$$

where $\gamma$ takes on the values 2 (half-wave frequency) and 4 (quarter wave frequency) for anechoic and rigid backing respectively.

A set of four variables is used to define the physical state of the isotropic elastic solid layer [140].

$$\mathbf{V}^s(M) = \begin{bmatrix} v_x^s(M) & v_z^s(M) & \sigma_{zz}^s(M) & \sigma_{xz}^s(M) \end{bmatrix}^T, \tag{3.9}$$

where $v_x^s$ and $v_z^s$ are the $x$ and $z$-components of the velocity, respectively. $\sigma_{zz}^s$ and $\sigma_{xz}^s$ are the normal and shear stresses at point $M$. One may note that the physical behaviour along $x$ and $y$ directions would be the same, as the layer under consideration is isotropic in nature. Then, a 4×4 transfer matrix $[T^s]$ that relates the state vector at both sides of the layer can be obtained. The elements of $[T^s]$ can be found in the Appendix A.

## 3.3 Transfer matrices of porous layer

A simple representation of the procedure to obtain the transfer matrix of the porous material (with and without heterogeneities) is given by Fig. 3.2. If the porous layer does not have heterogeneities (for example, double porosity, porous composite etc.), then the acoustic characteristics are used to get equivalent density ($\rho_{\text{eq}}$) and bulk modulus ($K_{\text{eq}}$) of the layer from a suitable fluid dissipation model. In the presence of heterogeneities, the equivalent density and bulk modulus would be modified to account for their effects on the dissipation mechanisms. Then the specific skeleton nature of the porous layer (rigid or limp) can be taken into account to describe the inertial effects of the porous layer through $\rho_{\text{eq}}$ and $K_{\text{eq}}$. The detailed explanations on each of the models and procedure in the Fig. 3.2 are discussed in this section.

### 3.3.1 Fluid dissipation models

Based on the porous material morphology, fluid dissipation models explain the viscous and thermal dissipation mechanisms occurring in the fluid phase of the material. The following models provide the equivalent fluid properties (typically density and bulk modulus as functions of frequency) which would be used to obtain the transfer matrices of the porous material.

#### Delany-Bazley (DB) model

Based on numerous experiments conducted by Delany and Bazley for fibrous materials with porosity approximately equal to 1, empirical relations for the characteristic

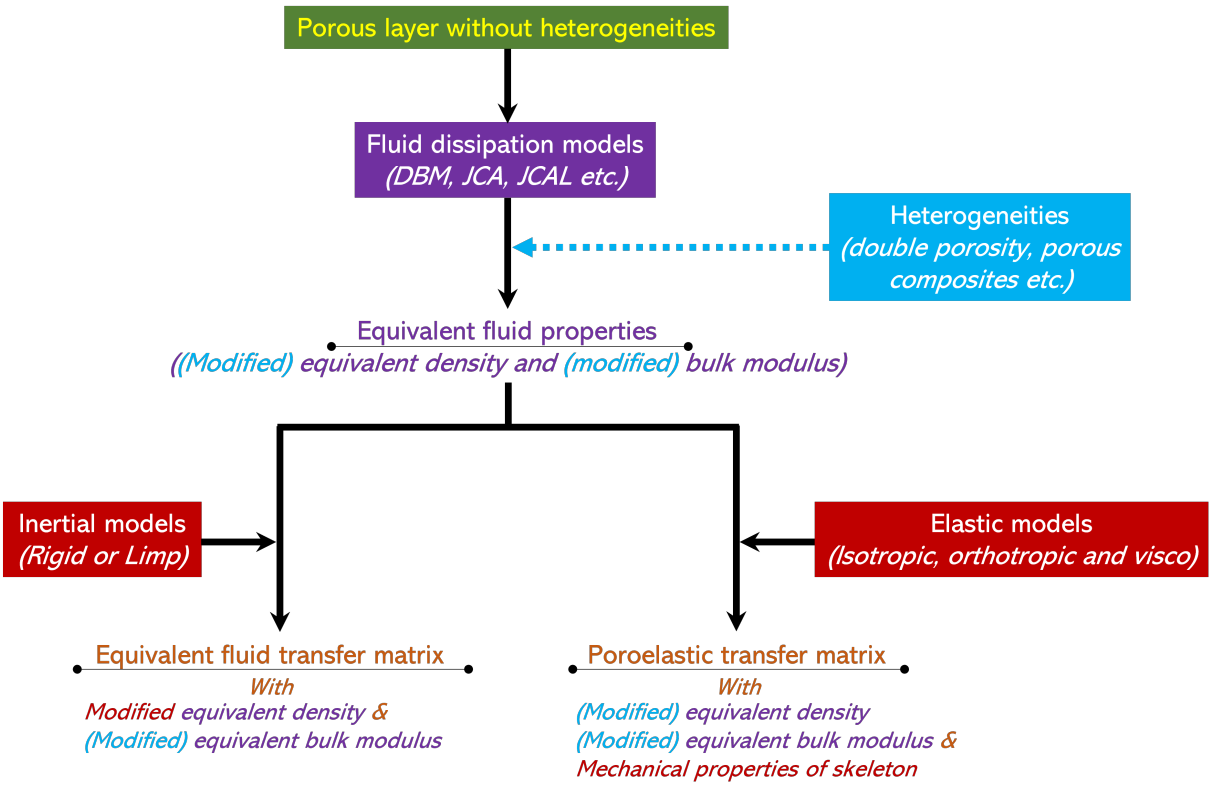


Figure 3.2: Methods to obtain transfer matrix of poro-elastic layer with and without heterogeneities.

impedance and wave number are given as [141]:

$$Z_c = \rho_0 c_0 \left[ 1 + 9.08 \left( 10^3 \frac{f}{\sigma} \right)^{-0.75} - \mathrm{j}11.9 \left( 10^3 \frac{f}{\sigma} \right)^{-0.73} \right]; \tag{3.10}$$

$$k_{\mathrm{eq}} = \frac{\omega}{c_0} \left[ 1 + 10.8 \left( 10^3 \frac{f}{\sigma} \right)^{-0.70} - \mathrm{j}10.3 \left( 10^3 \frac{f}{\sigma} \right)^{-0.59} \right]. \tag{3.11}$$

Note that $Z_c = \sqrt{\widetilde{\rho}_{\mathrm{eq}} \widetilde{K}_{\mathrm{eq}}}$ and $k_{\mathrm{eq}} = \omega \sqrt{\widetilde{\rho}_{\mathrm{eq}} / \widetilde{K}_{\mathrm{eq}}}$. In the above equations, $\rho_0$ is the density of the fluid medium (air) and $\sigma$ is the air flow resistivity of the porous layer in the propagating wave direction.

### Delany-Bazley-Miki (DBM) model

Miki [142] observed negative values for the characteristic impedance at low frequencies. As a result of this observation, Miki modified the expressions for the characteristic impedance

and wavenumber as follows:

$$Z_c = \rho_0 c_0 \left[ 1 + 5.50 \left( 10^3 \frac{f}{\sigma} \right)^{-0.632} - \mathrm{j}8.43 \left( 10^3 \frac{f}{\sigma} \right)^{-0.632} \right]; \tag{3.12}$$

$$k_{\mathrm{eq}} = \frac{\omega}{c_0} \left[ 1 + 7.81 \left( 10^3 \frac{f}{\sigma} \right)^{-0.618} - \mathrm{j}11.41 \left( 10^3 \frac{f}{\sigma} \right)^{-0.618} \right]. \tag{3.13}$$

The boundaries of validity for the DBM model is $0.01 < (f/\sigma) < 1$.

### Johnson-Champoux-Allard (JCA) model

The Johnson-Champoux-Allard model is based on the dissipative mechanisms due to visco-inertial [143] and thermal effects [144]. The dynamic density and bulk modulus are given as follows:

$$\widetilde{\rho} = \frac{\alpha_\infty \rho_0}{\phi} \left[ 1 + \frac{\sigma \phi}{\mathrm{j}\omega \rho_0 \alpha_\infty} \sqrt{1 + \mathrm{j} \frac{4 \alpha_\infty^2 \eta_0 \rho_0 \omega}{\sigma^2 \Lambda^2 \phi^2}} \right], \tag{3.14}$$

$$\widetilde{K} = \frac{\gamma_0 P_0 / \phi}{\gamma_0 - (\gamma_0 - 1) \left[ 1 - \mathrm{j} \frac{8 \kappa_0}{\Lambda'^2 C_p \rho_0 \omega} \sqrt{1 + \mathrm{j} \frac{\Lambda'^2 C_p \rho_0 \omega}{16 \kappa_0}} \right]^{-1}}, \tag{3.15}$$

where $\phi$ is the open porosity, $\alpha_\infty$ is the high frequency limit of the tortuosity, $\eta_0$ is the viscosity, $\Lambda$ is the viscous characteristic length, $\Lambda'$ is the thermal characteristic length, $P_0$ is the fluid equilibrium pressure, $\gamma_0 = C_p/C_v$ is the specific heat ratio and $\kappa_0$ is the thermal conductivity. It must be noted that the low frequency limit of the real part of the dynamic mass density expression of this model is not exact [145, 146] and there is lack of information at low frequencies for thermal effects [147].

### Johnson-Champoux-Allard Lafarge (JCAL) model

In this model, the dynamic density is kept the same, but the expression for dynamic bulk modulus is modified by Lafarge et al. [147] where the limitations in the low frequencies

for thermal effects were highlighted.

$$\widetilde{K} = \frac{\gamma_0 P_0/\phi}{\gamma_0 - (\gamma_0 - 1)\left[1 - \mathrm{j}\frac{\phi\kappa_0}{\Pi'_0 C_p \rho_0 \omega}\sqrt{1 + j\frac{4\Pi'^2_0 C_p \rho_0 \omega}{\kappa_0 \Lambda'^2 \phi^2}}\right]^{-1}}. \tag{3.16}$$

It must be noted that a new parameter, the static thermal permeability, $\Pi'_0$ is added in the above expression compared to JCA model.

**Johnson-Champoux-Allard Pride Lafarge (JCAPL) model**

JCA model was refined by Pride et al. [145] to account for pores with possible constrictions between them. Further, it was corrected by Lafarge [146] and the final expression of dynamic density is given as follows:

$$\widetilde{\rho} = \frac{\rho_0 \widetilde{\alpha}}{\phi}; \tag{3.17}$$

$$\widetilde{\alpha} = \alpha_\infty \left[1 + \frac{1}{\mathrm{j}\bar{\omega}}\widetilde{F}\right];\ \ \widetilde{F} = 1 - P + P\sqrt{1 + \frac{M}{2P^2}\mathrm{j}\bar{\omega}};\ \ \bar{\omega} = \frac{\omega\rho_0\Pi_0\alpha_\infty}{\eta_0\phi}; \tag{3.18}$$

$$M = \frac{8\Pi_0\alpha_\infty}{\phi\Lambda^2};\ \ P = \frac{M}{4\left(\frac{\alpha_0}{\alpha_\infty} - 1\right)}; \tag{3.19}$$

$$\widetilde{K} = \frac{\gamma_0 P_0}{\phi}\frac{1}{\widetilde{\beta}}; \tag{3.20}$$

$$\widetilde{\beta} = \gamma_0 - (\gamma_0 - 1)\left[1 + \frac{1}{\mathrm{j}\bar{\omega}'}\widetilde{F'}\right]^{-1};\ \ \widetilde{F'} = 1 - P' + P'\sqrt{1 + \frac{M'}{2P'^2}\mathrm{j}\bar{\omega}'}; \tag{3.21}$$

$$\bar{\omega}' = \frac{\omega\rho_0 C_p \Pi'_0}{\kappa_0\phi};\ \ M' = \frac{8\Pi'_0}{\phi\Lambda'^2};\ \ P' = \frac{M'}{4\left(\alpha'_0 - 1\right)}, \tag{3.22}$$

where $\Pi_0$ is the static viscous permeability, $\alpha_0$ is the static viscous tortuosity and $\alpha'_0$ is the static thermal tortuosity.

**Wilson model**

Since the models by Johnson, Koplik and Dashen for visco-inertial effects and models by Champoux-Allard or Champoux-Allard-Lafarge for thermal effects are developed to

match the low and high frequency behaviours of materials, Wilson [148] developed a model to match the medium frequency behaviour (or transition behaviour, when the viscous and thermal boundary layers are of the order of the pore size).

$$\widetilde{\rho} = \rho_\infty \frac{(1 + \mathrm{j}\omega\tau_{\mathrm{vor}})^{1/2}}{(1 + \mathrm{j}\omega\tau_{\mathrm{vor}})^{1/2} - 1}; \tag{3.23}$$

$$\widetilde{K} = K_\infty \frac{(1 + \mathrm{j}\omega\tau_{\mathrm{ent}})^{1/2}}{(1 + \mathrm{j}\omega\tau_{\mathrm{ent}})^{1/2} + \gamma_0 - 1}, \tag{3.24}$$

where $\rho_\infty$, $\tau_{\mathrm{vor}}$, $K_\infty$ and $\tau_{\mathrm{ent}}$ are the 4 parameters of Wilson's model and $\gamma_0$ is the ratio of specific heats.

### 3.3.2 Elastic models

Structural dissipation models are used to capture the vibrational behaviour of the porous material, which primarily depend on the material characteristics. These models account for the effects of mechanical properties of the skeleton material, for example, the effects of elasticity, visco-elasticity, anisotropy, orthotropy etc. These elastic models are then added with fluid dissipation (acoustic) model for the dissipation due to viscous and thermal effects [149] to finally compute the vibro-acoustic indicators.

For elastic isotropic frames of porous materials, according to Biot-Allard model [21], three different kinds of waves can propagate in the porous medium: a compressional and a shear wave in the solid phase and a compressional wave in the fluid phase. A transfer matrix could be formed from these types of wave propagation combining with visco-thermal dissipation (acoustic) models. For a complete description and derivation of the transfer matrix, the reader is referred to [21, 150]. By following the similar method for transversely isotropic medium, Khurana et al. [151] provided the description to obtain the transfer matrix, which could be extended for elastic orthotropic medium as well. Using the Stroh formalism, Parra Martinez [152] derived the transfer relations between the state

vectors for anisotropic poro-elastic media. As material properties of viscoelastic isotropic materials are frequency dependent, transfer matrix of elastic isotropic is used for further calculations. But it is to be noted that the material properties like Young's modulus ($\widetilde{E}$) would be rewritten as $\widetilde{E^*} = \widetilde{E}(1 + \mathrm{j}\widetilde{\eta})$ where $\widetilde{\eta}$ represents the structural damping factor. In general, Young's modulus ($\widetilde{E}$), damping factor ($\widetilde{\eta}$) and Poisson's ratio ($\widetilde{\nu}$) are the three material properties which are functions of frequency in a viscoelastic isotropic material.

### 3.3.3 Inertial models

If the fluid-structure interaction occurring between the saturating fluid and the porous skeleton is negligible, the entire porous material can be considered as an equivalent fluid. This situation is encountered either in the case the deformation energy governed by the stiffness is much higher than the inertial energy or vice-versa. These two situations correspond respectively to Rigid body or Limp behaviours.

#### Rigid body model

If the porous material moves as a whole without deforming or in a situation where the ratio of the Young's modulus to volumetric mass density is high, the porous material is assumed to be a rigid body. This situation may be encountered for stiff materials, though with a low mass density. In this case, the porous frame does not deform, but inertial effects may occur because the porous material is allowed to move in a rigid body motion [149]. For this rigid body model, expression of the equivalent density ($\widetilde{\rho}_{\mathrm{eq}}$) may be modified to improve the description of inertial effects [149]:

$$\frac{1}{\widetilde{\rho}_{\mathrm{eq}}^{RB}} = \frac{1}{\widetilde{\rho}_{\mathrm{eq}}} + \frac{\gamma'^2 + (1-\phi)\gamma'}{\widetilde{\rho}}; \tag{3.25}$$

$$\widetilde{K}_{\mathrm{eq}} = \widetilde{K}_f/\phi; \quad k_{\mathrm{eq}} = \omega\sqrt{\widetilde{\rho}_{\mathrm{eq}}/\widetilde{K}_{\mathrm{eq}}}, \tag{3.26}$$

where $\phi, \gamma', \widetilde{\rho}$ and $\widetilde{K}_f$ are porosity, coupling factor, modified Biot's density and bulk modulus of saturating air respectively. It may be noted that Eq. (3.25) is presented in the correct form after removing the typos in [149]. Detailed description of each of these parameters can be found in [149]. The equivalent parameters $\widetilde{\rho}_{\text{eq}}^{RB}$ and $k_{\text{eq}}$ are used in the fluid matrix given in Eq. (3.4) in places of $\rho$ and $k$ respectively.

**Limp model**

Limp model corresponds to situations where the ratio Young's modulus to volumetric mass density is small. Typical examples of limp materials are soft, highly porous fibrous materials. In this case, the bulk modulus and the shear modulus are assumed to have zero values. The modified equivalent mass density expression for the limp model is [153]:

$$\frac{1}{\widetilde{\rho}_{\text{eq}}^{\text{limp}}} = \frac{1}{\widetilde{\rho}_{\text{eq}}} + \frac{\gamma'^2}{\widetilde{\rho}}. \tag{3.27}$$

For the majority of the porous materials, the bulk modulus of the porous material is much larger than that of the fluid medium. In such cases, the effective density for the limp model is given as [153]:

$$\widetilde{\rho}_{\text{limp}} \approx \frac{\rho_t \widetilde{\rho}_{\text{eq}} - \rho_0^2}{\rho_t + \widetilde{\rho}_{\text{eq}} - 2\rho_0}; \;\; \rho_t = \rho_1 + \phi\rho_0, \tag{3.28}$$

where $\rho_0$ and $\rho_1$ are the densities of the fluid medium and porous material, respectively. Again, using these effective properties, the matrix representation of the limp frame limit is given by Eq. (3.4).

### 3.3.4 Models for poro-elastic material with heterogeneities

For the elaborated porous materials like double porosity materials with deformable skeleton [154] and porous composites [149], the equivalent fluid properties (obtained from fluid dissipation models) can be modified to correctly capture effects of heterogeneities. These modified equivalent fluid properties are then used in either structural or inertial dissipation models to compute the vibro-acoustic indicators of the poro-elastic material.

An illustration on the ways to obtain transfer matrix for poro-elastic layer is presented in the Fig. 3.2 whose state vector is given by,

$$\mathbf{V}^p(M) = \begin{bmatrix} v_x^s(M) & v_z^s(M) & v_z^f(M) & \sigma_{zz}^s(M) & \sigma_{xz}^s(M) & p^f(M) \end{bmatrix}^T. \tag{3.29}$$

## 3.4 Transfer matrices of elastic plate layer, septum layer and impervious screen

### 3.4.1 Elastic plate and septum layers

In case of elastic plate layer, the wave propagation is assumed to be controlled by bending and shear motion of the plate. One may remind that the elastic solid layer (see Section 3.2.2) allows compressional, bending and shear waves to propagate, whereas the elastic plate layer allows only bending and shear waves of the layer. In thin plates, bending wave is the only mode of wave propagation (follows thin plate theory by Love-Kirchoff [95]) whereas both bending and shear waves are the mode of wave propagation in thick plates (follows thick plate theory by Reissner-Mindlin [97, 99]). A set of two variables is needed to model the wave propagation in the elastic plates.

$$\mathbf{V}^{\text{ep}}(M) = \begin{bmatrix} v_z^{\text{ep}}(M) & \sigma_{zz}^{\text{ep}}(M) \end{bmatrix}^T, \tag{3.30}$$

where $v_z^{\text{ep}}$ and $\sigma_{zz}^{\text{ep}}$ are the $z$-component of the velocity and normal stress at the point, $M$ respectively. A 2×2 transfer matrix $[T^{\text{ep}}]$ gives the relation between these quantities at both sides of the layer,

$$[T^{\text{ep}}] = \begin{bmatrix} 1 & 0 \\ -Z_{\text{ep}} & 1 \end{bmatrix}. \tag{3.31}$$

Here, $Z_{\text{ep}}$ is the mechanical impedance of the plate, and it is expressed as below based on the theory adopted.

$$Z_{\text{ep}} = \begin{cases} Z_{\text{thin}} = \mathrm{j}\omega m_s \left(1 - \dfrac{D k_t^4}{\omega^2 m_s}\right) \\ Z_{\text{thick}} = \dfrac{k_t^4 D - m_s\omega^2 + \left(\dfrac{I_z m_s}{G^* h}\omega^2 - k_t^2 \dfrac{D m_s}{G^* h}\right)\omega^2 - k_t^2 I_z \omega^2}{\mathrm{j}\omega\left(1 + \dfrac{k_t^2 D - I_z\omega^2}{G^* h}\right)} \end{cases}, \tag{3.32}$$

where $m_s$ is the mass density per unit area, $D = \dfrac{E(1+\mathrm{j}\eta)h^3}{12(1-\nu^2)}$ is the bending stiffness, $G^* = G\kappa$ with $G$ as the shear modulus of the plate, $\kappa$ is the shear correction factor and $I_z = \dfrac{\rho h^3}{12}$ is the mass moment of inertia.

If one wants to express the state vector with pressure, then $\mathbf{V}^{\text{ep}}(M)$ takes the following form,

$$\mathbf{V}^{\text{ep}}(M) = \begin{bmatrix} p^{\text{ep}}(M) & v_z^{\text{ep}}(M) \end{bmatrix}^T, \tag{3.33}$$

which in turn results into the following transfer matrix form,

$$[T^{\text{ep}}] = \begin{bmatrix} 1 & Z_{\text{ep}} \\ 0 & 1 \end{bmatrix}. \tag{3.34}$$

A layer is called as septum (mass layer) when the bending stiffness is negligible. In this case, the mechanical impedance in Eq. (3.32) is reduced to $Z_{\text{sm}} = \mathrm{j}\omega m_s$.

### 3.4.2 Impervious screen

Impervious screens are generally used to protect acoustic materials. For the impervious screen bonded onto a porous material, the following set of variables is needed to characterize the acoustic field in the screen, as the modelling needs to account for the interface forces.

$$\mathbf{V}^{\text{imp}}(M) = \begin{bmatrix} v_x^{\text{imp}}(M) & v_z^{\text{imp}}(M) & \sigma_{zz}^{\text{imp}}(M) & \sigma_{xz}^{\text{imp}}(M) \end{bmatrix}^T, \tag{3.35}$$

where $v_x^{\text{imp}}$ and $v_z^{\text{imp}}$ are the $x$ and $z$-components of the velocity, respectively. $\sigma_{zz}^{\text{imp}}$ and $\sigma_{xz}^{\text{imp}}$ are the normal and shear stresses at point $M$. Then, a 4×4 transfer matrix $[T^{\text{imp}}]$ that relates these quantities at both sides of the layer is given by,

$$[T_{\text{imp}}] = \begin{bmatrix} 1 & 0 & 0 & 0 \\ 0 & 1 & 0 & 0 \\ 0 & -Z_{\text{imp}} & 1 & 0 \\ -Z'_{\text{imp}} & 0 & 0 & 1 \end{bmatrix}, \tag{3.36}$$

where $Z_{\text{imp}} = \mathrm{j}\omega m_s\left(1 - \frac{Dk_t^4}{\omega^2 m_s}\right)$, $Z'_{\text{imp}} = \mathrm{j}\omega m_s\left(1 - \frac{Sk_t^2}{\omega^2 m_s}\right)$ and $S$ is the membrane stiffness of the screen.

## 3.5 Coupling interface matrices

The transfer matrices of various types of layer were evaluated in the previous section. Following the work by Brouard et al. [19], the interface continuity conditions between two adjacent layers $i$ and $j$ are described as:

$$[I_{ij}]\mathbf{V}^i(M_i) + [J_{ij}]\mathbf{V}^j(M_j) = 0. \tag{3.37}$$

As the continuity conditions depend on the nature of the two layers that are in contact, the matrices $[I_{ij}]$ and $[J_{ij}]$ also depend on the same.

If the two layers are of the same nature, and they are not porous, the global transfer matrix is simply equal to the product of the transfer matrices of the two layers.

### 3.5.1 Porous-Porous interface

If two poro-elastic layers are in contact, the interface continuity conditions are influenced by the porosities of those two layers as shown below:

$$v_x^s(M_i) = v_x^s(M_j); \;\; v_z^s(M_i) = v_z^s(M_j);$$

$$\phi_i(v_z^f(M_i) - v_z^s(M_i)) = \phi_j(v_z^f(M_j) - v_z^s(M_j));$$

$$\sigma_{zz}^f(M_i)/\phi_i = \sigma_{zz}^f(M_j)/\phi_j; \;\; \sigma_{xz}^s(M_i) = \sigma_{xz}^s(M_j). \tag{3.38}$$

In this case, the global transfer matrix $[T^p]$ is written as:

$$[T^p] = [T_1^p][I_{pp}][T_2^p]. \tag{3.39}$$

Here, $[T_1^p]$ and $[T_2^p]$ are the transfer matrices of the two porous layers, and $[I_{pp}]$ is represented as shown from the Eq. (3.38):

$$[I_{pp}] = \begin{bmatrix} 1 & 0 & 0 & 0 & 0 & 0 \\ 0 & 1 & 0 & 0 & 0 & 0 \\ 0 & 1-\frac{\phi_2}{\phi_1} & \frac{\phi_2}{\phi_1} & 0 & 0 & 0 \\ 0 & 0 & 0 & 1 & 0 & 1-\frac{\phi_1}{\phi_2} \\ 0 & 0 & 0 & 0 & 1 & 0 \\ 0 & 0 & 0 & 0 & 0 & \frac{\phi_1}{\phi_2} \end{bmatrix}. \tag{3.40}$$

It is to be noted that $[I_{pp}]$ will be unit matrix if porosities of the two porous layers are equal.

### 3.5.2 Fluid-Solid interface

For a fluid and a solid in contact, the continuity conditions are,

$$v_z^f(M_i) = v_z^s(M_j); \;\; 0 = \sigma_{xz}^s(M_j); \;\; -p(M_i) = \sigma_{zz}^s(M_j). \tag{3.41}$$

The corresponding interface matrices are,

$$[I_{fs}] = \begin{bmatrix} 0 & -1 \\ 1 & 0 \\ 0 & 0 \end{bmatrix}; \quad [J_{fs}] = \begin{bmatrix} 0 & 1 & 0 & 0 \\ 0 & 0 & 1 & 0 \\ 0 & 0 & 0 & 1 \end{bmatrix}. \tag{3.42}$$

### 3.5.3 Fluid-Porous interface

For a fluid and a poro-elastic layer in contact, the continuity conditions are,

$$v_z^f(M_i) = (1-\phi_j)v_z^s(M_j) + \phi_j v_z^f(M_j);\;\; 0 = \sigma_{xz}^s(M_j);$$

$$-\phi_j p(M_i) = \sigma_{zz}^f(M_j);\;\; -(1-\phi_j)p(M_i) = \sigma_{zz}^s(M_j). \tag{3.43}$$

The corresponding interface matrices are,

$$[I_{fp}] = \begin{bmatrix} 0 & -1 \\ \phi_j & 0 \\ 1-\phi_j & 0 \\ 0 & 0 \end{bmatrix};\quad [J_{fp}] = \begin{bmatrix} 0 & 1-\phi_j & \phi_j & 0 & 0 & 0 \\ 0 & 0 & 0 & 0 & 0 & 1 \\ 0 & 0 & 0 & 1 & 0 & 0 \\ 0 & 0 & 0 & 0 & 1 & 0 \end{bmatrix}. \tag{3.44}$$

### 3.5.4 Solid-Porous interface

For a solid and a poro-elastic layer in contact, the continuity conditions are,

$$v_z^s(M_i) = v_z^s(M_j);\;\; v_x^s(M_i) = v_x^s(M_j);\;\; v_z^s(M_i) = v_z^f(M_j);$$

$$\sigma_{xz}^s(M_i) = \sigma_{xz}^s(M_j);\;\; \sigma_{zz}^s(M_i) = \sigma_{zz}^f(M_j) + \sigma_{zz}^s(M_j). \tag{3.45}$$

The corresponding interface matrices are,

$$[I_{sp}] = \begin{bmatrix} 1 & 0 & 0 & 0 \\ 0 & 1 & 0 & 0 \\ 0 & 1 & 0 & 0 \\ 0 & 0 & 1 & 0 \\ 0 & 0 & 0 & 1 \end{bmatrix};\quad [J_{sp}] = \begin{bmatrix} 1 & 0 & 0 & 0 & 0 & 0 \\ 0 & 1 & 0 & 0 & 0 & 0 \\ 0 & 0 & 1 & 0 & 0 & 0 \\ 0 & 0 & 0 & 1 & 0 & 0 \\ 0 & 0 & 0 & 0 & 1 & 1 \end{bmatrix}. \tag{3.46}$$

$[I_{ij}]$ and $[J_{ij}]$ matrices must be interchanged if the order of the layers are interchanged. For example, in case of porous-solid interface, $[I_{ps}] = [J_{sp}]$ and $[J_{ps}] = [I_{sp}]$.

## 3.6 Assembling the global transfer matrix

By combining all the transfer and interface matrices in the correct order, the multi-layered structure can be described. The following relations are formulated for the multi-layered structure of Fig. 3.1,

$$[I_{f1}]\mathbf{V}^f(O) + [J_{f1}][T^{(1)}]\mathbf{V}^{(1)}(M_2) = 0; \tag{3.47a}$$

$$[I_{i,i+1}]\mathbf{V}^i(M_{2i}) + [J_{i,i+1}][T^{(i+1)}]\mathbf{V}^{(i+1)}(M_{2(i+1)}) = 0, \;\; i = 1, n-1. \tag{3.47b}$$

The above equations can be written in matrix form as,

$$[D_0]\mathbf{V}_0 = 0, \tag{3.48}$$

where

$$[D_0] = \begin{bmatrix} [I_{f1}] & [J_{f1}][T^{(1)}] & 0 & \dots & 0 & 0 \\ 0 & [I_{12}] & [J_{12}][T^{(2)}] & \dots & 0 & 0 \\ \vdots & \vdots & \vdots & \ddots & \vdots & \vdots \\ 0 & 0 & 0 & \dots & [I_{n-1,n}] & [J_{n-1,n}][T^{(n)}] \end{bmatrix}, \tag{3.49}$$

and

$$\mathbf{V}_0 = \begin{bmatrix} V^f(O) & V^{(1)}(M_2) & V^{(2)}(M_4) & \dots & V^{(n)}(M_{2n}) \end{bmatrix}^T. \tag{3.50}$$

As the solution of the problem depends on boundary conditions on the left and right-hand side of the structure, the impedance at a point $N$ is written as follows by assuming

| Rear BC | $a$ | $b$ |
|---|---|---|
| Anechoic | 1 | $-Z_0/\cos\theta$ |
| Open end | 1 | 0 |
| Rigid backing | 0 | 1 |

Table 3.1: Values for $a$ and $b$ in Eq. (3.52) with respect to the rear boundary condition.

a semi-infinite air layer on the right-hand side,

$$p(N) - \frac{Z_0}{\cos\theta} v_z^f(N) = 0, \tag{3.51}$$

with $Z_0 = \rho_0 c_0$ being the characteristic impedance of air. In the cases of open end and rigidity backing at point $N$, the boundary conditions would be $p(N) = 0$ and $v_z^f(N) = 0$, respectively. Therefore, to accommodate all these three types of boundary conditions, the Eq. (3.48) is rewritten in the general form with this impedance equation as: $[D']\mathbf{V} = 0$, where

$$[D'] = \left[\begin{array}{cccc|cc} & & & & & 0 \\ & & [D_0] & & & \vdots \\ & & & & & 0 \\ \hline 0 & \dots & 0 & [I_{nf}] & & [J_{nf}] \\ 0 & \dots & 0 & 0 & a & b \end{array}\right], \tag{3.52}$$

and

$$\mathbf{V} = \begin{bmatrix} V_0 & V^f(N) \end{bmatrix}^T. \tag{3.53}$$

The values of $a$ and $b$ are listed in Table 3.1 with their respective boundary conditions (BCs) at point $N$. For transmission loss computations, the rear boundary condition would be defined by Eq. (3.51).

## 3.7 Calculation of the acoustic indicators

### 3.7.1 Surface impedance, reflection and absorption coefficients

The left-hand side boundary condition is expressed as a function of the surface impedance ($Z_s$) of the system as follows,

$$p(O) - Z_s v_z^f(O) = 0. \tag{3.54}$$

A set of linear equations can be written as given below by considering the above equation,

$$\left[\begin{array}{c|ccccc} 1 & -Z_s & 0 & \dots & 0 \\ \hline & & & & \\ & & [D'] & & \end{array}\right] \mathbf{V} = 0. \tag{3.55}$$

For non-trivial solution, the determinant of this matrix ($n \times n$ dimension) must be equal to zero. Therefore, $Z_s$ can be calculated by,

$$Z_s = -\frac{|D_1'|}{|D_2'|}, \tag{3.56}$$

where $|D_1'|$ and $|D_2'|$ are the determinant of the matrix obtained by removing the first and second columns respectively from $[D']$. Finally, the reflection coefficient ($R$) and the absorption coefficient ($\alpha$) are calculated by the following equations,

$$R = \frac{Z_s \cos\theta - Z_0}{Z_s \cos\theta + Z_0}; \quad \alpha = 1 - |R^2|. \tag{3.57}$$

The main advantage of this method is to compute only determinants of matrices instead of a full inversion.

### 3.7.2 Transmission coefficient

The transmission coefficient ($T$) is defined as the ratio of the pressure of the transmitted wave to that of the incident wave.

$$T = (1 + R)\frac{p(N)}{p(O)} = (1 + R)\frac{|D'_{n-1}|}{|D'_1|}, \tag{3.58}$$

where $|D'_{n-1}|$ is the determinant of the matrix obtained by removing the $(n-1)$th column from $[D']$. For a plane wave of incidence angle $\theta$, the transmission loss is defined by,

$$\mathrm{TL} = -10 \log_{10} \tau(\theta), \tag{3.59}$$

where $\tau(\theta) = |T^2(\theta)|$ is the transmission factor for the angle of the incidence $\theta$.

### 3.7.3 Acoustic indicators for diffuse field

In case of a diffuse field excitation with $\theta_{\min}$ and $\theta_{\max}$ being the selected diffuse field integration limits (usually 0 and $\pi/2$ respectively), the absorption coefficient and transmission loss are calculated as,

$$\alpha_d = \frac{\int_{\theta_{\min}}^{\theta_{\max}} \alpha(\theta) \cos\theta \sin\theta \mathrm{d}\theta}{\int_{\theta_{\min}}^{\theta_{\max}} \cos\theta \sin\theta \mathrm{d}\theta}; \tag{3.60}$$

$$\mathrm{TL}_d = -10 \log_{10} \left[ \frac{\int_{\theta_{\min}}^{\theta_{\max}} |\tau(\theta)|^2 \cos\theta \sin\theta \mathrm{d}\theta}{\int_{\theta_{\min}}^{\theta_{\max}} \cos\theta \sin\theta \mathrm{d}\theta} \right]. \tag{3.61}$$

## 3.8 A short description of finite size correction by FTMM

The TMM considers structures of infinite lateral dimensions to calculate the acoustic response. This methodology corresponds well with studies at mid to high frequencies for a wide variety of flat panels for transmission loss applications. On the other hand, discrep-

ancies are seen at low frequencies, particularly for small finite-sized panels. Therefore, Finite Transfer Matrix Method (FTMM), also called spatial windowing technique, is employed to account for the finite lateral dimensions of the multi-layer system. This method is rationalized by replacing the radiation efficiency in the receiving area with the radiation efficiency of an analogous baffled window. As a result, this method is only applicable to planar structures, by expressing the sound transmission coefficient as,

$$\tau_{\text{finite}} = \tau_{\text{infinite}} \sigma(k_t) \cos\theta, \tag{3.62}$$

where $\tau_{\text{infinite}}$ is the sound transmission coefficient when the structure is considered to be infinite. The radiation efficiency ($\sigma$) is expressed as follows:

$$\sigma(k_t) = \frac{\mathrm{j}k_0}{S} \int_0^{2\pi} \int_S \int_S \mathrm{e}^{-\mathrm{j}k_t(x\cos\phi + y\sin\phi)} G(M, M') \mathrm{e}^{-\mathrm{j}k_t(x'\cos\phi + y'\sin\phi)} \mathrm{d}x\mathrm{d}y\mathrm{d}x'\mathrm{d}y', \tag{3.63}$$

where $S$ is the area covered by the finite size of the rectangular structure of dimensions $L_x \times L_y$ and $G$ is the Green's function. One could observe that the above expression requires 5 integrals to estimate the value of the radiation efficiency (6 integrals in the diffuse field). Few popular FTMM models used in the industries are listed in [24–28]. All these models attempt to solve the same radiation equation (3.63) which uses 5 integrals while using different simplifications. Most of the models use 1D approximation considering $L_x \approx L_y$. Out of these five models, Rhazi and Atalla [26] model is the most accurate and applicable to all types of excitations since it solves the full equation while solving some integrals analytically without approximation. But this model attracts more computational time for the same reason. The model given by Bonfiglio et al. [28] is also applicable for all types of excitations and, absorption and transmission loss calculations. This model gains its advantage over other models since it is a good compromise between accuracy and computational time, but it uses 1D approximation.

## 3.9 Preliminary condensation using TMM

As discussed in Section 2.5, condensed models would serve as handy tools to understand the physical behaviour of the multi-layer structures and to reduce the computational time by reducing the total degrees of freedom during numerical simulations. One of the major shortcomings of the existing condensed models is excluding the symmetric motion (or compressional/dilatational/breathing motions) of the multi-layer structure. This is due to the assumption that the multi-layer is defined with constant displacement along the thickness direction, which prevents the stretching motion. Since large number of industrial multi-layer applications exhibit symmetric motion even at the low-frequencies ($100 - 500$ Hz), the existing condensed models need to be extended further to include the symmetric motions into the formulation. As a first step towards this goal, a simple condensation procedure through TMM is explained in this section.

### 3.9.1 Global matrix into $2 \times 2$ condensed transfer matrix

Since the multi-layer is surrounded by two fluid domains, its response is assumed to be condensed into $2 \times 2$ transfer matrix as shown below.

$$\begin{Bmatrix} p(O) \\ v_z(O) \end{Bmatrix} = \begin{bmatrix} T_{11} & T_{12} \\ T_{21} & T_{22} \end{bmatrix} \begin{Bmatrix} p(N) \\ v_z(N) \end{Bmatrix} = [T_{\text{eq}}] \begin{Bmatrix} p(N) \\ v_z(N) \end{Bmatrix}. \tag{3.64}$$

Nevertheless, this $2 \times 2$ condensed matrix is not intrinsic, since it has to be recomputed for each transverse wavenumber (or each incident angle).

In order to find the transfer matrix coefficients, two loads are applied on the above equation. When $p(N) = 0$ (corresponds to open end condition), the following transfer matrix coefficients are computed from the $[D']$ matrix (see Eq. (3.52)):

$$p(O) = T_{12} v_z(N) \;\; \Rightarrow \;\; T_{12} = -\frac{|D'_1|}{|D'_n|}; \tag{3.65a}$$

$$v_z(O) = T_{22} v_z(N) \;\; \Rightarrow \;\; T_{22} = \frac{|D'_2|}{|D'_n|}. \tag{3.65b}$$

Similarly, when $v_z(N) = 0$ (corresponds to rigid backing condition), the following transfer matrix coefficients can be computed:

$$p(O) = T_{11} p(N) \;\; \Rightarrow \;\; T_{11} = \frac{|D'_1|}{|D'_{n-1}|}; \tag{3.66a}$$

$$v_z(O) = T_{21} p(N) \;\; \Rightarrow \;\; T_{21} = -\frac{|D'_2|}{|D'_{n-1}|}. \tag{3.66b}$$

It may be noted that the condensed 2×2 transfer matrix can also be derived by a Schur's complement method [57] as follows. Let us express the global assembled matrix $[D']$ without the boundary condition as,

$$[\overline{D}] = \left[\begin{array}{ccc|c} & & & 0 \\ & [D_0] & & \vdots \\ & & & 0 \\ \hline 0 & \dots & 0 \quad [I_{nf}] & [J_{nf}] \end{array}\right] \left\{\begin{array}{c} V^f(O) \\ V^{(1)}(M_2) \\ \vdots \\ V^f(N) \end{array}\right\} = \mathbf{0}, \tag{3.67}$$

The matrix $[\overline{D}]$ of size $n \times n$ is rearranged and expressed as follows to have the external state variables of '$O$' and '$N$' adjacent to each other,

$$\left[\begin{array}{c|c} A_{2\times 4} & B_{2\times(n-4)} \\ \hline C_{(n-4)\times 4} & E_{(n-4)\times(n-4)} \end{array}\right] \left\{\begin{array}{c} V^f(O) \\ V^f(N) \\ V^{(1)}(M_2) \\ \vdots \\ V^{(n)}(M_{2n}) \end{array}\right\} = \mathbf{0} \Rightarrow \left[\begin{array}{c|c} A & B \\ \hline C & E \end{array}\right] \left\{\begin{array}{c} \mathbf{V}_{\text{ext}} \\ \mathbf{V}_{\text{int}} \end{array}\right\} = \mathbf{0}, \tag{3.68}$$

where $\mathbf{V}_{\text{ext}} = [V^f(O) \;\; V^f(N)]^T$ and $\mathbf{V}_{\text{int}} = [V^{(1)}(M_2) \; \ldots \; V^{(n)}(M_{2n})]^T$. From the second row of the above equation, $\mathbf{V}_{\text{int}}$ can be written as,

$$\mathbf{V}_{\text{int}} = -[E]^{-1}[C]\mathbf{V}_{\text{ext}}. \tag{3.69}$$

Substituting for $\mathbf{V}_{\text{int}}$ in Eq. (3.68), the equation given by the first row can be written as,

$$([A] - [B][E]^{-1}[C])\mathbf{V}_{\text{ext}} = \mathbf{0} \;\; \Rightarrow \;\; [T'_{(2\times 2)} \mid \overline{T}_{(2\times 2)}]\mathbf{V}_{\text{ext}} = \mathbf{0}. \tag{3.70}$$

As $\mathbf{V}_{\text{ext}} = [V^f(O) \;\; V^f(N)]^T = [p^f(O) \;\; v_z^f(O) \;\; p^f(N) \;\; v_z^f(N)]^T$, Eq. (3.70) can be rewritten as,

$$[T'] \begin{Bmatrix} p^f(O) \\ v_z^f(O) \end{Bmatrix} + [\overline{T}] \begin{Bmatrix} p^f(N) \\ v_z^f(N) \end{Bmatrix} = \mathbf{0} \;\; \Rightarrow \;\; \begin{Bmatrix} p^f(O) \\ v_z^f(O) \end{Bmatrix} = -[T']^{-1}[\overline{T}] \begin{Bmatrix} p^f(N) \\ v_z^f(N) \end{Bmatrix}. \tag{3.71}$$

From comparing Eq. (3.71) to Eq. (3.64), the $2 \times 2$ condensed matrix ($[T_{\text{eq}}]$) can be expressed as,

$$[T_{\text{eq}}] = -[T']^{-1}[\overline{T}] \tag{3.72}$$

One may note that the elements of $[T_{\text{eq}}]$ given by Eqs. (3.65) and (3.72) are the same. Therefore, the two-loads method presented in this section can be considered as an alternative strategy to the Schur's complement method to compute the condensed matrix without matrix inversions.

After obtaining the transfer matrix coefficients, the surface impedance can be calculated using the following relation:

$$Z_s = \frac{T_{12} + T_{11} Z_0 / \cos\theta}{T_{22} + T_{21} Z_0 / \cos\theta}. \tag{3.73}$$

The reflection and absorption coefficients can be computed using Eq. (3.57). Then, the

| | Plasterboard | Soft layer |
|---|---|---|
| $\rho$ (kg m$^{-3}$) | 700 | 55 |
| $E$ (Pa) | $3\times10^9$ | $43\times10^3$ |
| $\nu$ | 0.22 | 0.4 |
| $\eta$ | 0.08 | 0.3 |

Table 3.2: Mechanical properties of the isotropic layers used in this chapter.

transmission coefficient is obtained from

$$T = \frac{1+R}{T_{11} + T_{12}\dfrac{\cos\theta}{Z_0}} \quad \Rightarrow T = \frac{2}{T_{11} + T_{22} + \dfrac{T_{12}\cos\theta}{Z_0} + T_{21}\dfrac{Z_0}{\cos\theta}}. \tag{3.74}$$

For the transmission loss computations, under plane wave and/or diffuse field, Eqs. (3.59)-(3.61) can be used with transmission coefficient from Eq. (3.74). As an example, for a three-layer sandwich structure with sequence plasterboard/soft layer/plasterboard (material properties can be referred from Table 3.2), the transmission loss obtained from this approach can be compared against that of the TMM. From the comparison plot of transmission loss (see Fig. 3.3), it can be seen that the condensed matrix approach results in the same response as that of the TMM.

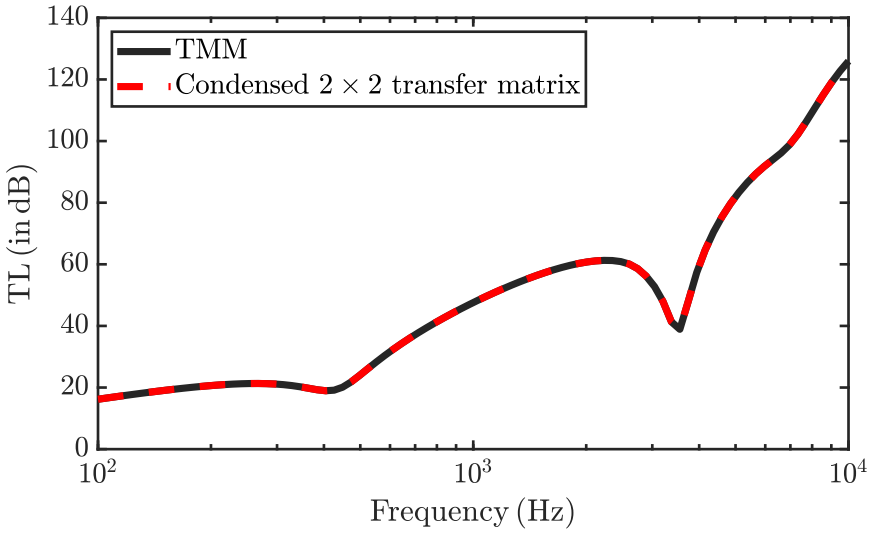


Figure 3.3: Transmission loss computations from the TMM and condensed matrix approaches for three-layer sandwich plasterboard (12.5 mm)/soft layer (3 mm)/plasterboard (12.5 mm). The calculation is done for plane wave excitation with 60° incidence. Material properties can be referred from Table 3.2.

Another useful relation can be obtained for the transmission factor of a single layer plate using the Eq. (3.74). Since the plate layer has state vector with pressure and velocity, by comparing the transfer matrices from Eqs. (3.34) and (3.64), transmission factor for plates can be written as,

$$\tau\left(\theta\right) = \left|T^2(\theta)\right| = 1/\left|1 + \frac{Z_{\mathrm{ep}}\cos\theta}{2Z_0}\right|^2. \tag{3.75}$$

### 3.9.2 Intrinsic properties of the condensed layer

Intrinsic or characteristic properties of the condensed layer are the properties which describe the natural response of the structure and do not depend on the incident angle of the plane wave. Since the multi-layer is condensed into the layer whose transfer matrix relation is defined by Eq. (3.64), the intrinsic properties of the condensed layer could be found by comparing the transfer matrix $[T_{\mathrm{eq}}]$ to either the transfer matrix of the fluid layer ($[T^f]$) or that of the plate layer ($[T^{\mathrm{ep}}]$). If the condensed (or equivalent) layer is assumed to be of fluid nature, then the intrinsic properties would be $\widetilde{\rho}_{\mathrm{eq}}$ and $\widetilde{K}_{\mathrm{eq}}$. But this may be not be always possible, as it requires at least the symmetry of $[T_{\mathrm{eq}}]$. On the other hand, in case of thin multi-layer structure, the transfer matrix $[T_{\mathrm{eq}}]$ could be compared to the plate transfer matrix $[T^{\mathrm{ep}}]$ which would yield $\widetilde{D}_{\mathrm{eq}}$ and $\rho_{\mathrm{eq}}$ as intrinsic properties. Again, this approach requires $T_{11} = T_{22}$, and additionally $T_{11} = T_{22} \approx 1$ and $T_{21} \approx 0$ conditions also need to be met. All of these conditions are difficult to be satisfied for many multi-layer applications and further, the elements of $[T_{\mathrm{eq}}]$ are angle dependant which result in the angle dependency of the condensed layer properties. This is considered to be the limitation of the present condensation approach.

### 3.9.3 Condensation approach for symmetric multi-layers

According to Dym and Lang [155], the anti-symmetric and symmetric motions are decoupled for the physically symmetric multi-layer system and two types of impedances corresponding to these motions can be defined. This assumption holds true since the

coupling components of each symmetric layer are balanced and therefore can be ignored when computing the system's kinematic and deformation energies. As a result, the system's symmetric ($Z_S$) and anti-symmetric ($Z_A$) impedances may be used to describe both behaviors independently.

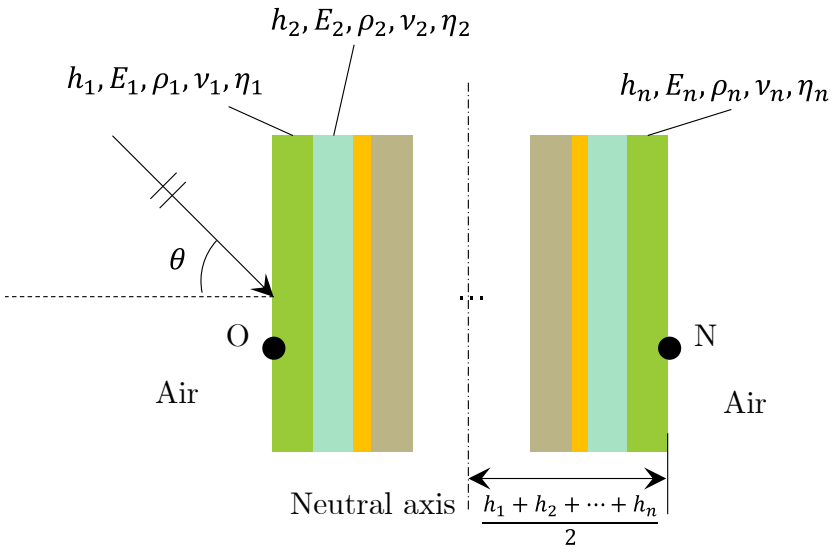


Figure 3.4: Schematic representation of the symmetric multi-layer structure subjected to plane wave incidence.

For the symmetric multi-layer system shown in Fig. 3.4, Dym and Lang [155] define symmetric and anti-symmetric impedances, in terms of pressure ($p$) and velocities ($v$) at points 'O' and 'N', as:

$$Z_{\mathrm{S}} = -\frac{p(O) + p(N)}{\overline{v}_z} = 2\frac{p(O) + p(N)}{v_z(O) - v_z(N)}, \tag{3.76}$$

$$Z_{\mathrm{A}} = \frac{p(O) - p(N)}{\breve{v}_z} = 2\frac{p(O) - p(N)}{v_z(O) + v_z(N)}, \tag{3.77}$$

where $\overline{v}_z$ and $\breve{v}_z$ denote the symmetric and anti-symmetric normal velocities. The above equations are rearranged to formulate the following transfer matrix in terms of the anti-

symmetric ($Y_{\mathrm{A}} = 1/Z_{\mathrm{A}}$) and symmetric ($Y_{\mathrm{S}} = 1/Z_{\mathrm{S}}$) admittances:

$$\begin{Bmatrix} p(O) \\ v_z(O) \end{Bmatrix} = \begin{bmatrix} \dfrac{Y_{\mathrm{A}} + Y_{\mathrm{S}}}{Y_{\mathrm{A}} - Y_{\mathrm{S}}} & \dfrac{1}{Y_{\mathrm{A}} - Y_{\mathrm{S}}} \\ \dfrac{4Y_{\mathrm{A}}Y_{\mathrm{S}}}{Y_{\mathrm{A}} - Y_{\mathrm{S}}} & \dfrac{Y_{\mathrm{A}} + Y_{\mathrm{S}}}{Y_{\mathrm{A}} - Y_{\mathrm{S}}} \end{bmatrix} \begin{Bmatrix} p(N) \\ v_z(N) \end{Bmatrix}. \tag{3.78}$$

From Eq. (3.64) and Eq. (3.78), the symmetric and anti-symmetric admittances are expressed in terms of the transfer matrix elements as:

$$Y_{\mathrm{S}} = \frac{T_{11} - 1}{2T_{12}}, \tag{3.79}$$

$$Y_{\mathrm{A}} = \frac{T_{11} + 1}{2T_{12}}. \tag{3.80}$$

For thin multi-layer structures where the anti-symmetric motions like bending and shear contribute more than the symmetric motions, $Y_S \approx 0$. This would result to simplify the Eq. (3.78) as follows:

$$\begin{Bmatrix} p(O) \\ v_z(O) \end{Bmatrix} = \begin{bmatrix} 1 & 1/Y_{\mathrm{A}} \\ 0 & 1 \end{bmatrix} \begin{Bmatrix} p(N) \\ v_z(N) \end{Bmatrix} = \begin{bmatrix} 1 & Z_A \\ 0 & 1 \end{bmatrix} \begin{Bmatrix} p(N) \\ v_z(N) \end{Bmatrix}. \tag{3.81}$$

The above transfer matrix is in the same form as the plate transfer matrix ($[T^{\mathrm{ep}}]$) and therefore, the condensed layer properties ($\widetilde{D}_{\mathrm{eq}}$ and $\rho_{\mathrm{eq}}$) given by the existing condensed plate models [7, 131, 133, 138, 156] would be indeed the intrinsic properties. If symmetric motions also give important contribution to the resulting motion, the intrinsic parameters corresponding to the symmetric motion need to be derived. Chapter 6 addresses the ways to obtain the symmetric intrinsic parameters for symmetric multi-layer structures.

## 3.10 Conclusion

Vibro-acoustic Transfer Matrix Method (TMM) approach that is used to compute the acoustic indicators of the multi-layer system has been recalled in this chapter. Transfer

matrices corresponding to fluid, elastic solid, plate, impervious layer and poro-elastic layer are presented as they would be used in the subsequent chapters of this thesis. A preliminary condensation procedure is presented to condense behaviour of the mutli-layer structure into a simple $2 \times 2$ transfer matrix relation with only pressure and velocity states. Nevertheless, this condensed matrix is not intrinsic since it has to be recomputed for each transverse wavenumber (or each incident angle). Finally, intrinsic properties can be characterized if one is able to identify a known $2 \times 2$ transfer matrix (fluid or thin plate). Although this condensation procedure is still limited for most of practical cases, it provides some possible directions in which the methodology could evolve to include compressional motion. Further, in Chapter 6, it serves as a handy tool to develop a novel condensed model to include compressional motion of the multi-layer structure and to compute vibro-acoustic indicators using $2 \times 2$ transfer matrix.

As the existing condensed plate models use thin plate theory to model the natural behaviour of the multi-layer structure, these models would be typically limited up to certain frequency. Also, in the literature, no clear-cut expression is available for the plate theories. Therefore, in the next chapter, frequency limit expressions of commonly employed plate theories are derived using the wavenumber and admittance analyses.

# Chapter 4

# Accuracy limits of plate theories

In this chapter, analytical expressions for the applicability limits in the spectral domain for thin and thick plate theories are derived for the first time. As these plate theories are widely used in many acoustic applications, applicability limits of these theories gain a particular interest, to avoid any mistakes in the design of acoustic packages which might arise from not satisfying the assumptions of these theories in a particular frequency range. Qualitative and approximate frequency limits are given in the literature, but it is often a tedious task to find an analytical expression for applicability limits. Through analysis of the propagating wavenumbers and admittances of the investigated panels, the expected accuracy of each theory is quantified.

**Note**

Most of the contents presented in this chapter has been taken from the published article [157]:

> **Arasan, U.**, Marchetti, F., Chevillotte, F., Tanner, G., Chronopoulos, D., Gourdon, E. (2021). "On the accuracy limits of plate theories for vibro-acoustic predictions". *Journal of Sound and Vibration*, 493, 115848.

Regarding the contributions made to the above-mentioned article, the author of this thesis has done the following tasks: methodology, investigation, validation, article writing and review.

The chapter is organized as follows: Section 4.2 describes the dispersion behaviour of thin and thick plates. As mentioned in the earlier chapters, the theory of elastic solids is treated as a reference for comparing the plate theories, since it describes the complete motion of an infinite layer [158]. In Section 4.3, expressions for the limits of applicability of thin plate theories are discussed by comparing propagating wavenumbers of thin and thick plate theories. Additionally, refined expressions for the coincidence and critical frequencies are also presented. In Section 4.4, an expression for the frequency limit of applicability of plate theories is derived by comparing the order of magnitudes of both symmetric and anti-symmetric admittances of the plate. In Section 4.5, analytical expressions for the frequency limits of different plate theories are presented along with sound transmission loss computations for classical industrial materials for validation purposes.

## 4.1 Background

When studying the sound insulation of a wall, the main acoustic indicator is the transmission loss (TL) which is controlled by the combination of several fundamental vibrating modes of the wall. For example, a typical sound transmission problem encountered in building applications is presented schematically in Fig. 4.1 along with its vibrating modes as the acoustic energy transmitted through the wall depends on its vibro-acoustic behaviour. Although the wall vibrates in a complex manner for the given acoustic excitation, this complex motion can be obtained by superposing the fundamental motions (bending, shear and compressional/dilatational motions). Generally, looking at the TL characteristics of a single wall as a function of frequency, three regions can be identified which are controlled by the mass, damping and stiffness of the wall respectively. The mass and stiffness control zones are separated by a critical region where strong reduction of transmission loss is observed. This critical zone is characterized by its frequency, which is called the critical frequency. Various vibro-acoustic models of varying complexity have been developed to predict the sound insulation properties of plate structures, especially with regard to noise attenuation problems. An early model was developed by Cremer [159] which was applied to the computation of the TL across infinite, thin walls. Related

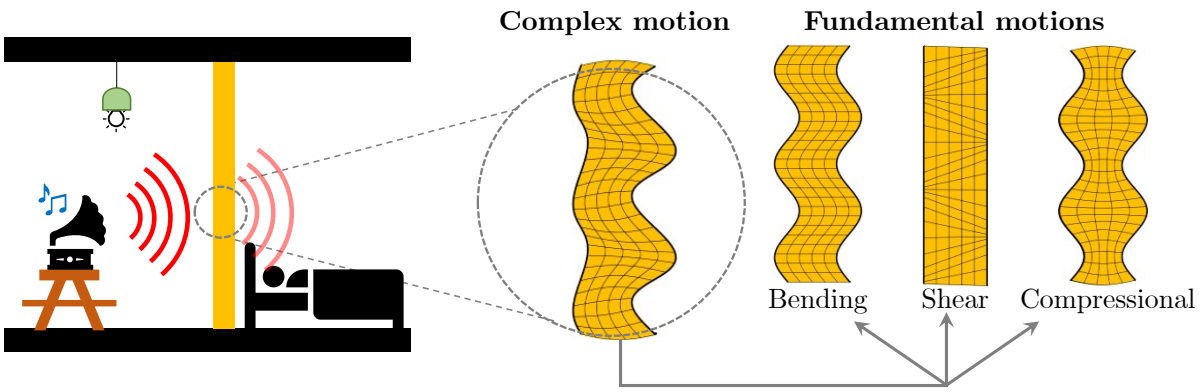


Figure 4.1: Schematic representation of vibrating motion of a single wall subjected to acoustic excitation.

work approaching the same problem of computing the acoustic insulation indicators of a thin wall are presented in [25, 60, 160–162]. In Cremer's model, it is assumed that the motion of the plate is described only by the bending wave equation, which is based on the classical plate theory [163].

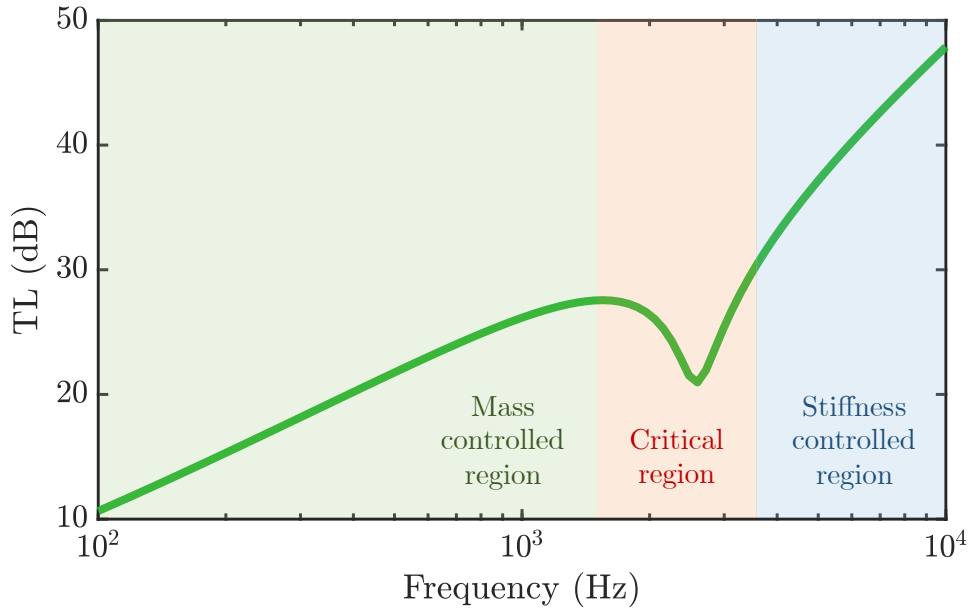


Figure 4.2: Three regions of transmission loss curve for a plasterboard layer of 12.5 mm under diffuse field. Material properties can be referred from Table 4.1.

Davy [164] argues that Cremer's model can only be used below the critical frequency, since most of the approximations are not valid within and above the critical region. Improving on Cremer's theory, Heckl and Donner [165] developed a model based on the first order shear deformation theory (FSDT) [97–99] which could be applied to thicker walls to compute sound TL. In this model, motion due to the transverse shear is also included

along with the flexural motion of the plate. The corrected TL expression accounting for shear deformation of the plate can be found in [166]. Heckl and Donner [165] point out that their model is valid only at frequencies well below the first dilatational or compressional frequency of the plate. This is due to the fact that the FSDT does not account for the thickness stretch motion of the plate, as it assumes constant velocity at all points through the thickness direction. Consequently, the symmetric motion of the plate is not taken into account in zero, first and higher order plate theories. This may lead to deviations between the predictions and the actual motion of the plate at higher frequencies, especially when the material is soft. In the work published by Ljunggren [166, 167], the general expression to compute the TL of an infinite wall with arbitrary uniform thickness is given, accounting for both anti-symmetric and symmetric motions of the plate.

In recent years, instead of single wall structures, multi-layered structures have been used widely for better sound comfort and noise attenuation. These structures provide the designers with more choices for tuning the vibro-acoustic performance, leading to better sound insulation characteristics. Advanced composite structures are one example of multi-layer systems that are progressively used in different fields such as the space, energy and aeronautical industries. In transport and construction industries, sandwich structures are widely used as they provide high stiffness with significantly low weight. In most cases, two face sheets are bonded with a viscoelastic layer to improve the overall damping response of the structure. There exist many theoretical models dedicated to the analysis of the behaviour of multi-layer structures. Since industrial multi-layer structures are manufactured with a diversity of materials, they naturally increase the computational burden for detailed finite element modelling, and it is therefore of interest to condense the behaviour of the multi-layer system into a single layer. A detailed summary on these kinds of different analytical models is given in Chapter 2 (literature survey) of this manuscript. Concerning the condensed (or equivalent) plate models, the goal of these models is to find the frequency dependent mechanical parameters of the equivalent thin plate that incorporates the bending and shear motions of the multi-layer structures. Since plate theories do not account for the dilatational or compressional motion of the structure,

finding a frequency domain of validity is necessary to safely use these equivalent plate models.

The reader may note that the words 'frequency limit' of a theory refer here to the frequency up to which the theory can be applied within pre-defined accuracy intervals for computing the desired acoustic indicators. Although in structural mechanics and dynamics, thin and thick plates are distinguished based on the thickness to lateral dimensions' ratio [168, 169], such rules may not be sufficient for vibro-acoustic calculations as they depend on the material properties of the plate as well. Additionally, although plate theories (both for thin and thick plates) are commonly employed in computing the acoustic indicators of infinite and finite walls, there is currently no clear-cut frequency limit to restrict the applicability of these theories. In the following sections, these frequency limits are derived from the wavenumber and admittance analyses of both thin and thick plate theories.

## 4.2 Dispersion relations from plate theories

This section starts by analysing the dispersion relations of some commonly used theories such as the Love-Kirchoff [96, 163] or the Reissner-Mindlin [97–99], to describe the vibro-acoustic behaviour of isotropic, single wall structures. In subsequent sections, these theories are compared, and their limitations are discussed.

Let us consider a structure with only one infinitely extended elastic plate layer with thickness $h$. For this case, Fig. 3.1 will be modified and represented schematically as shown in Fig. 4.3. The reader may recall that the transfer matrix of a plate layer is given by Eq. (3.34) and the state vector is defined with pressure and velocity at points 'O' and 'N'. The mechanical impedance of the plate layer, with respect to thin and thick plate theories, can be referred from Eq. (3.32). Given the mechanical impedances of the structure, dispersion relations are often obtained by setting the impedance to zero. In other words, dispersion relations are used to understand the wave propagation in the structure under natural or free vibration conditions.

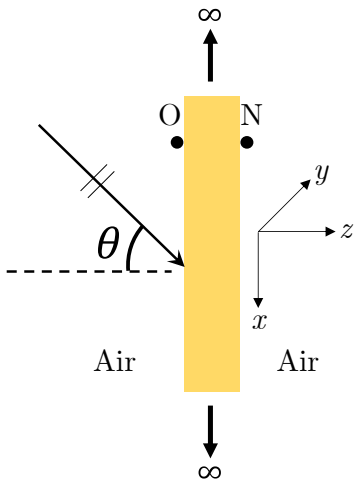


Figure 4.3: An oblique plane wave impinging on an infinitely extending elastic isotropic plate layer with incident angle $\theta$.

For Love-Kirchoff plates (or thin plates), by setting the mechanical impedance equal to zero, it can be observed that only one type of wave propagation is possible, that is,

$$Z_{\text{thin}} = 0 \quad \Rightarrow k_p^4 D - m_s\omega^2 = 0 \quad \Rightarrow k_p = k_b = \sqrt{\omega\sqrt{\frac{m_s}{D}}}, \tag{4.1}$$

where $k_b$ corresponds to the bending wavenumber and $k_p$ is the natural propagating wavenumber of the plate.

For Reissner-Mindlin plates (or thick plates), the dispersion relation is obtained as

$$Z_{\text{thick}} = 0 \quad \Rightarrow k_p^4 D - m_s\omega^2 + \left(\frac{I_z m_s}{G^* h}\omega^2 - k_p^2\frac{D m_s}{G^* h}\right)\omega^2 - k_p^2 I_z\omega^2 = 0. \tag{4.2}$$

There are four solutions possible for the above quartic equation, that is,

$$k_p = \pm\sqrt{\frac{m_s\omega^2}{2G^*h} + \frac{I_z\omega^2}{2D} \pm \sqrt{\frac{m_s\omega^2}{D} + \left(\frac{m_s\omega^2}{2G^*h} - \frac{I_z\omega^2}{2D}\right)^2}}. \tag{4.3}$$

Out of the four solutions, two correspond to outgoing waves, that is, the real part of the wavenumber is positive; these are

$$k_p = k_{RM_{1,2}} = \sqrt{\frac{m_s\omega^2}{2G^*h} + \frac{I_z\omega^2}{2D} \pm \sqrt{\frac{m_s\omega^2}{D} + \left(\frac{m_s\omega^2}{2G^*h} - \frac{I_z\omega^2}{2D}\right)^2}}. \tag{4.4}$$

It is observed from the above equation that the propagating wavenumber ($k_{RM_1}$) has

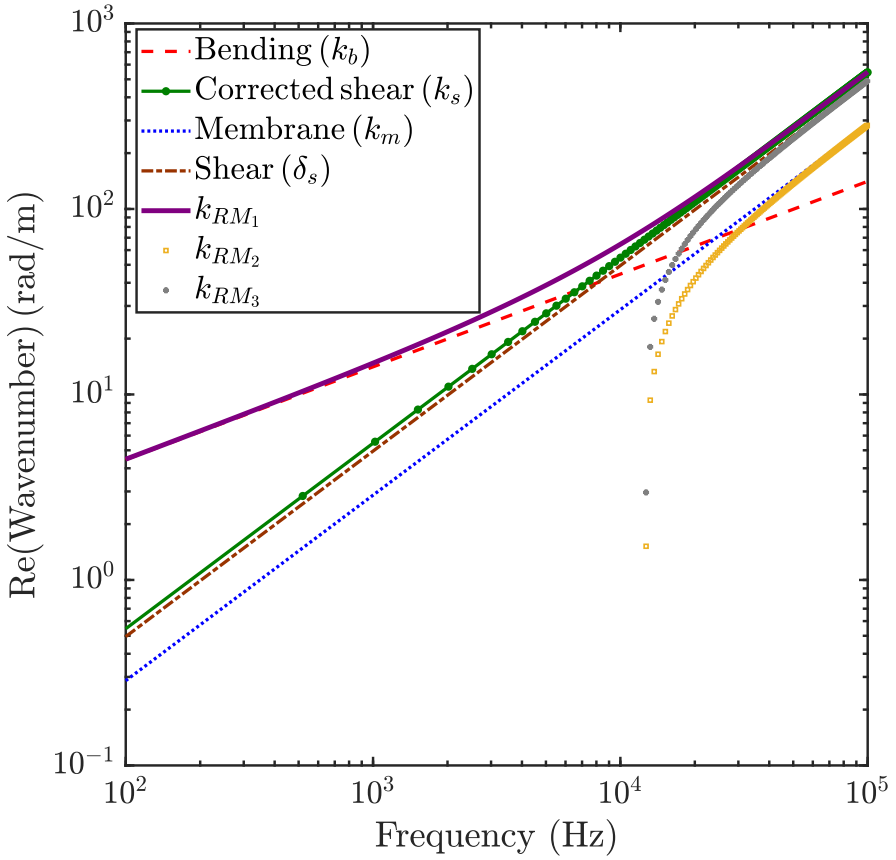


Figure 4.4: Propagating wavenumbers of a Reissner-Mindlin plate (50 mm plasterboard with mechanical properties mentioned in Table 4.1) and its asymptotic behaviours. It is observed that the main natural propagating wavenumber $k_{RM_1}$ is approaching bending ($k_b$) and corrected shear wavenumbers ($k_s$) at low and high frequencies, respectively.

different asymptotic behaviour with respect to low and high frequencies as shown in Fig. 4.4, here for the example of a 50 mm plasterboard with mechanical properties listed in Table 4.1. One finds in particular:

– At low frequency (or $\omega \to 0$), we have

$$\frac{m_s}{D} \gg \left(\frac{m_s}{2G^* h} - \frac{I_z}{2D}\right)^2 \omega^2 \tag{4.5}$$

which results in $k_{RM_1}$ tending to $k_b$

– At high frequency (or $\omega \to +\infty$), we find

$$\frac{m_s}{D} \ll \left(\frac{m_s\omega^2}{2G^*h} - \frac{I_z}{2D}\right)^2 \omega^2 \tag{4.6}$$

which results in $k_{RM_1}$ tending to $k_s = \omega\sqrt{\frac{m_s}{G^*h}}$ with $k_s$, the corrected shear wavenumber.

– $k_{RM_2}$ is evanescent until the cut-on frequency given by Eq. (4.8) after which it becomes propagating and reaches the membrane wavenumber $k_m = \omega\sqrt{\frac{I_z}{D}}$ at high frequency.

– $k_s$ is always greater than $k_m$ since $\frac{k_s}{k_m} = \sqrt{\frac{2}{\kappa(1-\nu)}} > 1$,

where $\kappa$ and $\nu$ are the shear correction factor and Poisson's ratio, respectively. Note that the ratio $k_s/k_m$ is simplified to the above form by employing the relations between the isotropic material properties.

Based on the above observations, Eq. (4.4) is rewritten in a compact form as,

$$k_{RM_{1,2}} = \sqrt{\frac{1}{2}\left[k_s^2 + k_m^2 \pm \sqrt{4k_b^4 + (k_s^2 - k_m^2)^2}\right]}. \tag{4.7}$$

The cut-on frequency can be obtained by considering $k_{RM_2} = 0$, that is,

$$k_s^2 + k_m^2 = \sqrt{4k_b^4 + (k_s^2 - k_m^2)^2} \quad \Rightarrow \quad k_b^4 = k_s^2 k_m^2,$$

and thus

$$f_{\text{cut-on}} = \frac{1}{2\pi}\sqrt{\frac{G^*h}{I_z}}. \tag{4.8}$$

Further, it is observed that the high frequency asymptote given by Ghinet and Atalla [71] as

$$k_{G\&A} = \omega\sqrt{\frac{4I_z m_s}{G^*hI_z + m_s D}}. \tag{4.9}$$

differs from the correct estimation of the high frequency asymptote $k_s$. It may be noted

that Eq. (4.2) can be obtained from two of the three equilibrium equations (derived by a Newtonian approach) for thick plates [170]. For the sake of completeness, the dispersion relation resulting from third equilibrium equation [71] is presented here. The natural wavenumber from the third equilibrium equation is given by,

$$k_p = k_{RM_3} = \sqrt{\frac{2}{1-\nu}\frac{I_z\omega^2 - G^* h}{D}} = \sqrt{\delta_s^2 - \frac{2}{1-\nu}\frac{k_b^4}{k_s^2}}, \tag{4.10}$$

where $\delta_s = \omega\sqrt{\frac{\rho}{G}}$ is the pure shear wavenumber of the isotropic elastic layer (refer Section 3.2.2). Similar to $k_{RM_2}$, $k_{RM_3}$ is also evanescent until a cut-on frequency ($f_{\text{cut-on}}$) but reaches the asymptote $\delta_s$ at higher frequencies as

$$\delta_s^2 \gg \frac{2}{1-\nu}\frac{k_b^4}{k_s^2}$$

when $\omega \to +\infty$.

Table 4.1: Material properties of few typical elastic isotropic layers used in this chapter

| | Aluminium | Plasterboard | Concrete | Soft layer |
|---|---|---|---|---|
| $\rho$ (kg m$^{-3}$) | 2780 | 700 | 2150 | 8 |
| $E$ (Pa) | $71\times10^9$ | $3\times10^9$ | $33\times10^9$ | $16\times10^4$ |
| $\eta$ | 0.01 | 0.08 | 0.1 | 0.1 |
| $\nu$ | 0.3 | 0.22 | 0.23 | 0.44 |

Fig. 4.4 illustrates these asymptotic behaviours of the solutions of $k_{RM}$ for a plasterboard of thickness 50 mm. Mechanical properties of the materials used in this chapter can be obtained from Table 4.1. It must be realized that both thin and thick plate theories neglect the compressional mode (also called the symmetric or dilatational mode) and allow only anti-symmetric modes (i.e, bending and/or shear modes), since the plate velocity is assumed to be constant through the thickness direction.

Since the motion both of the anti-symmetric and compressional mode of an infinite layer of finite thickness can be expressed based on the theory of elasticity, calculations of the transfer matrix for elastic solids are considered here as reference to the analysis using plate theories. By referring to the two fundamental wavenumbers ($\delta_l$ and $\delta_s$) of the

elastic isotropic solid, it can be understood that the bending wavenumber is a complex combination of these fundamental wavenumbers. It is, however, not straightforward to see this relation from the above equations for elastic isotropic solids.

## 4.3 Comparison between thin and thick plate theories

### 4.3.1 Frequency limit of thin plate theory in comparison with thick plate theory

In this section, natural propagating wavenumbers of thin and thick plate theories are used to find the frequency limit of the thin plate theory. From the Fig. 4.4, it can be seen that the thick plate wavenumber ($k_{RM_1}$) clearly deviates from the bending wavenumber ($k_b$) after certain frequency. It may be noted that, though there are totally three outgoing waves characterized by wavenumbers ($k_{RM_1}, k_{RM_2}$ & $k_{RM_3}$), $k_{RM_1}$ is considered for the present analysis as it is the only wavenumber that is always propagative. Additionally, since the deviation between $k_{RM_1}$ and $k_b$ starts well before the cut-on frequency ($f_{\text{cut-on}}$), $k_{RM_1}$ would be appropriate to derive the frequency limit of thin plate theory. By defining $C_k = \dfrac{k_b}{k_s}$, the ratio between bending and shear wavenumbers, error percentage ($\epsilon$) between the propagating wavenumbers of the thin and thick plate theories is expressed as

$$\epsilon = \left(1 - \frac{1}{k_{RM_1}/k_b}\right)100\%, \tag{4.11}$$

where,

$$\frac{k_{RM_1}}{k_b} = \frac{1}{2}\sqrt{\frac{2+\kappa(1-\nu)}{C_k^2} + \sqrt{16 + \left[\frac{2-\kappa(1-\nu)}{C_k^2}\right]^2}}, \tag{4.12}$$

which is obtained using Eq. (4.7).

The thin plate theory will be valid, while $k_s$ is negligible compared to $k_b$ ($k_b \geqslant C_k k_s$). The value for $C_k$ can be chosen such that $\epsilon$ is below an accepted error percentage, and the

frequency range of validity for thin isotropic plate can be expressed as given by Eq. (4.13).

$$k_b \geqslant C_k k_s \Rightarrow f \leqslant f_{\text{thin/thick}} = \frac{G^* h}{2\pi C_k^2}\sqrt{\frac{1}{m_s D}} = \frac{\kappa}{4\pi h C_k^2}\sqrt{\frac{12E}{\rho}\frac{1-\nu}{1+\nu}}, \tag{4.13}$$

where $f_{\text{thin/thick}}$ is the frequency limit of the 'thin' plate theory by keeping the 'thick' plate theory as reference. For instance, choosing $C_k = 4$ for typical isotropic layer corresponds to an error percentage ($\epsilon$) around 2% between $k_{RM_1}$ and $k_b$ (see Fig. 4.5).

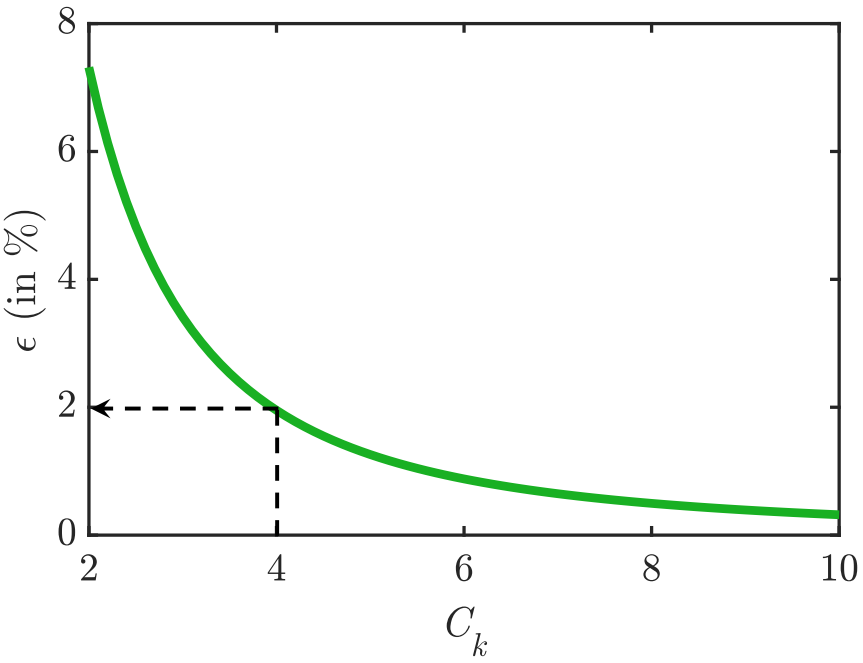


Figure 4.5: Relation between $C_k = k_b/k_s$ and error percentage (between the propagating wavenumbers from thin and thick plate theories) for $\kappa = 5/6$ and $\nu = 0.33$.

### 4.3.2 Coincidence and critical frequencies of thick plate

As discussed in the earlier sections, thin plate theory allows only bending waves to propagate in the elastic plate and shear wave propagation is included by thick plate theory to correctly capture the anti-symmetric motion of the plate. Due to this additional anti-symmetric motion in the plate, the coincidence and critical frequency expressions obtained from thin plate theory need to be rewritten with terms corresponding to shear and rotational inertia.

The coincidence frequency between a plate and an acoustic wave incident on the plate at an angle $\theta$ is defined as the frequency at which the transverse component of the incident wavenumber is equal to the natural propagating wavenumber of the plate. In the case of thin plates, the natural propagating wavenumber is the bending wavenumber and the coincidence frequency is expressed as,

$$k_b = k_0 \sin\theta \Longrightarrow f_{\mathrm{coinc_{thin}}} = \frac{1}{2\pi}\left(\frac{c_0}{\sin\theta}\right)^2 \sqrt{\frac{m_s}{D}}. \tag{4.14}$$

For thick plates, as the natural propagating wavenumber is given by $k_{RM_1}$, the coincidence frequency is expressed as,

$$k_{RM_1} = k_0 \sin\theta \Longrightarrow f_{\mathrm{coinc_{thick}}} = \frac{(c_0/\sin\theta)^2}{2\pi\sqrt{\left(\frac{D}{m_s} - \frac{c_0^2}{\sin^2\theta}\frac{I_z}{m_s}\right)\left(1 - \frac{c_0^2}{\sin^2\theta}\frac{m_s}{G^* h}\right)}}. \tag{4.15}$$

In case of diffuse field excitation, the elastic layer is subjected to all coincidence frequencies corresponding to $\theta = [0,\, \pi/2]$ and the lowest coincidence frequency is called the critical frequency. In other words, it is the frequency at which the speed of sound is equal to the speed of natural propagating waves of the plate. This can be computed by letting $\sin\theta = 1$ in the coincidence frequency expression. The critical frequency obtained from thin plate theory is given by $k_b = k_0$, that is,

$$f_{\mathrm{cri_{thin}}} = \frac{c_0^2}{2\pi}\sqrt{\frac{m_s}{D}}. \tag{4.16}$$

From the Eq. (4.15), the critical frequency for thick plate is obtained from $k_{RM_1} = k_0$, that is,

$$f_{\mathrm{cri_{thick}}} = \frac{c_0^2}{2\pi\sqrt{\left(\frac{D}{m_s} - c_0^2\frac{I_z}{m_s}\right)\left(1 - c_0^2\frac{m_s}{G^* h}\right)}}. \tag{4.17}$$

It may be noted that the Eqs. (4.15) and (4.17) tend to coincidence and critical frequencies obtained from thin plate theory as $I_z \to 0$ and $G^* \to \infty$. As an illustration, for 12.5 mm plasterboard, the coincidence frequencies computed from both plate theories are indicated

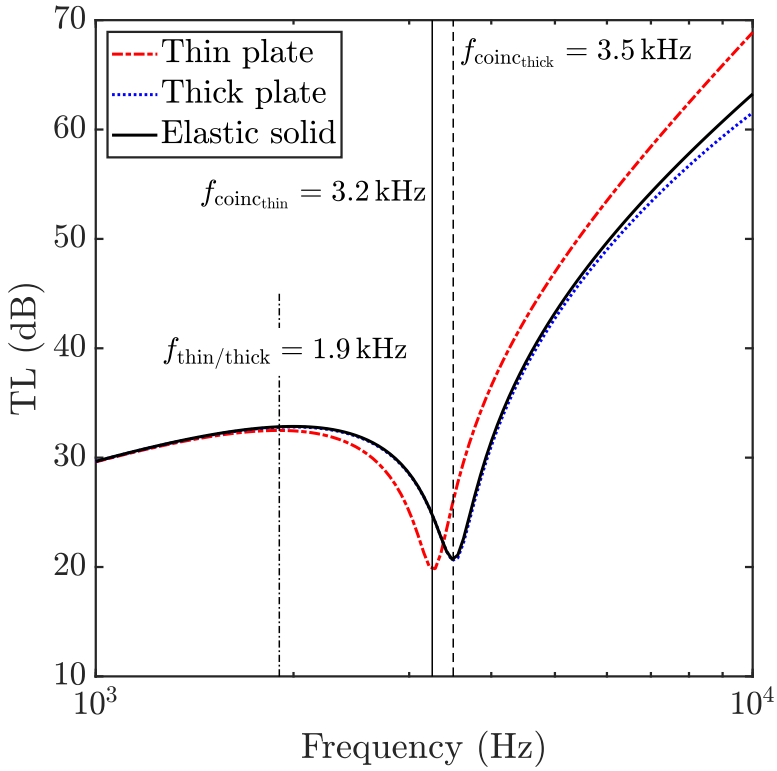


Figure 4.6: Transmission loss for the infinitely extent plasterboard of thickness 12.5 mm (properties are mentioned in Table 4.1) under plane wave excitation with $\theta = 60^o$ with coincidence frequencies computed from thin & thick theories, and it can be observed that the estimation of coincidence frequency from thick plate theory is in good agreement with theory of elasticity computation.

in the Fig. 4.6. It is observed from the Fig. 4.6 that the coincidence frequency computed from Eq. (4.15) is in good agreement with elasticity theory. One may note that the incidence angle 60° is randomly chosen to illustrate the good agreement on the coincidence frequency estimation given by Eq. (4.15). However, the expression has been tested and is valid for any angle of incidence. Therefore, it is worth noting that Eqs. (4.14) and (4.16) are indeed limited to thin plates only, where the transition from thin to thick plates is given by the frequency $f_{\text{thin/thick}}$ in Eq. (4.13).

## 4.4 Frequency limit of plate theories in comparison with theory of elasticity

When the thickness of the layer is small compared to the lateral dimension and the longitudinal wavelength ($\lambda_l = 2\pi/\delta_l$) is large compared to thickness, a plate theory, controlled by the anti-symmetric motion, is generally considered. On the contrary, when the thickness of the plate is of the order of magnitude of longitudinal wavelength, due to the variation in velocity through the thickness of the layer, both symmetric and anti-symmetric motions contribute to the resulting motion of the plate after a certain frequency (Fig. 4.7). This implies that plate theories might not be able to predict the correct vibro-acoustic

(a) Symmetric mode (b) Anti-symmetric mode

Figure 4.7: Vibrating modes of an infinitely extent elastic layer. While the symmetric mode corresponds to the thickness stretch motion of the layer where the particle velocity varies through the thickness, the anti-symmetric motion corresponds to the bending and shear motions of the layer where the particle velocity is constant through the thickness.

behaviour of the elastic layer after this frequency, as they assume only anti-symmetric motions in the plate. Therefore, finding this frequency limit of plate theories is necessary and in this section, based on the symmetric and anti-symmetric motions of the plate, the analytical expression of the frequency limit of plate theories is derived.

Contributions of symmetric and anti-symmetric motions of an isotropic layer can be quantified by the impedances or admittances, by following Dym and Lang [155]. Section 3.9.3 describes the transfer matrix relationship of symmetric multi-layer structure in terms of anti-symmetric and symmetric admittances. Since the single layer is also a structure of symmetric type, the transfer matrix given by Eq. (3.78) holds true for the single layer as well. As demonstrated in Section 3.9.3, it can be checked from Eq. (3.78) that, when the anti-symmetric admittance is larger than the symmetric admittance (or $Y_A \gg Y_S$), the transfer matrix in Eq. (3.78) reduces to the transfer matrix of the plate

given by Eq. (3.34). Thus, the ratio between $Y_A$ and $Y_S$ could be a good criterion to obtain the frequency limit of plate theories. Comparing the longitudinal wavelength ($\lambda_l$) to the thickness of the plate seems less accurate, as it does not compare the symmetric motion to the anti-symmetric motion. One may also analyse the propagating wavenumbers (dispersion curves) of the structure to get the frequency limit using Lamb waves [101] for a planar structure or Wave Finite Element Method (WFEM) [171] for more complex structures. Nevertheless, these methods would be cumbersome and quite challenging for analytical and/or numerical computations.

Since the symmetric motion is controlled by the longitudinal wave of the layer, the transfer matrix for elastic solid layer (refer Appendix A) is reduced at normal incidence, as

$$\begin{Bmatrix} p(O) \\ v_z(O) \end{Bmatrix} = \begin{bmatrix} \cos h\delta_l & \dfrac{\mathrm{j}\omega\rho}{\delta_l}\sin h\delta_l \\ \dfrac{\mathrm{j}\delta_l}{\omega\rho}\sin h\delta_l & \cos h\delta_l \end{bmatrix} \begin{Bmatrix} p(N) \\ v_z(N) \end{Bmatrix}. \tag{4.18}$$

One may note that the above transfer matrix is in the similar form of the fluid transfer matrix given by Eq. (3.4). By equating the above equation with Eq. (3.78), the symmetric admittance is obtained as

$$Y_S = \frac{h\delta_l(\cos h\delta_l - 1)}{2\mathrm{j}m_s\omega\sin h\delta_l} = -\frac{h\delta_l}{2\mathrm{j}m_s\omega}\tan\frac{h\delta_l}{2}. \tag{4.19}$$

Approximating the tangent function by a Taylor series expansion (up to first order), the symmetric admittance can be written as,

$$\tan\frac{h\delta_l}{2} \approx \frac{h\delta_l}{2} \quad \Longrightarrow \quad Y_S \approx \widetilde{Y_S} = -\frac{(h\delta_l/2)^2}{\mathrm{j}\omega m_s} = \frac{\mathrm{j}\omega h}{4\overline{C}}, \tag{4.20}$$

where $\overline{C} = \lambda + 2\mu$ is the compressional modulus of the elastic solid.

Since the anti-symmetric motion is controlled by the transverse wavenumber of the incident wave and plate theories capture this type of motion, anti-symmetric admittance is computed from plate theories as given by Eq. (3.32).

The minimum value of the absolute ratio between the anti-symmetric and symmetric admittance, denoted by $C_y$, is used to find the frequency limit of plate theories. Expressing the anti-symmetric admittance ($Y_A$) from thin plate theory and the symmetric admittance ($\widetilde{Y_S}$) from Eq. (4.20), the frequency limit of plate theories is expressed as,

$$\left|\frac{Y_A}{\widetilde{Y_S}}\right| \geqslant C_y \Rightarrow f \leqslant f_{\text{plate/solid}_{\text{oi}}} = \frac{c_0^2}{2\pi \sin^2\theta}\sqrt{\frac{m_s}{2D} \pm \sqrt{\left(\frac{m_s}{2D}\right)^2 \pm \frac{4\overline{C}}{hC_yD}\frac{\sin^4\theta}{c_0^4}}}. \tag{4.21}$$

The above expression is valid for oblique incidence whereas in case of diffuse field excitation, the following expression may be used to compute the frequency limit of plate theories.

$$\left|\frac{Y_A}{\widetilde{Y_S}}\right| \geqslant C_y \Rightarrow f \leqslant f_{\text{plate/solid}_{\text{df}}} = \frac{c_0^2}{2\pi}\sqrt{\frac{m_s}{2D} \pm \sqrt{\left(\frac{m_s}{2D}\right)^2 \pm \frac{4\overline{C}}{hC_yD}\frac{1}{c_0^4}}}. \tag{4.22}$$

The above frequency limits are computed by keeping the loss factor ($\eta$) to be zero. The subscript 'plate/solid' in the above equations means that the frequency limit is for 'plate' theories in general (as even higher order plate theories also do not account for symmetric motion) by keeping as a reference the theory of 'elastic solids'. Further, the sub-subscripts 'oi' and 'df' correspond to 'oblique incidence' and 'diffuse field' respectively. It may be observed that the relation $\left|\frac{Y_A}{\widetilde{Y_S}}\right| \geqslant C_y$ yields four positive roots for the frequency. Out of these four roots, only the minimum of pure real roots is considered for $f_{\text{plate/solid}_{\text{oi}}}$ and $f_{\text{plate/solid}_{\text{df}}}$. It may also be noted that the expression for $f_{\text{plate/solid}_{\text{df}}}$ can be modified in two ways. First, by including higher order terms for the tangent function to get $\widetilde{Y_S}$. Second, by using the anti-symmetric mechanical admittance from thick plate theory. Though these two ways might improve the frequency limit, the final expression for $f_{\text{plate/solid}_{\text{df}}}$ would become more complex. Further, as discussed in the next section, the frequency limits given by Eqs. (4.21) and (4.22) are sufficient for typical single layer walls used in industry. A concrete layer of 140 mm is taken to illustrate the nature of the symmetric and anti-symmetric admittances of the elastic layer and presented in the Fig. 4.8.

From the Fig. 4.8, it can be seen that the anti-symmetric admittance is larger compared

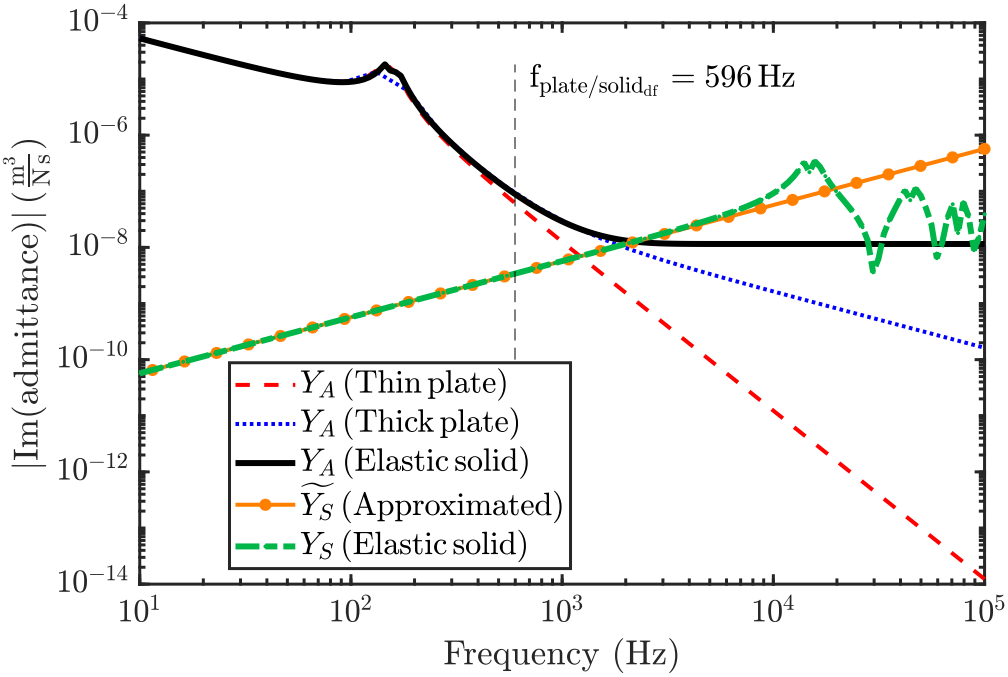


Figure 4.8: Admittances of a concrete layer of thickness 140 mm (properties are mentioned in Table 4.1) under plane wave excitation with $\theta = 60^o$. It is observed that, from low frequencies till the limiting frequency ($f_{\mathrm{plate/solid_{df}}}$), the symmetric admittance is lesser compared to the anti-symmetric admittance which supports the applicability of plate theories till $f_{\mathrm{plate/solid_{df}}}$.

to the symmetric admittance at low frequency range. The symmetric admittance is seen to become of the same order of magnitude or larger compared to the anti-symmetric impedance at around 2000 Hz. By letting the factor $C_y$ be 10, the frequency limit of plate theories is computed from Eq. (4.22). This means that the anti-symmetric admittance is one order of magnitude larger than the symmetric admittance and from this frequency onwards use of plate theories is not recommended to compute the acoustic indicators. Therefore, it is advisable to adopt the theory of elasticity for computations after this frequency limit. One may note that although the frequency limit expressions given by Eqs. (4.13), (4.21) and (4.22) include the effect of loss factor through the Young's modulus of the layer, the influence of the loss factor on these frequency limits is observed to be smaller compared to that of other material properties.

## 4.5 Numerical examples

In this section, transmission loss (TL) of different material layers (with properties listed in Table 4.1) are presented to illustrate the frequency limits obtained in sections 4.3 and 4.4. The readers are referred to Section 3.7 for TL computations by the TMM. Further, the TL from plate theories can be computed using the transmission coefficient given by Eq. (3.75). Both, oblique plane wave incidence of 60° and diffuse fields, are used to compute TL. Since $f_{\text{plate/solid}_{\text{df}}}$ is the minimum of all the possible coincidence frequencies obtained from $f_{\text{plate/solid}_{\text{oi}}}$, in this section, $f_{\text{plate/solid}_{\text{df}}}$ is indicated as the limit of plate theory. Though elasticity theory is considered as reference to analyse the plate theories, additional validation from finite element method (FEM) is also presented in some TL plots in this section.

FEM simulations are computed using Comsol Multiphysics© software. The acoustical variables (pressure, velocity fields...) are computed in the coupled system (PML-air-material-air-PML) (Fig. 4.9) using the "Comsol Pressure Acoustics" interface (Helmholtz equation) for air and "Structural Mechanics branch" for the material (elastic material in "Solid Mechanic"). The interface between air and the material is modelized using "fluid-structure interface". The dimensions of each material are 60 cm × 60 cm (the thickness is the real thickness) and periodic lateral conditions are chosen. The domain is adjusted (in particular the dimensions of the air domains) and meshed with respect to a 10 elements per wavelength (of the incident plane wave excitation) criterion based on the maximal frequency. For example, at 125 Hz, the number of resolved degrees of freedom is 444675, the complete mesh consists of 29889 domain elements, 8802 boundary elements and 812 edge elements. Linear hexahedral elements are used to mesh the structure, and the mean computational time is 3 minutes per incidence per frequency. This translates to a mean computational time of 1.5 - 2 hours for an oblique incidence for 30 frequencies. Additionally, the maximum frequency is limited to 5000 Hz to reduce the total computational time as it would be expensive for computation due to mesh refinement at higher frequencies.

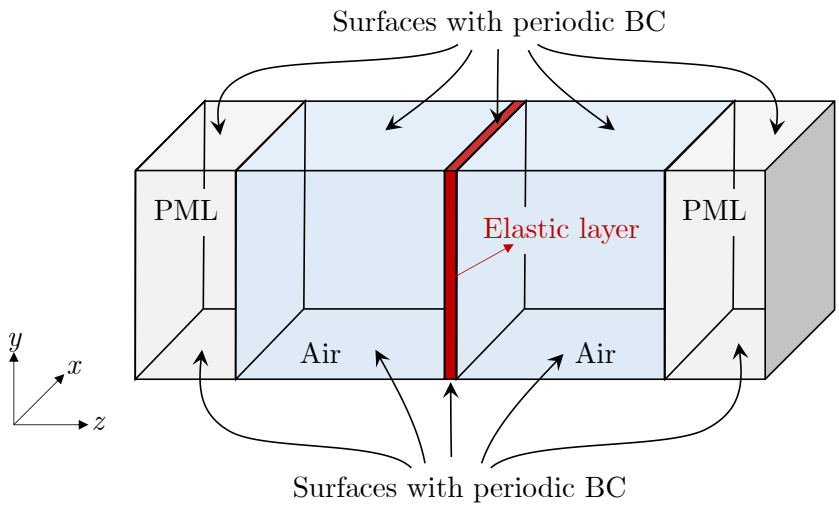


Figure 4.9: Schematic representation of the finite element system to calculate transmission loss of an elastic layer.

In Figs. 4.10 and 4.11, TL computed from different theories (discussed in sections 3.2.2 and 3.4.1) are presented for comparison along with frequency limits expressed in sections 4.3 and 4.4. It is observed from these plots that, for stiff material like aluminium (with typical value of thickness used in industries), the thin plate theory would be sufficient to model the vibro-acoustic behaviours as both $f_{\text{thin/thick}}$ and $f_{\text{plate/solid}_{\text{df}}}$ are spotted near the maximum audible frequency.

In the next example, an industrial plasterboard layer of 12.5 mm is chosen to see the influence of shear on the TL response. For this layer, it is seen from the Figs. 4.12 and 4.13 that TL computed from thin plate theory is beginning to deviate from the elasticity theory computation whereas thick plate theory is still in good agreement with the elasticity theory until the limiting frequency $f_{\text{plate/solid}_{\text{df}}}$ (despite the closer responses between different theories due to the averaging effect in diffuse field). This explains the need to include the effect of shear into the anti-symmetric motion via thick plate theory. Therefore, for this kind of materials, thick plate theory would be appropriate to compute the acoustic indicators.

In the next example, a concrete layer with 140 mm thickness is presented to see the validity of thin plate theory even for thicker structures. For this case, it is noted from Figs. 4.14 and 4.15 that a similar trend is observed as for the plasterboard, that is, thin

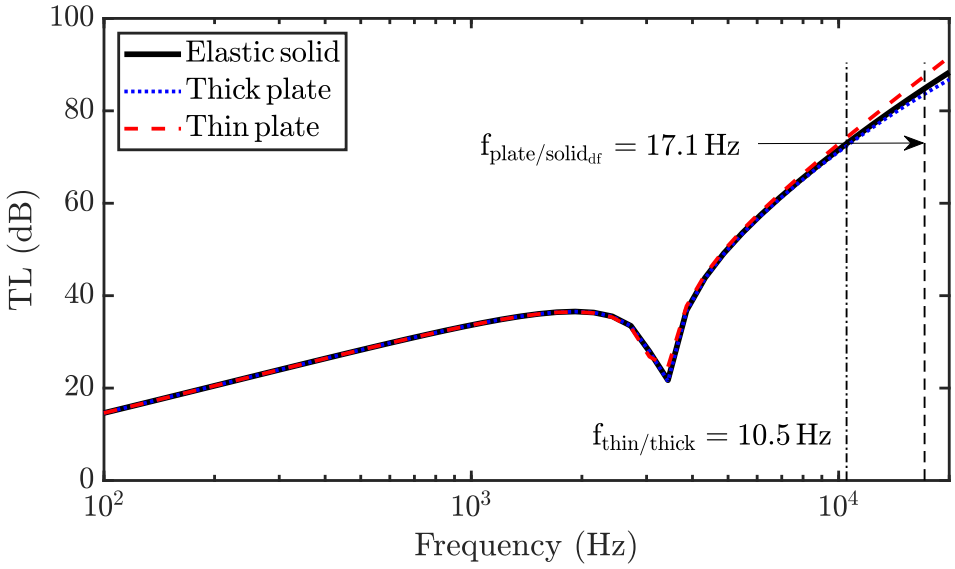


Figure 4.10: Transmission loss for an aluminium layer of thickness 5 mm (properties mentioned in Table 4.1) under plane wave excitation with $\theta = 60^o$. It is seen that thin plate theory is adequate to compute the vibro-acoustic indicators, as both limiting frequencies ($f_{\text{thin/thick}}$ & $f_{\text{plate/solid}_{\text{df}}}$) are in the high frequencies.

and thick plate theories are starting to deviate from the elasticity theory computation at frequencies above $f_{\text{thin/thick}}$ and $f_{\text{plate/solid}_{\text{df}}}$, respectively. One might also observe two notable points from the TL plots of concrete and plasterboard. First, the coincidence frequency occurs after the limit frequency of thin plate ($f_{\text{thin/thick}}$) in plasterboard, whereas it can be spotted before $f_{\text{thin/thick}}$ in concrete. This implies that even for thicker material, the thin plate theory might be still valid after the coincidence frequency. The second notable point is that the symmetric motion (or compressional motion) effect clearly appears in concrete.

In Fig. 4.15, the second minima in the TL computed from the theory of elasticity corresponds to the compressional frequency ($f_{\text{comp}} \approx 15\,\text{kHz}$) given by Eq. (3.8). Therefore, it is inferred that the compressional mode can still be neglected for plasterboard whereas it has to be taken into account for the concrete layer and this is possible via employing the theory of elasticity. The same is observed in the TL plot (Fig. 4.16) of soft layer (melamine foam with only elastic properties is taken to see the effect of compressional motion) with 20 mm thickness. It can be seen that TL of soft layer is greatly influenced by the symmetric motion after the frequency limit $f_{\text{plate/solid}_{\text{df}}}$.

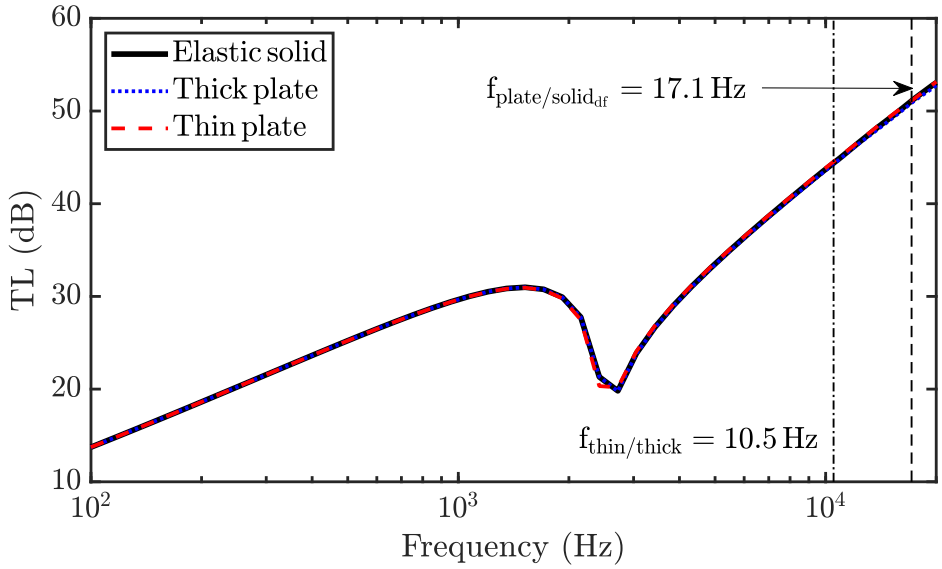


Figure 4.11: Transmission loss for an aluminium layer of thickness 5 mm (properties mentioned in Table 4.1) under diffuse field excitation. It is seen that thin plate theory is adequate to compute the vibro-acoustic indicators, as both limiting frequencies ($f_{\text{thin/thick}}$ & $f_{\text{plate/solid}_{\text{df}}}$) are in the high frequencies.

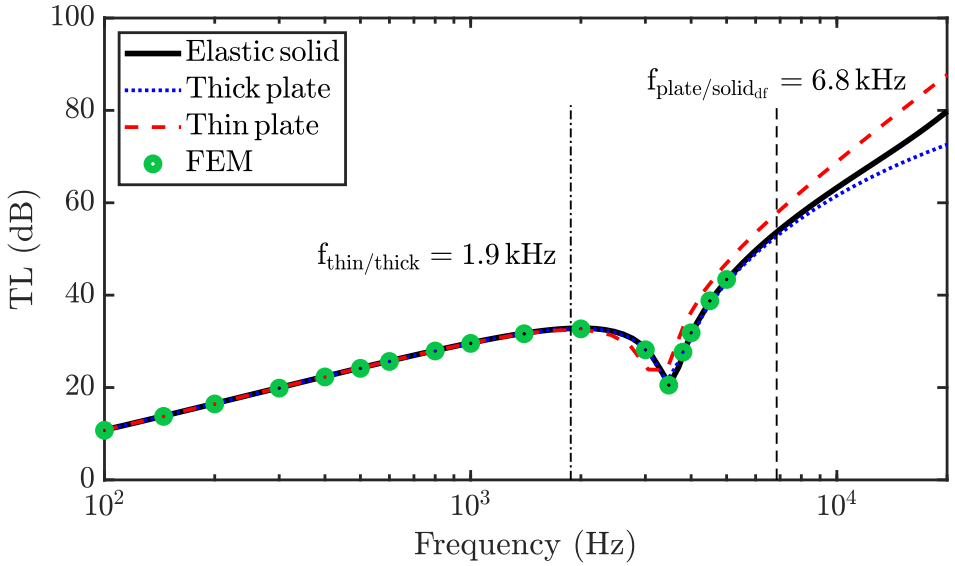


Figure 4.12: Transmission loss for a plasterboard layer of thickness 12.5 mm (properties mentioned in Table 4.1) under plane wave excitation with $\theta = 60^o$. Deviations of thin and thick plate theories from the elastic solid theory (or FEM) are observed after $f_{\text{thin/thick}}$ and, $f_{\text{plate/solid}_{\text{df}}}$ respectively.

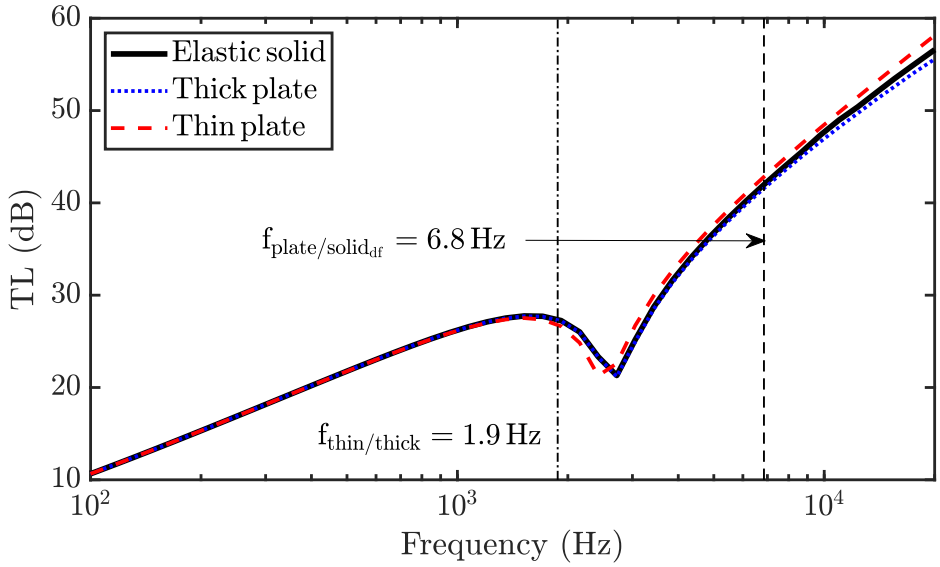


Figure 4.13: Transmission loss for a plasterboard layer of thickness 12.5 mm (properties mentioned in Table 4.1) under diffuse field excitation. Deviations of thin and thick plate theories from the elastic solid theory are observed after $f_{\text{thin/thick}}$ and, $f_{\text{plate/solid}_{\text{df}}}$ respectively.

One can also observe from Eq. (4.13) that, for different materials of infinitely extending layers with the same thickness, the frequency limit $f_{\text{thin/thick}}$ would result in different values despite thicknesses being the same. Therefore, it can be inferred that the use of thin plate theory requires proper combination of thickness and material properties (as given by Eq. (4.13)) rather than comparing the thickness to the lateral dimensions. Similar argument holds for $f_{\text{plate/solid}_{\text{df}}}$ as well. In the previous TL plots, the choice of the values of $C_k = 4$ and $C_y = 10$ are further confirmed by the TL variation of plate theories from the elasticity theory and the TL difference between the elasticity theory and plate theories are observed to be below 1 dB at the frequency limits. Of course, one can conveniently choose the appropriate value of $C_k$ and $C_y$ based on the tolerance accepted for the particular acoustic design.

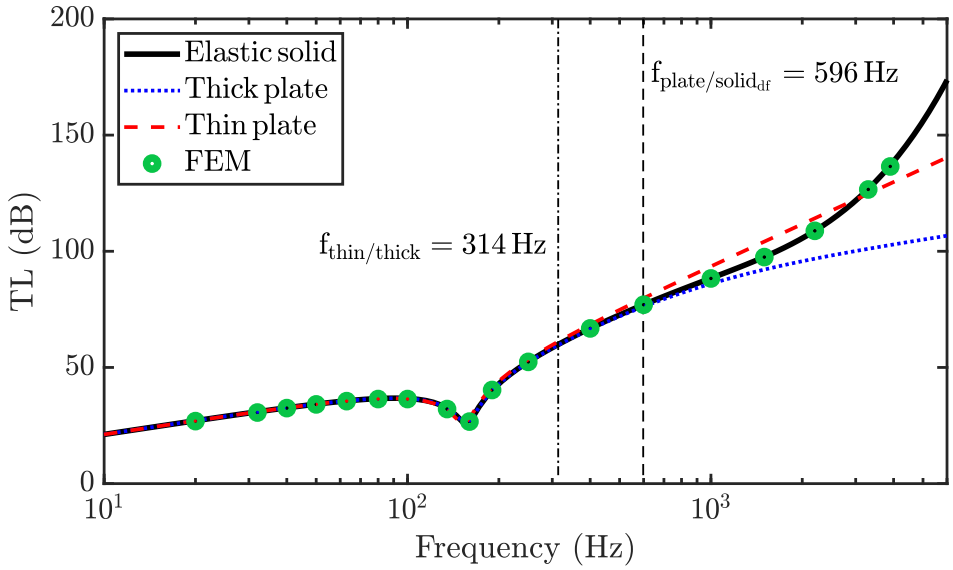


Figure 4.14: Transmission loss for a concrete layer of thickness 140 mm (properties mentioned in Table 4.1) under plane wave excitation with $\theta = 60^o$. Deviations of thin and thick plate theories from the elastic solid theory (or FEM) start to appear after $f_{\text{thin/thick}}$ and, $f_{\text{plate/solid}_{\text{df}}}$ respectively.

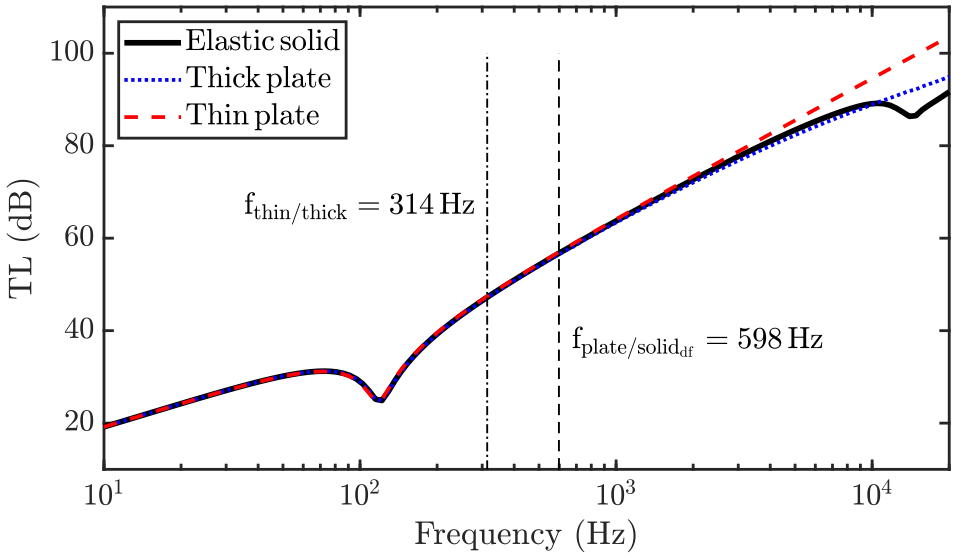


Figure 4.15: Transmission loss for a concrete layer of thickness 140 mm (properties mentioned in Table 4.1) under diffuse field excitation. Deviations of thin and thick plate theories from the elastic solid theory start to appear after $f_{\text{thin/thick}}$ and, $f_{\text{plate/solid}_{\text{df}}}$ respectively.

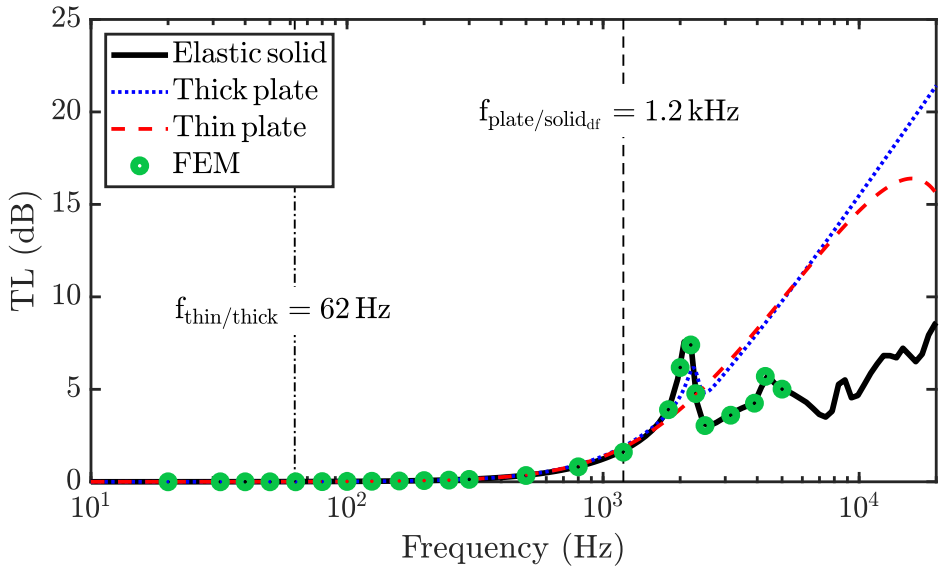


Figure 4.16: Transmission loss for a soft layer of thickness 20 mm (properties mentioned in Table 4.1) under diffuse field excitation. Deviations of plate theories from the elastic solid theory (or FEM) start to appear after $f_{\text{plate/solid}_{\text{df}}}$.

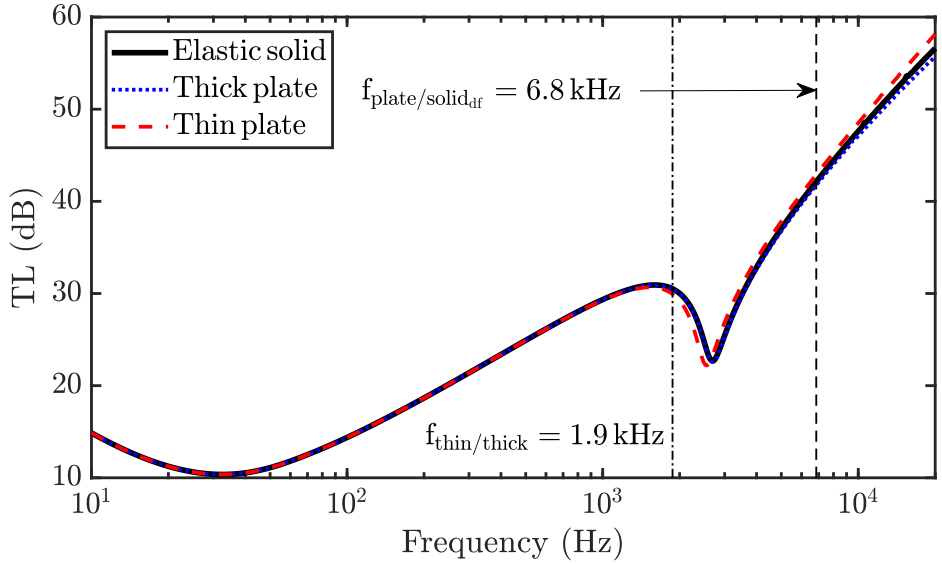


Figure 4.17: Transmission loss, computed from spatial windowing method by Rhazi and Atalla [26], across a finite size (3 m × 4 m) plasterboard of thickness 12.5 mm (properties are mentioned in Table 4.1) under diffuse field excitation. It is observed that limiting frequencies computed for infinite plate are still valid for the finite plates, as the size correction effects minimal near the critical frequency of the plate.

### 4.5.1 Further observation

In the case of finite sized plates, generally, the acoustic indicators computed from the infinitely extent layer theories would yield some discrepancies in the low to mid-frequencies

compared with experimental tests. Therefore, there are some work in the literature [25, 26] which focus on correcting the acoustic indicators by introducing correction factors that account for geometrical size effect. Since the radiation efficiency (which accounts for size correction in sound transmission problems) is reaching unity near the critical frequency of the plate [172], the effects due to finite size are mainly visible at low frequencies below the critical frequency. Since the frequency limits ($f_{\text{thin/thick}}$ and $f_{\text{plate/solid}_{\text{df}}}$) of typical industrial materials fall near and/or after the critical frequency, these limiting expressions obtained from infinite plate theories are applicable to the finite size plate as well. For example, this can be observed from the transmission loss computed from the finite size correction model by Rhazi and Atalla [26] for the plasterboard of 12.5 mm thickness under diffuse field excitation in Fig 4.17. One may refer to Section 3.8 for the summary of the finite size correction models.

## 4.6 Conclusion

The assumptions used in thin and thick plate theories limit their employability in commonly used industrial materials after a certain frequency. Thin plate theory attains the limitation since it does not account for the shear effect in the anti-symmetric motion of the plate, whereas this is taken care off in thick plate theories. Nevertheless, both types of plate theories are approximations, since they neglect symmetric motion of the plate completely in their theoretical formulation. By analysing the wavenumbers and admittances of plate theories, two frequency limits are presented in this chapter: 1) from the wave propagation analysis of the thick plate model, based on the Reissner-Mindlin plate hypothesis, the analytical expression for the limiting frequency of the thin plate model is derived, 2) from comparing the symmetric and anti-symmetric admittances, an analytical expression for limiting frequency of plate theories is derived. These two simple analytical expressions for computing the limit of thin and thick plate theories can be useful to choose the appropriate model in each case. Deviations of transmission loss curves obtained from different models are observed above these two limiting frequencies. It is also shown that, although the limiting expressions are derived from infinite layer

theories, it can be applied to finite sized layer as well. Due to the omission of shear effect in thin plate theories, the refined coincidence and critical frequencies are derived from thick plate theories. Finally, it is observed that plate theories quickly fail for materials that are too soft in terms of longitudinal compression.

It is observed from the dispersion analysis that a single layer plate has two asymptotic characteristics i.e, low-frequency region controlled by bending and high-frequency region controlled by shear and this information is useful to understand the involved physical behaviour in a given frequency range. Similar to this, different regimes of a three-layer system are observed by Boutin and Viverge [72] and based on these asymptotic behaviours, a simple equivalent plate model is developed in the next chapter, for a three-layer sandwich structure.

# Chapter 5

# Equivalent plate model for three-layer panels

In Chapter 2, many analytical models including the category of condensed or equivalent plate models have been discussed in details. In particular, the equivalent plate models are being used in various industries to reduce the computation time in Finite Element (FE) modelling. Out of the available equivalent plate models, the model developed by Guyader [131] exhibits high agreement with Lamb wave theory but it requires considerable time for implementation. Therefore, in this chapter, a simple model is developed to quickly compute the dynamic equivalent parameters of a three-layer sandwich panel. Although the simple model is formulated from only four parameters, which could be easily computed via the asymptotic and transition behaviours of the sandwich panel (as described by Boutin and Viverge [173]), it is shown to be able to capture the equivalent dynamic response for the entire frequency range.

Note

Most of the contents presented in this chapter has been taken from the published article [174]:

**Arasan, U.**, Marchetti, F., Chevillotte, F., Jaouen, L., Chronopoulos, D., Gourdon, E. (2021). "A simple equivalent plate model for dynamic bending stiffness of three-layer sandwich panels with shearing core". *Journal of Sound and Vibration*, 500, 116025.

Regarding the contributions made to the above-mentioned article, the author of this thesis has done the following tasks: methodology, investigation, validation, article writing and review.

This chapter is organized with two main sections: first, development of a simple model to find the dynamic equivalent bending stiffness of a three-layer sandwich panel is presented; then the results obtained using this new model are compared with the model developed by Guyader [131] for validation.

## 5.1 Background

As mentioned in earlier chapters, multi-layered partitions have been commonly used in recent years to enhance sound comfort and noise attenuation. Sandwich composites which can exhibit high stiffness and damping with lightweight are widely employed in the transportation and building industries. This type of multi-layer is also called laminate and is often made up of three layers. One soft layer embedded between two hard skins. This kind of laminate enables to ensure a bending rigidity while increasing the dissipation by forcing the shear of the viscoelastic core. Automotive [175] and aerospace [176] industries also use sandwich structures as a passive way to reduce the structure-borne noise. Constrained layers are typically used in automobile, aircraft and railway industries to improve the damping response of the vibrating systems. In civil applications, acoustic plasterboards (with high-density core) are used to improve the sound insulation performance.

Equivalent methodologies are often applied to condense the behaviour of the multi-layer structure into an equivalent single-layer governed by frequency-dependent properties (refer Section 2.5). The equivalent methodology consists in assuming that the multi-layer behaves as a thin plate under Love-Kirchhoff's theory. As a result, an equivalent parameter corresponding to the flexural rigidity of the thin plate can be identified as a function of frequency. It may be noted that, even though the equivalent plate models assume the multi-layer plate as equivalent Love-Kirchhoff plate, they account for both bending and shear motions of multi-layer plate (but not necessarily in each layer) through the frequency dependent flexural rigidity. Since Guyader's model describes two anti-symmetric motions (bending and shear) in each layer, it exhibits high agreement with an exact model based on Lamb waves [177] until the frequencies where symmetric motions are no longer negligible.

Among the existing condensed (or equivalent) plate models available in the literature, Guyader's model might be more appropriate to analyse the vibro-acoustic performance of a three-layer system of isotropic materials which are commonly used across various industries. Although Guyader's model performs better compared to the other equivalent plate models, it often requires some initial work for implementation as it requires many constant coefficients to be defined. Additionally, it also requires the symbolic computation of solutions from a non-linear equation, which further requires solution tracing techniques to correctly capture the physically meaningful solution for the dynamic bending stiffness. Therefore, in this chapter, a simple dynamic model for sandwich structure based on its asymptotic behaviours is presented to reconstruct the dynamic response of the structure in a similar manner of the principles used for the modelling of porous media [143] or the length correction of perforated plates [178].

## 5.2 Development of a simple model to compute equivalent bending stiffness of a three-layer sandwich panel

### 5.2.1 Dynamic behaviour of a three-layer sandwich panel

For the theoretical development of the proposed model, Fig. 5.1 is used to schematically represent a generic three-layer sandwich panel of infinite extent in $x$ and $y$ directions. The

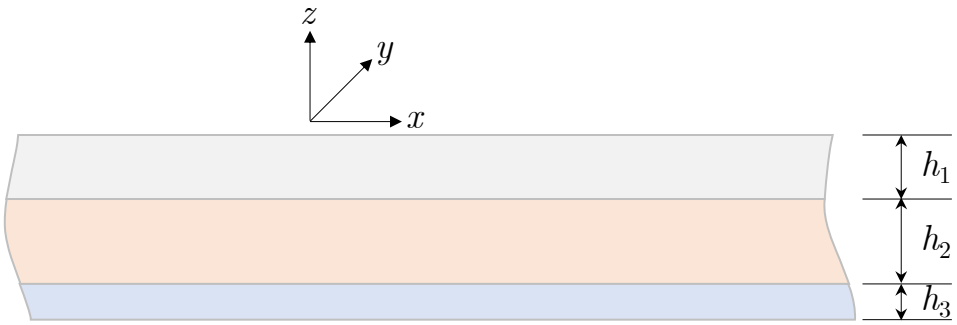


Figure 5.1: Schematic representation of the cross-section of a generic three-layer sandwich panel.

$i-$th layer of the sandwich panel is assumed to be made of isotropic material with thickness $h_i$, Young's modulus $E_i$, mass density $\rho_i$, Poisson's ratio $\nu_i$ and loss/damping factor $\eta_i$. It is further assumed that only anti-symmetric motions (i.e, bending, shear and membrane motions) are considered for the analysis. Different configurations of layers are considered in this work using the materials (aluminium, steel, plasterboard, shear layer and polymer) listed in Table 5.1. The shear layer corresponds to a layer that is sufficiently soft to exhibit shearing effects but still rigid enough to avoid compressional or dilatational effects.

The asymptotic behaviours on the natural propagating wavenumber of the sandwich panel for different configurations are observed. If all three layers are of the same material, the sandwich could be considered as a homogeneous isotropic single layer. For this configuration, the natural propagating wavenumber is computed from the first-order shear deformation plate theory [97–99] and it is observed from Fig. 5.2a that the natural propagating wavenumber has low and high frequency asymptotes corresponding to the bending

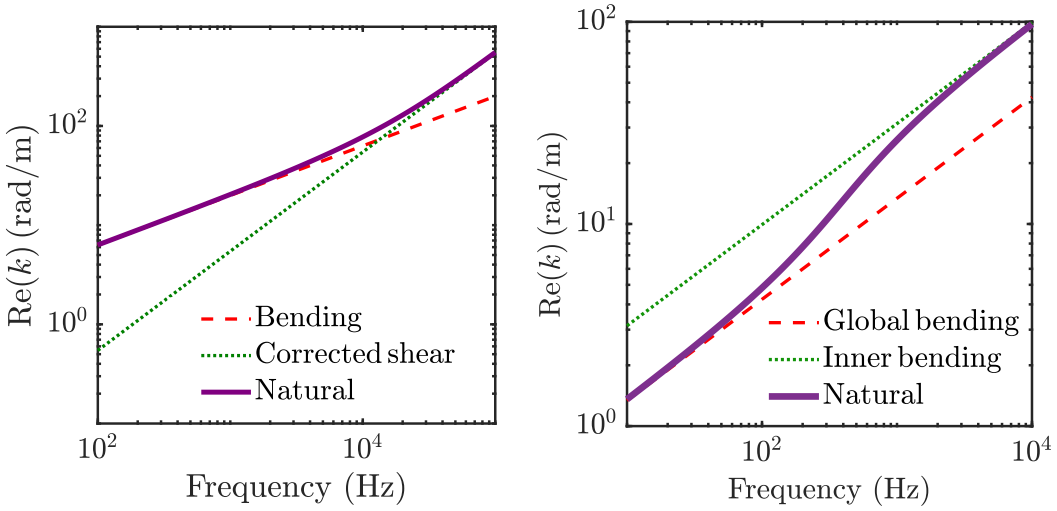


Figure 5.2: Natural propagating wavenumbers for (a) plasterboard of 25 mm (b) aluminium (5 mm)/shear layer (10 mm)/aluminium (3 mm) sandwich structure of infinite extent (material properties are listed in Table 5.1).

and shear motions of the panel. Few more information on the dispersion behaviour of the homogeneous plate are given in Section 4.2. In case of a sandwich panel made of

Table 5.1: Material properties of few typical elastic isotropic layers used in this chapter

| | Aluminium | Steel | Plasterboard | Shear layer | Polymer |
|---|---|---|---|---|---|
| $\rho$ (kg m$^{-3}$) | 2780 | 7800 | 700 | 200 | 580 |
| $E$ (GPa) | 71 | 210 | 3 | 0.1 | 0.25 |
| $\eta$ | 0.01 | 0.005 | 0.08 | 0.5 | 0.05 |
| $\nu$ | 0.3 | 0.3 | 0.22 | 0.33 | 0.33 |

two stiff skins (5 mm aluminium each) bonded together with a shear layer of thickness 10 mm, the asymptotic behaviour of the natural propagating wavenumber is observed to be different from that of the isotropic single layer as shown in Fig. 5.2b. Furthermore, the natural propagating wavenumber of a three-layer sandwich panel could be characterized by the properties of three zones namely low-frequency, transition and high-frequency regions [179].

The low and high frequency asymptotes correspond to the global and inner bending behaviours, respectively [173]. The term "global bending" describes the bending behaviour of a three-layer sandwich panel, where each layer contributes to the total bending. This

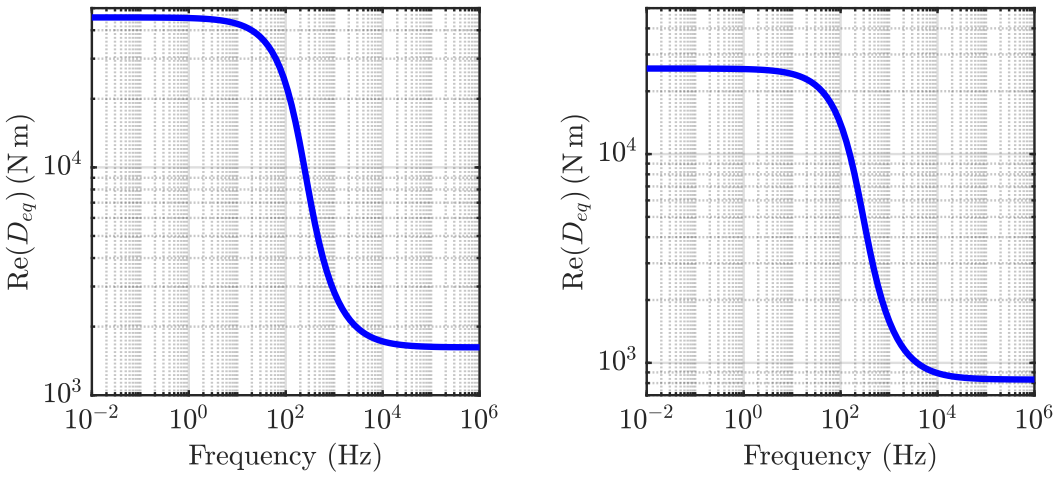


Figure 5.3: Equivalent bending rigidity profile obtained from Guyader's equivalent plate model for (a) aluminium (5 mm)/shear layer (10 mm)/aluminium (5 mm) (b) steel (1 mm)/shear layer (10 mm)/aluminium (5 mm) sandwich structures of infinite extent (material properties are listed in Table 5.1).

particular behaviour is described by "added stiffness model" which is detailed in Section 2.5.3. In case of "inner bending", only the outer layers (i.e, skins) contribute to the bending behaviour. One could note that the natural propagating wavenumber of the sandwich panel in Fig. 5.2b is computed from the equivalent plate model by [125, 126, 131] and this can also be computed from other models [7, 71, 133, 156] in the literature.

### 5.2.2 Sigmoid model for equivalent properties

One can observe that the equivalent bending stiffness, computed from Guyader's model, has the shape of a sigmoid function for both symmetric and asymmetric sandwich structures of different configurations (Fig. 5.3). Thus, the goal of this chapter consists in describing the equivalent parameter using this function. The sigmoid function is defined by four characteristic parameters ($D_{\text{low}}, D_{\text{high}}, f_T$ and $\hat{R}$) as shown in Fig. 5.4. Hence, the following expression is proposed for the equivalent bending stiffness of a sandwich structure made of isotropic layers,

$$\log_{10} \widetilde{D}_{\text{eq}}(f) = \frac{f_T^{\hat{R}} \log_{10} D_{\text{low}} + f^{\hat{R}} \log_{10} D_{\text{high}}}{f^{\hat{R}} + f_T^{\hat{R}}}, \tag{5.1}$$

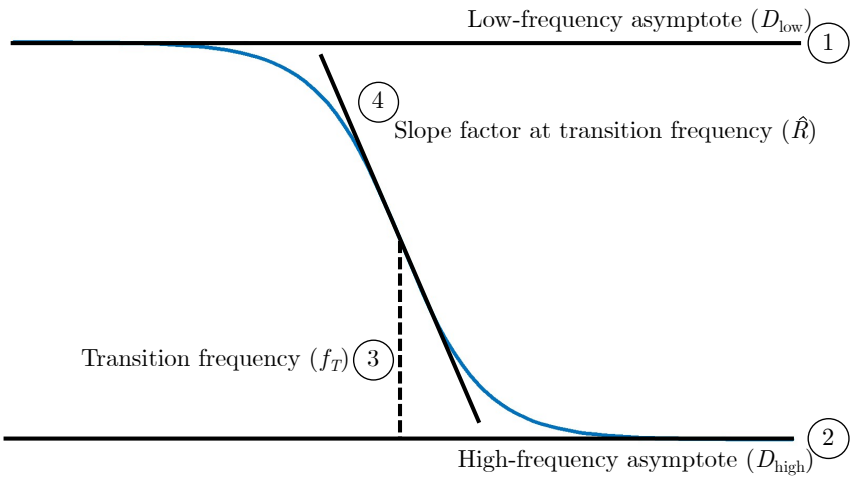


Figure 5.4: Schematic representation of the bending stiffness profile of the sigmoid model and its four characteristic parameters to describe equivalent bending stiffness of a sandwich structure made of isotropic layers.

where $D_{\text{low}}, D_{\text{high}}, f_T$ and $\hat{R}$ are low-frequency and high-frequency dynamic bending stiffness asymptotes, transition frequency and slope factor at transition frequency respectively.

In the following subsections, these characteristic parameters will be derived based on the relationship (refer Eq. (2.13)) between the equivalent bending stiffness and material properties of the sandwich panel, given by Guyader and Cacciolati [131] to compute the equivalent bending stiffness of a multi-layer structure.

### 5.2.3 Low-frequency asymptote

The lower frequency asymptote of the equivalent bending stiffness could be obtained by letting $\omega \to 0$ in the Eq. (2.13). This results as

$$A_4 D^{3/2} - A_1 A_4 D^{1/2} = 0 \Rightarrow D = D_{\text{low}} = A_1. \tag{5.2}$$

One may note that $A_1$ is equal to the sum of bending stiffness contribution from each layer with respect to the neutral layer position of the multi-layer structure, which is given by the added stiffness model described in Section 2.5.3.

Therefore, $D_{\text{low}}$ is computed by adding the flexural rigidities of all the layers (recalled from Eq. (2.22)):

$$D_{\text{low}} = \sum_{i=1}^{n} \frac{E_i}{1-\nu_i^2} \frac{(z_{ui}-\bar{z})^3 - (z_{li}-\bar{z})^3}{3}, \tag{5.3}$$

where $z_{ui}$ and $z_{li}$ are the upper and lower coordinates respectively of $i-$th layer along $z-$direction. Readers are referred to see "added stiffness model" described in the Section 2.5.3 for the detailed explanation of the Eq. (5.3).

In case of a symmetric sandwich panel, $D_{\text{low}}$ would reduce to the form:

$$D_{\text{low}} = D_1 \left(8 + \frac{12h_2}{h_1} + \frac{6h_2^2}{h_1^2}\right) + D_2, \tag{5.4}$$

where $D_i$ represents the bending stiffness of the $i-$th layer. If the core layer of the sandwich is soft compared to the skins (or outer layers), then $D_1, D_3 \gg D_2$ which gives the following form for the low-frequency asymptote ($D_{\text{low}}$) of the equivalent bending stiffness ($\widetilde{D}_{\text{eq}}$) of the sandwich panel.

$$D_{\text{low}} = D_1 \left(8 + \frac{12h_2}{h_1} + \frac{6h_2^2}{h_1^2}\right) \quad \text{(for soft core)}. \tag{5.5}$$

It may be noted that this asymptotic limit can be deduced from the work by Boutin and Viverge [173] and $D_{\text{low}}$ can be understood as the result due to a phenomenon where all the layers in the sandwich panel behave as a monolithic plate governed by the global bending.

### 5.2.4 High-frequency asymptote

The high-frequency asymptote of the equivalent bending stiffness could be obtained by letting $\omega \to \infty$ in the Eq. (2.13). This results in

$$A_3 D - A_1 A_3 + A_2 = 0 \Rightarrow D = D_{\text{high}} = A_1 - \frac{A_2}{A_3}. \tag{5.6}$$

If the core layer of the sandwich is soft compared to the skins (or outer layers), then $D_1, D_3 \gg D_2$ and this gives the following form for the high-frequency asymptote ($D_{\text{high}}$) of the equivalent bending stiffness ($\widetilde{D}_{\text{eq}}$) of the sandwich panel:

$$D_{\text{high}} = D_1 + D_3. \tag{5.7}$$

$D_{\text{high}}$ can be understood as the result due to a phenomenon where all three layers in the sandwich panel slide on each other and the value of $D_{\text{high}}$ is governed by the intrinsic bending of each skin layers [173].

### 5.2.5 Transition frequency

Since the sigmoid curve in Eq. (5.1) changes its sign of curvature at the geometric mean value ($D_T$) of the curve (or arithmetic mean value in the log-log scale (Fig. 5.3)),

$$\log_{10} D_T = \frac{\log_{10} D_{\text{low}} + \log_{10} D_{\text{high}}}{2} \Rightarrow D_T = \sqrt{D_{\text{low}} D_{\text{high}}}, \tag{5.8}$$

the transition frequency (with respect to the curvature sign of the sigmoid) is computed by substituting $D = D_T$ in Eq. (2.13) as,

$$f_T = \frac{1}{2\pi} \frac{A_4 \sqrt[4]{D_T}(\sqrt{D_T} - A_1)}{A_3' D_T + A_2' - A_1 A_3'}, \tag{5.9}$$

where $A_2' = \sqrt{m_s}\left(\lambda_4 - \dfrac{\lambda_5 \lambda_6}{\lambda_3}\right)^2$ and $A_3' = \sqrt{m_s}\left(\lambda_2 - \dfrac{\lambda_6^2}{\lambda_3}\right)^2$. The constants $\lambda_i$ are given in Appendix B.

For softer core ($D_1, D_3 \gg D_2$), the transition frequency takes the following form.

$$f_T = \frac{1}{2\pi} \frac{G_2}{12 h_2} \frac{D_{\text{low}}}{\sqrt{m_s D_T}} \left(\frac{h_1^2}{D_1} + \frac{h_3^2}{D_3}\right). \tag{5.10}$$

In case of symmetric sandwich panel, Eq. (5.10) can be written as,

$$f_T = \frac{1}{2\pi} \frac{G_2 h_1^2}{3 h_2} \frac{D_{\text{low}}}{D_{\text{high}}} \frac{1}{\sqrt{m_s D_T}}. \tag{5.11}$$

From the wavenumber analysis of the sandwich panel with a thicker core ($h_2 \gg h_1, h_3$), an alternate and simpler expression for the transition frequency could be derived. From Fig. 5.5a and 5.5b, it is observed that both equivalent bending (Eq. (2.15)) and shear wavenumbers (Eq. (5.12)) are equal at the transition zone when the core thickness is greater than that of the skins.

$$k_{\mathrm{eq_{shear}}} = \omega\sqrt{\frac{m_s}{G_2 h_t}}. \tag{5.12}$$

On the contrary, it is also observed that this may not be valid when the core thickness is lower or equal to that of the skins. For example, from Fig. 5.5c, it is seen that both equivalent bending and shear wavenumbers do not have the same values at the transition zone. From the parametric study, it is further observed that the influence of the material properties of the core is less significant than the influence of the core thickness to have the equal values of equivalent bending and shear wavenumber at the transition zone. This is also complying with impedance and wave speed analysis of symmetric sandwich panel by Kurtze and Watters [180].

Hence, for a thicker core, the transition frequency takes the following simpler form.

$$k_{\mathrm{eq_{bending}}} = k_{\mathrm{eq_{shear}}} \Rightarrow \sqrt{\omega_T\sqrt{\frac{m_s}{D_T}}} = \omega_T\sqrt{\frac{m_s}{G_2 h_t}} \Rightarrow \widetilde{f_T} = \frac{1}{2\pi}\frac{G_2 h_t}{\sqrt{m_s D_T}}. \tag{5.13}$$

It may be noted that, for a typical sandwich panel with a soft core, the deviation percentage of Eq. (5.13) from Eq. (5.10) would serve as an indicator on the influence of the core layer in determining the transition frequency.

### 5.2.6 Slope factor at the transition frequency

The slope of the sigmoid curve at the transition frequency is given by (from Eq. (5.1)),

$$\left.\frac{\mathrm{d}\widetilde{D}_{\mathrm{eq}}}{\mathrm{d}f}\right|_{f=f_T} = \hat{R}\left[\frac{D_T}{4f_T}\ln\left(\frac{D_{\mathrm{high}}}{D_{\mathrm{low}}}\right)\right] \tag{5.14}$$

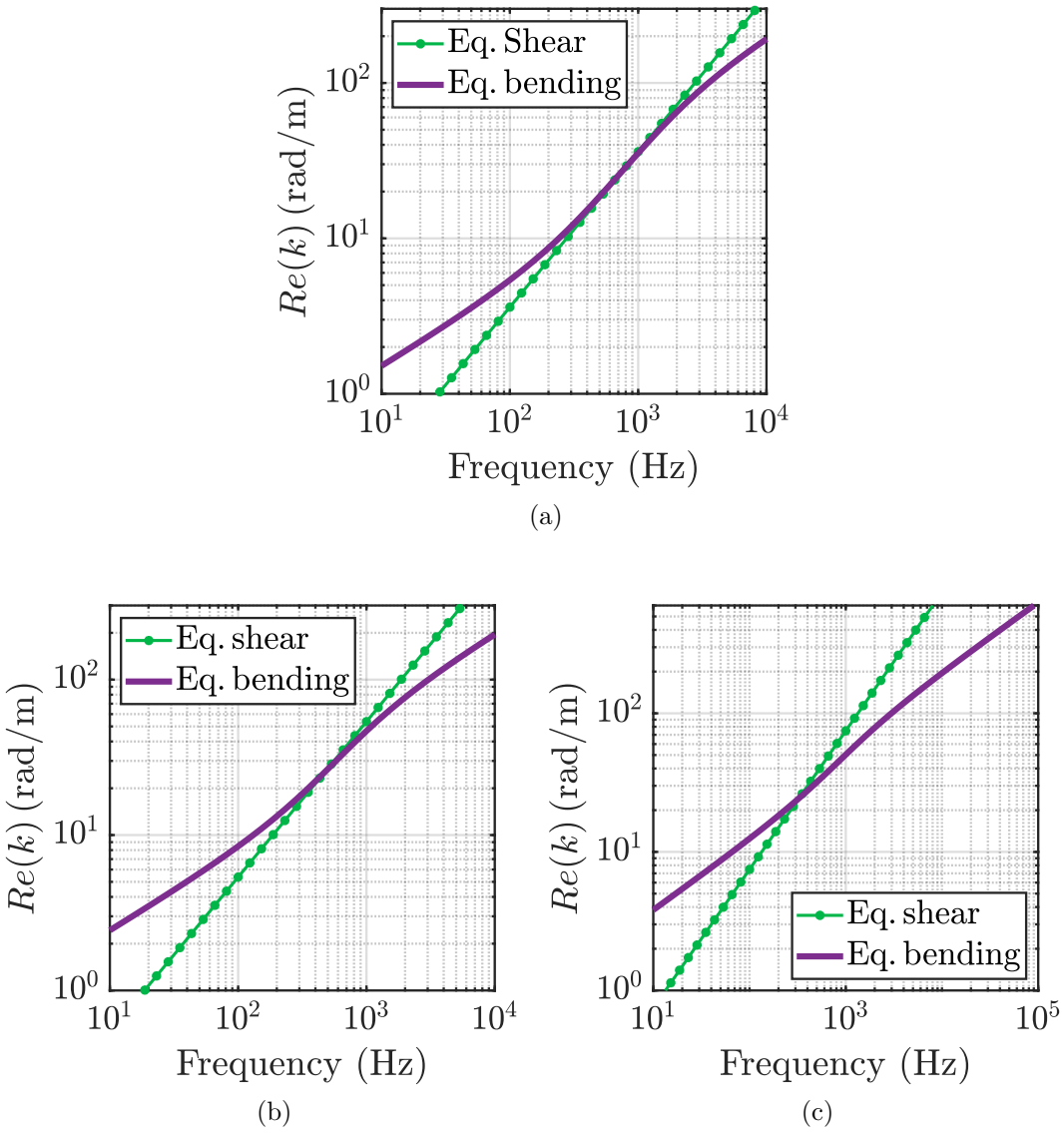


Figure 5.5: Equivalent bending and shear wavenumbers for a sandwich panel of infinite extent with steel skins of 1 mm and shear layer as core with thickness (a) 10 mm (b) 3 mm (c) 0.5 mm (material properties are listed in Table 5.1). Influence of core thickness on the transition zone can be observed from these plots.

Since we are not able to analytically compute the slope ,$\left.\frac{\mathrm{d}\widetilde{D}_{\mathrm{eq}}}{\mathrm{d}f}\right|_{f=f_T}$, from the Guyader's model, a parametric study is preferred to compute the slope factor ($\hat{R}$). The following range of values are used for this parametric study (with symmetric case) for Young's modulus and density of the core respectively: $1\times10^{-5}E_s < E_2 < 0.1E_s$, $0.2\rho_s < \rho_2 < 2.4\rho_s$ where $E_s$ and $\rho_s$ are the reference values for Young's modulus and density for the skin respectively and Gamma distribution is considered for each parameter. The Gamma distributions are built in a usual way with two parameters $(\alpha, \beta)$ as,

$$f(x|\alpha,\beta) = \frac{x^{\alpha-1}\mathrm{e}^{-\beta x}\beta^{\alpha}}{\int_0^{\infty} x^{\alpha-1}\mathrm{e}^{-x}\mathrm{d}x}. \tag{5.15}$$

The mean ($\mu$) and standard deviation ($\sigma$) values are assumed for each material property and two parameters (say $\alpha$ and $\beta$) of the Gamma distributions are then computed as, $\alpha = \sigma^2/\mu$; $\beta = (\mu/\sigma)^2$. As an example, the mechanical properties of aluminium could be taken for the skin to decide the range of values for the mechanical properties of the core.

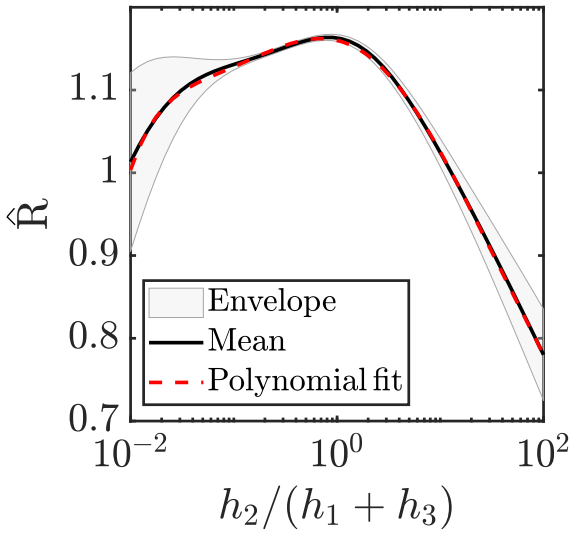


Figure 5.6: Envelope of $\hat{R}$ and its mean against the ratio between thicknesses of core and skins.

From the parametric study, the envelope of the values of $\hat{R}$ and its mean value are plotted in the Fig. 5.6 and for the practical values of core to skin thickness ratio, the

mean curve of $\hat{R}$ is fitted into the following polynomial.

$$\hat{R} = 1.16 - \frac{27\varphi^6 - 52\varphi^5 - 189\varphi^4 + 275\varphi^3 + 995\varphi^2 + 291\varphi}{10^4}, \tag{5.16}$$

where $\varphi = \log_{10}\left(\frac{h_2}{h_1 + h_3}\right)$. Contrary to the assumption that $\hat{R}$ would be influenced by both geometric and material properties, it is observed that only geometric dependence is significant on the $\hat{R}$ values. It is due to the fact that the distance between the skins (i.e, thickness of the core) strongly affects $D_{\text{low}}$ and thus the ratio $D_{\text{low}}/D_{\text{high}}$. It is to be noted that the parametric study is also conducted for the asymmetric case by varying the material and geometric parameters of the core and skin layers (for example, $0.5h_1 < h_3 < 3h_1$ which includes possible practical configurations). On the range of values of $\varphi$, the low-end value is chosen to include practical core thicknesses of thin film or glue and the high-end value is chosen to have a logarithmic symmetry. It is also observed that reducing the high-end value does not lead to reduction in the order of the polynomial fit. The optimum values of $\hat{R}$ are computed in the least square sense with the nonlinear equation (Eq. (5.1)) to have a good correspondence with those of the Guyader's model. The mean curve for $\hat{R}$-value obtained for asymmetric case results in maximum deviation to be lower than 1.5% to that of the symmetric case. The maximum deviation in $D_{\text{eq}}$ due to these R values are observed to be lesser than 2% between the Guyader and the sigmoid models. Therefore, the polynomial fit for $\hat{R}$-value given by the Eq. (5.16) could be applied for asymmetric configurations as well, and this $\hat{R}$ value is the representative of most of the practical configurations.

## 5.3 Numerical examples

In this section, numerical examples of the sigmoid model to compute equivalent bending stiffness (from Eq. (5.1)) of a sandwich panel and the corresponding equivalent bending wavenumber (from Eq. (2.15)) are presented. Since Guyader's model exhibit equally good response compared to Lamb wave model [101] below the zeroth-order symmetric mode [181], Guyader's model [131] is taken as a reference to compare the results of the sigmoid

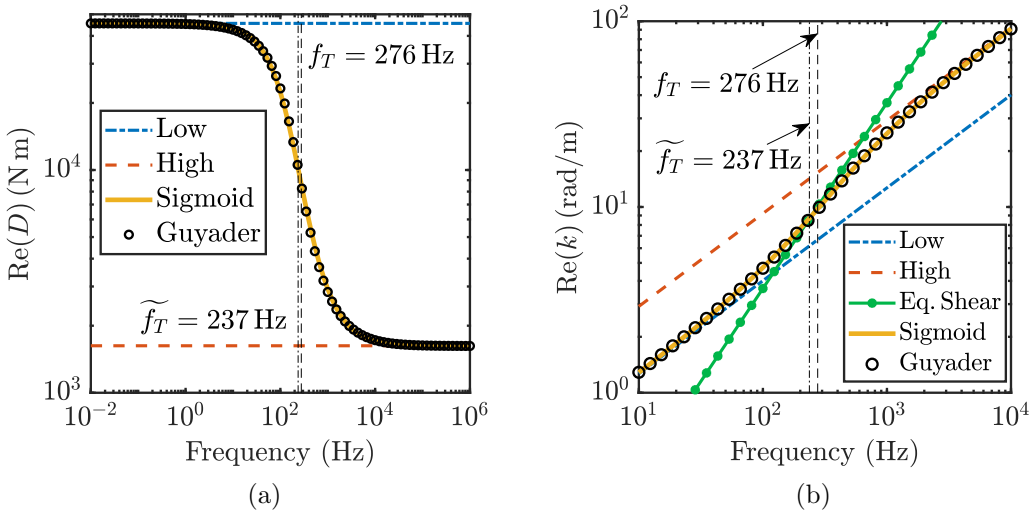


Figure 5.7: (a) Equivalent bending rigidity and (b) equivalent wavenumbers obtained from the sigmoid model for aluminium (5 mm)/shear layer (10 mm)/aluminium (5 mm) symmetric sandwich panel of infinite extent (material properties are listed in Table 5.1). Guyader's model is taken as reference to compare the sigmoid model.

model.

In Fig. 5.7, for a symmetric sandwich panel made of aluminium (5 mm)/soft core (10 mm)/aluminium (5 mm), $\widetilde{D}_{\text{eq}}$ and $k_{\text{eq}_{\text{bending}}}$ computed from the sigmoid model are presented for comparison, along with the transition frequency computed from Eq. (5.10). It can be seen from these plots that, the sigmoid model is in high agreement with the Guyader's model throughout the frequency range and the observed maximum error percentage is 4.9% in comparison with Guyader's model. Furthermore, it is observed from Fig. 5.7b that the transition frequency zone is controlled by the shear of the sandwich core, as the core has double the thickness of the skin. Due to this reason, the simpler expression from Eq. (5.13) estimates the transition frequency as 237 Hz, which is deviated around 14% from the value (276 Hz) computed by Eq. (5.10). One may note that this percentage of deviation would be further reduced if the thickness of the core layer is increased.

In Fig. 5.8, for an asymmetric sandwich panel made of steel (1 mm)/shear layer (0.5 mm)/aluminium (5 mm), $\widetilde{D}_{\text{eq}}$ and $k_{\text{eq}_{\text{bending}}}$ computed from the sigmoid model are presented for comparison, along with the transition frequency computed from Eq. (5.10).

From these plots as well, it can be seen that the sigmoid model is in high agreement with the Guyader's model throughout the frequency range and the observed maximum error percentage is 2.1% in comparison with Guyader's model. Unlike the previous sandwich configuration, it is observed from Fig. 5.8b that the transition frequency zone is not controlled by the shear of the sandwich core, as the core has a lesser value of thickness to that of the skins. This also reflects with a greater percentage of deviation (around 83%) for the simpler expression of transition frequency from Eq. (5.13) with that of the same from Eq. (5.10).

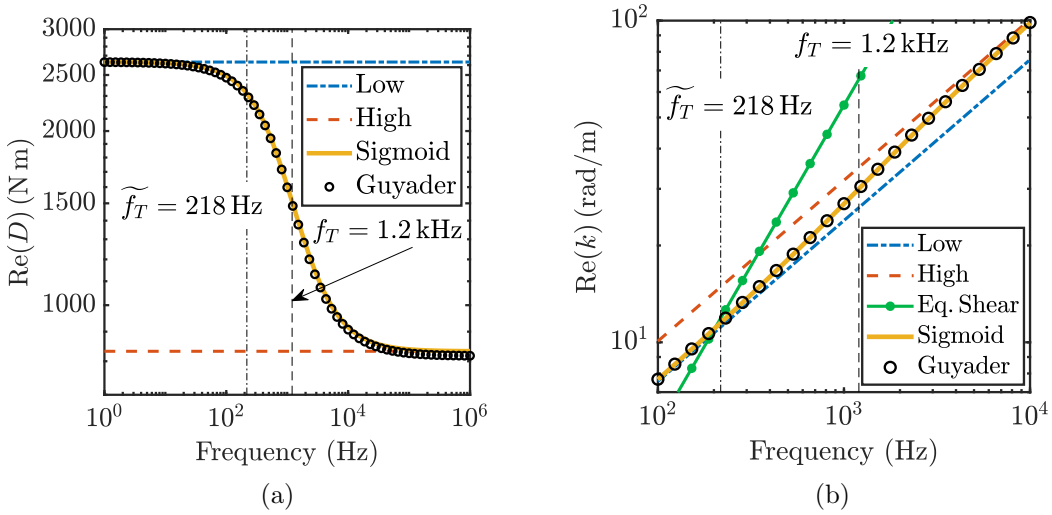


Figure 5.8: (a) Equivalent bending rigidity and (b) equivalent wavenumbers obtained from the sigmoid model for steel (1 mm)/shear layer (0.5 mm)/aluminium (5 mm) asymmetric sandwich panel of infinite extent (material properties are listed in Table 5.1). Guyader's model is taken as reference to compare the sigmoid model.

## 5.4 Experimental validation and further observation

In this section, the sigmoid model is compared with the experimental data, measured by Ege et al. [181], for the purpose of validation. A symmetric sandwich plate made of steel (0.18 mm)/polymer (0.69 mm)/steel (0.18 mm) with in-plane dimensions $300 \times 400$ mm$^2$, is considered for the experimental study and the data are measured through the contactless measurements (scanning laser vibrometer). Further, the CFAT (Corrected Force Analysis Technique) [86] methodology is used to estimate the bending stiffness of the structure. The

dynamic bending stiffness can be quickly constructed, through the sigmoid model, using only four parameters from Eqs. (5.3), (5.7), (5.10) and (5.16) which are substituted in Eq. (5.1). Finally, the equivalent Young's modulus, $\widetilde{E}_{\text{eq}}$, is computed from Eq. (2.14a) and compared against experimental data as shown in Fig. 5.9. A high agreement is observed between the estimation by equivalent plate models and the measured data which validates the applicability of the sigmoid model.

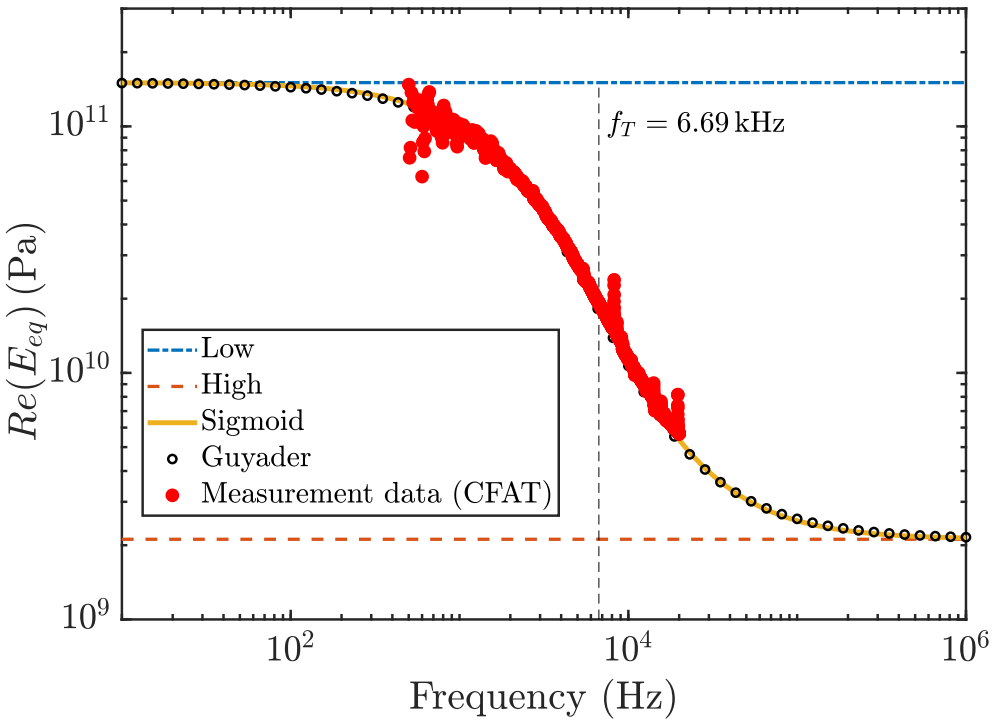


Figure 5.9: Comparison of equivalent plate models (sigmoid model and Guyader's model) with experimentally measured data of the equivalent Young's modulus for the steel (0.18 mm)/polymer (0.69 mm)/steel (0.18 mm) sandwich panel with in-plane dimensions $300 \times 400$ mm$^2$ (material properties are listed in Table 5.1).

Through these numerical examples discussed in this work, on the implementation side, the sigmoid model has its advantage of using only five equations (i.e, Eqs. (5.1), (5.3), (5.7), (5.10) and (5.16)) whereas Guyader's model requires to define seven constants and few other matrix definitions to compute the equivalent bending stiffness (see Appendix B). Further, in the Guyader's model, Eq. (2.13) need to be solved symbolically to obtain the solutions and solution tracing techniques have to be applied to correctly capture the physically meaningful solution for $\widetilde{D}_{\text{eq}}$. Such complexities do not present in the sigmoid

model, and it gives a straightforward solution for $\widetilde{D}_{\text{eq}}$. On an additional note, although the sigmoid model focuses on reconstructing the equivalent dynamic bending stiffness values of Guyader's model, it is observed from the Figs. 5.10 and 5.11 that the new model captures the equivalent dynamic loss factor of the system with the high agreement with Guyader's model and experimental data. It may be noted that the noise in the measured data of Fig. 5.11 may be due to the instability of the experimental method at low frequencies. Further, it is also observed that a slightly different Young's modulus (300 MPa) is used for the polymer by Ege et al. [181] to improve their fit on the damping loss factor. The reader may note that, although equivalent plate models account for both bending and shear motions of the multi-layer structures through dynamic bending stiffness, they may overestimate the equivalent loss factor when the dynamic of the multi-layer is controlled by the shear motion. Nevertheless, it can be corrected by the ratio between the phase and group velocities of the structure [139].

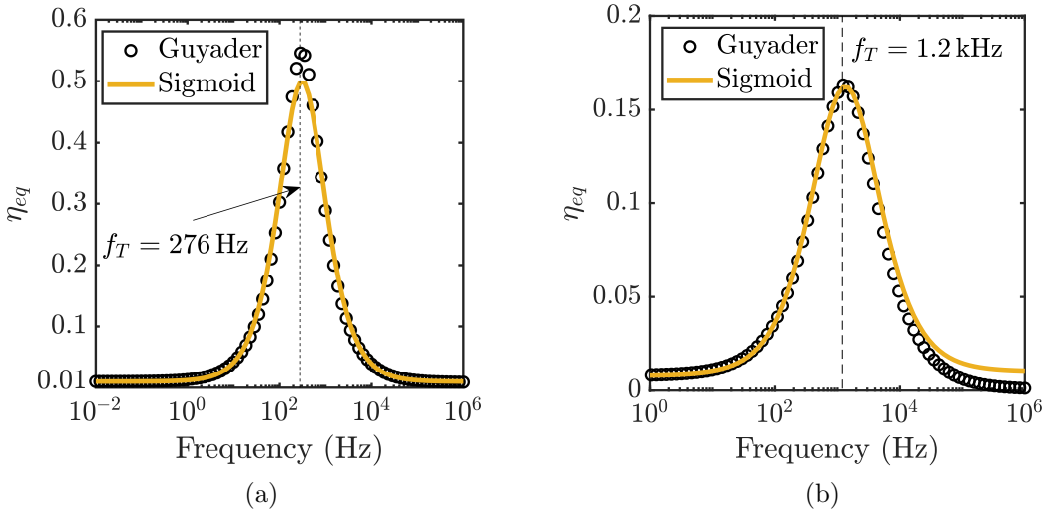


Figure 5.10: Equivalent loss factor for (a) symmetric aluminium (5 mm)/shear layer (10 mm)/aluminium (5 mm) (b) asymmetric steel (1 mm)/shear layer (0.5 mm)/aluminium (5 mm) sandwich panel of infinite extent (material properties are listed in Table 5.1). Guyader's model is taken as reference to compare the sigmoid model.

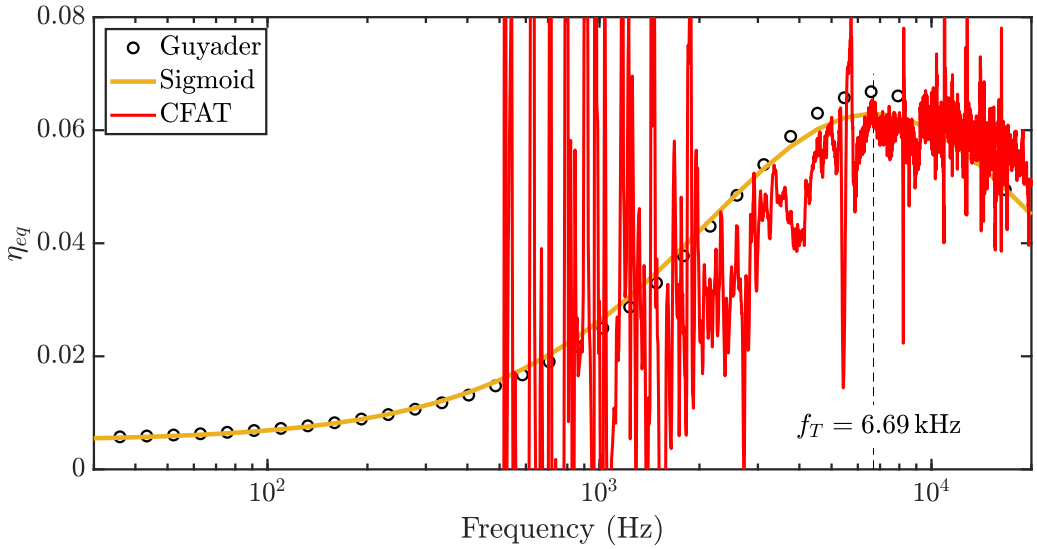


Figure 5.11: Comparison of equivalent plate models (sigmoid model and Guyader's model) with experimentally measured data of the equivalent loss factor for the steel (0.18 mm)/polymer (0.69 mm)/steel (0.18 mm) sandwich panel with in-plane dimensions $300 \times 400$ mm$^2$ (material properties are listed in Table 5.1).

Considering all the observations made in this work, the sigmoid model has its following advantages over the existing models in the literature: first, this model can be quickly implemented compared to the other equivalent plate models to compute the equivalent parameters of a three-layer sandwich panel (symmetric and asymmetric configurations); second, since the model is based on the asymptotic behaviours at different frequency regimes (low, high and transition), it can be used to understand the physics behind the response of a three-layer sandwich system at those frequency regimes and to identify the corresponding governing parameters; third, the new model will be a handy tool to optimize the layer parameters to achieve the desired damping performance of the three-layer sandwich panel due to its straightforward formulation. On the limitation side, similar to RKU model [7, 133, 156], this model also would be applicable only to three-layer structures where the core is softer than the skins. Usually, this may not be a problem, as most of the practical applications would fall under this assumption. The reader may refer to Table 5.2 for the summary of all the expressions for the sigmoid model.

Table 5.2: Summary of the expressions used in the sigmoid model

| Param. | Generic ($D_2 < D_1, D_3$) | Symmetric ($D_2 < D_1$) | Symmetric ($D_2 \ll D_1$) |
|---|---|---|---|
| $D_{\text{low}}$ | $\sum_{i=1}^{n} \frac{E_i}{1-\nu_i^2} \frac{(z_{ui}-\bar{z})^3 - (z_{li}-\bar{z})^3}{3}$ | $D_1\left(8 + \frac{12h_2}{h_1} + \frac{6h_2^2}{h_1^2}\right) + D_2$ | $D_1\left(8 + \frac{12h_2}{h_1} + \frac{6h_2^2}{h_1^2}\right)$ |
| $D_{\text{high}}$ | $D_1 + D_3$ | $2D_1$ | |
| $f_T$ | $\frac{1}{2\pi}\frac{G_2}{12h_2}\frac{D_{\text{low}}}{\sqrt{m_s D_T}}\left(\frac{h_1^2}{D_1} + \frac{h_3^2}{D_3}\right)$ | $\frac{1}{2\pi}\frac{G_2 h_1^2}{3h_2}\frac{D_{\text{low}}}{D_{\text{high}}}\frac{1}{\sqrt{m_s D_T}}$ | |
| | $\frac{1}{2\pi}\frac{G_2 h_t}{\sqrt{m_s D_T}}$ (for thicker core, $h_2 \gg h_1, h_3$) | | |
| $\hat{R}$ | $1.16 - \frac{27\varphi^6 - 52\varphi^5 - 189\varphi^4 + 275\varphi^3 + 995\varphi^2 + 291\varphi}{10^4}$, where $\varphi = \log_{10}\left(\frac{h_2}{h_1+h_3}\right)$ | | |
| Equivalent properties : $\log_{10}\widetilde{D}_{\text{eq}}(f) = \frac{f_T^{\hat{R}}\log_{10} D_{\text{low}} + f^{\hat{R}}\log_{10} D_{\text{high}}}{f^{\hat{R}} + f_T^{\hat{R}}}$; $\widetilde{\eta}_{\text{eq}}(f) = \frac{\text{Im}(\widetilde{D}_{\text{eq}})}{\text{Re}(\widetilde{D}_{\text{eq}})}$ | | | |
| $\bar{z} = \frac{\sum z_i b_i h_i}{\sum b_i h_i}$; $b_i = \frac{E_i(1-\nu_{\text{ref}}^2)}{E_{\text{ref}}(1-\nu_i^2)}$; $m_s = \sum_{i=1}^{n}\rho_i h_i$; $D_T = \sqrt{D_{\text{low}} D_{\text{high}}}$; $h_t = \sum_{i=1}^{n} h_i$ | | | |

## 5.5 Conclusion

A simple equivalent plate model is presented to compute the dynamic equivalent properties of a three-layer sandwich panel of infinite extent and made of isotropic materials. Though the formalization of the presented model is based on the physical behaviours at only three frequency regimes (low, high and transition), described by Boutin and Viverge [173], it is showed that the simple model is indeed valid for the entire frequency range. In comparison with other existing equivalent plate models, the new model will be easier to implement and would serve as a tool to quickly optimize the sandwich panel parameters to obtain the desired performance.

As the condensed models account for only anti-symmetric motions (bending, shear and membrane), they are limited to thin multi-layers where longitudinal compression is avoided. If the multi-layer structure is thick and/or includes a soft core, then the dilatational motion cannot be ignored. Therefore, in the next chapter, a novel condensed model is developed to include the dilatational motion of the thick multi-layer structures.

# Chapter 6

# Condensed model for thick symmetric multi-layers including dilatational motion

In the previous chapters, the advantages of the condensed plate models have been discussed and one of the key benefits is saving the computational power during Finite Element (FE) simulations of the multi-layer structures. Although, they have the potential to be utilized in multiple applications, the condensed plate models have some limitations as well. Since condensed plate models assume constant normal displacement of the multi-layer structure, they allow only anti-symmetric motions (bending and shear) and omit the symmetric motion (dilatational or compressional). Applicable frequency limits for such kind of assumption are described in Chapter 4. However, in many applications, the symmetric motions can happen even at low frequencies. For example, in the classical double wall partition widely used in building applications, the compressional mode could be excited at low frequencies. This brings a necessity to improve the equivalent plate models [7, 131, 133, 138, 156, 174], to allow symmetric motions along with anti-symmetric motions. Therefore, in this chapter, a novel condensed model based on the symmetric and anti-symmetric admittances of the multi-layer structures is presented.

**Note**

Most of the contents presented in this chapter has been taken from the published article [182]:

Marchetti, F., **Arasan, U.**, Chevillotte, F., Ege, K. (2021). "On the condensation of thick symmetric multilayer panels including dilatational motion". *Journal of Sound and Vibration*, 502, 116078.

Regarding the contributions made to the above-mentioned article, the author of this thesis has done the following tasks: formal analysis, article writing, editing and review.

In line with this point, this chapter is divided into three major sections: 1) in Section 6.1, limitations of the condensed (or equivalent) plate models are discussed, 2) in Section 6.2, an advanced vibro-acoustic condensed model, including symmetric motion, for physically symmetric multi-layer structures is presented, 3) in Section 6.3, transmission loss computations of multi-layer structures made of elastic and/or poro-elastic layers, which experience compression motions, are presented for the purpose of validating the new condensed model.

## 6.1 Limitations of condensed (or equivalent) plate models

This section discusses the limitations of the equivalent plate models when it comes to account for the symmetric motion. The reader may note that different authors use other terminologies for the symmetric motion, such as compressional, breathing or dilational motion. To illustrate the exclusion of symmetric motion in the condensed plate models, few observations can be made on the transmission loss and the admittances of the multi-layer structures that are obtained from the condensed plate models. Guyader's model is considered as a representative example of the condensed approaches which consider only the anti-symmetric motions. Computations obtained using the Transfer Matrix Method

| | Skins (steel) | Stiff core | Soft core |
|---|---|---|---|
| $\rho$ (kg m$^{-3}$) | 7800 | 1000 | 55 |
| $E$ (Pa) | $210\times10^9$ | $0.2\times10^9$ | $43\times10^3$ |
| $\nu$ | 0.3 | 0.48 | 0.4 |
| $\eta$ | 0.03 | 0.05 | 0.3 |

Table 6.1: Mechanical properties of the isotropic layers used in this chapter.

(TMM) will be used as a reference, as this model is based on a full field approach which inherently includes both the anti-symmetric and symmetric motions (see Fig. 6.1 for a schematic representation of these motions). Computation of vibro-acoustic quantities using TMM and its theoretical background are detailed in the Chapter 3 of this manuscript.

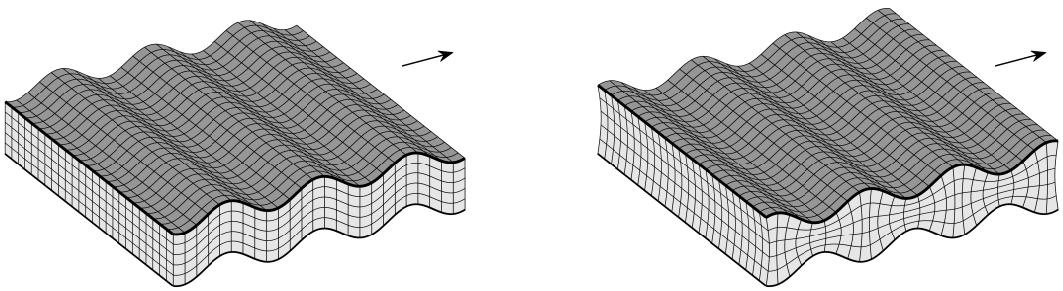

(a) (b)

Figure 6.1: Anti-symmetric (a) and symmetric (b) waves propagating in a plate.

### 6.1.1 Transmission Loss (TL)

Two sandwich configurations are considered to demonstrate the limitations of condensed plate models. Typically, sandwich plates with a stiff core layer or soft layer would be ideal candidates to apply these models. This is demonstrated with the first sandwich configuration type, which has steel layers as skins and a core that is thin and stiff enough so that the compression mode is shifted after the maximum audible frequency. The elastic properties of the materials used in this chapter are listed in Table 6.1.

As mentioned in the previous chapters, condensed plate models yield the intrinsic dynamic bending stiffness ($\widetilde{D}_{\mathrm{eq}}$) parameter of the multi-layer structure, assuming a homogenized equivalent thin plate. The impedance of an equivalent thin plate ($Z_{\mathrm{ep}}$) which is required to compute the transmission coefficient from Eq. (3.75) can be taken from Eq. (3.32). For the sake of readability, the expression is recalled here:

$$Z_{\mathrm{ep}} = Z_{\mathrm{thin}} = \mathrm{j}\omega m_s \left(1 - \frac{\widetilde{D}_{\mathrm{eq}} k_t^4}{\omega^2 m_s}\right). \tag{6.1}$$

Then, the Transmission Loss (TL) may be calculated from Eq. (3.59) for oblique incidence and from Eq. (3.61) for diffuse field.

Similar to Fig. 4.2, the expected behaviour of the sandwich structure is observed from Fig. 6.2 for both models: the low frequency is controlled by the mass and can be approximated with a good accuracy using the mass law and the high frequency range controlled by the stiffness. The transition between the two regimes occurs at the so-called coincidence frequency (the frequency at which the transverse wavenumber is equal to the bending wavenumber). In this region, the transmission loss is controlled by the structural damping inside the structure. One could also observe that, for this type of sandwich configuration, the Guyader's model gives the same response as that of TMM up to $f <$ 10 kHz, and it also estimates the correct coincidence frequency at $f \approx 5.2$ kHz.

In the second sandwich configuration, a soft core is sandwiched by the two steel skins and a similar transmission loss comparison is shown in Fig. 6.3. Two important observations are made from the response given by the equivalent plate models. The first observation is that this sandwich exhibits two singularities in the transmission loss, unlike Fig. 6.2 where only one singularity exists. At a lower frequency around $f \approx 260$ Hz, the multi-layer resonates like a mass-spring-mass system, which leads to the singularity at that frequency. This frequency is commonly termed as breathing frequency or compressional frequency of the system. Since the equivalent plate models assume a constant normal velocity all through the thickness of the multi-layer system, they would not be able to capture this compressional motion and, therefore, deviates after 150 Hz. Due to

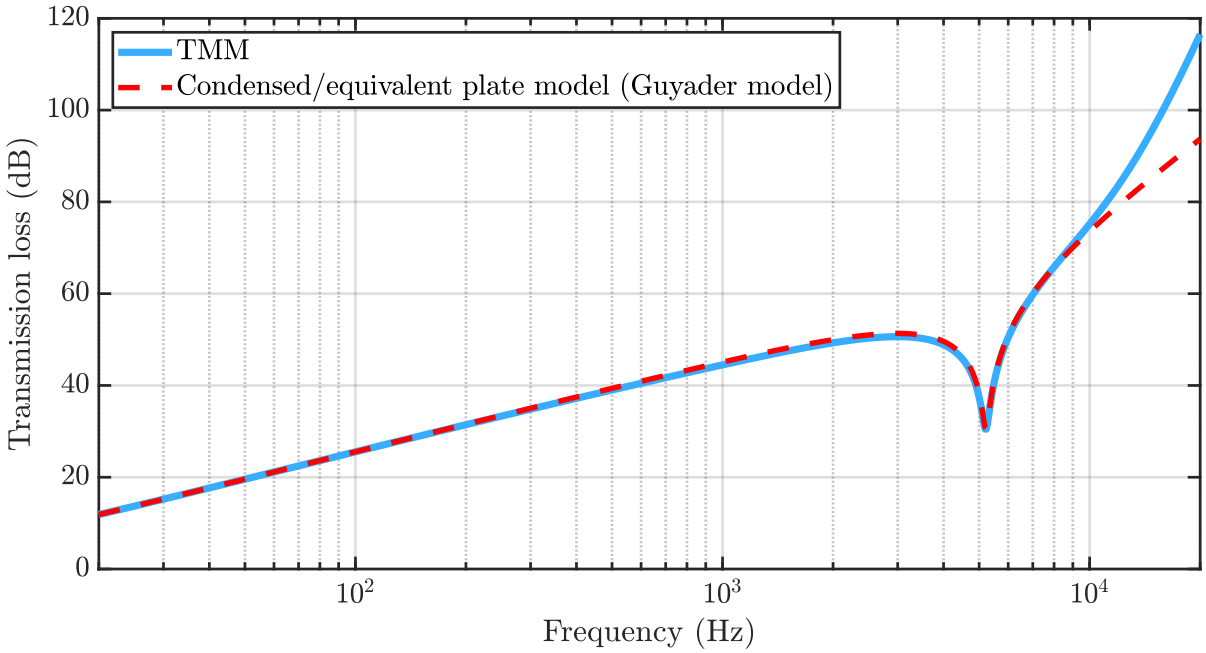


Figure 6.2: Transmission loss of the steel (3 mm)/stiff core (3 mm)/steel (3 mm) sandwich estimated using the TMM and Guyader's equivalent plate model for the 60° plane wave incidence. Material properties are listed in Table 6.1.

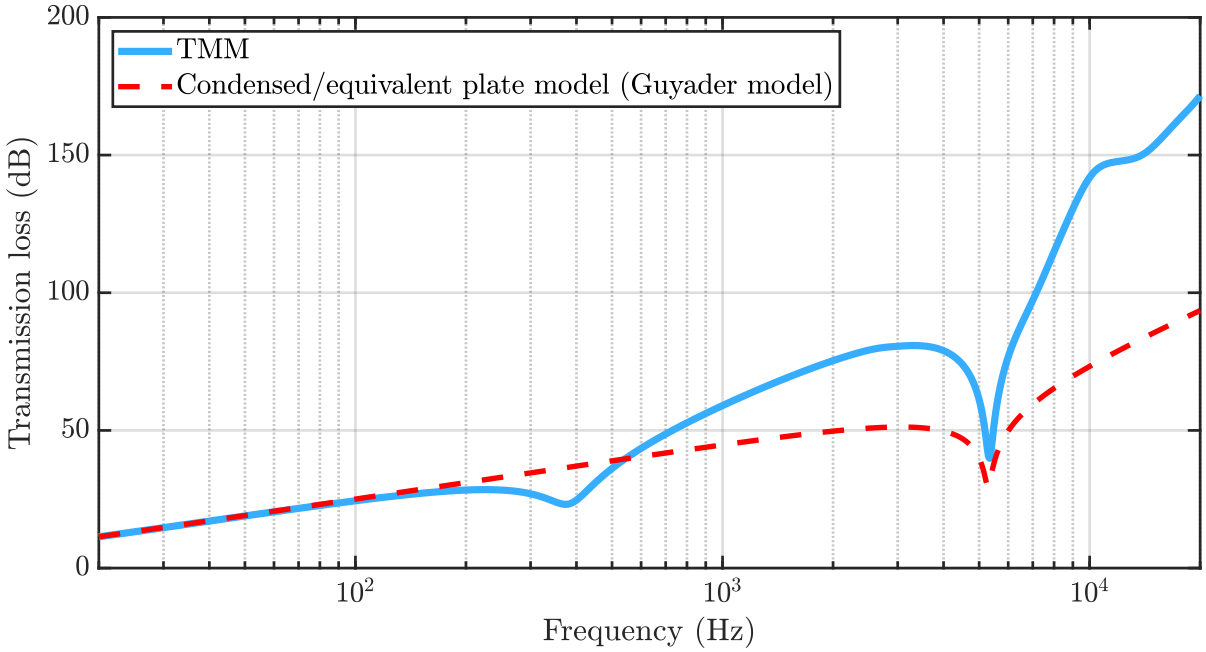


Figure 6.3: Transmission loss of the steel (3 mm)/soft core (3 mm)/steel (3 mm) sandwich estimated using the TMM and Guyader's equivalent plate model for the 60° plane wave incidence. Material properties are listed in Table 6.1.

this, the transmission loss computed by the Guyader's model (or similar equivalent or condensed plate model) is underestimated after the compressional frequency. The second observation is that, though it missed predicting the compressional frequency, it correctly computes the coincidence frequency as it is captured by the anti-symmetric motion of the multi-layer structures which is well described by the equivalent plate models.

### 6.1.2 Admittances

As stated earlier, the existing condensed plate models do not account for dilatational or breathing motion of the multi-layer structure, since they assume constant deformation through the thickness. Similar to the admittance analysis carried out for a single layer in Section 4.4, this section focuses on the study of the anti-symmetric and symmetric motions of the multi-layer structure, by comparing the admittances of both motions, in order to understand the differences between the condensed model and the complete modelling of multi-layers with the TMM.

For the first sandwich configuration (steel/stiff core/steel), the admittances are calculated using the TMM and are presented in Fig. 6.4, considering a plane wave at 60° of incidence using Eq. (3.79) and Eq. (3.80). It is observed that the anti-symmetric admittance computed from the equivalent plate model is in good agreement with the TMM at all frequencies. It also predicts the coincidence frequency correctly, as it is already seen from the TL plots. On the other hand, the symmetric admittance has lower order compared to anti-symmetric admittance at low frequencies and reaches the same value after 10 kHz. This means that the multi-layer structure is mainly controlled by the anti-symmetric motions below 10 kHz, and both motions are equally contributing to the resulting motion of the structure beyond this frequency. Fig. 6.4 also shows the response from the Guyader's model, and it is seen that $Y_{\text{eq}} = 1/Z_{\text{eq}}$ follows the anti-symmetric admittance calculated from the TMM for all the frequencies. Further, it also confirms that the condensed plate models account only for the anti-symmetric motions and neglect the symmetric motion. Due to the same reason, the differences are appeared in Fig. 6.2 after 10 kHz, since the symmetric admittance ($Y_S$) is no longer negligible after this frequency. It may be noted

that this frequency limit for the condensed plate models can be derived by observing the symmetric and anti-symmetric admittances, similar to the one presented in Section 4.4 for a single layer. This corresponds to the limit between plate and full elasticity theories, and Eq. (4.22) should be modified to account for the frequency dependent bending stiffness and the modified symmetric admittance of the multi-layer structure.

Fig. 6.5 shows the admittances plot for the second type of sandwich configuration (steel/soft core/steel). For this case, the symmetric admittance has its first peak at the compressional frequency (around 250 Hz) while the anti-symmetric admittance has its peak around the coincidence frequency. Further, once the symmetric admittance reaches the anti-symmetric admittance, it also starts to have its peak around coincidence frequency. The reason for this phenomenon can be explained by the theory of Lamb waves. Although, both TMM and Lamb wave theory are formulated from the principles of elasticity, an acoustic wave with transverse wavenumber ($k_t$) is imposed by the TMM whereas Lamb wave theory finds the natural wavenumbers by assuming that the multi-layer structure is in vacuum. The readers are referred to [101, 177] to know more on the theory of Lamb waves. For the purpose of completeness, Appendix C describes shortly on how the wavenumbers of a multi-layer structure are obtained using Lamb waves. The zeroth-order dispersion curves correspond to two types of motions, i.e. anti-symmetric ($A_0$) and symmetric ($S_0$) motions, of the second sandwich configuration are shown in Fig. 6.6 as determined by the Lamb waves model. Two key observations from this plot are:

- While the anti-symmetric wave ($A_0$) is propagative at all frequencies, the symmetric wave ($S_0$) has a cut-on frequency around 250 Hz and reaches the anti-symmetric wavenumber at higher frequency. This would explain the reason for the coincidence frequencies of anti-symmetric and symmetric motions being the same, as both curves are closer to each other at higher frequencies.

- The transverse wavenumber ($k_t$), imposed by the TMM at 60°, cuts the zeroth-order Lamb waves at two frequencies. The breathing mode of the structure occurs when it cuts $S_0$ wave at around 250 Hz, and the coincidence mode of the structure occurs

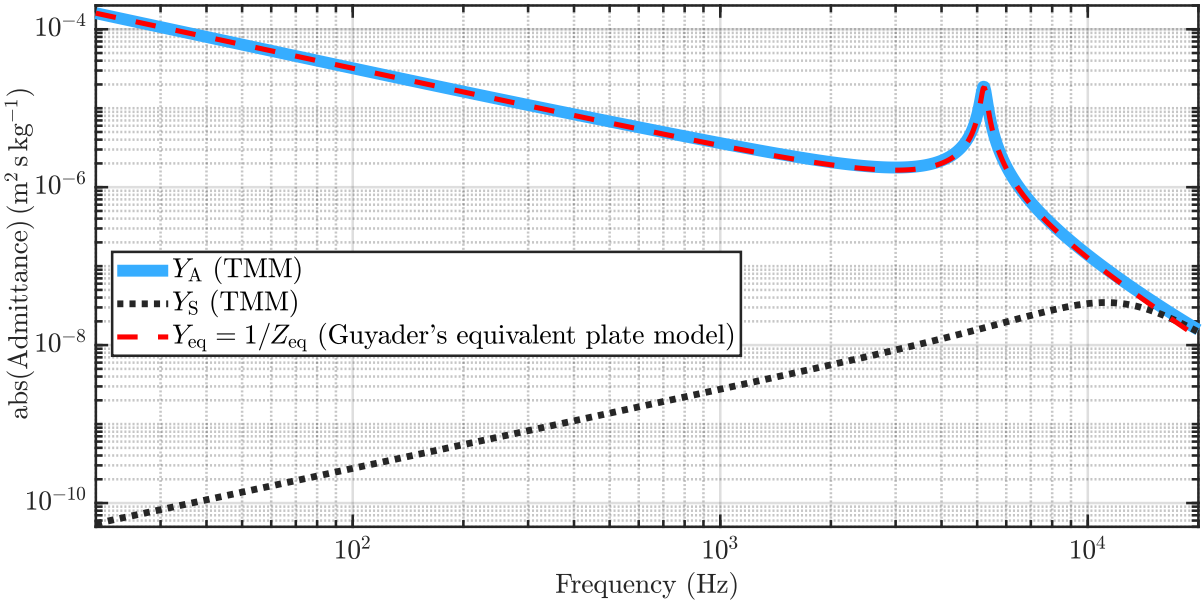


Figure 6.4: Admittances of the steel (3 mm)/stiff core (3 mm)/steel (3 mm) sandwich estimated using the TMM and Guyader's equivalent plate model for the 60° plane wave incidence. Material properties are listed in Table 6.1.

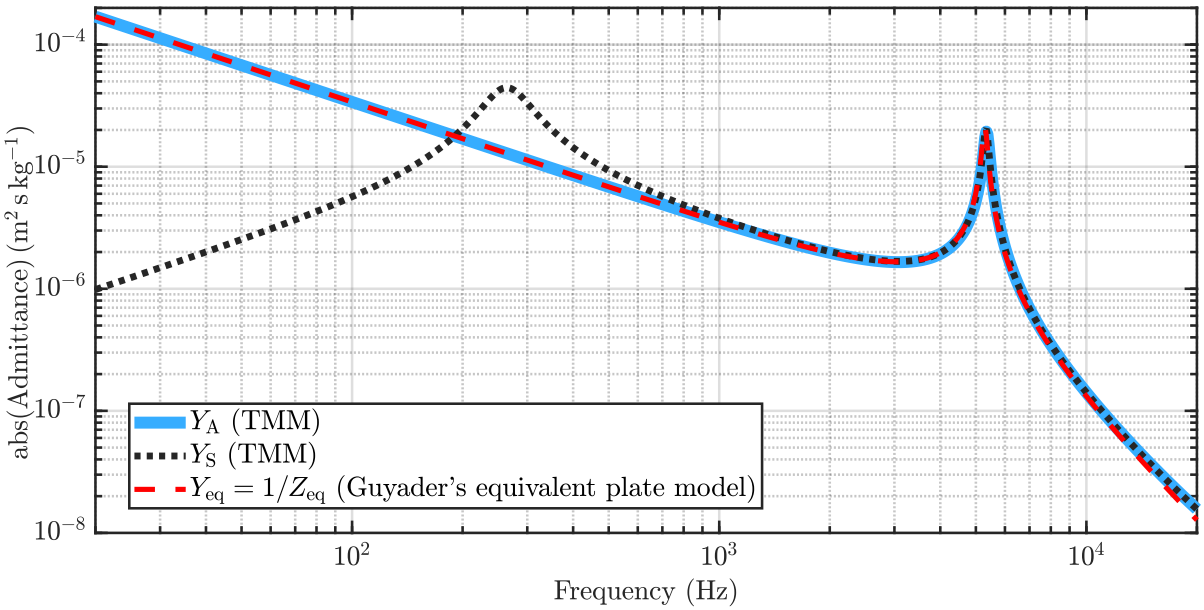


Figure 6.5: Admittances of the steel (3 mm)/soft core (3 mm)/steel (3 mm) sandwich estimated using the TMM and Guyader's equivalent plate model for the 60° plane wave incidence. Material properties are listed in Table 6.1.

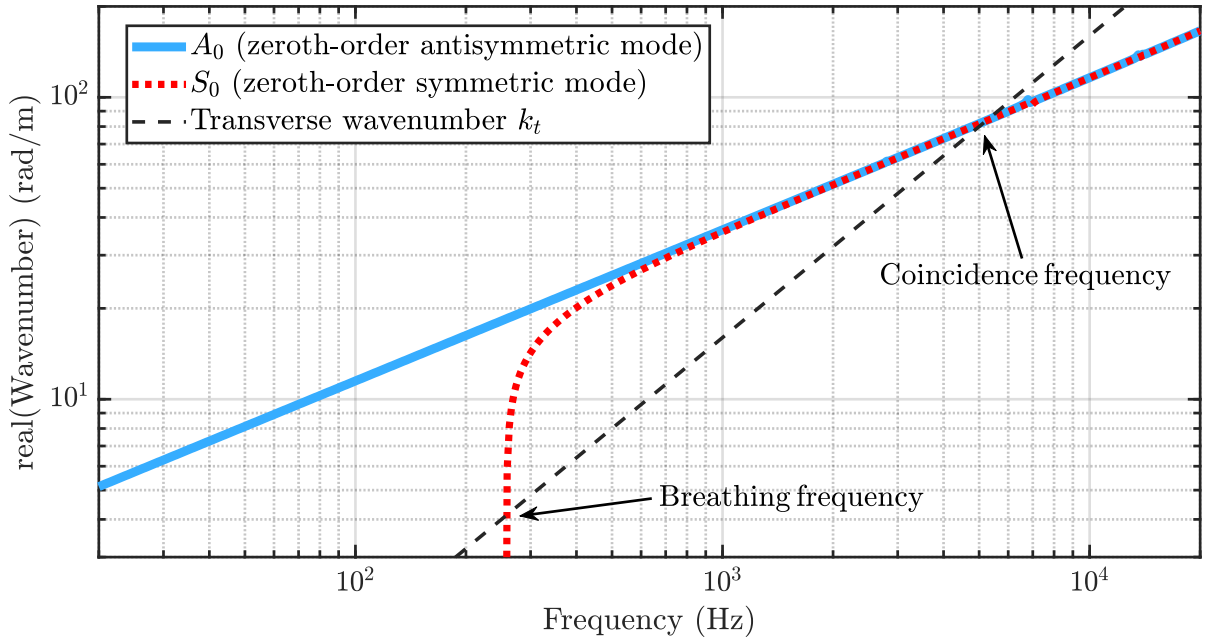


Figure 6.6: Dispersion curves of the steel (3 mm)/soft core (3 mm)/steel (3 mm) sandwich estimated using the Lamb wave model. The dashed black line corresponds to the transverse wavenumber of the plane wave incidence at 60°. Material properties are listed in Table 6.1.

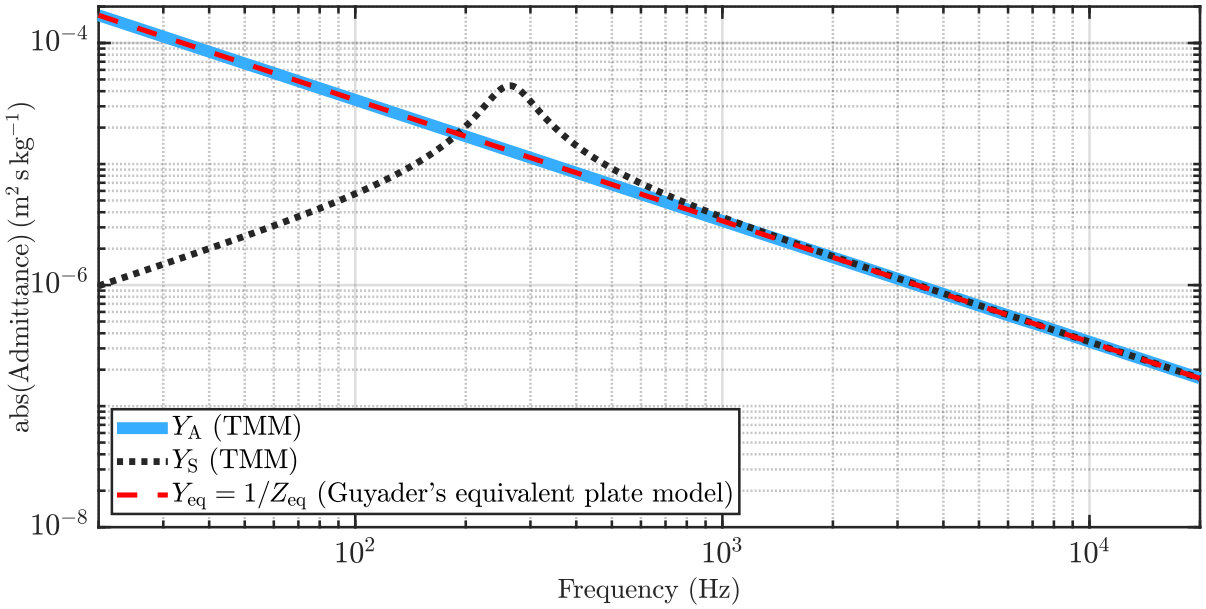


Figure 6.7: Admittances of the steel (3 mm)/soft core (3 mm)/steel (3 mm) sandwich estimated using the TMM and Guyader's equivalent plate model for the normal incidence. Material properties are listed in Table 6.1.

when it cuts both $A_0$ and $S_0$ at around 5000 Hz. One may note from the Figs. 6.3 and 6.5 that, the singularities in the TL and admittances occur at these breathing and coincidence frequencies.

These observations would serve as important information to formulate the new condensed model in the following sections. It is also observed from the Fig. 6.5 that the equivalent admittance is again in high agreement with the anti-symmetric admittance computed from the TMM. This means that the equivalent plate model provides a correct response of the anti-symmetric motion of the sandwich even though the core is soft in nature. Finally, it is noted that the symmetric motion should not be neglected after 150 Hz, which corresponds to the frequency where the TL computed from the Guyader's model begins to deviate from that of the TMM (see Fig. 6.3).

Another important observation on symmetric admittance can be drawn from Fig. 6.7, in the case of normal incidence. It reveals that the symmetric admittance still has its peak around the same breathing or compressional frequency (around 250 Hz), which is computed for 60° incidence. While the mass law mainly controls the anti-symmetric motion, the symmetric motion is controlled by the compressional effect of the multi-layer system (or by the mass-spring-mass resonance). Therefore, it is realized that the compressional effect does not depend on the angle of incidence.

From these transmission loss and admittance observations, it can be understood that the condensed/equivalent plate models correctly capture the anti-symmetric motion of the multi-layer structure while they fail to predict its behaviour with symmetric motions. It is due to the assumption of constant deformation along the thickness direction.

## 6.2 Advanced vibro-acoustic condensed model

In this section, an advanced condensed model is developed which accounts for both symmetric and anti-symmetric motions of physically symmetric mutli-layer structures. Fig. 6.8 presents the schematic representation of the condensed model discussed in this

section.

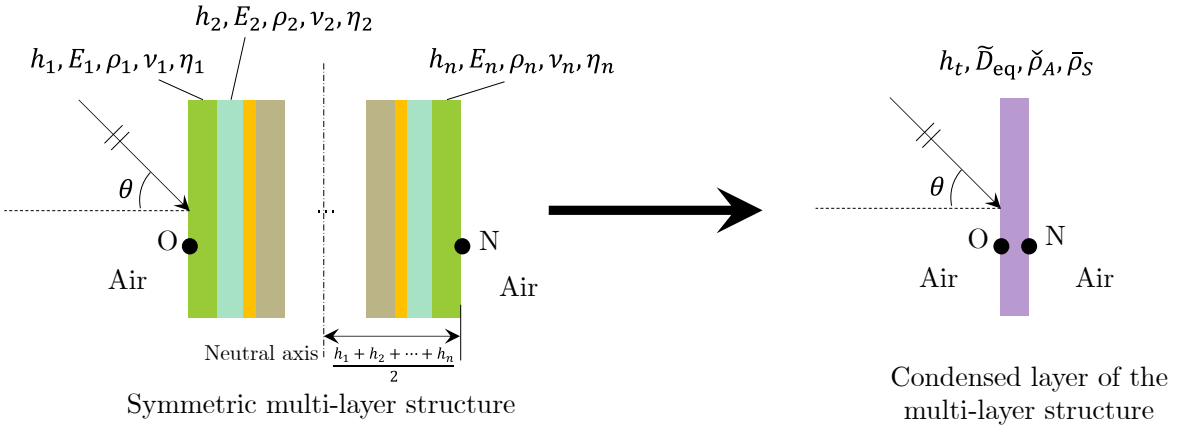


Figure 6.8: Schematic representation of the novel condensed model, applied to physically symmetric multi-layer structure.

### 6.2.1 Equivalent admittances of the condensed model

#### Equivalent symmetric admittance

We know that the anti-symmetric impedance of an equivalent thin plate by Love-Kirchhoff is defined as (refer Eq. (3.32)),

$$Z_{\text{eq}} = \mathrm{j}\omega m_s \left(1 - \frac{\widetilde{D}_{\text{eq}} k_t^4}{\omega^2 m_s}\right) = \frac{1}{\mathrm{j}\omega}\left(\widetilde{D}_{\text{eq}} k_t^4 - \rho_{\text{eq}} h_t \omega^2\right). \tag{6.2}$$

The idea here is to formulate a similar form for the symmetric impedance to capture the behaviour of symmetric motions. As it is observed in the previous section, both anti-symmetric and symmetric admittances exhibit same coincidence frequencies. Since the stiffness-controlled term ($\widetilde{D}_{\text{eq}} k_t^4$) affects the position of the coincidence frequency, this term is kept in the symmetric impedance as well. Additionally, we observed from the Figs. 6.5 to 6.7 that the estimation of the breathing frequency is unaffected by the transverse wavenumber ($k_t$). This means that the breathing effect is controlled by an intrinsic property of the system, and such property can be attributed to the mass density of the equivalent thin plate. Therefore, the frequency-independent parameter $\rho_{\text{eq}}$ (theoretical mass density of the structure) of Eq. (6.2) is changed to a frequency-dependent parameter

$\overline{\rho}_S$ to include the breathing or dilatational effect of the multi-layer structure. Due to this change, the Eq.(6.2) takes the following form to define the equivalent symmetric impedance:

$$Z_{\mathrm{S,eq}} = \frac{1}{\mathrm{j}\omega}\left(\widetilde{D}_{\mathrm{eq}}k_t^4 - \overline{\rho}_{\mathrm{S}}h_t\omega^2\right). \tag{6.3}$$

The equivalent symmetric admittance is then calculated using,

$$Y_{\mathrm{S,eq}} = 1/Z_{\mathrm{S,eq}}. \tag{6.4}$$

**Equivalent anti-symmetric admittance**

It is observed from the previous sections that the equivalent anti-symmetric admittance estimated by the condensed/equivalent plate models provides similar response to the anti-symmetric admittance of the multi-layer structure computed by the TMM. This means that the equivalent anti-symmetric impedance still takes the same form as in Eq. (6.2), but the mass density is replaced with a dynamic intrinsic parameter to improve the accuracy of the new condensed model. Therefore, the equivalent anti-symmetric impedance is redefined as,

$$Z_{\mathrm{A,eq}} = \frac{1}{\mathrm{j}\omega}\left(\widetilde{D}_{\mathrm{eq}}k_t^4 - \breve{\rho}_{\mathrm{A}}h_t\omega^2\right). \tag{6.5}$$

The reason and advantages of using the newly introduced density $\breve{\rho}_A$ over the theoretical mass density ($\rho_{\mathrm{eq}}$) will be discussed in Sections 6.2.2 and 6.2.3. Finally, the equivalent anti-symmetric admittance is then calculated using,

$$Y_{\mathrm{A,eq}} = 1/Z_{\mathrm{A,eq}}. \tag{6.6}$$

Since the coefficients $\breve{\rho}_{\mathrm{A}}, \overline{\rho}_{\mathrm{S}}$ and $\widetilde{D}_{\mathrm{eq}}$ do not depend on the angle of incidence of the acoustic wave, they correspond to the dynamic intrinsic properties of the proposed condensed layer.

### 6.2.2 Identification of the three dynamic parameters of the condensed model

As the coincidence frequency is correctly captured by the existing condensed/equivalent plate models, the dynamic parameter $\widetilde{D}_{\mathrm{eq}}$ can be computed from any equivalent plate model [7, 131, 133, 138, 156, 174]. For the other two dynamic mass densities, $\overline{\rho}_{\mathrm{S}}$ and $\breve{\rho}_{\mathrm{A}}$, two strategies are proposed as explained in the following subsections.

#### Transfer matrix at normal incidence

In this first strategy, the two dynamic mass densities are derived from computing the condensed transfer matrix at normal incidence (see Section 3.9.2 for the similar approach). At first, the symmetric and anti-symmetric admittances are computed using the Eq. (3.79) and Eq. (3.80). Then by substituting $k_t = 0$ (as it corresponds to normal incidence) in Eq. (6.3) and Eq. (6.5), the dynamic mass densities are computed as follows:

$$\breve{\rho}_{\mathrm{A}} = \frac{1}{\mathrm{j}h_t\omega}\frac{1}{Y_{\mathrm{A}}}\bigg|_{\theta=0} \quad ; \quad \overline{\rho}_{\mathrm{S}} = \frac{1}{\mathrm{j}h_t\omega}\frac{1}{Y_{\mathrm{S}}}\bigg|_{\theta=0}. \tag{6.7}$$

Compared to the next strategy, this one provides more advantages as it applies to symmetric systems comprising any type of materials (fluid, solid, poro-elastic) and for an arbitrary number of layers.

#### Mass-spring-mass system at normal incidence

The second strategy follows the description of symmetric motion defined for sandwich structures by a mass-spring-mass system [183]. In this approach, the skins are considered as masses with surface mass $\mathcal{M} = \rho_1 h_1 = \rho_3 h_3$ and the core is considered as a spring with a compliance $\mathcal{C}$. For this system, the transfer matrix relation can be expressed as:

$$\begin{Bmatrix} p(O) \\ v_z(O) \end{Bmatrix} = \begin{bmatrix} 1 & \mathrm{j}\omega\mathcal{M} \\ 0 & 1 \end{bmatrix} \begin{bmatrix} 1 & 0 \\ \mathrm{j}\omega\mathcal{C} & 1 \end{bmatrix} \begin{bmatrix} 1 & \mathrm{j}\omega\mathcal{M} \\ 0 & 1 \end{bmatrix} \begin{Bmatrix} p(N) \\ v_z(N) \end{Bmatrix}, \tag{6.8}$$

$$\Rightarrow \begin{Bmatrix} p(O) \\ v_z(O) \end{Bmatrix} = \begin{bmatrix} 1-\omega^2\mathcal{C}\mathcal{M} & \mathrm{j}\omega(2\mathcal{M}-\omega^2\mathcal{C}\mathcal{M}^2) \\ \mathrm{j}\omega\mathcal{C} & 1-\omega^2\mathcal{C}\mathcal{M} \end{bmatrix} \begin{Bmatrix} p(N) \\ v_z(N) \end{Bmatrix}. \tag{6.9}$$

It may be noted that if the core is solid, the compliance is $\mathcal{C}_{\text{solid}} = h_2/(\lambda_2 + 2\mu_2)$ where $\lambda_2 = E_2\nu_2/\left((1+\nu_2)(1-2\nu_2)\right)$ and $\mu_2 = E_2/\left(2(1+\nu_2)\right)$ are the Lamé coefficients of the core. In case of poro-elastic core, the compliance can be calculated by the model proposed by Biot [22, 23] or can be obtained by adding the fluid phase and solid phase stiffnesses in parallel. In the latter case, the compliance is $\mathcal{C}_{\text{porous}} = \mathcal{C}_{\text{fluid}}\mathcal{C}_{\text{solid}}/(\mathcal{C}_{\text{fluid}} + \mathcal{C}_{\text{solid}})$, where $\mathcal{C}_{\text{fluid}}$ is the compliance of the fluid and this could be approximated by $\mathcal{C}_{\text{fluid}} = h_2/P_0$ at low frequency for materials having a porosity close to 1, with $P_0$ being the atmospheric pressure. Then, the symmetric mass density ($\overline{\rho}_{\text{S}}$) is computed as follows from the symmetric admittance computed at normal incidence (given by Eq. (3.79)).

$$\overline{\rho}_{\text{S}} = -\frac{4\mathcal{M}-2\omega^2\mathcal{C}\mathcal{M}^2}{h_t\omega^2\mathcal{C}\mathcal{M}} = 2\frac{\mathcal{M}}{h_t}\left(1-\frac{2}{\omega^2\mathcal{C}\mathcal{M}}\right). \tag{6.10}$$

For the anti-symmetric motion, the theoretical mass density is taken as the dynamic mass density: $\breve{\rho}_{\text{A}} = \rho_{\text{eq}}$ which results in the same anti-symmetric admittance as computed by other equivalent plate models, i.e, $Z_{\text{A,eq}} = Z_{\text{eq}}$.

It may be noted that this method could be used on a multi-layer system of any number of layers, with each $i-$th layer defined by the mass $\mathcal{M}_i$ and the compliance $\mathcal{C}_i$. In this case, the transfer matrix relation can be expressed as:

$$\begin{Bmatrix} p(O) \\ v_z(O) \end{Bmatrix} = \begin{bmatrix} 1 & \mathrm{j}\omega\mathcal{M}_1 \\ \mathrm{j}\omega\mathcal{C}_1 & 1 \end{bmatrix} \ldots \begin{bmatrix} 1 & \mathrm{j}\omega\mathcal{M}_i \\ \mathrm{j}\omega\mathcal{C}_i & 1 \end{bmatrix} \ldots \begin{bmatrix} 1 & \mathrm{j}\omega\mathcal{M}_N \\ \mathrm{j}\omega\mathcal{C}_N & 1 \end{bmatrix} \begin{Bmatrix} p(N) \\ v_z(N) \end{Bmatrix}. \tag{6.11}$$

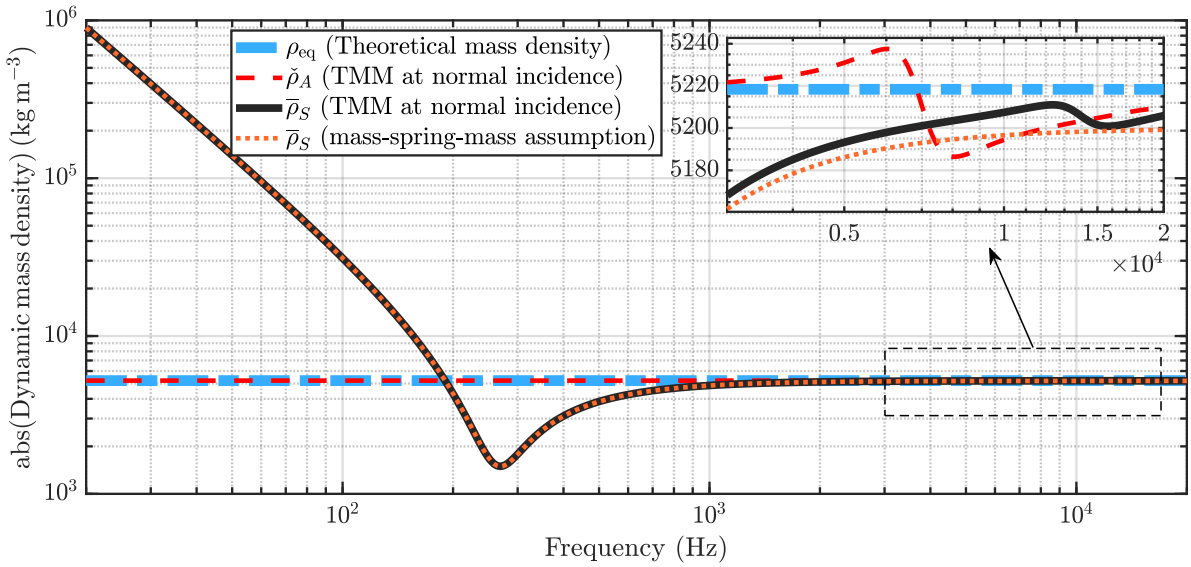


Figure 6.9: Absolute values of the dynamic mass densities $\breve{\rho}_{\mathrm{A}}$ and $\overline{\rho}_{\mathrm{S}}$ of the steel (3 mm)/soft core (3 mm)/steel (3 mm) sandwich estimated using the TMM and mass-spring-mass assumption. Material properties are listed in Table 6.1.

### 6.2.3 Comparison between theoretical and dynamic mass densities

The absolute values of the dynamic mass densities, estimated on the steel/soft core/steel sandwich using the two strategies discussed in the previous section, are compared in Fig. 6.9. We could see that the anti-symmetric mass density ($\breve{\rho}_{\mathrm{A}}$) is almost constant and close to the theoretical mass density ($\rho_{\mathrm{eq}}$) for the full frequency range. At low frequencies, the symmetric mass density ($\overline{\rho}_{\mathrm{S}}$) decreases and reaches its minimum value at the breathing frequency, after which, it increases again and reaches the theoretical mass density at higher frequencies. Although the two different strategies yield similar results of the symmetric mass density, few differences are observed at higher frequencies. Since the mass-spring-mass assumption do not consider the higher-order modes of the symmetric motion, this method produces a slight deviation in the symmetric mass density when it is compared to the TMM strategy.

## 6.3 Validation cases of the advanced condensed model

In this section, two sandwich configurations with soft elastic core and poro-elastic core are taken for the purpose of validating the condensed model. As explained earlier, for any symmetric multi-layer configurations, the dynamic bending stiffness $\widetilde{D}_{\mathrm{eq}}$ is computed from any equivalent plate models. The remaining two mass densities, $\breve{\rho}_{\mathrm{A}}$ and $\overline{\rho}_{\mathrm{S}}$, are computed from any of the two strategies discussed in Section 6.2.2. It may be recalled that these three dynamic parameters do not depend on the incident angle, and therefore they are intrinsic parameters of the studied multi-layer structure. In the following validation cases, the TL values of the sandwich structures are calculated for the diffuse field excitation.

For the sandwich made of steel/soft elastic solid/steel layers, the TL computed from the condensed models and TMM (considered as the reference) are presented in Fig. 6.10. It is observed that both strategies correctly captures the compressional and coincidence frequencies. While the first strategy is in high agreement with the reference at all frequencies, the second approach (mass-spring-mass at normal incidence) starts to deviate after the coincidence frequency, as it does not account for the higher-order resonances. Further, the TL contributions from symmetric and anti-symmetric motions are also plotted in Fig. 6.10. This reveals that both contributions need to be considered together to compute the TL accurately.

| Acoustic properties (JCA model) | |
|---|---|
| Open porosity $\phi$ (-) | 0.97 |
| Airflow resistivity $\sigma$ (N.s.m$^{-4}$) | 50 000 |
| Viscous characteristic length $\Lambda$ ($\mu$m) | 60 |
| Thermal characteristic length $\Lambda'$ ($\mu$m) | 160 |
| High frequency limit of the tortuosity $\alpha_\infty$ (-) | 1.1 |

Table 6.2: Acoustic properties of the polyurethane layer. Elastic properties of polyurethane layer are the soft layer properties listed in Table 6.1.

In the second validation case, the soft elastic solid core is replaced by a poro-elastic material (polyurethane) and its acoustical properties are assumed to be described by the Johnson-Champoux-Allard [143, 144] model for the visco-thermal dissipation. It may

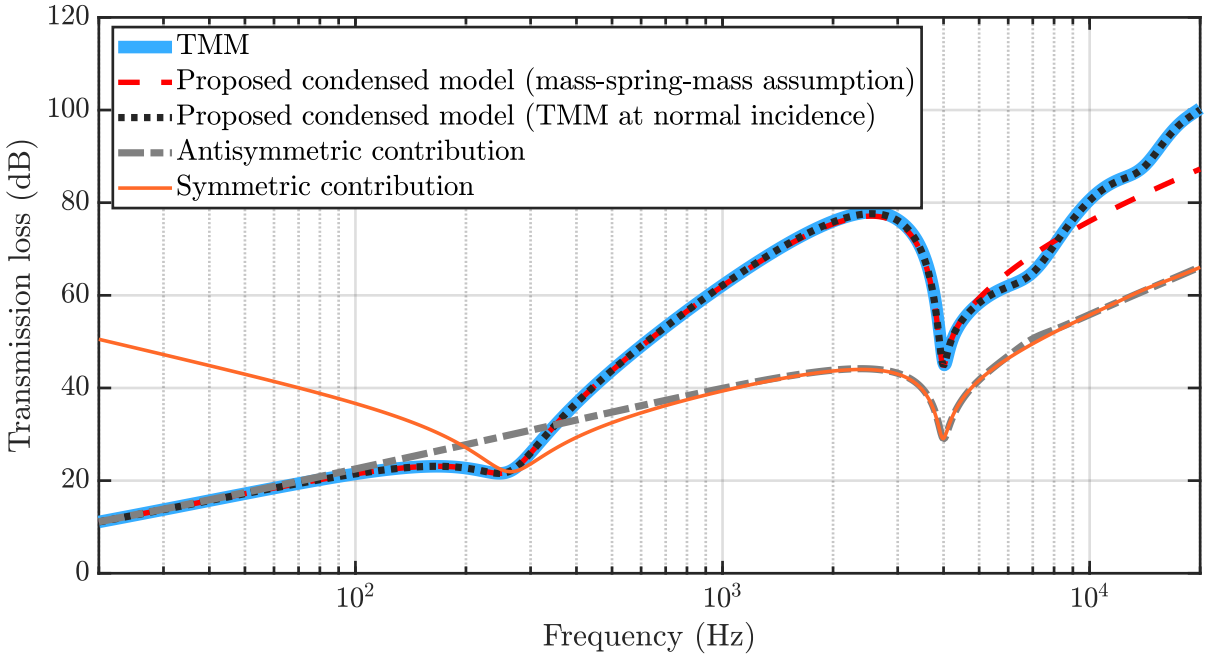


Figure 6.10: Transmission loss of the steel (3 mm)/soft core (3 mm)/steel (3 mm) sandwich estimated using the TMM and new condensed model for the diffuse field excitation. Material properties are listed in Table 6.1.

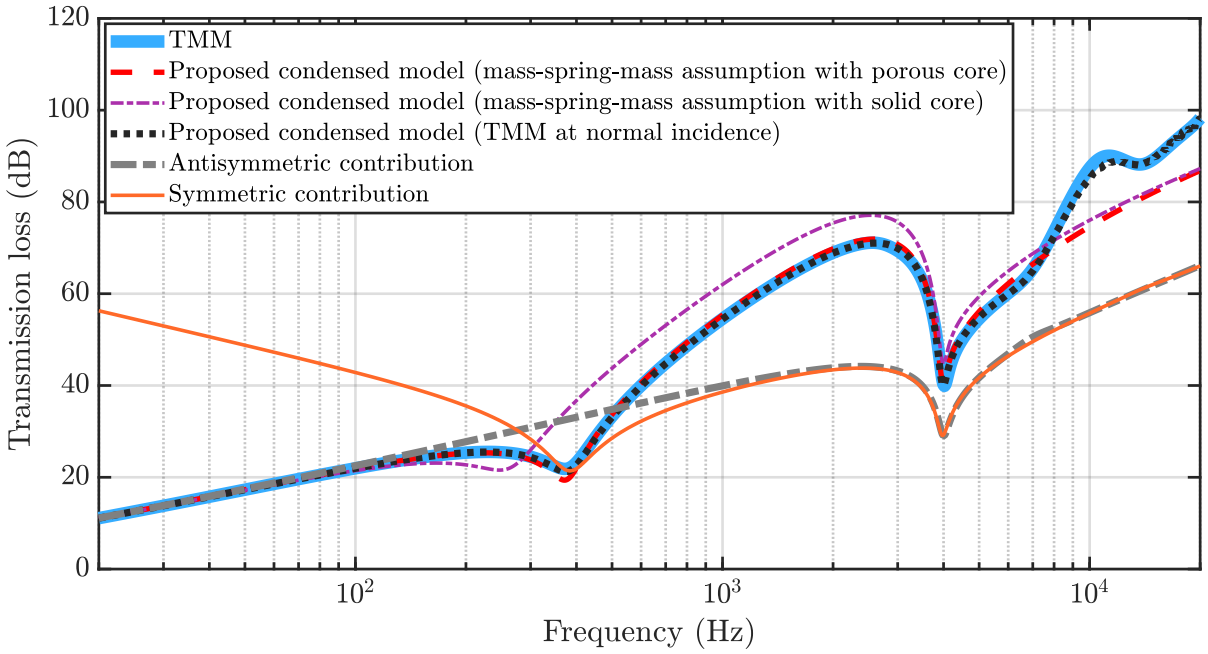


Figure 6.11: Transmission loss of the steel (3 mm)/polyurethane (3 mm)/steel (3 mm) sandwich estimated using the TMM and new condensed model for the diffuse field excitation. Material properties are listed in Tables 6.1 and 6.2.

be noted that different porous models can be used to correctly describe the dissipation mechanisms of the porous material. Section 3.3 of this manuscript may be referred to look for the different porous models used in the literature. Table 6.2 lists these acoustical properties of the polyurethane material. For this sandwich structure, the TL plot given in Fig. 6.11 shows the similar correspondences that were described previously for the sandwich structure with soft elastic core. It is also observed that the mass-spring-mass strategy results in poor results when the core is considered only elastic (i.e, only elastic properties are considered and acoustic properties are ignored) but gives much better correspondence with the TMM when the core is considered as poro-elastic (i.e, both elastic and acoustic properties are considered).

A few additional remarks may be noticed as well. Since the dynamic bending stiffness ($\widetilde{D}_{\mathrm{eq}}$) is computed from the existing condensed/equivalent plate models, it is independent of the acoustical properties of the multi-layer structures. If the multi-layer is symmetric, the equivalent mass densities presented in this chapter are still valid irrespective of the nature of layers in the structure. But the equivalent bending stiffness needs to be computed correctly, which depend on the nature of the layers and bonding conditions. For example, in a double-wall partition case where the nonhomogeneous core layer is typically not bonded to the skins, the equivalent bending stiffness is controlled by the skins and thus, the condensed model is still applicable for this multi-layer configuration. In case of orthotropic layers, the model by Marchetti et al. [139] can be used to compute the equivalent bending stiffness. Combining this bending stiffness with the two equivalent mass densities provided in this chapter, one would still be able to compute the vibroacoustic quantities. Further, the breathing frequency and its higher-order modes may vary with respect to the angle of incidence if the multi-layer structure comprises layers with low resistivity ($\sigma < 1000$ N s m$^{-4}$). Therefore, the proposed model may not be suitable for these low resistivity values.

## 6.4 Conclusion

In this chapter, a condensed model for a physically symmetric multi-layer that considers both anti-symmetric and symmetric motions is developed. The admittances of two equivalent thin plates are used to characterize both motions independently. The anti-symmetric (primarily bending, shearing) and symmetric (compressional or dilatational) motions may be represented by three intrinsic properties: a dynamic bending stiffness, which corresponds to the equivalent parameter found from the existing condensed/equivalent plate models, and two dynamic mass densities. In order to find the dynamic mass densities, two alternative techniques are established. The first describes the system's breathing frequency and resonances using the TMM method at normal incidence. In comparison to complete multi-layer modelling with the TMM in diffuse field, this approach, which may be used with any kind (fluid, solid and poro-elastic) and number of layers, produces excellent results. The multi-layer excited at normal incidence is described as a mass-spring-mass system in the second method. This technique provides a straightforward explanation of the breathing frequency while ignoring higher-order resonances. Using the dynamic intrinsic properties of the developed condensed model, the transfer matrix connecting the pressure and velocity on both sides of the multi-layer may be calculated at various angles of incidence. Finally, the suggested condensed model provides an accurate calculation of the transmission loss while simultaneously characterizing the structure anti-symmetric and symmetric motions.

In the next chapter, the developed condensed model will be used in a finite element framework as the initial application of this research. Using the identified dynamic intrinsic properties, a new finite element approach will be formulated to characterize the anti-symmetric and symmetric motions of the multi-layer structure.

# Chapter 7

# Condensed finite element scheme for thick symmetric multi-layer structures

One of the main aspects of the condensed models is to reduce the computational effort during Finite Element (FE) simulations of vibro-acoustic problems. As the condensed models fill in the natural response of a multi-layer system into a single layer with dynamically varying mechanical properties, they result in less number of degrees of freedom in the FE setup. Due to this, the overall computational time required to complete a simulation will be much less with condensed model properties, than the conventional three-dimensional FE approaches that are discussed in Chapter 2. In the previous chapter, a condensed model that includes both anti-symmetric and symmetric motions of thick symmetric multi-layer structures is presented. In line with this, the main objective of the present chapter is to develop a FE framework to implement this condensed model. One may understand from the previous chapter that the symmetric and anti-symmetric motions are decoupled for the physically symmetric multi-layers and therefore, the new condensed model allows condensing the structure into two equivalent thin plate models, corresponding to symmetric and anti-symmetric motions. This important takeaway is

considered to be the foundational information for the development of the condensed FE scheme presented in this chapter.

**Note**

Contents presented in this chapter has been submitted as an original article for review [184]:

> **Arasan, U.**, Sreekumar, A., Chevillotte, F., Triantafyllou, S. P., Chronopoulos, D., Gourdon, E. (2021). "Condensed finite element scheme for symmetric multi-layer structures including dilatational motion". Submitted to the *Journal of Sound and Vibration*.

Regarding the contributions made to the above-mentioned article, the author of this thesis has done the following tasks: methodology, investigation, implementation, validation, article writing and review.

The chapter is divided into two major sections. In the first section, the plate and shell element schemes are reviewed and a condensed FE scheme is proposed to include both symmetric and anti-symmetric motions of the multi-layer system. Secondly, three multi-layer cases (including a structure with poro-elastic layers) are chosen to compare the results of the proposed approach against the TMM and conventional 3D FE approaches.

## 7.1 Proposal of the finite element scheme for the condensed model

In this section, the Finite Element (FE) scheme for the condensed model, discussed in Chapter 6, is described. As most of the condensed models are based on the equivalent Love-Kirchhoff plate theory [96, 163], thin plate elements are suitable to model the condensed layer of the multi-layer structure for the FE computations. Due to its complexities involved in the thin plate FE implementation (as it requires dedicated higher-order polynomial shape functions with respect to order of the element), other elements such as thick

plate/shells are also investigated with necessary modifications to retrieve the thin plate behaviour.

### 7.1.1 Plate and shell elements

In order to study the effects due to different plate/shell element formulations, two types of plate elements are chosen in this section: 1) Love-Kirchhoff (thin) plate elements and 2) Reissner-Mindlin (thick) plate elements.

#### Thin plate elements

For thin plate elements, three degrees of freedom per node are assumed: the normal displacement ($w_n$) and the two rotations ($\theta'_x$ and $\theta'_y$). Unlike Reissner-Mindlin plates, the two rotations are coupled to the normal displacement under the Kirchhoff's hypothesis as follows:

$$\theta'_x = \frac{\partial w_n}{\partial x}; \quad \theta'_y = \frac{\partial w_n}{\partial y}. \tag{7.1}$$

One may refer to Eq. (2.11) for the displacement field of Love-Kirchhoff plates. Due to the relations given in Eq. (7.1), the Love-Kirchhoff plate is characterized by the single displacement ($w_n$) which leads to the advantage of having less challenges than the Reissner-Mindlin plate, in deriving the governing equations.

On the contrary, it possesses extra difficulty in FE implementation due to the necessity to satisfy continuity requirements for the normal displacement ($w_n$) and its derivatives, as it requires the computation of fourth-order derivatives to calculate the element matrices. Therefore, 3 dofs (normal displacement and two rotations) per node are still required for thin plate implementation. Additionally, a $C^1$ continuity (displacement and slope continuity ensured) has to be considered for thin plate elements. Since there are 12 unknowns (4 nodes $\times$ 3 dofs) for a first order element, a quartic polynomial is assumed for the normal displacement. A detailed derivation for the element matrices of this type of thin plate element can be found in [185, 186] with the shape functions derived by Melosh [187]. It may be noted that for higher order elements (8-nodes or higher), the formulation

and derivation of element matrices become cumbersome and not straightforward, as the Lagrange or isoparametric shape functions cannot be used for thin plate elements.

**Thick plate elements**

In case of moderately thick plates, the shear deformation also contributes along with the bending deformation to the resulting motion of the plate. Therefore, Reissner-Mindlin theory [97–99] decoupled the rotations and lateral deflections by introducing the shear deformations. Due to this reason, Eq. (7.1) is not valid for thick plates. This provides an advantage of using $C^0$-continuity (continuity ensured only on the nodal variable and not necessarily on its derivatives) plate element with 3 dofs per node ($w_n, \theta'_x$ and $\theta'_y$). Further, this allows in using the isoparametric concept into the analysis of moderately thick plates, which results in developing 4-node and 8-node quadrilateral plate bending elements without much difficulty.

The element stiffness matrix for the thick plate elements consists of both bending and shear contributions as follows:

$$[K^e]_{\text{plate}} = [K^e]_{\text{bending}} + [K^e]_{\text{shear}}. \tag{7.2}$$

Although this type of plate element provides appreciable results for moderately thick plates, they behave erratically in case of thin plates due to excessive influence of terms corresponding to transverse shear deformation. It is well observed in the literature [188–192] that the thick plate elements become stiffer when the plate is relatively thin. This is due to having spurious shear strains arising from the thick plate element formulation, which should not be appearing as per Kirchhoff's assumptions for thin plates. This situation is referred to as 'shear locking' in the literature, and it could be avoided by employing a reduced integration scheme on the shear stiffness matrix ($[K^e]_{\text{shear}}$). For the first order element, Hughes et al. [189] have shown the use of one-point integration for the computation of shear stiffness matrix and $2 \times 2$ integration for bending stiffness matrix, and it is observed that the element behaves well even for the thin plate situations. It is

also observed that the 'shear locking' could be avoided if higher-order thick plate element is used.

**Shell elements**

Thin structures that carry loads in all directions (for example, lightweight structures like aircraft fuselages) experience bending, shear, twisting along with membrane or in-plane deformations. This kind of structures are commonly called as shell structures and shell elements need to be employed for modelling these structures to handle all types of possible deformations. Shell elements are commonly applied to model the structures with curved geometry. Since this type of elements needs to handle various types of motions and curvature effects, this often results in more complexities for the formulation as well as implementation. Due to these challenges, a more popular approach to model the shell structures is to use a series of flat shell elements that is simpler and easier to implement.

Flat shell elements are constructed simply by combining the plate elements and membrane elements, which results in 6 dofs per node ($u, v, w, \theta'_x, \theta'_y$ and $\theta'_z$).

$$[K^e]_{\text{flat shell}} = \begin{bmatrix} [K^e]_{\text{membrane}} & 0 & 0 \\ 0 & [K^e]_{\text{plate}} & 0 \\ 0 & 0 & \epsilon' \end{bmatrix}, \tag{7.3a}$$

$$[M^e]_{\text{flat shell}} = \begin{bmatrix} [M^e]_{\text{membrane}} & 0 & 0 \\ 0 & [M^e]_{\text{plate}} & 0 \\ 0 & 0 & 0 \end{bmatrix}. \tag{7.3b}$$

It may be noted that membrane terms correspond to the in-plane displacements degrees of freedom and plate terms correspond to degrees of freedom for transverse displacement and rotations. In case of modelling the curved structures with flat shell elements, each element will have stiffness and mass element values computed with its local coordinate system. Since the normal direction of an element might be different from that of the

other element, for the purpose of assembling the matrices, the stiffness and mass values need to be transformed to global coordinate system. Therefore, the degrees of freedom corresponding to the out of plane rotation also needs to be added in the element matrices (as seen in Eq. (7.3)) and a fictitious stiffness value ($\epsilon'$) is added to avoid the singularity during the solving process.

Like Reissner-Mindlin plate elements for thin structures, it is observed that the Reissner-Mindlin shell elements also exhibit shear locking effect in thin shell structures. Furthermore, they display membrane locking as well that significantly affects the nodal solution [192]. Recently, Pillai et al. [193] developed a shell element of degenerated solid type (MITC4+ elements) to overcome these locking effects.

### 7.1.2 Selection of the element type for the condensed model

Since the condensed models assume the condensed layer as a Love-Kirchhoff plate, it is necessary to use the element types which support the Love-Kirchhoff hypothesis. Thin plate and shell elements are the candidates which satisfy these conditions inherently, due to the assumptions involved in their formulation, but they also add some complexities during the implementation compared to other element types. For example, it is simpler and straightforward to implement Reissner-Mindlin plate/shell elements than the Love-Kirchhoff elements, especially when higher-order elements need to be used. It is due to the reason that the classical isoparametric shape functions can be used for thick plates but not for the thin plates. Further, the Reissner-Mindlin plate/shell elements could also be used to simulate thin plate behaviour, by applying the penalty factor only on the shear modulus and by lowering the erroneous results due to shear locking through reduced order integration on shear terms for 1st order elements.

| | Aluminium | Shear layer | Plasterboard | Soft layer | Glasswool |
|---|---|---|---|---|---|
| $\rho$ (kg m$^{-3}$) | 2700 | 200 | 700 | 55 | 18 |
| $E$ (Pa) | $70\times10^9$ | $0.1\times10^9$ | $3\times10^9$ | $4.3\times10^4$ | $3\times10^3$ |
| $\nu$ | 0.3 | 0.33 | 0.33 | 0.4 | 0.21 |
| $\eta$ | 0.08 | 0.5 | 0.08 | 0.3 | 0.1 |

Table 7.1: Elastic properties of the layers used in this chapter.

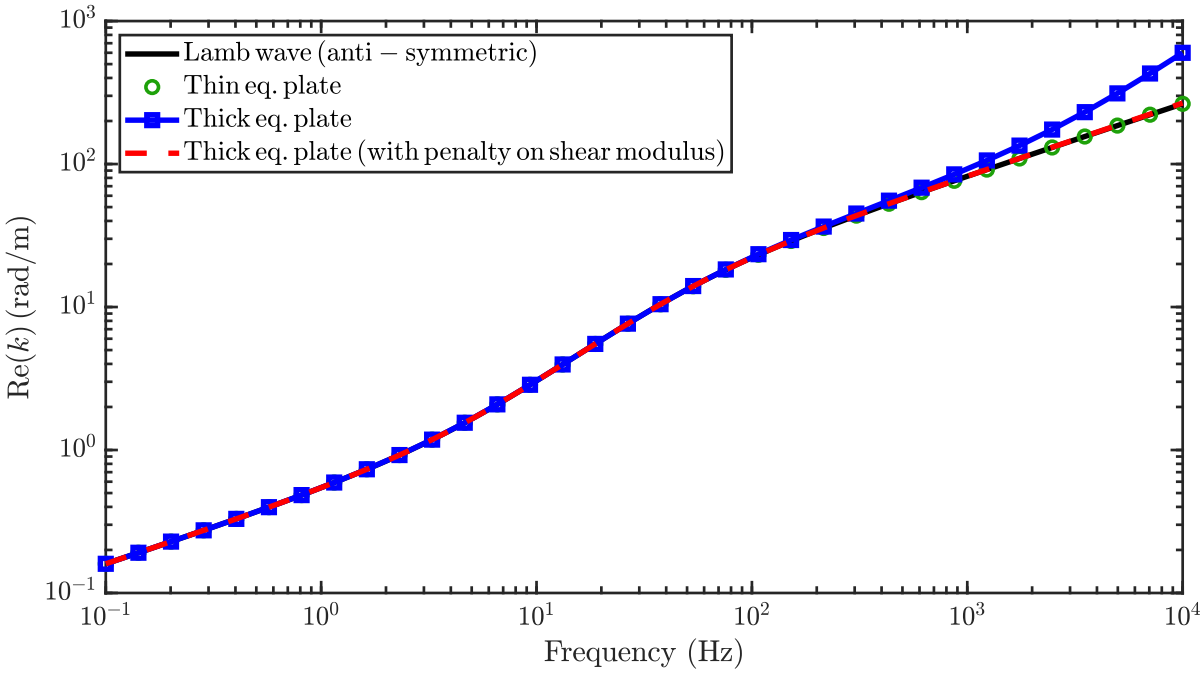


Figure 7.1: Natural propagating wavenumbers for aluminium (5 mm)/shear layer (15 mm)/aluminium (3 mm) sandwich structure of infinite extent (material properties can be referred from Table 7.1). Equivalent plate properties are computed from Guyader's model [131]. The penalty factor is chosen as $\vartheta = 100$.

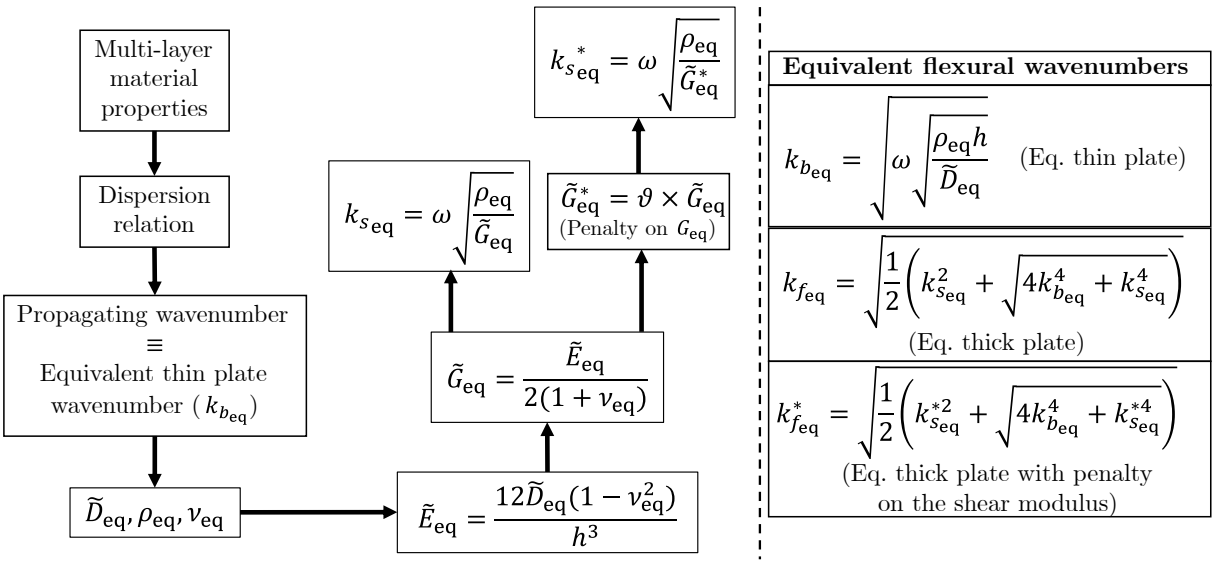


Figure 7.2: Schematic representation for computing equivalent wavenumbers from thin and thick plate theories.

For the purpose of illustrating this particular point, the propagating wavenumber for a three-layer aluminium (5 mm)/shear layer (15 mm)/aluminium (3 mm) sandwich (with properties mentioned in Table 7.1), computed from the anti-symmetric condensed plate model, is compared against the anti-symmetric Lamb wave solution (Fig. 7.1). Guyader's model [131] is chosen here to compute the equivalent bending wavenumber, and it is seen that the Guyader's model is in high agreement with the Lamb wave solution. One may recall from Chapter 5 that the propagating wavenumber of a three-layer sandwich system comprises three zones controlled by: 1) global bending, 2) core shear, and 3) inner bending. The dynamic properties are then used to recompute the response using thin and thick plate theories, with and without the penalty on the shear modulus, as shown in Fig. 7.2. The idea of the penalty procedure is to remove the shear contribution from the frequency range of interest and to keep only the equivalent bending contribution (see Figs. 4.4 and 5.2a).

The efficiency of the penalty procedure can be checked from the dispersion curve observation. It is seen from Fig. 7.1 that the wavenumber computed from thick plate theory matches with that of the Lamb wave and thin equivalent plate models, in the zones controlled by global bending and core shear, but has poor match with the zone controlled by inner bending. Further, it is also observed that the thick equivalent plate wavenumber computed with penalty on the shear modulus is in good agreement with the wavenumbers from the Lamb wave and thin equivalent plate models. It is worth to mention that, practically, this can be achieved with the penalty factor $\vartheta = 100$ for most of the multi-layer configurations. Similarly, this penalty factor ($\vartheta$) is applied to the shear stiffness matrix of the thick plate element in the FE scheme as,

$$[K^e]_{\text{plate}} = [K^e]_{\text{bending}} + \vartheta[K^e]_{\text{shear}}. \tag{7.4}$$

It may be noted that this value for the penalty factor is sufficient to reduce the effect of shear in the thick plate elements while avoiding ill-conditioning of the stiffness matrices. As a result, it can be seen from Fig. 7.3 that the transmission loss (for a plasterboard of

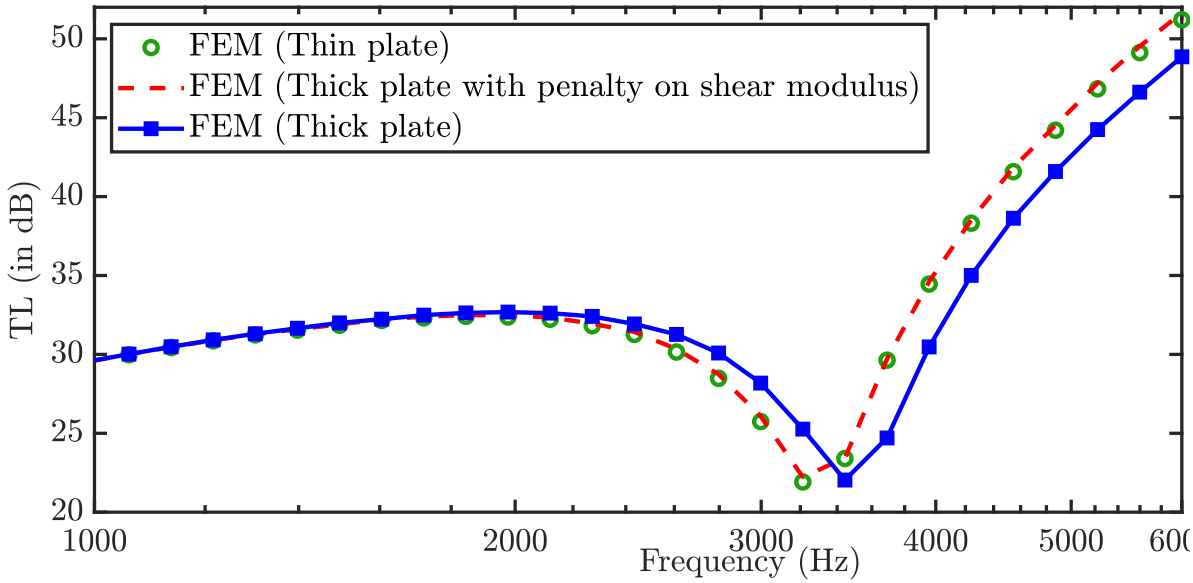


Figure 7.3: Transmission loss computed from FEM using thin and thick plate elements for the plasterboard of 12.5 mm under oblique plane wave incidence of 60°. Material properties can be referred from Table 7.1.

12.5 mm under 60° plane wave incidence) computed from the thick plate elements with penalty factor corresponds well to that obtained from the thin plate elements.

| Acoustic properties | |
|---|---|
| Open porosity $\phi$ (-) | 0.96 |
| Airflow resistivity $\sigma$ (N.s.m$^{-4}$) | 11500 |
| Viscous characteristic length $\Lambda$ ($\mu$m) | 108 |
| Thermal characteristic length $\Lambda'$ ($\mu$m) | 138 |
| High frequency limit of the tortuosity $\alpha_\infty$ (-) | 1.01 |
| Static thermal permeability $k_0'$ (m$^2$) | $4 \times 10^{-9}$ |

Table 7.2: Acoustic properties (JCAL model) of the glasswool layer used in this chapter.

Since the thick plate element with penalty on the shear modulus matches response with that of the thin plate element and as it is simpler and easier for FE implementation, it is practical to use this element for the condensed layer to compute the response of the multi-layer system. It is recalled that a thin plate formulation is required, since the equivalent bending stiffness $\widetilde{D}_{\text{eq}}$ is computed according to this model. Additionally, as the scope of this chapter is limited to planar structures, the membrane effects would be negligible. Thus, the use of shell elements is unnecessary at this stage, and it is time-consuming due to 6 degrees of freedom per node whereas the thick plate element requires

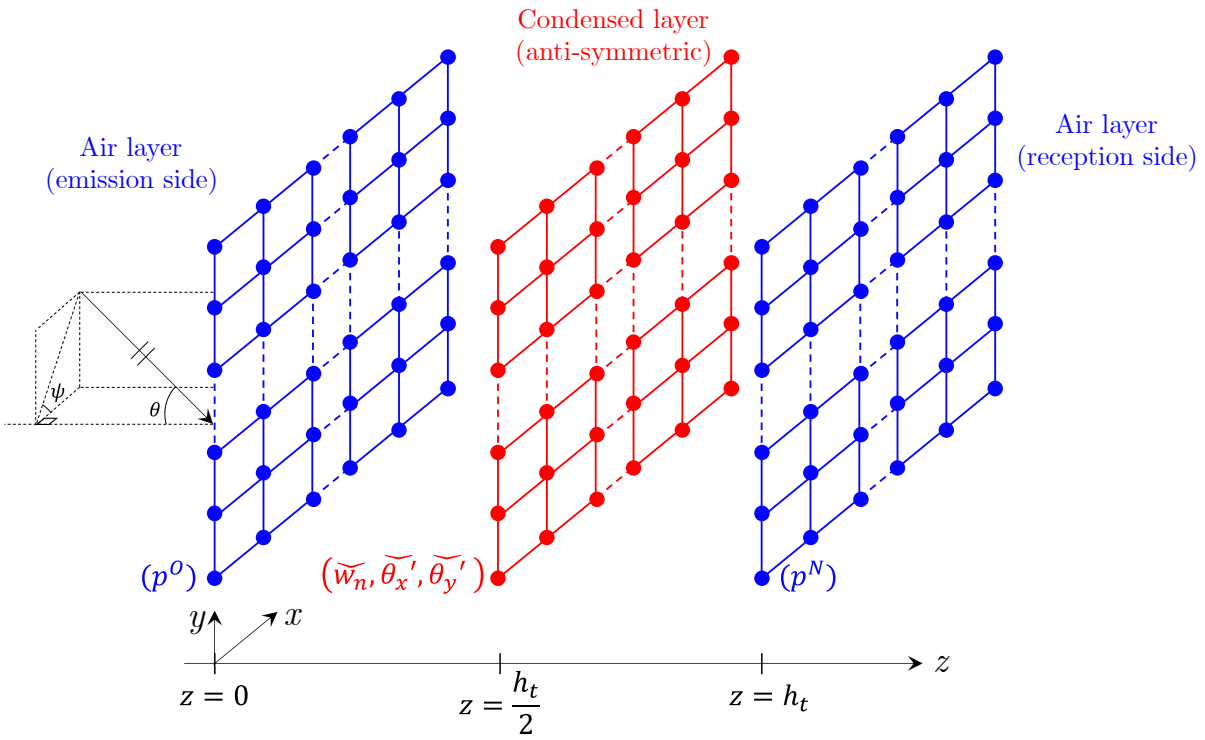


Figure 7.4: Schematic representation of the meshed layers to compute the sound transmission loss of a planar multi-layer structure (represented as anti-symmetric condensed layer).

only 3 degrees of freedom per node.

### 7.1.3 Finite element equations to compute vibro-acoustic quantities of multi-layer structures

#### Finite element matrices for condensed model with anti-symmetric motion

As many of the condensed models consider only the anti-symmetric motions (bending and shear) of the multi-layer structure to provide dynamic or equivalent properties, the stiffness and mass matrices of the condensed layer are written in terms of these equivalent properties. Fig. 7.4 shows the schematic representation of the meshed layers of the FE setup with an anti-symmetric condensed plate. The global matrices to solve for the acoustic problem with this condensed plate are,

$$[K] = [\breve{K}] = [K(\widetilde{D}_{\text{eq}})], \quad [M] = [\breve{M}] = [M(\rho_{\text{eq}})], \tag{7.5a}$$

$$[H] = \begin{bmatrix} [H^{\mathrm{O}}] & 0 \\ 0 & [H^{\mathrm{N}}] \end{bmatrix}, \quad [Q] = \begin{bmatrix} [Q^{\mathrm{O}}] & 0 \\ 0 & [Q^{\mathrm{N}}] \end{bmatrix}, \tag{7.5b}$$

where 'O' and 'N' represent the emission and reception sides, respectively. $\{\breve{W}\} = [\breve{w}_{n1}, \breve{\theta}'_{x1}, \breve{\theta}'_{y1}, ..., \breve{w}_{nr}, \breve{\theta}'_{xr}, \breve{\theta}'_{yr}]^T, \{P\} = [p_1^O, p_2^O, ..., p_r^O, p_1^N, p_2^N, ..., p_r^N]^T$ are the nodal variables of the anti-symmetric condensed plate (solid phase) and air layer (fluid phase) respectively. The symbol $\breve{}$ on top of the variables represents the anti-symmetric contribution of the plate, $r$ denotes the number of nodes on the air/condensed layer and conformal meshing (same number of elements with same dimensions for all the layers) is used in this chapter. Finally, the generic fluid-solid interaction relation (Eq. (2.1)) presented in Section 2.2.2 is recalled here for substituting these FE matrices to obtain the nodal solution.

$$\begin{pmatrix} [K] - \omega^2[M] & -[C] \\ -[C]^T & \dfrac{[H]}{\omega^2} - [Q] \end{pmatrix} \begin{Bmatrix} \{W\} \\ \{P\} \end{Bmatrix} = \begin{Bmatrix} 0 \\ 0 \end{Bmatrix}. \tag{7.6}$$

**Acoustic loads:** Excitations can be imposed through incident pressure or displacement at the emission side of the system. In this chapter, the incident pressure field condition is applied on the emission side air layer to solve for the vibro-acoustic problem:

$$p^O = \overline{p} e^{-\mathrm{i}k_0(x \sin\theta \cos\psi + y \sin\theta \sin\psi + z \cos\theta)}, \tag{7.7}$$

where the superscript '$O$' represents the emission side, $k_0 = \omega/c_0$ is the wavenumber in air, $\theta$ is the incident angle and $\psi$ is the azimuthal angle of the incident wave measured from the $x-$axis. If the emission side air layer is placed at $z = 0$ and $\psi = 0$, then the incident pressure would simply be,

$$p^O = \overline{p} e^{-\mathrm{i}k_0 x \sin\theta}. \tag{7.8}$$

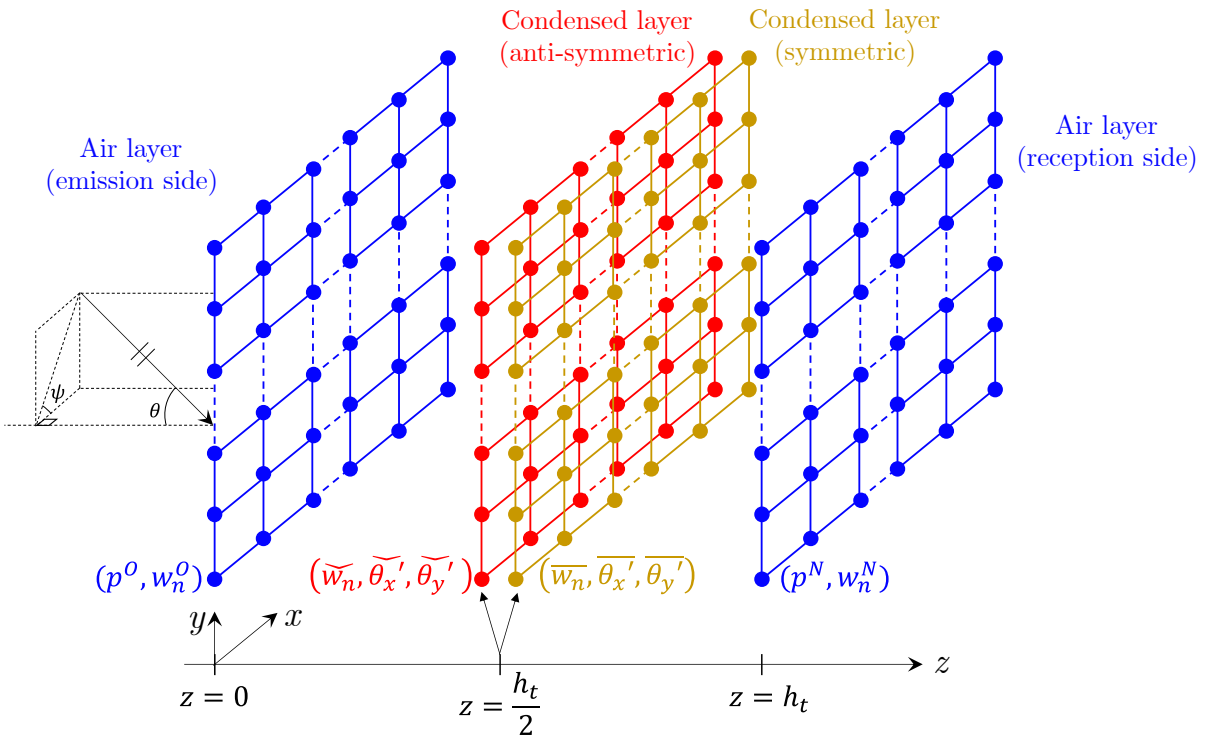


Figure 7.5: Schematic representation of the meshed layers to compute the sound transmission loss of a planar multi-layer structure (represented as two parallel condensed layers).

### Finite element equation for a thick symmetric multi-layer structure

In this section, the modified form of the FE equation (Eq. (7.6)) is proposed to couple two fluid domains with a condensed layer including both anti-symmetric and symmetric motions. In this approach, two thin (plate or shell) layers are used to represent the anti-symmetric and symmetric motion of the multi-layer structure respectively (as shown in Fig. 7.5), with the dynamic properties obtained from the condensed model presented in Chapter 6. While the nodal variables of anti-symmetric layer are denoted with $\breve{}$ symbol on top, the symmetric layer nodal variables are represented with a bar symbol $\bar{}$. According to Dym and Lang [155], the displacements corresponding to symmetric and anti-symmetric motions respectively, of a physically symmetric multi-layer can be defined as,

$$\overline{w}_n = \frac{w_n^N - w_n^O}{2}; \quad \breve{w}_n = \frac{w_n^N + w_n^O}{2}, \tag{7.9a}$$

$$\Rightarrow w_n^O - \breve{w}_n + \overline{w}_n = 0; \quad w_n^N - \breve{w}_n - \overline{w}_n = 0, \tag{7.9b}$$

where $w_n^O$ and $w_n^N$ are the normal displacements of the fluid-solid interfaces at points 'O' and 'N' respectively. Note that the above equations are retrieved from Eqs. (3.76) and (3.77).

In the FE setup, two decoupled plates (correspond to symmetric and anti-symmetric motions) are meshed at the mid-position of the multi-layer structure (as shown in Fig. 7.5). The coupling between these two plates can be made through Eq. (7.9) and for this purpose, the pressure variables are split into two vectors as,

$$\{P\} = \begin{Bmatrix} \{P^O\} \\ \{P^N\} \end{Bmatrix} \tag{7.10}$$

. By rewriting the pressure vector as above, two types of coupling matrices are defined to satisfy the conditions given by Eq. (7.9). Referring to Eq. (2.7),

$$\begin{aligned} \int_\Gamma w_n^O \delta p^O \,\mathrm{d}\Gamma &= \int_\Gamma (\breve{w}_n - \overline{w}_n)\delta p^O \,\mathrm{d}\Gamma = \int_\Gamma \breve{w}_n \delta p^O \,\mathrm{d}\Gamma - \int_\Gamma \overline{w}_n \delta p^O \,\mathrm{d}\Gamma \\ &\approx \{P^O\}^T[C]\{\breve{W}\} - \{P^O\}^T[C]\{\overline{W}\} \end{aligned} \tag{7.11}$$

$$\begin{aligned} \int_\Gamma w_n^N \delta p^N \,\mathrm{d}\Gamma &= \int_\Gamma (\breve{w}_n + \overline{w}_n)\delta p^N \,\mathrm{d}\Gamma = \int_\Gamma \breve{w}_n \delta p^N \,\mathrm{d}\Gamma + \int_\Gamma \overline{w}_n \delta p^N \,\mathrm{d}\Gamma \\ &\approx \{P^N\}^T[C]\{\breve{W}\} + \{P^N\}^T[C]\{\overline{W}\} \end{aligned} \tag{7.12}$$

Then, the global FE equation in Eq. (7.6) is modified as shown below :

$$\begin{bmatrix} [\breve{K}] - \omega^2[\breve{M}] & [0] & -[C] & -[C] \\ [0] & [\overline{K}] - \omega^2[\overline{M}] & [C] & -[C] \\ -[C]^T & [C]^T & \dfrac{[H^O]}{\omega^2} - [Q^O] & [0] \\ -[C]^T & -[C]^T & [0] & \dfrac{[H^N]}{\omega^2} - [Q^N] \end{bmatrix} \begin{Bmatrix} \{\breve{W}\} \\ \{\overline{W}\} \\ \{P^O\} \\ \{P^N\} \end{Bmatrix} = \begin{Bmatrix} 0 \\ \vdots \\ 0 \end{Bmatrix}, \tag{7.13}$$

where $\{\overline{W}\} = [\overline{w}_{n1}, \overline{\theta}'_{x1}, \overline{\theta}'_{y_1}, ..., \overline{w}_{nr}, \overline{\theta}'_{xr}, \overline{\theta}'_{y_r}]^T$ are the nodal variables of the symmetric con-

densed plate and $\{w_n\} = [w^O_{n1}..., w^O_{nr}, w^N_{n1}, ..., w^N_{nr}]^T$ are nodal variables of the fluid layers at points 'O' and 'N' respectively. As per the condensed model presented in Chapter 6, the stiffness matrices of the anti-symmetric and symmetric condensed plates are equal i.e, $[\breve{K}] = [\overline{K}] = [K(\widetilde{D}_{\text{eq}})]$, but the mass matrices of these two plates are defined by the two dynamic mass densities as,

$$[\breve{M}] = [M(\breve{\rho}_A)]; \quad [\overline{M}] = [M(\overline{\rho}_S)]. \tag{7.14}$$

Finally, after solving the above finite element system, the transmission loss of the structure is computed as follows:

$$\text{TL} = 10 \log_{10} \left( \frac{\Pi_{Oi}}{\Pi_N} \right), \tag{7.15}$$

where $\Pi_{Oi} = \dfrac{1}{2} p^2_{\text{inc}} \dfrac{\cos\theta}{Z_0}$ is the incident power and the incident pressure ($p_{\text{inc}}$) is computed as, $p_{\text{inc}} = p^O/(1+R)$. The reflection coefficient ($R$) can be computed using the Eq. (3.57). The outlet power is computed using the relation, $\Pi_N = \dfrac{1}{2} \Re(p^N v^N_*)$ where $p^N$ and $v^N_*$ are the pressure and conjugate velocity at the outlet.

### 7.1.4 Summary of the proposed FE scheme

This section summarizes the key points of the proposed FE setup to solve the vibro-acoustic problem of a thick symmetric multi-layer structure. Fig. 7.6 lays out the generic flow of the FE procedure along with two different approaches (i.e, condensed model and classical 3D elements approaches) that are used to mesh the multi-layer structure.

In 3D elements approach, the minimum wavelength ($\lambda_{\text{min}}$) may be computed from two ways: 1) for the coarse mesh, $\lambda_{\text{min}}$ is from the wavelength of incident air and 2) for the fine mesh, $\lambda_{\text{min}}$ is from the wavelength set comprised of all possible waves that could propagate inside each layer of the multi-layer structure and the incident wavelength of air. From this minimum wavelength, the element side length is determined as $\lambda_{\text{min}}/\bar{q}$ where $\bar{q}$ is the number of elements per wavelength. Each layer in the multi-layer structure is then meshed with 3D elements (hexahedral, for example).

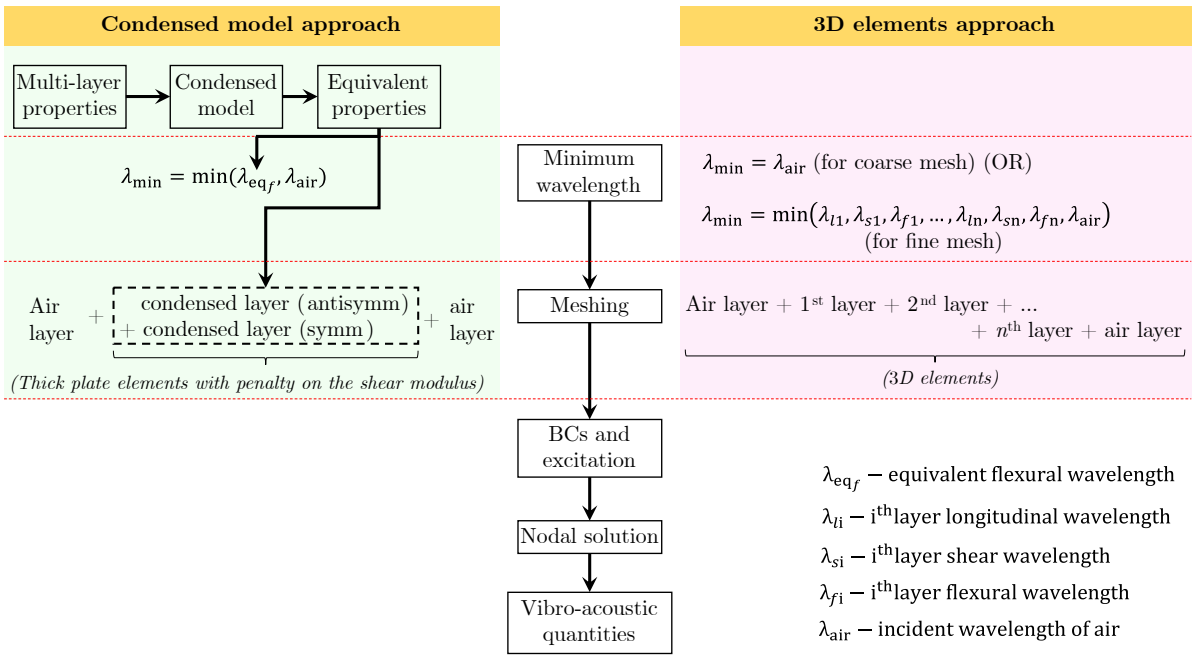


Figure 7.6: Generic flow of the FE approaches followed in this chapter.

In the proposed condensed model approach, the minimum wavelength is computed from the equivalent flexural wave and incident wave in the air. It may be noted that the equivalent flexural wavelength is characterized by the dynamic properties given by the condensed model (Chapter 6) and the minimum flexural wavelength is computed from the minimum value of $\widetilde{D}_{\text{eq}}$, that is estimated at the maximum frequency ($f_{\max}$) (see Fig. 5.3). The element side length is determined as $\lambda_{\min}/\bar{q}$, which decides the mesh characteristics of the condensed layers. In the meshing stage, unlike 3D elements approach, only two condensed layers (for symmetric and anti-symmetric motions) are meshed, whose mechanical properties are controlled by the three dynamic properties that are obtained from the condensed model. It is important to note that these anti-symmetric and symmetric condensed layers are meshed as thick plate elements with penalty on the shear modulus. Although the dynamic or equivalent properties obtained from the condensed model are obtained using thin plate theory, thin plate elements posses some challenges in terms of the FE implementation. Therefore, thick plate elements with penalty on the shear modulus are chosen to ease the implementation process without compromising the response as that of the thin plate elements (see section 7.1.2).

## 7.2 Numerical examples

Three symmetric multi-layer structures are examined to validate the proposed condensed FE approach and to compare the computational efficiency with respect to 3D FE approach. In this chapter, the FE simulations to compute the transmission loss (TL) of a given multi-layer structure is done under the following conditions: $f_{\min} = 50$ Hz, $f_{\max} = 5000$ Hz, $\bar{q} = 6$ and infinite lateral dimensions. The cross-section of the structure is $20 \times 20$ mm$^2$ and periodic boundary conditions along the lateral directions are considered to mimic the response of an infinitely extended structure. One may note that the damping of each layer is introduced in their respective Young's modulus as $E_i^* = E_i(1 + \mathrm{j}\eta_i)$. Further, for the 3D FE approach, the results are presented with the coarse mesh (according to minimum wavelength in air), since no considerable difference has been observed between both coarse and fine meshes (for the three cases discussed in this section). The TL computations from the FE simulations are done for both oblique incidence of 60° and diffuse field (with 52 number of Gauss integration points) excitations. Since planar multi-layers of infinite lateral dimensions are studied, the results from different FE simulations are compared against the reference solution given by the Transfer Matrix Method (TMM). The FE computations (in serial implementation) are done with Intel(R) Core(TM) i3-8100 processor, 3.6 GHz frequency and 8 GB RAM. The material properties of various layers used in this section can be found in Table 7.1.

### 7.2.1 Case 1: Three-layer sandwich with thin soft elastic core

A three-layer sandwich structure with skins made of plasterboard material (12.5 mm each) and a thin soft core (0.05 mm) is considered. It may be noted that as the core is thin compared to the skins, the structure would normally be controlled by the anti-symmetric motions and thus, vibro-acoustic response of this kind of structures is usually captured well by the condensed plate model of only anti-symmetric type [7, 131, 133, 156, 174] (see Section 2.5).

In the condensed FE simulations, two versions of condensed model are followed (as

| FE approach | Order | #Nodes | #Dofs | $t_{\text{oblique}}$ | $t_{\text{diffuse}}$ |
|---|---|---|---|---|---|
| Condensed | 1 | 27 | 45 | 0.2 s | 10 s |
| (Anti-symm.) | 2 | 75 | 105 | 0.4 s | 16 s |
| Condensed | 1 | 27 | 72 | 0.3 s | 13 s |
| (Anti-symm. & Symm.) | 2 | 75 | 168 | 0.5 s | 24 s |
| 3D | 1 | 54 | 180 | 1.8 s | 100 s |
| | 2 | 275 | 555 | 24.4 s | 1327 s |

Table 7.3: Computational efficiency comparison for three-layer sandwich structure with sequence: plasterboard (12.5 mm)/soft layer (0.05 mm)/plasterboard (12.5 mm) of cross-section $20\times20$ mm$^2$.

discussed in Section 7.1.3): 1) condensed FE approach with anti-symmetric motions only (for example, Guyader's model [131]) and 2) condensed FE approach with both symmetric and anti-symmetric motions (Chapter 6). Table 7.3 lists the total number of nodes, total number of degrees of freedoms on the meshed setup (see Figs. 7.4 and 7.5 for the schematic representation) along with the time required (average of five runs) for solving the system under oblique incidence and diffuse field. The TL results obtained under diffuse field from different FE approaches are compared against the reference solution from TMM in Fig. 7.7. Note that, thanks to the periodic BC, the lateral size is relatively small. Of course, the difference in terms of computational time will increase if the lateral dimension is increased.

Although the condensed FE approach with only anti-symmetric motion results in slightly mismatched response before critical frequency, it is observed that the overall predictions from both condensed FE approaches are in good agreement with the 3D FE approach and the TMM reference. This shows that the multi-layer structure under consideration is largely influenced by the anti-symmetric motions of the structure. It is also noted that the condensed FE with both motions slightly underpredicts the critical frequency. On the other hand, in the case of stiffer skins (with aluminium, steel etc.), critical frequencies are predicted well by the proposed condensed FE scheme and this may be due to neglecting rotational inertia effects of the condensed layer in the theoretical formulation, which is currently under study. On the computational efficiency side, it can be seen from Table 7.3 that the condensed FE approaches are more than 50 times faster

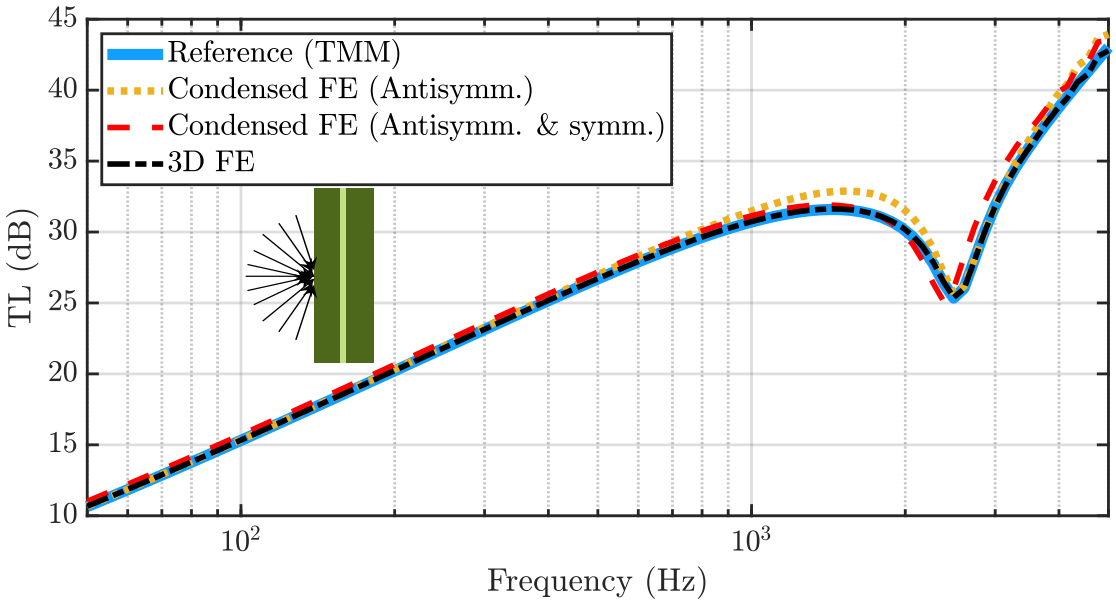


Figure 7.7: Comparison of transmission loss obtained from different FE approaches (with 2nd order elements) for the three-layer sandwich plasterboard (12.5 mm)/soft layer (0.05 mm)/plasterboard (12.5 mm) of cross section $20\times20$ mm$^2$ under diffuse field. Material properties can be referred from Table 7.1.

than the 3D FE approach in both excitation types when using 2nd order elements. For the same mesh, though the first order elements (from all three FE approaches) predict the correct critical and breathing frequencies, they do not provide well-matched results when compared to second order elements. Therefore, in this chapter, TL computations are presented only from second order elements.

### 7.2.2 Case 2: Three-layer sandwich with thick soft elastic core

Fig. 7.8 shows the TL response of the above discussed three-layer sandwich structure if the core thickness is increased from 0.05 mm to 3 mm.

It is observed that as the core thickness increases, the symmetric motion or the compressional motion of the structure also governs the resulting response of the structure after the mass law, along with anti-symmetric motions. The so-called breathing frequency, due to the mass-spring-mass resonance, is clearly seen around 400 Hz. Fig. 7.8 shows that this behaviour is not captured by the condensed plate model only with anti-symmetric motion, although it correctly predicts the value of the critical frequency of the structure.

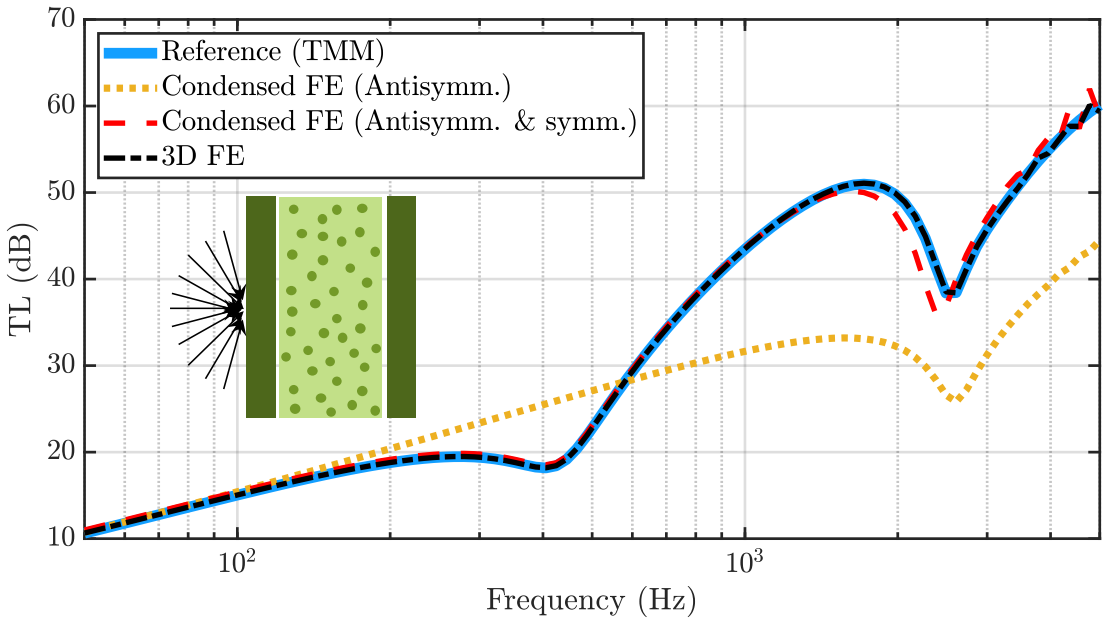


Figure 7.8: Comparison of transmission loss obtained from different FE approaches (with 2nd order elements) for the three-layer sandwich plasterboard (12.5 mm)/soft layer (3 mm)/plasterboard (12.5 mm) of cross-section 20×20 mm$^2$ under diffuse field. Material properties can be referred from Table 7.1.

| FE approach | Order | #Nodes | #Dofs | $t_{\text{oblique}}$ | $t_{\text{diffuse}}$ |
|---|---|---|---|---|---|
| Condensed | 1 | 27 | 45 | 0.5 s | 10 s |
| (Anti-symm.) | 2 | 75 | 105 | 0.4 s | 16 s |
| Condensed | 1 | 27 | 72 | 0.3 s | 13 s |
| (Anti-symm. & Symm.) | 2 | 75 | 168 | 0.5 s | 27 s |
| 3D | 1 | 54 | 180 | 1.9 s | 93 s |
| | 2 | 275 | 555 | 24.3 s | 1352 s |

Table 7.4: Computational efficiency comparison for three-layer sandwich structure with sequence: plasterboard (12.5 mm)/soft layer (3 mm)/plasterboard (12.5 mm) of cross-section 20×20 mm$^2$. Material properties can be referred from Table 7.1.

The condensed FE approach with both anti-symmetric and symmetric motions is in good agreement with 3D FE solution and the TMM reference (except slight underprediction of the critical frequency). The high frequency oscillations in TL can be reduced if the number of Gauss integration points are increased, but at the cost of increasing the computational time for the diffuse field excitation.

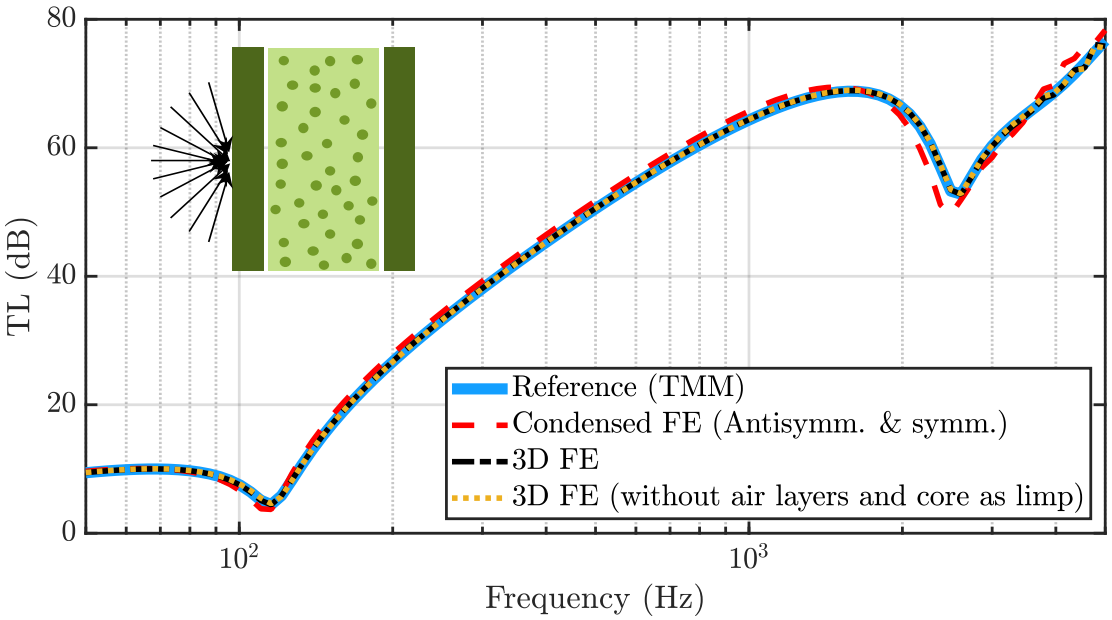


Figure 7.9: Comparison of transmission loss obtained from different FE approaches (with 2nd order elements) for the double-wall partition structure with sequence: plasterboard (12.5 mm)/air (1.5 mm)/glasswool (45 mm)/air (1.5 mm)/plasterboard (12.5 mm) of cross-section 20×20 $mm^2$ under diffuse field. Material properties can be referred from Table 7.1.

On the computational efficiency front, as seen in the previous case, the proposed condensed FE approach is more than 50 times faster than the 3D FE approach with 2nd order elements for both excitation types (see Table 7.4).

### 7.2.3 Case 3: Double-wall partition with poro-elastic core

A similar comparison plot is presented in Fig. 7.9 for a five layer double-wall partition with poro-elastic core: plasterboard (12.5 mm)/air (1.5 mm)/glasswool (45 mm)/air (1.5 mm)/plasterboard (12.5 mm). The glasswool is a poro-elastic material which is described with the Biot's model [22, 23] and the Johnson–Champoux–Allard-Lafarge [143, 144, 147] model (or JCAL model) for the visco-thermal dissipation mechanisms inside the porous layer. The JCAL model depends on six acoustic properties (open porosity, airflow resistivity, viscous characteristic length, thermal characteristic length, high frequency limit of tortuosity and static thermal permeability). Table 7.2 summarizes the values of these parameters.

| FE approach | Order | #Nodes | #Dofs | $t_{\text{oblique}}$ | $t_{\text{diffuse}}$ |
|---|---|---|---|---|---|
| Condensed | 1 | 27 | 72 | 0.3 s | 13 s |
| (Anti-symm. & Symm.) | 2 | 75 | 168 | 0.5 s | 24 s |
| 3D (5 layers including poro-elastic core) | 1 | 108 | 414 | 8 s | 402 s |
| | 2 | 575 | 1252 | 258 s | 13216 s |
| 3D (without air layers and | 1 | 81 | 225 | 2 s | 110 s |
| core with limp model) | 2 | 425 | 669 | 30 s | 1539 s |

Table 7.5: Computational efficiency comparison for double-wall partition structure with sequence: plasterboard (12.5 mm)/air (1.5 mm)/glasswool (45 mm)/air (1.5 mm)/plasterboard (12.5 mm) of cross-section $20\times20$ mm$^2$. Material properties can be referred from Table 7.1.

Concerning the TL response of this double-wall partition, the proposed condensed FE approach (with both anti-symmetric and symmetric motion) results in good agreement with the TMM reference as well as 3D FE approach by correctly computing the breathing frequency and with a small difference on the critical frequency of the multi-layer structure. Regarding the computational efficiency of the proposed FE approach, from Table 7.5, an interesting computational gain can be observed. If the multi-layer structure has many layers of different materials and/or has thicker layers, the 3D FE approach would result in higher number of dofs which is computationally expensive. On the contrary, the proposed condensed FE approach would always result in same and low number of dofs irrespective of the number of layers, material types and/or thicknesses of the layers. This is due to the reason that the condensed model (Chapter 6) converts the physically symmetric multi-layer system with each layer of any material type (fluid, solid and porous) into a single condensed layer (see Fig. 6.8) with intrinsic dynamic properties ($\widetilde{D}_{\text{eq}}, \breve{\rho}_A$ and $\overline{\rho}_S$). Therefore, for the present case, it can be seen that the condensed FE approach works 550 times faster than the 3D FE approach.

Additionally, TL response of the double-wall partition without air layers is presented in Fig. 7.9 (for 3D FE approach), where the glasswool is modelled as a limp layer. It can be observed that, the TL of this three-layer structure matches with the five-layer structure with air layers. Since the core is decoupled from the skins by air layers (in the five-layer system), the influence of the core elastic properties is weak, and the core can be modelled as a limp model. Due to this reason, it provides the matched vibro-acoustic response to

that of the three-layer sandwich structure, where the core is considered as limp. Even for this simplified case, the condensed model runs 60 times faster than the 3D FE approach (see Table 7.5).

It is worth to mention that the proposed condensed FE scheme would be computationally far lighter than the conventional 3D FEM simulations, for furthermore complex practical applications such as cabin flooring of aircraft and trains, windshield of an automotive vehicle etc. As the number of degrees of freedom is quite large for these practical cases due to the larger size of the structures (compared to the examples presented in this section), the computational gain with the proposed FE scheme would be significant compared to other conventional FE methods. Finally, the condensed elements proposed in this chapter could be easily connected with other element types to perform the computations. This ability of the condensed element comes from the fact that the condensed element simply uses the thick plate element formulation with a penalty factor on the shear modulus.

## 7.3 Conclusion

In this chapter, a FE scheme for the condensed model (presented in Chapter 6) is proposed by considering the anti-symmetric and symmetric motions of the physically symmetric multi-layer system. In the FE scheme, the multi-layer structure is converted into two decoupled condensed plates corresponding to anti-symmetric and symmetric motions of the structure with three intrinsic dynamic properties (a dynamic bending stiffness, which corresponds to the equivalent parameter identified from any anti-symmetric condensed plate models, and two dynamic mass densities). The coupling between these two plates are achieved through the definitions of anti-symmetric and symmetric displacements of the structure, which are the functions of the fluid displacements at the emission and reception sides. Although the three intrinsic dynamic parameters are defined for the condensed thin plates, thick plate elements with penalty on the shear modulus are used in the proposed FE approach for the ease of implementation. It is showed that, through

three cases of multi-layer structures, the proposed condensed FE approach gives high computational gain over the conventional 3D FE approach as it significantly results in low number of degrees of freedoms while maintaining good agreement with the reference (TMM) solution. The condensed multi-layer has to be symmetric but can include solid, fluid or poro-elastic layers.

# Chapter 8

# General conclusion and perspectives

This thesis work concerns the development of advanced vibro-acoustic tools to understand the physical behaviour of the multi-layer structures and thereby efficiently estimate their vibro-acoustic responses. Usage of multi-layer structures are growing in many industries including aerospace, automotive and building. They attract considerable attention due to their interesting mechanical properties in terms of overall weight, stiffness and damping that classical materials do not provide. On the other hand, they often result in many challenging complexities while modelling. Although many types of vibro-acoustic models are available in the literature, condensed models have its peculiar advantage of converting the multi-layer structure into a single condensed layer while simulating the same natural response. Therefore, usage of these models offer greater advantage in finite element modelling since they significantly reduce the computational power and time compared to the conventional three-dimensional finite element approaches. The work carried out during this thesis is therefore focused on the research, study and improvement of the condensed models for vibro-acoustic applications. Fig. 8.1 shows the developed models of the thesis and summarizes the advantages and limitations of each of these models. It may be noted that the models presented in this thesis are developed for linear elastic materi-

als. Nevertheless, in the case of nonlinear materials, where material properties changes in nonlinear sense with respect to the static load or displacement, these models would be still applicable if the dynamic load is small enough to ignore its effects on the material properties (result of small deformation hypothesis).

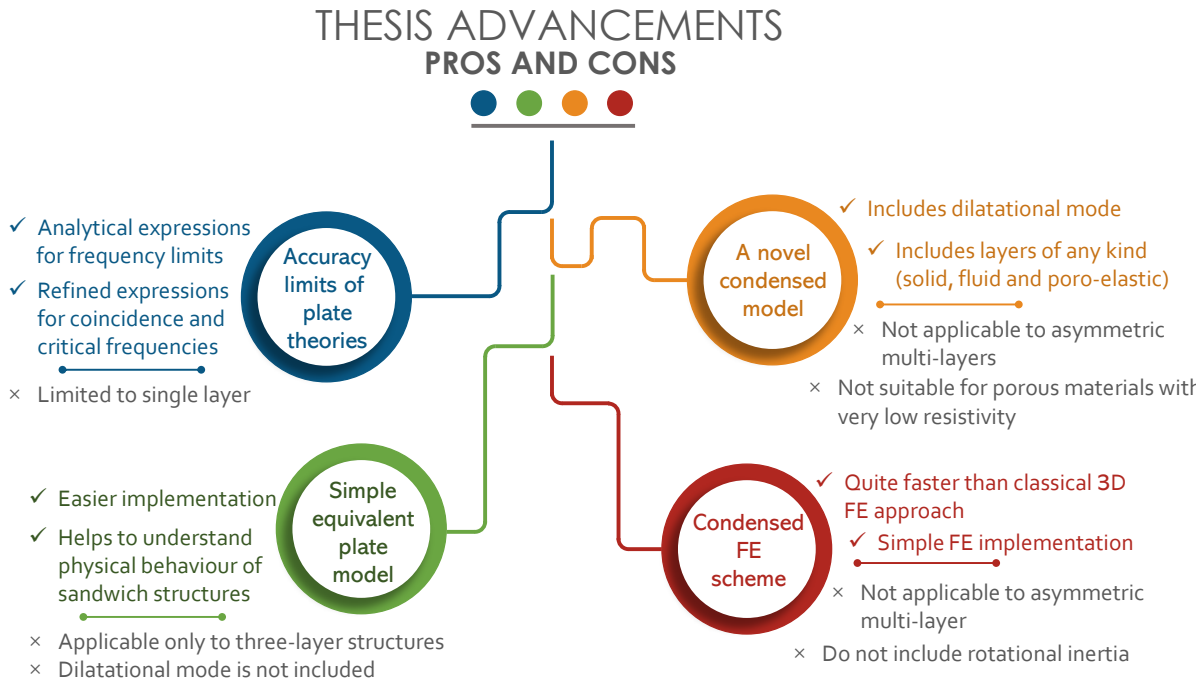


Figure 8.1: Advantages and limitations of the developed models.

The literature review provided in the first chapter has allowed to classify the different types of vibro-acoustic methods that are applied to model and characterize the multi-layer structures. Several analytical models of multi-layers are generally valid for a given frequency range as well as a particular type of structure. In most of these models, the focus is given to the bending mode of the structure due to its higher acoustic radiation than that of the other modes like shear and compression. More precise models introduce the shearing motion along with bending motion to each individual layer. These descriptions are valid if the layers are thin and therefore, these models are limited to thin multi-layer structures. When the thickness of the layer is moderately high or if the layer is sensitive to compression, the resulting behaviour is not only controlled by anti-symmetric motions (bending, shear and membrane) but modified by the symmetric motion (compressional/dilatational) as well. The equivalent or condensed methodology derived from

these existing models also possess this limitation. This understanding has aided to identify the possibilities from which the new improvements can be made to address the current challenges.

The general principles of an accurate method called "Transfer Matrix Method (TMM)" to compute vibro-acoustic quantities of planar multi-layers are presented in Chapter 3. Since this method describes the complete description of propagating waves in a layer, the computations from this method are used for validating the new developments made in other chapters. Additionally, an initial condensation procedure is presented based on the global transfer matrix computation from the TMM. Although this approach suggests a possible direction towards obtaining the intrinsic properties of an equivalent fluid or thin plate, it is limited for most of the practical cases of multi-layer structures.

Analytical expressions of frequency limits of plate theories, which are commonly used in many vibro-acoustic analytical models (including condensed models), are derived in Chapter 4. Limitations of Love-Kirchhoff [95, 96] and Reissner-Mindlin [97–99] plate theories come from excluding shear and compressional motions, respectively. Observation from the dispersion curves of both plate theories lead to find the limiting frequency for the Love-Kirchhoff theory, whereas, analysis of admittances let to derive the same for plate theories which assume constant normal displacement. Validation of these frequency limits are attained by comparing the Transmission Loss (TL) plots obtained from the plate theories with those from the TMM. In addition, the coincidence and critical frequency expressions are refined using Reissner-Mindlin plate theory for the correct estimation. Although analytical expressions for frequency limits are given, these are limited to only a single layer. However, similar dispersion and admittance analyses could be performed for equivalent plates to derive frequency limits.

A simplified condensed plate model for three-layer sandwich structures is presented in Chapter 5, to reduce the challenges in the implementation processes of existing condensed plate models. This simple model has its foundation in understanding the physical behaviour of three-layer system at three frequencies regimes (namely low, transition and

high) to derive only four key parameters that are sufficient to compute the natural response at all frequencies. The dynamic condensed properties obtained from this model are compared against the existing condensed model as well as the experimental data and it is showed that the new model gives matched response with both of them. Although the model is effective in reducing the implementation challenges, it limits its applicability to only three-layer sandwich systems. Additionally, like other condensed plate models, this model also accounts only for anti-symmetric motions and not dilatational motion, and thus, limited to only thin multi-layer structures.

One of the objectives of this thesis is to develop a condensed model that could capture the effect of compressional/dilatational motion of the multi-layer structure. Therefore, a novel condensed model is presented in Chapter 6 that could handle both symmetric (compressional) and anti-symmetric (bending, shear and membrane) motions. The condensed properties, dynamic bending stiffness and two equivalent mass densities, are derived by assuming two uncoupled equivalent thin plates corresponding to symmetric and anti-symmetric motions. This new model has its applicability advantages on multi-layer structures that contain thick/soft layers of any kind (elastic solid, fluid and poro-elastic). Although the effects of dilatational mode are included, this model would be limited only to symmetric multi-layers, as the intrinsic properties are obtained from the assumption that the anti-symmetric and symmetric admittances are decoupled. Also, the presented model may not be suitable for the multi-layer structure with porous layers of very low resistivity values.

An important application of the novel condensed model is to use them in the finite element framework that aims to effectively reduce the computational time. Therefore, a dedicated Finite Element (FE) scheme is proposed in Chapter 7 to compute the vibro-acoustic response of thick symmetric multi-layers. Two decoupled plates are meshed with three dynamic condensed properties, and they are finally coupled using the anti-symmetric and symmetric velocity definitions of the layered structure. The computational efficiency of the proposed FE scheme is demonstrated using several multi-layer configurations and,

as expected, it is observed that the condensed FE scheme runs quite faster than the conventional three-dimensional FE approach. On the limitation side, the condensed FE scheme slightly underpredicts the critical frequency due to negligence of rotational inertia of the thick multi-layer structure. Therefore, further investigation need to be carried out in the future to account for an equivalent rotational inertia.

# Perspectives

**Perspectives**

| | |
|---|---|
| The condensation approach presented in Chapter 3 can be extended to get the equivalent fluid properties of heterogeneous porous media and metamaterials. | 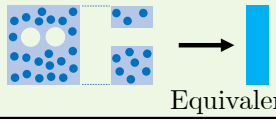  |
| Similar to the procedure followed to obtain the frequency limit of an isotropic plate, a frequency limit expression can be derived for condensed plate theories. This can be done by analysing the anti-symmetric and symmetric admittances that are obtained for the multi-layer structure. | 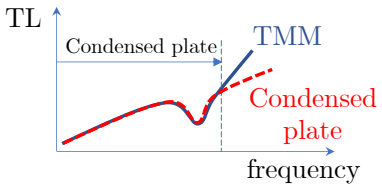  |
| From the wavenumber analysis, a simple condensed plate has been developed by observing the asymptotic behaviours for three-layer structures. Possibilities of extending the similar approach to any number of layers can be investigated. |   |
| Condensed model presented in Chapter 6 could be extended to asymmetric multi-layer structures. Since the anti-symmetric and symmetric admittances are coupled for the asymmetric multi-layers, obtaining the condensed properties requires to account for this coupling while using intrinsic parameters. |   |
| The applicability limits for curved structures could be investigated using shell element implementation with the condensed properties obtained from Chapter 6. | 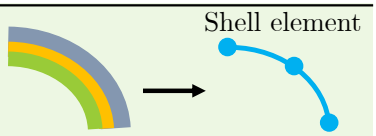  |
| The condensed FE scheme presented in Chapter 7 could be tested with other excitations such as point load, rain fall, turbulent boundary layer etc. |   |
| An interesting aspect would be introducing the bonding imperfections between the layers in the condensed models. The current models are based on the condition that the layers are either perfectly bonded or sliding. Therefore, introducing the bonding imperfections in the condensed models would make them even more efficient to estimate the effects of the different bonding conditions (shear, dissipation) on the resulting vibro-acoustic response. | 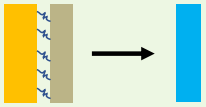  |

Figure 8.2: Possible future work that can be carried out after this thesis.

Several perspectives can be proposed as shown in Fig. 8.2 to extend the application range of the condensed models. All of these extensions, however, would result in substantial complexity of the model and must thus be chosen with caution in accordance with the required conditions.

# Bibliography


[1] Directorate-General for Mobility and Transport (DG MOVE). *Transport in the European Union – current trends and issues*. Mobility and Transport, 2019.

[2] E. H. Lee and W. H. Yang. "On Waves in Composite Materials with Periodic Structure". In: *SIAM J. Appl. Math.* 25.3 (1973), pp. 492–499.

[3] P. Lienard. "Étude d'une méthode de mesure du frottement intérieur de revêtements plastiques travaillant en flexion". In: *La Recherche Aeronautique* 20 (1951), pp. 11–22.

[4] H. Oberst and K. Frankenfeld. "Über die Dämpfung der Biegeschwingungen dünner Bleche durch fest haftende Beläge". In: *Acta Acustica united with Acustica* 2.6 (1952), pp. 181–194.

[5] H. Oberst, G. W. Becker, and K. Frankenfeld. "Über die Dämpfung der Biegeschwingungen dünner Bleche durch fest haftende Beläge II". In: *Acta Acustica united with Acustica* 4.4 (1954), pp. 433–444.

[6] H. Oberst. "Werkstoffe mit extrem hoher innerer Dämpfung". In: *Acta Acustica united with Acustica* 6.1 (1956), pp. 144–153.

[7] E. M. Kerwin Jr. "Damping of flexural waves by a constrained viscoelastic layer". In: *The Journal of the Acoustical society of America* 31.7 (1959), pp. 952–962.

[8] R. A. DiTaranto. "Theory of vibratory bending for elastic and viscoelastic layered finite-length beams". In: *Journal of Applied Mechanics* 32.4 (1965), pp. 881–886.

[9] D. J. Mead and S. Markus. “The forced vibration of a three-layer, damped sandwich beam with arbitrary boundary conditions”. In: *Journal of sound and vibration* 10.2 (1969), pp. 163–175.

[10] M.-J. Yan and E. H. Dowell. “Governing equations for vibrating constrained-layer damping sandwich plates and beams”. In: *Journal of Applied Mechanics* 39.4 (1972), pp. 1041–1046.

[11] Y.-Y. Yu. “Damping of flexural vibrations of sandwich plates”. In: *Journal of the Aerospace Sciences* 29.7 (1962), pp. 790–803.

[12] S.-W. Kung and R. Singh. “Vibration analysis of beams with multiple constrained layer damping patches”. In: *Journal of Sound and Vibration* 212.5 (1998), pp. 781–805.

[13] R. N. Miles and P. G. Reinhall. “An analytical model for the vibration of laminated beams including the effects of both shear and thickness deformation in the adhesive layer”. In: *Journal of Vibration and Acoustics* 108 (1985), pp. 56–64.

[14] P. J. Shorter. “Wave propagation and damping in linear viscoelastic laminates”. In: *The Journal of the Acoustical Society of America* 115.5 (2004), pp. 1917–1925.

[15] N. A. Haskell. “The Dispersion of Surface Waves in Multi-Layered Media”. In: *Bulletin of the Seismological Society of America* 43 (1953), pp. 17–43.

[16] B. Hosten and M. Castaings. “Transfer Matrix of Multilayered Absorbing and Anisotropic Media. Measurements and Simulations of Ultrasonic Wave Propagation through Composite Materials”. In: *The Journal of the Acoustical Society of America* 94.3 (1993), pp. 1488–1495.

[17] W. T. Thomson. “Transmission of Elastic Waves through a Stratified Solid Medium”. In: *Journal of applied Physics* 21.2 (1950), pp. 89–93.

[18] W. Lauriks, P. Mees, and J.-F. Allard. “The Acoustic Transmission through Layered Systems”. In: *Journal of sound and vibration* 155.1 (1992), pp. 125–132.

[19] B. Brouard, D. Lafarge, and J.-F. Allard. “A General Method of Modelling Sound Propagation in Layered Media”. In: *Journal of Sound and Vibration* 183.1 (1995), pp. 129–142.

[20] J. S. Bolton, N.-M. Shiau, and Y. J. Kang. "Sound Transmission through Multi-Panel Structures Lined with Elastic Porous Materials". In: *Journal of sound and vibration* 191.3 (1996), pp. 317–347.

[21] J.-F. Allard and N. Atalla. *Propagation of sound in porous media: modelling sound absorbing materials 2e*. John Wiley & Sons, 2009.

[22] M. A. Biot. "Theory of propagation of elastic waves in a fluid-saturated porous solid. I Low-frequency range". In: *Journal of the Acoustical Society of America* 28 (1956), 168—178.

[23] M. A. Biot. "Theory of propagation of elastic waves in a fluid-saturated porous solid. II Higher-frequency range". In: *Journal of the Acoustical Society of America* 28 (1956), 179–191.

[24] S.-I. Thomasson. *Theory and experiments on the sound absorption as function of the area*. Department of Acoustics, Royal Institute of Technology, 1982.

[25] M. Villot, C. Guigou, and L. Gagliardini. "Predicting the acoustical radiation of finite size multi-layered structures by applying spatial windowing on infinite structures". In: *Journal of sound and vibration* 245.3 (2001), pp. 433–455.

[26] D. Rhazi and N. Atalla. "A Simple Method to Account for Size Effects in the Transfer Matrix Method". In: *The Journal of the Acoustical Society of America* 127.2 (2010), EL30–EL36.

[27] T. E. Vigran. "Predicting the sound reduction index of finite size specimen by a simplified spatial windowing technique". In: *Journal of Sound and Vibration* 325.3 (2009), pp. 507–512.

[28] P. Bonfiglio, F. Pompoli, and R. Lionti. "A reduced-order integral formulation to account for the finite size effect of isotropic square panels using the transfer matrix method". In: *The Journal of the Acoustical Society of America* 139.4 (2016), pp. 1773–1783.

[29] M. Castaings and B. Hosten. "Delta Operator Technique to Improve the Thomson–Haskell-Method Stability for Propagation in Multilayered Anisotropic Absorbing Plates". In: *The Journal of the Acoustical Society of America* 95.4 (1994), pp. 1931–1941.

[30] J. Jocker, D. Smeulders, G. Drijkoningen, C. van der Lee, and A. Kalfsbeek. "Matrix Propagator Method for Layered Porous Media: Analytical Expressions and Stability Criteria". In: *Geophysics* 69.4 (2004), pp. 1071–1081.

[31] C. Potel and J.-F. de Belleval. "Acoustic Propagation in Anisotropic Periodically Multilayered Media: A Method to Solve Numerical Instabilities". In: *Journal of applied physics* 74.4 (1993), pp. 2208–2215.

[32] B. Quintal, S. M. Schmalholz, and Y. Y. Podladchikov. "Low-Frequency Reflections from a Thin Layer with High Attenuation Caused by Interlayer Flow". In: *Geophysics* 74.1 (2009), N15–N23.

[33] S. I. Rokhlin and L. Wang. "Stable Recursive Algorithm for Elastic Wave Propagation in Layered Anisotropic Media: Stiffness Matrix Method". In: *The Journal of the Acoustical Society of America* 112.3 (2002), pp. 822–834.

[34] O. Dazel, J.-P. Groby, B. Brouard, and C. Potel. "A Stable Method to Model the Acoustic Response of Multilayered Structures". In: *Journal of Applied Physics* 113.8 (2013), p. 083506.

[35] A. N. Stroh. "Steady State Problems in Anisotropic Elasticity". In: *Journal of Mathematics and Physics* 41.1-4 (1962), pp. 77–103.

[36] Y. J. Kang and J. S. Bolton. "A Finite Element Model for Sound Transmission through Foam-Lined Double-Panel Structures". In: *The Journal of the Acoustical Society of America* 99.5 (1996), pp. 2755–2765.

[37] R. Panneton and N. Atalla. "Numerical Prediction of Sound Transmission through Finite Multilayer Systems with Poroelastic Materials". In: *The Journal of the Acoustical Society of America* 100.1 (1996), pp. 346–354.

[38] I. L. Vér and L. L. Beranek. *Noise and Vibration Control Engineering: Principles and Applications*. John Wiley & Sons, 2005.

[39] A. Craggs. "A Finite Element Model for Rigid Porous Absorbing Materials". In: *Journal of Sound and Vibration* 61.1 (1978), pp. 101–111.

[40] R. Panneton, N. Atalla, and F. Charron. "A Finite-Element Formulation for the Vibroacoustic Behaviour of Double-Plate Structures with Cavity Absorption". In: *Canadian Aeronautics and Space Journal* 41.1 (1995), pp. 5–12.

[41] Y. J. Kang and J. S. Bolton. "Finite Element Modeling of Isotropic Elastic Porous Materials Coupled with Acoustical Finite Elements". In: *The journal of the acoustical society of america* 98.1 (1995), pp. 635–643.

[42] T. F. Johansen, J.-F. Allard, and B. Brouard. "Finite Element Method for Predicting the Acoustical Properties of Porous Samples". In: *Acta acustica (Les Ulis)* 3.5 (1995), pp. 487–491.

[43] J. P. Coyette and H. Wynendaele. "A Finite Element Model for Predicting the Acoustic Transmission Characteristics of Layered Structures". In: *INTER-NOISE and NOISE-CON Congress and Conference Proceedings*. Vol. 1995. Institute of Noise Control Engineering. 1995, pp. 1279–1282.

[44] R. Panneton and N. Atalla. "An Efficient Finite Element Scheme for Solving the Three-Dimensional Poroelasticity Problem in Acoustics". In: *The Journal of the Acoustical Society of America* 101.6 (1997), pp. 3287–3298.

[45] P. Göransson. "A Weighted Residual Formulation of the Acoustic Wave Propagation through a Flexible Porous Material and a Comparison with a Limp Material Model". In: *Journal of Sound and Vibration* 182.3 (1995), pp. 479–494.

[46] N. Atalla, R. Panneton, P. Debergue, and J.-F. Allard. "A Mixed Displacement-Pressure Formulation for Biot's Poroelastic Equations." In: *The Journal of the Acoustical Society of America* 99.4 (1996), pp. 2487–2500.

[47] N. Atalla, R. Panneton, and P. Debergue. "A mixed displacement-pressure formulation for poroelastic materials". In: *The Journal of the Acoustical Society of America* 104 (1998), pp. 1444–1452.

[48] P. Debergue, R. Panneton, and N. Atalla. "Boundary Conditions for the Weak Formulation of the Mixed (u, p) Poroelasticity Problem". In: *The Journal of the acoustical Society of america* 106.5 (1999), pp. 2383–2390.

[49] N. Atalla and F. Sgard. *Finite Element and Boundary Methods in Structural Acoustics and Vibration*. CRC Press, 2015.

[50] P. Leroy, N. Atalla, A. Berry, and P. Herzog. "Three Dimensional Finite Element Modeling of Smart Foam". In: *the Journal of the Acoustical Society of America* 126.6 (2009), pp. 2873–2885.

[51] L. Alimonti, N. Atalla, A. Berry, and F. Sgard. "A Hybrid Finite Element–Transfer Matrix Model for Vibroacoustic Systems with Flat and Homogeneous Acoustic Treatments". In: *The Journal of the Acoustical Society of America* 137.2 (2015), pp. 976–988.

[52] J.-P. Coyette, G. Lielens, B. Van den Nieuwenhof, C. Bertolini, C. Gaudino, K. Misaji, and F. Ide. *From Body in White to Trimmed Body Models in the Low Frequency Range: A New Modeling Approach*. Tech. rep. SAE Technical Paper, 2007.

[53] B. Van den Nieuwenhof, G. Lielens, J. Coyette, F. Acher, and D. d'Udekem. "Efficient Analysis of Large Trimmed Configurations Using Modal Approaches". In: *Proceedings of ISMA08, International Conference on Modal Analysis Noise and Vibration Engineering*. 2008, pp. 15–17.

[54] F. Acher, K. Ege, C. Sandier, and Y. Gerges. "Vibro-Acoustic Modeling of a Trimmed Truck Cabin in Low Frequency Range to Tackle the Challenge of Weight Reduction". In: *10th International Styrian Noise, Vibration & Harshness Congress: The European Automotive Noise Conference*. 2018.

[55] S. P. S. Maluski and B. M. Gibbs. "Application of a Finite-Element Model to Low-Frequency Sound Insulation in Dwellings". In: *The Journal of the Acoustical Society of America* 108.4 (2000), pp. 1741–1751.

[56] T. Hou and Y. Efendiev. *Multiscale Finite Element Methods*. 2009.

[57] F. Zhang. *The Schur complement and its applications*. Vol. 4. Springer Science & Business Media, 2006.

[58] R. R. Craig Jr and M. C. Bampton. "Coupling of substructures for dynamic analyses." In: *AIAA journal* 6.7 (1968), pp. 1313–1319.

[59] R. H. Lyon, R. G. DeJong, and M. Heckl. *Theory and Application of Statistical Energy Analysis*. 1995.

[60] M. J. Crocker and A. J. Price. "Sound transmission using statistical energy analysis". In: *Journal of Sound and Vibration* 9.3 (1969), pp. 469–486.

[61] A. J. Price and M. J. Crocker. "Sound Transmission through Double Panels Using Statistical Energy Analysis". In: *The Journal of the Acoustical Society of America* 47.3A (1970), pp. 683–693.

[62] A. Brekke. "Calculation Methods for the Transmission Loss of Single, Double and Triple Partitions". In: *Applied Acoustics* 14.3 (1981), pp. 225–240.

[63] B. Craik. "Statistical Energy Analysis". In: *Gower, England* (1996).

[64] R. J. M. Craik and R. Wilson. "Sound Transmission through Masonry Cavity Walls". In: *Journal of sound and vibration* 179.1 (1995), pp. 79–96.

[65] R. J. M. Craik and R. S. Smith. "Sound Transmission through Double Leaf Lightweight Partitions Part I: Airborne Sound". In: *Applied Acoustics* 61.2 (2000), pp. 223–245.

[66] A. Dijckmans, G. Vermeir, and W. Lauriks. "Sound Transmission through Finite Lightweight Multilayered Structures with Thin Air Layers". In: *The Journal of the Acoustical Society of America* 128.6 (2010), pp. 3513–3524.

[67] M. Barbagallo. "Statistical Energy Analysis and Variational Principles for the Prediction of Sound Transmission in Multilayered Structures". PhD thesis. KTH Royal Institute of Technology, 2013.

[68] R. Cherif, A. Wareing, and N. Atalla. "Evaluation of a Hybrid TMM-SEA Method for Prediction of Sound Transmission Loss through Mechanically Coupled Aircraft Double-Walls". In: *Applied Acoustics* 117 (2017), pp. 132–140.

[69] E. Carrera. "An assessment of mixed and classical theories on global and local response of multilayered orthotropic plates". In: *Composite structures* 50.2 (2000), pp. 183–198.

[70] E. Manconi and B. R. Mace. "Estimation of the loss factor of viscoelastic laminated panels from finite element analysis". In: *Journal of Sound and Vibration* 329.19 (2010), pp. 3928–3939.

[71] S. Ghinet and N. Atalla. "Modeling thick composite laminate and sandwich structures with linear viscoelastic damping". In: *Computers & Structures* 89.15-16 (2011), pp. 1547–1561.

[72] C. Boutin and K. Viverge. "Generalized plate model for highly contrasted laminates". In: *European Journal of Mechanics-A/Solids* 55 (2016), pp. 149–166.

[73] K. Viverge, C. Boutin, and F. Sallet. "Model of highly contrasted plates versus experiments on laminated glass". In: *International Journal of Solids and Structures* 102 (2016), pp. 238–258.

[74] A. Loredo and A. Castel. "A multilayer anisotropic plate model with warping functions for the study of vibrations reformulated from Woodcock's work". In: *Journal of Sound and Vibration* 332.1 (2013), pp. 102–125.

[75] A. Loredo and A. Castel. "Two multilayered plate models with transverse shear warping functions issued from three dimensional elasticity equations". In: *Composite Structures* 117 (2014), pp. 382–395.

[76] N. S. Ferguson, C. R. Halkyard, B. R. Mace, and K. H. Heron. "The Estimation of Wavenumbers in Two-Dimensional Structures". In: (2002).

[77] J. Berthaut. "Contribution à l'identification Large Bande Des Structures Anisotropes : Application Aux Tables d'harmonie Des Pianos". PhD Thesis. Ecole Centrale de Lyon, 2004.

[78] L. Hillström, M. Mossberg, and B. Lundberg. "Identification of Complex Modulus from Measured Strains on an Axially Impacted Bar Using Least Squares". In: *Journal of Sound and Vibration* 230.3 (2000), pp. 689–707.

[79] J. G. McDaniel, P. Dupont, and L. Salvino. "A Wave Approach to Estimating Frequency-Dependent Damping under Transient Loading". In: *Journal of sound and vibration* 231.2 (2000), pp. 433–449.

[80] J. Berthaut, M. N. Ichchou, and L. Jezequel. "K-Space Identification of Apparent Structural Behaviour". In: *Journal of Sound and Vibration* 280.3-5 (2005), pp. 1125–1131.

[81] M. N. Ichchou, O. Bareille, and J. Berthaut. "Identification of Effective Sandwich Structural Properties via an Inverse Wave Approach". In: *Engineering Structures* 30.10 (2008), pp. 2591–2604.

[82] R. Cherif, J.-D. Chazot, and N. Atalla. "Damping Loss Factor Estimation of Two-Dimensional Orthotropic Structures from a Displacement Field Measurement". In: *Journal of sound and vibration* 356 (2015), pp. 61–71.

[83] N. B. Roozen, Q. Leclère, K. Ege, and Y. Gerges. "Estimation of Plate Material Properties by Means of a Complex Wavenumber Fit Using Hankel's Functions and the Image Source Method". In: *Journal of Sound and Vibration* 390 (Mar. 2017), pp. 257–271. ISSN: 0022-460X.

[84] C. Pezerat and J.-L. Guyader. "Two inverse methods for localization of external sources exciting a beam". In: *Acta Acustica* 3.1 (1995), pp. 1–10.

[85] C. Pezerat and J.-L. Guyader. "Force analysis technique: reconstruction of force distribution on plates". In: *Acta Acustica united with Acustica* 86.2 (2000), pp. 322–332.

[86] Q. Leclere and C. Pézerat. "Vibration source identification using corrected finite difference schemes". In: *Journal of Sound and Vibration* 331.6 (2012), pp. 1366–1377.

[87] F. Ablitzer, C. Pézerat, J.-M. Génevaux, and J. Bégué. "Identification of stiffness and damping properties of plates by using the local equation of motion". In: *Journal of Sound and Vibration* 333.9 (2014), pp. 2454–2468.

[88] Q. Leclère, F. Ablitzer, and C. Pézerat. "Practical Implementation of the Corrected Force Analysis Technique to Identify the Structural Parameter and Load Distributions". In: *Journal of Sound and Vibration* 351 (Sept. 2015), pp. 106–118. ISSN: 0022-460X.

[89] A. K. Noor and W. S. Burton. "Three-Dimensional Solutions for the Free Vibrations and Buckling of Thermally Stressed Multilayered Angle-Ply Composite Plates". In: (1992).

[90] N. J. Pagano. “Exact Solutions for Rectangular Bidirectional Composites and Sandwich Plates”. In: *Journal of composite materials* 4.1 (1970), pp. 20–34.

[91] S. Srinivas, C. V. J. Rao, and A. K. Rao. “An Exact Analysis for Vibration of Simply-Supported Homogeneous and Laminated Thick Rectangular Plates”. In: *Journal of sound and vibration* 12.2 (1970), pp. 187–199.

[92] E. Carrera. “CZ Requirements—Models for the Two Dimensional Analysis of Multilayered Structures”. In: *Composite structures* 37.3-4 (1997), pp. 373–383.

[93] J. N. Reddy and D. H. Robbins Jr. “Theories and computational models for composite laminates”. In: (1994).

[94] E. Carrera. “Theories and Finite Elements for Multilayered, Anisotropic, Composite Plates and Shells”. In: *Archives of Computational Methods in Engineering* 9.2 (2002), pp. 87–140.

[95] A. E. H. Love. *The Small Free Vibrations and Deformation of a Thin Elastic Shell, Philos.* Tech. rep. TR Soc. A, 179, 491–546, doi: 10.1098/rsta, 1888.

[96] G. Kirchhoff. *Über das Gleichgewicht und die Bewegung einer elastischen Scheibe.* 1850.

[97] E. Reissner. “The effect of transverse shear deformation on the bending of elastic plates”. In: *J. appl. Mech.* (1945), A69–A77.

[98] H. Hencky. “Über die Berücksichtigung der Schubverzerrung in ebenen Platten”. In: *ingenieur-archiv* 16.1 (1947), pp. 72–76.

[99] R. D. Mindlin. “Influence of rotary inertia and shear on flexural motions of isotropic elastic plates”. In: *ASME Journal of Applied Mechanics* 18.A31 (1951).

[100] B. F. Vlasov et al. “On the Equations of Bending of Plates”. In: *Dokla Ak Nauk Azerbeijanskoi-SSR* 3 (1957), pp. 955–979.

[101] H. Lamb. “On Waves in an Elastic Plate”. In: *Proceedings of the Royal Society of London. Series A, Containing papers of a mathematical and physical character* 93.648 (1917), pp. 114–128.

[102] J. N. Reddy and N. D. Phan. "Stability and Vibration of Isotropic, Orthotropic and Laminated Plates According to a Higher-Order Shear Deformation Theory". In: *Journal of sound and vibration* 98.2 (1985), pp. 157–170.

[103] P. Margerit. "Caractérisation Large Bande Du Comportement Dynamique Linéaire Des Structures Hétérogènes Viscoélastiques Anisotropes: Application à La Table d'harmonie Du Piano". PhD thesis. Paris Est, 2018.

[104] P. F. Pai. "A New Look at Shear Correction Factors and Warping Functions of Anisotropic Laminates". In: *International Journal of Solids and Structures* 32.16 (1995), pp. 2295–2313.

[105] J. M. Whitney. "Shear Correction Factors for Orthotropic Laminates under Static Load". In: (1973).

[106] M. Levinson. "An Accurate, Simple Theory of the Statics and Dynamics of Elastic Plates". In: *Mechanics Research Communications* 7.6 (1980), pp. 343–350.

[107] J. N. Reddy. "A Simple Higher-Order Theory for Laminated Composite Plates". In: *Journal of Applied Mechanics* 51.4 (1984), pp. 745–752.

[108] M. Touratier. "An Efficient Standard Plate Theory". In: *International Journal of Engineering Science* 29.8 (1991), pp. 901–916.

[109] K. P. Soldatos and T. Timarci. "A Unified Formulation of Laminated Composite, Shear Deformable, Five-Degrees-of-Freedom Cylindrical Shell Theories". In: *Composite Structures* 25.1-4 (1993), pp. 165–171.

[110] M. Karama, K. S. Afaq, and S. Mistou. "Mechanical Behaviour of Laminated Composite Beam by the New Multi-Layered Laminated Composite Structures Model with Transverse Shear Stress Continuity". In: *International Journal of Solids and Structures* 40.6 (2003), pp. 1525–1546.

[111] J. L. Mantari, A. S. Oktem, and C. G. Soares. "A New Higher Order Shear Deformation Theory for Sandwich and Composite Laminated Plates". In: *Composites Part B: Engineering* 43.3 (2012), pp. 1489–1499.

[112] J. M. Whitney and C. T. Sun. "A Higher Order Theory for Extensional Motion of Laminated Composites". In: *Journal of Sound and Vibration* 30.1 (1973), pp. 85–97.

[113] A. M. Zenkour. "Transverse Shear and Normal Deformation Theory for Bending Analysis of Laminated and Sandwich Elastic Beams". In: *Mechanics of Composite Materials and Structures* 6.3 (1999), pp. 267–283.

[114] S. Srinivas. "A Refined Analysis of Composite Laminates". In: *Journal of Sound and Vibration* 30.4 (1973), pp. 495–507.

[115] J. N. Reddy. "A generalization of two-dimensional theories of laminated composite plates". In: *Communications in applied numerical methods* 3.3 (1987), pp. 173–180.

[116] A. Nosier, R. K. Kapania, and J. N. Reddy. "Free Vibration Analysis of Laminated Plates Using a Layerwise Theory". In: *AIAA journal* 31.12 (1993), pp. 2335–2346.

[117] S. G. Lekhnitskii et al. "Strength Calculation of Composite Beams". In: *Vestnik inzhen i tekhnikov* 9 (1935), pp. 137–148.

[118] J. G. Ren. "Bending Theory of Laminated Plate". In: *Composites science and technology* 27.3 (1986), pp. 225–248.

[119] S. A. Ambartsumian. "On the Theory of Bending Plates". In: *Izv Otd Tech Nauk AN SSSR* 5.5 (1958), pp. 69–77.

[120] J. M. Whitney. "The Effect of Transverse Shear Deformation on the Bending of Laminated Plates". In: *Journal of Composite Materials* 3.3 (1969), pp. 534–547.

[121] H. Murakami. "Laminated Composite Plate Theory with Improved In-Plane Responses". In: (1986).

[122] E. Reissner. "On a Mixed Variational Theorem and on Shear Deformable Plate Theory". In: *International Journal for Numerical Methods in Engineering* 23.2 (1986), pp. 193–198.

[123] A. Toledano and H. Murakami. "A Composite Plate Theory for Arbitrary Laminate Configurations". In: (1987).

[124] L. Demasi. "Refined Multilayered Plate Elements Based on Murakami Zig–Zag Functions". In: *Composite Structures* 70.3 (2005), pp. 308–316.

[125] J.-L. Guyader and C. Lesueur. "Acoustic transmission through orthotropic multilayered plates, Part I: Plate vibration modes". In: *Journal of Sound and Vibration* 58.1 (1978), pp. 51–68.

[126] J.-L. Guyader and C. Lesueur. "Acoustic transmission through orthotropic multilayered plates, part II: transmission loss". In: *Journal of Sound and Vibration* 58.1 (1978), pp. 69–86.

[127] C.-T. Sun and J. M. Whitney. "Theories for the dynamic response of laminated plates". In: *AIAA journal* 11.2 (1973), pp. 178–183.

[128] R. L. Woodcock. "Free vibration of advanced anisotropic multilayered composites with arbitrary boundary conditions". In: *Journal of Sound and Vibration* 312.4-5 (2008), pp. 769–788.

[129] A. Castel. "Comportement Vibratoire de Structures Composites Intégrant Des Éléments Amortissants". PhD thesis. Dijon, 2013.

[130] A. Loredo. "A Multilayered Plate Theory with Transverse Shear and Normal Warping Functions". In: *Composite Structures* 156 (2016), pp. 361–374.

[131] J.-L. Guyader and C. Cacciolati. "Viscoelastic properties of single layer plate material equivalent to multi-layer composites plate". In: vol. 3. 2007, pp. 1558–1567.

[132] D. Ross, E. E. Ungar, and E. M. Kerwin. "Damping of plate flexural vibrations by means of viscoelastic laminae". In: *Structural Damping*. Ed. by J. E. Ruzicka. Oxford: Pergamon Press, 1960, pp. 49–87.

[133] E. E. Ungar and E. M. Kerwin Jr. "Loss factors of viscoelastic systems in terms of energy concepts". In: *The Journal of the acoustical Society of America* 34.7 (1962), pp. 954–957.

[134] A. D. Nashif, D. I. G. Jones, and J. P. Henderson. *Vibration damping*. John Wiley & Sons, 1985.

[135] L. L. Beranek and I. L. Ver. "Noise and vibration control engineering-principles and applications". In: *Noise and vibration control engineering-Principles and applications John Wiley & Sons, Inc., 814 p.* (1992).

[136] R. C. Hibbeler. *Mechanics of Materials*. Prentice Hall, 2011. ISBN: 978-0-13-602230-5.

[137] O. Zarraga, I. Sarría, J. García-Barruetabeña, and F. Cortés. "Dynamic Analysis of Plates with Thick Unconstrained Layer Damping". en. In: *Engineering Structures* 201 (Dec. 2019), p. 109809. ISSN: 01410296. DOI: 10.1016/j.engstruct.2019.109809.

[138] O. Zarraga, I. Sarría, J. García-Barruetabeña, and F. Cortés. "Homogenised Formulation for Plates with Thick Constrained Viscoelastic Core". en. In: *Computers & Structures* 229 (Mar. 2020), p. 106185. ISSN: 00457949. DOI: 10.1016/j.compstruc.2019.106185.

[139] F. Marchetti, K. Ege, Q. Leclere, and N. B. Roozen. "On the Structural Dynamics of Laminated Composite Plates and Sandwich Structures; a New Perspective on Damping Identification". In: *Journal of Sound and Vibration* 474 (2020), p. 115256.

[140] D. L. Folds and C. D. Loggins. "Transmission and reflection of ultrasonic waves in layered media". In: *The Journal of the Acoustical Society of America* 62.5 (1977), pp. 1102–1109.

[141] M. E. Delany and E. N. Bazley. "Acoustical properties of fibrous absorbent materials". In: *Applied acoustics* 3.2 (1970), pp. 105–116.

[142] Y. Miki. "Acoustical properties of porous materials-Modifications of Delany-Bazley models". In: *Journal of the Acoustical Society of Japan (E)* 11.1 (1990), pp. 19–24.

[143] D. L. Johnson, J. Koplik, and R. Dashen. "Theory of dynamic permeability and tortuosity in fluid-saturated porous media". In: *J. Fluid Mech.* 176 (1987), pp. 379–402.

[144] Y. Champoux and J.-F. Allard. "Dynamic tortuosity and bulk modulus in air-saturated porous media". In: *J. Appl. Phys.* 70 (1991), pp. 1975–1979.

[145] S. R. Pride, F. D. Morgan, and A. F. Gangi. "Drag forces of porous-medium acoustics". In: *Physical review B* 47.9 (1993), p. 4964.

[146] D. Lafarge. “Propagation du son dans les matériaux poreux à structure rigide saturés par un fluide viscothermique: Définition de paramètres géométriques, analogie electromagnétique, temps de relaxation”. PhD thesis. Le Mans, 1993.

[147] D. Lafarge, P. Lemarinier, J.-F. Allard, and V. Tarnow. “Dynamic compressibility of air in porous structures at audible frequencies”. In: *J. Acoust. Soc. Am.* 102(4) (1997), pp. 1995–2006.

[148] D. K. Wilson. “Relaxation-matched modeling of propagation through porous media, including fractal pore structure”. In: *The Journal of the Acoustical Society of America* 94.2 (1993), pp. 1136–1145.

[149] F.-X. Bécot and L. Jaouen. “An alternative Biot’s formulation for dissipative porous media with skeleton deformation”. In: *The Journal of the Acoustical Society of America* 134.6 (2013), pp. 4801–4807.

[150] C. De Pollier. “Theorie de biot et prediction des proprietes acoustiques des materiaux poreux: propagation dans les milieux acoustiques desordonnes”. PhD thesis. Le Mans, 1989.

[151] P. Khurana, L. Boeckx, W. Lauriks, P. Leclaire, O. Dazel, and J.-F. Allard. “A description of transversely isotropic sound absorbing porous materials by transfer matrices”. In: *The Journal of the Acoustical Society of America* 125.2 (2009), pp. 915–921.

[152] J. P. Parra Martinez. “On multilayered system dynamics and waves in anisotropic poroelastic media”. PhD thesis. Le Mans, 2016.

[153] R. Panneton. “Comments on the limp frame equivalent fluid model for porous media”. In: *The Journal of the Acoustical Society of America* 122.6 (2007), EL217–EL222.

[154] O. Dazel, F.-X. Bécot, and L. Jaouen. “Biot effects for sound absorbing double porosity materials”. In: *Acta Acustica united with Acustica* 98.4 (2012), pp. 567–576.

[155] C. L. Dym and M. A. Lang. “Transmission of sound through sandwich panels”. In: *The Journal of the Acoustical Society of America* 56.5 (1974), pp. 1523–1532.

[156] D. Ross. "Damping of Plate Flexural Vibrations by Means of Viscoelastic Laminae". In: *Structural Damping* (1959), pp. 49–97.

[157] U. Arasan, F. Marchetti, F. Chevillotte, G. Tanner, D. Chronopoulos, and E. Gourdon. "On the Accuracy Limits of Plate Theories for Vibro-Acoustic Predictions". In: *Journal of Sound and Vibration* 493 (2021), p. 115848. DOI: 10.1016/j.jsv.2020.115848.

[158] J.-F. Allard and N. Atalla. *Propagation of Sound in Porous Media: Modelling Sound Absorbing Materials 2e*. John Wiley & Sons, 2009. ISBN: 0-470-74734-X.

[159] L. Cremer. "Theorie der Schalldämmung dünner Wände bei schrägem Einfall". In: *Akustische Zeitschrift* 7.3 (1942), pp. 81–104.

[160] E. C. Sewell. "Transmission of reverberant sound through a single-leaf partition surrounded by an infinite rigid baffle". In: *Journal of Sound and Vibration* 12.1 (1970), pp. 21–32.

[161] F. G. Leppington, K. H. Heron, E. G. Broadbent, and S. M. Mead. "Resonant and non-resonant acoustic properties of elastic panels. II. The transmission problem". In: *Proceedings of the Royal Society of London. A. Mathematical and Physical Sciences* 412.1843 (1987), pp. 309–337.

[162] S. Ljunggren. "A new type of solution for plate vibrations at low frequencies". In: *Journal of sound and vibration* 116.1 (1987), pp. 125–136.

[163] A. E. H. Love. "XVI. The small free vibrations and deformation of a thin elastic shell". In: *Philosophical Transactions of the Royal Society of London.(A.)* 179 (1888), pp. 491–546.

[164] J. L. Davy. "Predicting the sound insulation of single leaf walls: Extension of Cremer's model". In: *The Journal of the Acoustical Society of America* 126.4 (2009), pp. 1871–1877.

[165] M. Heckl and U. Donner. "Schalldämmung dicker Wände (Sound insulation of thick walls)". In: *Rundfunktech Mitt* 29 (1985), pp. 287–291.

[166] S. Ljunggren. "Airborne sound insulation of thick walls". In: *The Journal of the Acoustical Society of America* 89.5 (1991), pp. 2338–2345.

[167] S. Ljunggren. "Forced vibrations of infinite plates". In: *Journal of sound and vibration* 121.2 (1988), pp. 221–236.

[168] Ö. Civalek. "Harmonic Differential Quadrature-Finite Differences Coupled Approaches for Geometrically Nonlinear Static and Dynamic Analysis of Rectangular Plates on Elastic Foundation". In: *Journal of Sound and Vibration* 294.4-5 (2006), pp. 966–980.

[169] K. Bhaskar and T. K. Varadan. *Plates: Theories and Applications*. John Wiley & Sons, 2014.

[170] J.-M. Berthelot and F. F. Ling. *Composite Materials: Mechanical Behavior and Structural Analysis*. Springer, 1999. ISBN: 0-387-98426-7.

[171] B. F. Shorr and G. Melnikova. *The wave finite element method*. Vol. 10. Springer Science & Business Media, 2004.

[172] L. Cremer and M. Heckl. *Structure-borne sound: structural vibrations and sound radiation at audio frequencies*. Springer Science & Business Media, 2013.

[173] C. Boutin and K. Viverge. "Generalized Plate Model for Highly Contrasted Laminates". en. In: *European Journal of Mechanics - A/Solids* 55 (2016), pp. 149–166. ISSN: 09977538. DOI: 10.1016/j.euromechsol.2015.08.008.

[174] U. Arasan, F. Marchetti, F. Chevillotte, L. Jaouen, D. Chronopoulos, and E. Gourdon. "A Simple Equivalent Plate Model for Dynamic Bending Stiffness of Three-Layer Sandwich Panels with Shearing Core". In: *Journal of Sound and Vibration* 500 (2021), p. 116025. DOI: 10.1016/j.jsv.2021.116025.

[175] S. Subramanian, R. Surampudi, K. R. Thomson, and S. Vallurupalli. "Optimization of Damping Treatments for Structure Borne Noise Reduction". en. In: *Sound and Vibration* (2004), p. 4.

[176] M. D. Rao. "Recent Applications of Viscoelastic Damping for Noise Control in Automobiles and Commercial Airplanes". en. In: *Journal of Sound and Vibration* 262.3 (May 2003), pp. 457–474. ISSN: 0022460X. DOI: 10.1016/S0022-460X(03)00106-8.

[177] I. A. Viktorov. *Rayleigh and Lamb waves: physical theory and applications*. Translated from the Russian. New York: Springer Science + Business Media, 2013. ISBN: 978-1-4899-5683-5.

[178] L. Jaouen and F. Chevillotte. "Length Correction of 2D Discontinuities or Perforations at Large Wavelengths and for Linear Acoustics". en. In: *Acta Acustica united with Acustica* 104.2 (Mar. 2018), pp. 243–250. ISSN: 1610-1928. DOI: 10.3813/AAA.919166.

[179] F. J. Fahy and P. Gardonio. *Sound and Structural Vibration: Radiation, Transmission and Response*. Elsevier, 2007.

[180] G. Kurtze and B. G. Watters. "New Wall Design for High Transmission Loss or High Damping". en. In: *The Journal of the Acoustical Society of America* 31.6 (June 1959), pp. 739–748. ISSN: 0001-4966. DOI: 10.1121/1.1907780.

[181] K. Ege, N. B. Roozen, Q. Leclere, and R. G. Rinaldi. "Assessment of the Apparent Bending Stiffness and Damping of Multilayer Plates; Modelling and Experiment". In: *Journal of Sound and Vibration* 426 (2018), pp. 129–149. DOI: 10.1016/j.jsv.2018.04.013.

[182] F. Marchetti, U. Arasan, F. Chevillotte, and K. Ege. "On the Condensation of Thick Symmetric Multilayer Panels Including Dilatational Motion". en. In: *Journal of Sound and Vibration* 502 (June 2021), p. 116078. ISSN: 0022460X. DOI: 10.1016/j.jsv.2021.116078.

[183] J. L. Davy. "Sound Transmission of Cavity Walls Due to Structure Borne Transmission via Point and Line Connections". en. In: *The Journal of the Acoustical Society of America* 132.2 (Aug. 2012), pp. 814–821. ISSN: 0001-4966. DOI: 10.1121/1.4733533.

[184] U. Arasan, A. Sreekumar, F. Chevillotte, S. P. Triantafyllou, D. Chronopoulos, and E. Gourdon. "Condensed finite element scheme for symmetric multi-layer structures including dilatational motion". In: *Journal of Sound and Vibration* (Submitted for review).

[185] S. S. Bhavikatti. *Finite Element Analysis*. New Age International, 2005.

[186] M. A. Neto, A. Amaro, L. Roseiro, J. Cirne, and R. Leal. *Engineering Computation of Structures: The Finite Element Method*. Springer, 2015.

[187] R. J. Melosh. "Structural Analysis of Solids". In: *ASCE Struct J* 504.89 (1963), p. 4.

[188] O. C. Zienkiewicz, R. L. Taylor, and J. Too. "Reduced Integration Technique in General Analysis of Plates and Shells". In: *International Journal for Numerical Methods in Engineering* 3.2 (1971), pp. 275–290.

[189] T. J. R. Hughes, R. L. Taylor, and W. Kanoknukulchai. "A Simple and Efficient Finite Element for Plate Bending". In: *International Journal for Numerical Methods in Engineering* 11.10 (1977), pp. 1529–1543.

[190] M. Mukhopadhyay and D. K. Dinker. "Isoparametric Linear Bending Element and One-Point Integration". In: *Computers & Structures* 9.4 (1978), pp. 365–369.

[191] G. Prathap and S. Viswanath. "An Optimally Integrated Four-Node Quadrilateral Plate Bending Element". In: *International Journal for Numerical Methods in Engineering* 19.6 (1983), pp. 831–840.

[192] Y. Ko, P.-S. Lee, and K.-J. Bathe. "A New MITC4+ Shell Element". In: *Computers & Structures* 182 (2017), pp. 404–418.

[193] U. Pillai, S. P. Triantafyllou, I. Ashcroft, Y. Essa, and F. M. de la Escalera. "Phase-Field Modelling of Brittle Fracture in Thin Shell Elements Based on the MITC4+ Approach". In: *Computational Mechanics* (2020), pp. 1–20.

# Appendix A

# Transfer matrix of an elastic isotropic solid

The transfer matrix of an elastic isotropic layer (defined by the equation $\mathbf{V}^s(M_{2i-1}) = [T^s]\mathbf{V}^s(M_{2i})$ where $\mathbf{V}^s(M) = \begin{bmatrix} v_x^s(M) & v_z^s(M) & \sigma_{zz}^s(M) & \sigma_{xz}^s(M) \end{bmatrix}^T$) based on elasticity theory can be written as follows:

$$[T^s]_{4\times 4} = \frac{1}{D_1 + D_2 k_t}[T_{pq}^s] \quad \text{where } p, q = 1 \text{ to } 4.$$

The matrix elements ($T_{pq}^s$) are,

$T_{11} = T_{44} = D_1 \cos(hk_{sz}) + D_2 k_t \cos(hk_{lz})$,

$T_{22} = T_{33} = D_1 \cos(hk_{lz}) + D_2 k_t \cos(hk_{sz})$,

$T_{12} = T_{34} = -\mathrm{j}[D_2 k_{lz} k_{sz} \sin(hk_{sz}) - D_1 k_t \sin(hk_{lz})]/k_{lz}$,

$T_{21} = T_{43} = \mathrm{j}[D_2 k_{sz} k_{lz} \sin(hk_{lz}) - D_1 k_t \sin(hk_{sz})]/k_{sz}$,

$T_{13} = T_{24} = \omega k_t[\cos(hk_{sz}) - \cos(hk_{lz})]$,

$T_{31} = T_{42} = \left(\frac{D_1 D_2}{\omega^2 k_t}\right) T_{13}$,

$T_{14} = -\mathrm{j}\omega[k_{lz} k_{sz} \sin(hk_{sz}) + k_t^2 \sin(hk_{lz})]/k_{lz}$,

$T_{23} = -\mathrm{j}\omega[k_{lz} k_{sz} \sin(hk_{lz}) + k_t^2 \sin(hk_{sz})]/k_{sz}$,

$T_{32} = -\mathrm{j}[D_2^2 k_{lz} k_{sz} \sin(hk_{sz}) + D_1^2 \sin(hk_{lz})]/(\omega k_{lz})$,

$T_{41} = -\mathrm{j}[D_2^2 k_{lz} k_{sz} \sin(hk_{lz}) + D_1^2 \sin(hk_{sz})]/(\omega k_{sz})$,

where $D_1 = \mu(k_{sz}^2 - k_t^2)$, $D_2 = 2\mu k_t$, $k_{lz} = \sqrt{\delta_l^2 - k_t^2}$ and $k_{sz} = \sqrt{\delta_s^2 - k_t^2}$.

# Appendix B

# Definitions of constants used in Guyader model

For $n-$layer multi-layer structure, the constants used in Guyader model [131] to compute equivalent bending stiffness are,

$$\lambda_1 = \sum_{i=1}^{n} C_{11}^i \left( \frac{h_i^3}{12} + h_i \beta_i^2 \right) \tag{B.1}$$

$$\lambda_2 = \sum_{i=1}^{n} C_{11}^i \left( \frac{h_i^3 \alpha_i^2}{12} + h_i \gamma_i^2 \right) \tag{B.2}$$

$$\lambda_3 = \sum_{i=1}^{n} C_{11}^i h_i \tag{B.3}$$

$$\lambda_4 = \sum_{i=1}^{n} C_{11}^i \left( \frac{h_i^3 \alpha_i^2}{12} + h_i \beta_i \gamma_i \right) \tag{B.4}$$

$$\lambda_5 = \sum_{i=1}^{n} C_{11}^i h_i \beta_i \tag{B.5}$$

$$\lambda_6 = \sum_{i=1}^{n} C_{11}^i h_i \gamma_i \tag{B.6}$$

$$\lambda_{37} = \sum_{i=1}^{n} C_{55}^i h_i \alpha_i^2 \tag{B.7}$$

where $C_{11}^i = \dfrac{E_i}{1-\nu_i^2}$ and $C_{55}^i = \dfrac{E_i}{2(1+\nu_i)}$.
The constants $\alpha_i, \beta_i$ and $\gamma_i$ are computed as follows:

For $i = 1$,

$$\begin{Bmatrix} \alpha_1 \\ \beta_1 \\ \gamma_1 \end{Bmatrix} = \begin{Bmatrix} 1 \\ 0 \\ 0 \end{Bmatrix} \tag{B.8}$$

For $i \geqslant 2$,

$$\begin{Bmatrix} \alpha_i \\ \beta_i \\ \gamma_i \end{Bmatrix} = \begin{Bmatrix} N_i(2,2) \\ N_i(3,1) \\ N_i(3,2) \end{Bmatrix} \tag{B.9}$$

where

$$N_i = \begin{bmatrix} 1 & 0 & 0 \\ 0 & B_i & 0 \\ C_i & F_i & 1 \end{bmatrix} N_{i-1} \tag{B.10}$$

with $N_1$ being the unit matrix and the constants $B_i, C_i$ and $F_i$ are defined as,

$$B_i = C_{55}^{i-1}/C_{55}^i \tag{B.11a}$$

$$C_i = -(h_{i-1} + h_i)/2 \tag{B.11b}$$

$$F_i = -(h_{i-1} + A_i h_i)/2 \tag{B.11c}$$

# Appendix C

# Dispersion curves from the theory of Lamb waves

The Lamb wave model was developed by Lamb [101] and was notably explained well by Viktorov [177]. Fig. C.1 shows the schematic representation of a multi-layer structure in vacuum, composed of '$n$' isotropic layers and the structure has infinite dimensions along the $x$ and $y$ directions while the $z-$axis being defined according to the thickness of the structure. Since Lamb wave theory defines the kinematic relations at each layer, the number of unknowns depend on the number of layers in the multi-layer structure. It is due to this reason, the Lamb wave model falls under the category of Layer-Wise models, discussed in Section 2.4.2 of this manuscript.

Typically, the longitudinal and transverse components of the Lamb waves at an $i-$th layer are defined by the two potentials $\phi_i$ and $\psi_i$, which follows the wave equations:

$$\frac{\partial^2 \phi_i}{\partial x^2} + \frac{\partial^2 \phi_i}{\partial z^2} + \delta_{l,i}^2 \phi_i = 0; \tag{C.1a}$$

$$\frac{\partial^2 \psi_i}{\partial x^2} + \frac{\partial^2 \psi_i}{\partial z^2} + \delta_{s,i}^2 \psi_i = 0, \tag{C.1b}$$

where $\delta_{l,i} = \omega/c_{l,i}$ and $\delta_{s,i} = \omega/c_{s,i}$ are the longitudinal and transverse wavenumbers of an

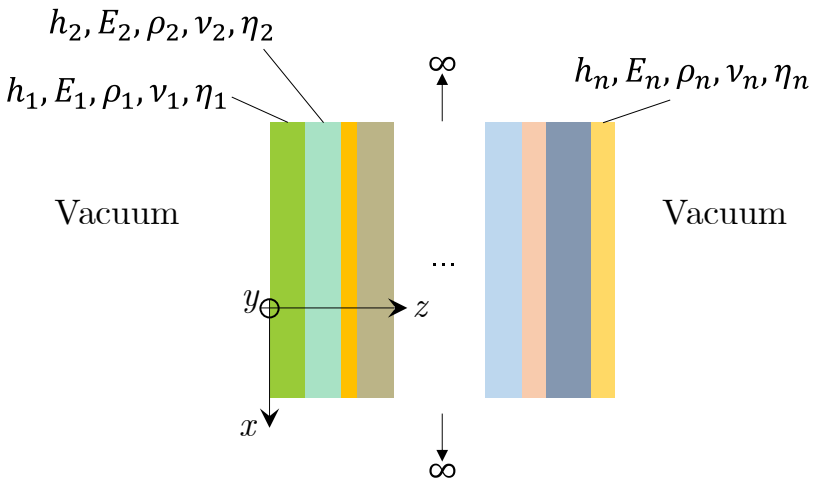


Figure C.1: Schematic representation of the multi-layer structure with infinite lateral dimensions in vacuum.

$i-$th layer, respectively, and $i = 1, 2, ..., n$. The corresponding longitudinal and transverse velocities, $c_{l,i}$ and $c_{s,i}$ respectively, are defined as follows:

$$c_{l,i} = \sqrt{\frac{\lambda_i + 2\mu_i}{\rho_i}}; \quad c_{s,i} = \sqrt{\frac{\mu_i}{\rho_i}}, \tag{C.2}$$

where $\lambda_i$ and $\mu_i$ are the Lamé coefficients of an $i-$th layer. Further, $\rho_i$ represents the $i-$th layer density and $\omega$ is the angular frequency.

Since the potentials follow the wave equations as in Eq. (C.1), the displacement ($u$) and stress ($\sigma$) fields of the $i-$th layer along the $x$ and $z$ directions can be written as follows:

$$u_{x,i} = \frac{\partial \phi_i}{\partial x} - \frac{\partial \psi_i}{\partial z}; \quad u_{z,i} = \frac{\partial \phi_i}{\partial z} + \frac{\partial \psi_i}{\partial x}; \tag{C.3a}$$

$$\sigma_{xx,i} = \rho_i \left[ c_{l,i}^2 \frac{\partial u_{x,i}}{\partial x} + (c_{l,i}^2 - 2c_{s,i}^2) \frac{\partial u_{z,i}}{\partial z} \right]; \tag{C.3b}$$

$$\sigma_{zz,i} = \rho_i \left[ (c_{l,i}^2 - 2c_{s,i}^2) \frac{\partial u_{x,i}}{\partial x} + c_{l,i}^2 \frac{\partial u_{z,i}}{\partial z} \right]; \tag{C.3c}$$

$$\sigma_{xz,i} = \rho_i c_{s,i}^2 \left( \frac{\partial u_{x,i}}{\partial z} + \frac{\partial u_{z,i}}{\partial x} \right). \tag{C.3d}$$

A particular solution of the wave equations (Eq. (C.1)) can be suggested using the potentials:

$$\phi_i = \left(A_i e^{-(k^2-\delta_{l,i}^2)z} + B_i e^{(k^2-\delta_{l,i}^2)z}\right) e^{\mathrm{j}(\omega t - kx)}; \tag{C.4a}$$

$$\psi_i = \left(C_i e^{-(k^2-\delta_{s,i}^2)z} + D_i e^{(k^2-\delta_{s,i}^2)z}\right) e^{\mathrm{j}(\omega t - kx)}, \tag{C.4b}$$

where $k$ is the wavenumber of the propagating wave inside the multi-layer, whose amplitudes are represented by the constants $A_i, B_i, C_i$ and $D_i$. Further, $\mathrm{j} = \sqrt{-1}$ and $t$ represents the time.

A system of linear equations can be formulated from the interface continuity conditions (on the normal and transverse components of displacements and stresses) and vacuum boundary conditions (on the normal and transverse stresses). The interface conditions are,

$$u_{x,i}(z = z_i) = u_{x,i+1}(z = z_i); \quad u_{z,i}(z = z_i) = u_{z,i+1}(z = z_i); \tag{C.5a}$$

$$\sigma_{zz,i}(z = z_i) = \sigma_{zz,i+1}(z = z_i); \quad \sigma_{xz,i}(z = z_i) = \sigma_{xz,i+1}(z = z_i), \tag{C.5b}$$

and the vacuum boundary conditions are,

$$\sigma_{zz,1}(z = 0) = 0; \quad \sigma_{xz,i}(z = 0) = 0; \tag{C.6a}$$

$$\sigma_{zz,n}(z = h_t) = 0; \quad \sigma_{xz,n}(z = h_t) = 0, \tag{C.6b}$$

where $h_t$ is the total thickness of the multi-layer structure.

The system is then composed of $4n$ equations for $4n$ unknowns and can be rewritten in matrix form. The dispersion curves ($k$ as a function of $\omega$) of the structure are then obtained from forcing the determinant of this matrix to be zero.

# Appendix D

# Element matrices of the condensed finite element scheme

Element stiffness matrix of the condensed thick plate with equivalent bending stiffness is written as,

$$[K(\widetilde{D}_{\mathrm{eq}})] = \int_{\Omega} [B_b]^T [D_b][B_b] \mathrm{d}\Omega + \vartheta \int_{\Omega} [B_s]^T [D_s][B_s] \mathrm{d}\Omega \tag{D.1a}$$

where, $[B_b]$ and $[B_s]$ are the strain-displacement matrices of the bending and shear contributions respectively, and $\Omega$ is the surface area of an element. The matrices $[D_b]$ and $[D_s]$ are,

$$[D_b] = \widetilde{D}_{\mathrm{eq}} \begin{bmatrix} 1 & \nu & 0 \\ \nu & 1 & 0 \\ 0 & 0 & \dfrac{1-\nu}{2} \end{bmatrix}, \; [D_s] = \widetilde{G}_{\mathrm{eq}} \begin{bmatrix} 1 & 0 \\ 0 & 1 \end{bmatrix}.$$

The mass matrices are written as,

$$[M(\rho_{\mathrm{eq}})] = \rho_{\mathrm{eq}} \int_{\Omega} [N]^T [I_m][N] \mathrm{d}\Omega; \tag{D.1c}$$

$$[M(\breve{\rho}_A)] = \breve{\rho}_A(\omega)\int_\Omega [N]^T[I_m][N]\mathrm{d}\Omega;\ \ [M(\overline{\rho}_S)] = \overline{\rho}_S(\omega)\int_\Omega [N]^T[I_m][N]\mathrm{d}\Omega \tag{D.1d}$$

where,

$$\underset{3\times 12}{[N]} = \begin{bmatrix} N_1 & 0 & 0 & \dots & N_4 & 0 & 0 \\ 0 & N_1 & 0 & \dots & 0 & N_4 & 0 \\ 0 & 0 & N_1 & \dots & 0 & 0 & N_4 \end{bmatrix}$$

and the shape functions are defined as follows.

For the first order (4-node) element:

$N_i = (1+\zeta\zeta_i)(1+\varrho\varrho_i)/4,\ i = 1,2,3,4.$

For the second order (8-node) element:

$N_i = (1+\zeta\zeta_i)(1+\varrho\varrho_i)(\zeta\zeta_i+\varrho\varrho_i-1)/4,\ i = 1,2,3,4;$

$N_i = (1-\zeta^2)(1+\varrho\varrho_i)/2,\ i = 5,7;$

$N_i = (1+\zeta\zeta_i)(1-\varrho^2)/2,\ i = 6,8.$

Here, $\zeta$ and $\varrho$ are the local coordinate values that vary from $-1$ to 1. The inertial matrix $[I_m]$ is defined as,

$$[I_m] = \begin{bmatrix} h_t & 0 & 0 \\ 0 & 0 & 0 \\ 0 & 0 & 0 \end{bmatrix}.$$

It may be noted that the rotational inertia terms are kept as zero as the condensed model neglects the inertial effects of the condensed layer due to rotations.

The element matrices correspond to the fluid phase are written as,

$$[H^O] = [H^N] = \int_\Omega \frac{1}{\rho_0}[\nabla N^*]^T[\nabla N^*]\mathrm{d}\Omega \tag{D.1e}$$

$$[Q^O] = [Q^N] = \int_\Omega \frac{1}{\rho_0 c_0^2}[N^*]^T[N^*]\mathrm{d}\Omega;\ \ [C] = \int_\Omega [N^*]^T[N]\mathrm{d}\Omega \tag{D.1f}$$

where,

$$[N^*] = \begin{bmatrix} N_1^* & N_2^* & N_3^* & N_4^* \end{bmatrix}; \underset{2\times 8}{[\nabla N^*]} = \begin{bmatrix} N_{1,\zeta}^* & 0 & \dots & N_{4,\zeta}^* & 0 \\ 0 & N_{1,\eta}^* & \dots & 0 & N_{4,\eta}^* \end{bmatrix},$$

and $N_i^* = N_i$.

# Appendix E

# Objectifs et conclusion de la thèse

Les industries mondiales des transports sont les leaders mondiaux dans le développement et la production de produits structurels. Malgré cela, les industries des transports sont confrontées à trois défis importants, à savoir a) la dépendance au pétrole, b) le contrôle des émissions et c) la concurrence [1]. Des développements technologiques continus sont inévitables et cruciaux pour surmonter ces défis et maintenir un bon taux de réussite face à ses concurrents. Du point de vue structurel, l'efficacité de la structure dépend du rapport résistance/poids élevé des matériaux utilisés, en particulier dans les industries aéronautique et automobile. Dans les applications de transport modernes, les structures multicouches sont pertinentes à cet égard et ceci est obtenu en réduisant la masse structurelle sans affecter l'intégrité structurelle, ce qui entraînera considérablement de faibles coûts d'exploitation, des coûts de carburant et une consommation d'énergie.

Les composites sont des matériaux constitués d'au moins deux ou plusieurs matériaux constitutifs ayant des propriétés physiques et chimiques très différentes. A titre d'exemple, un composite renforcé de fibres aura deux matériaux différents appelés (a) fibre (généralement verre ou carbone) et (b) matrice (généralement résine époxy). Lorsque ces deux constituants sont combinés, ils présentent des performances structurelles bonnes ou améliorées par rapport à leurs caractéristiques matérielles individuelles. Par exemple, dans les applications de génie civil, les bétons armés et le bois composite (contreplaqué) sont largement

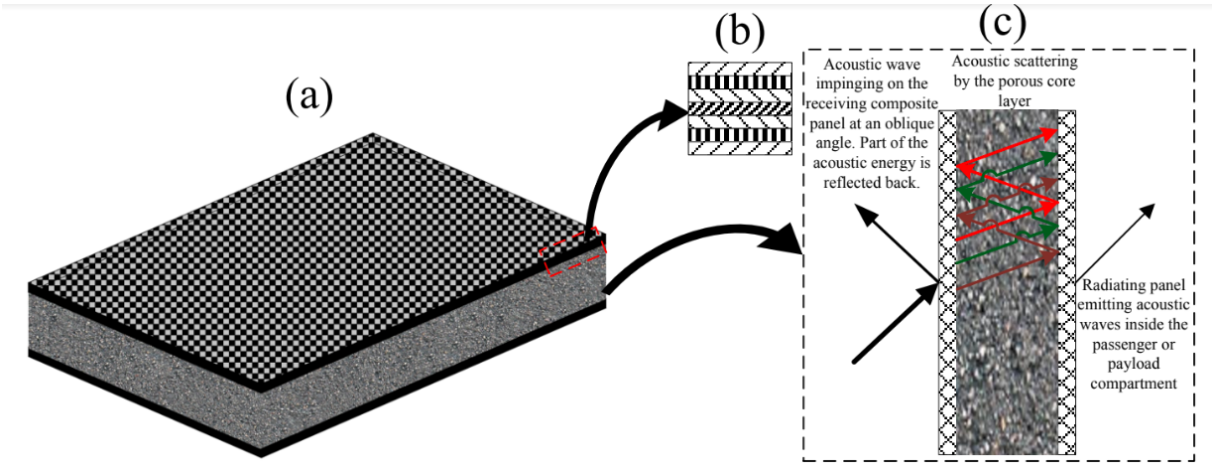


Figure E.1: Un exemple illustratif d'un panneau stratifié et composite complexe, couplé à une couche de mousse métallique (a), combinant une rigidité structurelle élevée, une atténuation acoustique élevée, un amortissement structurel élevé et une faible masse. Une illustration de la stratification typiquement antisymétrique pour la feuille de parement composite (b), ainsi que du phénomène de transmission acoustique à travers la structure multicouche modélisée (c) est également montrée.

utilisés.

Le confort est le facteur clé qui affecte la qualité et la compétitivité des produits structurels. Affectant la vie des humains dans le monde entier, le bruit est la principale forme de pollution environnementale qui a de graves effets sur les relations socio-économiques. Bien que les matériaux composites présentent des caractéristiques structurelles supérieures, ils s'avèrent peu performants en termes de niveaux d'isolation vibratoire et acoustique. De plus, en raison de l'augmentation de l'épaisseur, une structure sandwich légère très connue (faite de composites Fig. E.1) permet aux multiples nombres de vibrations et d'ondes acoustiques de se propager en leur sein, ce qui affecte leurs performances vibro-acoustiques globales. [2].

Une augmentation des niveaux de bruit jusqu'à 7 dB (dans certaines gammes de fréquences) a été observée dans les composites en remplacement des structures métalliques conventionnelles de l'aérospatiale. Pour améliorer l'efficacité mécanique, la sécurité et le confort des passagers, l'isolation vibro-acoustique est incontournable et importante. Des mécanismes de contrôle actif du bruit et d'amortissement visco-élastique sont généralement utilisés, mais cela conduit souvent à des systèmes complexes et lourds. Tout en offrant

Figure E.2: Structure multicouche avec matériaux composites et mousses poro-élastiques.

des comportements vibro-acoustiques améliorés, ces ensembles sonores compromettent les avantages de légèreté qui découlent de l'utilisation de matériaux composites.

Une nouvelle alternative intéressante à ces ensembles sonores conventionnels est l'utilisation de matériaux poro-élastiques dans ces composites multicouches. Ces matériaux poreux peuvent être couplés avec des segments composites multicouches existants soit sous forme de couche poro-élastique supplémentaire, soit sous forme d'inclusions poro-élastiques au sein d'une seule couche. Les matériaux poro-élastiques sont constitués d'au moins deux phases : une phase solide constituée du squelette poreux, et une phase fluide constituée du fluide interstitiel interstitiel. Ce fluide est assez souvent supposé être de l'air, pour les études acoustiques. Les multicouches formées en combinant des couches de nature différente (composites empilés avec des boîtiers sonores poreux, comme le montre la Fig. E.2) offrent de nombreux avantages par rapport aux matériaux conventionnels. En général, les structures multicouches ont une capacité d'amortissement des vibrations très élevée par rapport aux structures métalliques, et elles sont beaucoup plus légères que les mécanismes actifs de contrôle du bruit.

Les multicouches sont également largement utilisés dans l'industrie du bâtiment, où l'isolation acoustique est un critère critique. En utilisant les matériaux traditionnels, tels que les murs en béton, l'augmentation de l'épaisseur d'une couche homogène augmente la masse surfacique mais aussi la rigidité en flexion. Cependant, l'utilisation de parois épaisses n'est pas financièrement faisable. Un autre type de matériau multicouche, connu sous le nom de sandwich, a ensuite été utilisé pour atteindre des performances comparables ou supérieures aux matériaux traditionnels tout en ayant des épaisseurs de paroi et des

coûts réduits. Les sandwichs sont également employés dans les transports (par exemple, les vitrages des véhicules) et la protection des personnes (casques, gilets par balle).

Les matériaux multicouches sont principalement appréciés pour leurs caractéristiques mécaniques polyvalentes, que les matériaux homogènes traditionnels ne fournissent pas. La connaissance de leur comportement dynamique, en revanche, est nécessaire pour exploiter pleinement leurs potentiels. La caractérisation de la structure apparaît alors comme un aspect fondamental du processus de conception.

## Objectifs et structure de la thèse

Comme différents types de matériaux sont utilisés dans le système multicouche, la modélisation de ce système nécessite souvent des types de maillage adaptés au matériau utilisé et augmente le nombre total de mailles dans la modélisation classique par éléments finis. De plus, cela conduirait à un temps de calcul élevé en raison de ces complexités. D'autre part, pour des bandes de fréquences particulières, il reste un défi important de concevoir des structures sandwich (système multicouche) ayant des propriétés d'amortissement optimisées ainsi que de bonnes performances d'isolation acoustique. Par conséquent, dans de nombreux cas d'ingénierie, il est très intéressant de condenser le comportement d'un système multicouche à un matériau monocouche. Cela vise à réduire la taille du maillage du modèle d'éléments finis (EF), ce qui conduira à moins de temps de calcul.

Bien que les modèles de plaques condensées (ou équivalents) existants soient largement utilisés, ils font certaines hypothèses sur les types d'ondes se propageant dans les structures. Par exemple, si une structure multicouche contient une couche molle sensible à la compression longitudinale, le mode de respiration (ou compression) doit être pris en compte dans la formulation théorique des modèles condensés pour prédire correctement le comportement vibro-acoustique du système . Étant donné que les modèles condensés actuels supposent un déplacement normal constant le long de la direction de l'épaisseur multicouche (ignorant ainsi les mouvements d'étirement de l'épaisseur de la structure), ils limitent leur applicabilité aux structures multicouches relativement minces. De plus,

les modèles existants ne peuvent être appliqués que si les couches sont minces et de nature isotrope ou orthotrope. Cela signifie que, dans les cas de couches molles ou épaisses et d'inclusions poro-élastiques dans le système multicouche, ces modèles ne peuvent pas être appliqués. Dans le même ordre d'idées, étant donné que les théories des plaques couramment utilisées pour les applications vibro-acoustiques n'incluent pas le mouvement de compression de la structure, l'estimation d'une limite de fréquence supérieure de ces théories est nécessaire pour leur application en toute sécurité. De plus, les modèles condensés existants conduisent souvent à un temps considérable de mise en œuvre en raison de leurs approches complexes. Cette thèse de doctorat tentera de relever les défis mentionnés ci-dessus en développant des outils robustes, précis et efficaces pour prédire la transmission du son et des vibrations à travers des milieux stratifiés comprenant des matériaux poro-élastiques. Un modèle condensé avancé serait développé et pourrait être appliqué aux systèmes multicouches épais, y compris les poro-élastiques, en capturant les types possibles d'ondes se propageant dans la structure.

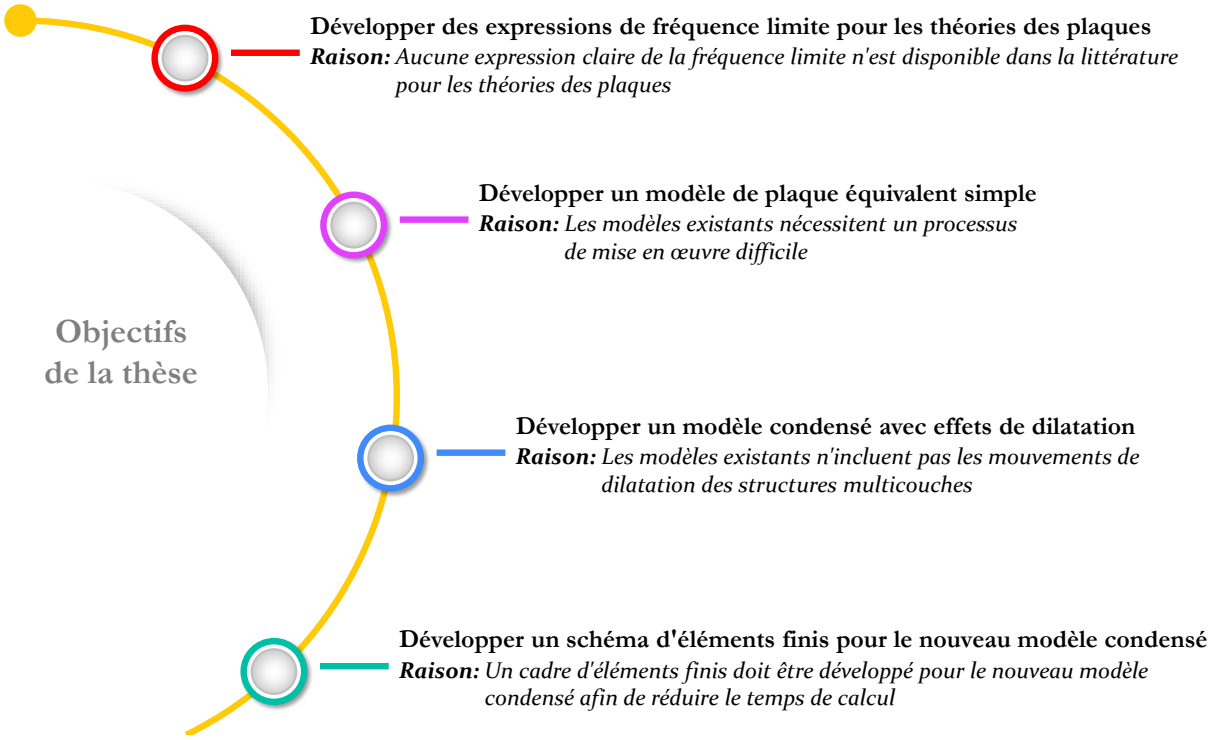


Figure E.3: Objectifs de la thèse.

Dans ce contexte, comme le montre la Fig. E.3, les objectifs scientifiques de cette thèse sont :

1. Développer des expressions analytiques pour les limites de fréquence des théories des plaques couramment utilisées dans les applications vibro-acoustiques;

2. Développer un modèle de plaque condensé (ou équivalent) simple pour les structures à trois couches afin de faciliter les processus de mise en œuvre;

3. Développer un modèle condensé pour le système multicouche qui pourrait simuler le comportement en compression des matériaux souples/épais et poro-élastiques utilisés dans le drapage;

4. Développer un schéma d'éléments finis pour mettre en œuvre le nouveau modèle condensé pour simuler toutes les propagations d'ondes fondamentales, y compris le mouvement de dilatation des structures multicouches.

Concernant la structure de cette thèse, ainsi que la revue complète de la littérature existante, chacun des objectifs mentionnés ci-dessus est abordé dans un chapitre dédié comme le montre la Fig. E.4.

## E.1 Conclusions générales sur les avancées de cette thèse

Les expressions analytiques des limites de fréquence des théories des plaques, qui sont couramment utilisées dans de nombreux modèles analytiques vibro-acoustiques (y compris les modèles condensés), sont dérivées au chapitre 4. Les limites des théories des plaques de Love-Kirchhoff [95, 96] et Reissner-Mindlin [97–99] proviennent respectivement de l'exclusion des mouvements de cisaillement et de compression. L'observation à partir des courbes de dispersion des deux théories des plaques conduit à trouver la fréquence limite pour la théorie de Love-Kirchhoff, alors que l'analyse des admittances permet de déduire la même chose pour les théories des plaques qui supposent un déplacement normal

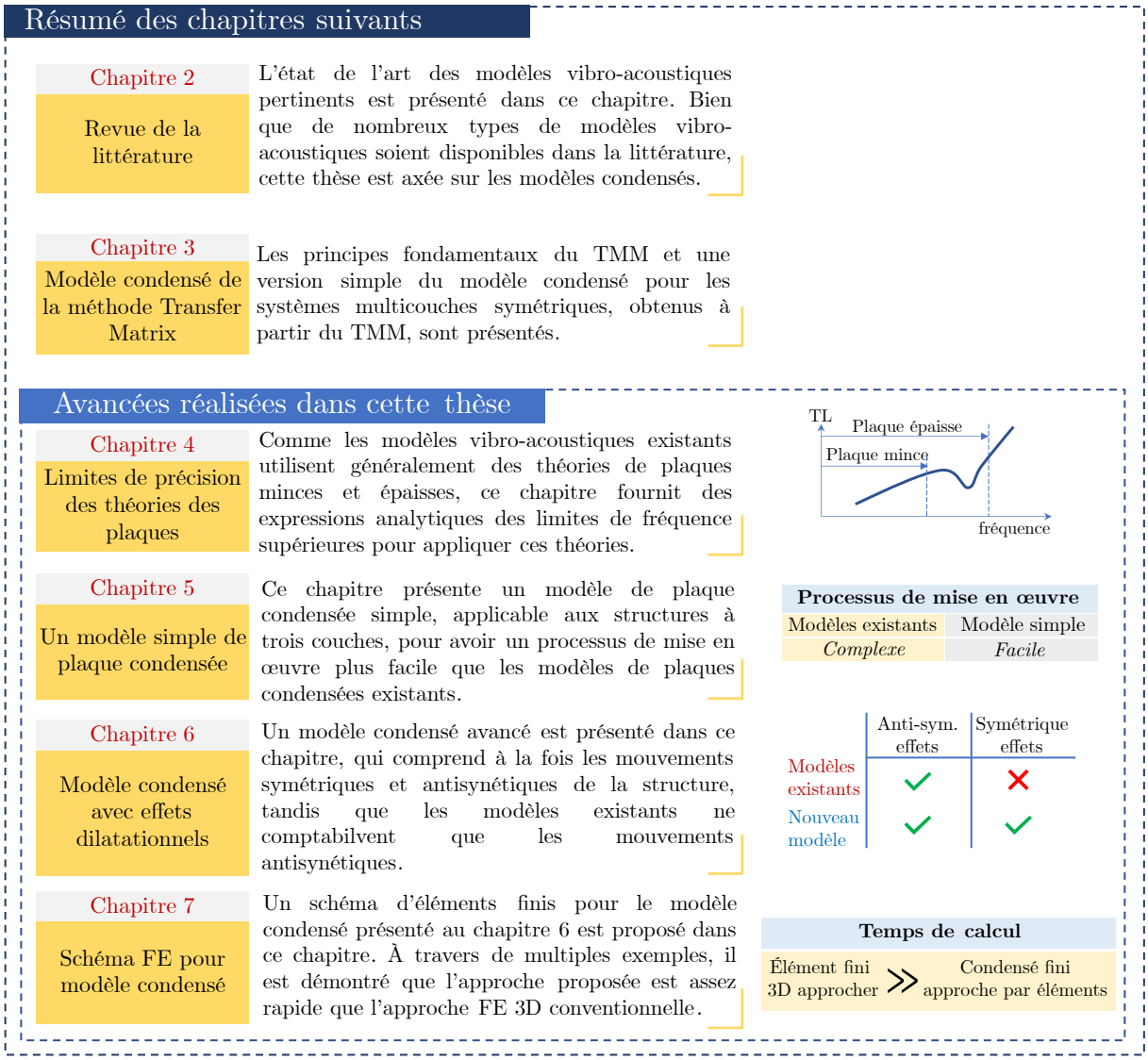


Figure E.4: Organisation et résumé des chapitres suivants de cette thèse.

constant. La validation de ces limites de fréquence est obtenue en comparant les tracés de perte de transmission (TL) obtenus à partir des théories des plaques avec ceux du TMM. De plus, les expressions de coïncidence et de fréquence critique sont affinées à l'aide de la théorie des plaques de Reissner-Mindlin pour une estimation correcte. Bien que des expressions analytiques pour les limites de fréquence soient données, celles-ci sont limitées à une seule couche. Cependant, des analyses de dispersion et d'admittance similaires pourraient être effectuées pour des plaques équivalentes afin de dériver des limites de fréquence.

Un modèle de plaque condensée simplifié pour les structures sandwich à trois couches est présenté dans le chapitre 5, afin de réduire les défis dans les processus de mise en œuvre des modèles de plaques condensées existants. Ce modèle simple a pour fondement la compréhension du comportement physique du système à trois couches à trois régimes de fréquences (à savoir bas, transition et haut) pour dériver seulement quatre paramètres clés qui sont suffisants pour calculer la réponse naturelle à toutes les fréquences. Les propriétés dynamiques condensées obtenues à partir de ce modèle sont comparées au modèle condensé existant ainsi qu'aux données expérimentales, et il est montré que le nouveau modèle donne une réponse adaptée avec les deux. Bien que le modèle soit efficace pour réduire les défis de mise en œuvre, il limite son applicabilité aux seuls systèmes sandwich à trois couches. De plus, comme d'autres modèles de plaques condensées, ce modèle ne prend également en compte que les mouvements antisymétriques et non les mouvements de dilatation, et est donc limité aux structures multicouches minces.

L'un des objectifs de cette thèse est de développer un modèle condensé qui pourrait capturer l'effet du mouvement de compression/dilatation de la structure multicouche. Par conséquent, un nouveau modèle condensé est présenté dans le chapitre 6 qui pourrait gérer à la fois les mouvements symétriques (compression) et antisymétriques (flexion, cisaillement et membrane). Les propriétés condensées, la rigidité à la flexion dynamique et deux densités de masse équivalentes, sont dérivées en supposant deux plaques minces équivalentes non couplées correspondant à des mouvements symétriques et antisymétriques. Ce nouveau modèle a ses avantages d'applicabilité sur les structures multicouches qui contiennent des couches épaisses/molles de toute nature (solide élastique, fluide et poro-élastique). Bien que les effets du mode dilatationnel soient inclus, ce modèle serait limité uniquement aux multicouches symétriques car les propriétés intrinsèques sont obtenues à partir de l'hypothèse que les admittances antisymétriques et symétriques sont découplées. De plus, le modèle présenté peut ne pas convenir à la structure multicouche avec des couches poreuses de très faibles valeurs de résistivité.

Une application importante du nouveau modèle condensé est de les utiliser dans le cadre des éléments finis qui vise à réduire efficacement le temps de calcul. Par conséquent, un schéma d'éléments finis (EF) dédié est proposé au chapitre 7 pour calculer la réponse vibro-acoustique de multicouches symétriques épaisses. Deux plaques découplées sont maillées avec trois propriétés dynamiques condensées et elles sont finalement couplées en utilisant les définitions de vitesse antisymétrique et symétrique de la structure en couches. L'efficacité de calcul du schéma FE proposé est démontrée à l'aide de plusieurs configurations multicouches et, comme prévu, on observe que le schéma FE condensé s'exécute plus rapidement que l'approche FE tridimensionnelle conventionnelle. Du côté de la limitation, le schéma FE condensé sous-estime légèrement la fréquence critique en raison de la négligence de l'inertie de rotation de la structure multicouche épaisse. Par conséquent, une enquête plus approfondie doit être menée à l'avenir pour tenir compte de l'inertie de rotation équivalente.